

# A Biomechanical Evaluation of Cast Porous Ti-6Al-7Nb Implants for Orthopedic Applications by using a Comparative Finite Element Analysis

DISSERTATION

zur Erlangung des Grades eines Doktors  
der Ingenieurwissenschaften

vorgelegt von

M.Sc. Mustafa ALTINDIŞ

eingereicht bei der Naturwissenschaftlich-Technischen Fakultät

der Universität Siegen

Siegen 2019

Referent: Prof. Dr.-Ing. habil. Ulrich Krupp

Koreferent: Prof. Dr.-Ing. habil. Hans-Jürgen Christ

Tag der Disputation: 20.12.2018

I would like to dedicate this dissertation to my mother, Nazime Altindiş. Her support, encouragement, and constant love have sustained me throughout my life. I owe every bit of my existence to her.



## **Acknowledgements**

First and foremost, I would like to express my special appreciation and thanks to my advisor Professor Dr.-Ing. habil. Ulrich Krupp for encouraging my research and for allowing me to grow as a research scientist. His guidance, knowledge, and stimulation of critical thinking and independent ideas have contributed to my success and development. I would also like to thank my co-advisor Professor Dr.-Ing. habil. Hans-Jürgen Christ, for his help and guidance throughout this project and for providing me with the opportunity to complete my PhD thesis at the University of Siegen. I am very grateful to the further members of my dissertation committee.

Ender Koç and Prof. Dr.-Ing. Bernd Schwarze have been very kind and patient whenever I approached them and I acknowledge and appreciate them for all their efforts.

A special thanks also goes to all my colleagues of the MEDFOAM project for their support in the completion of this thesis. Also, thanks Frauke Barske, Dennis Newson, and Dipl.-Phys. Katrin Jahns for proofreading the manuscript.

I gratefully acknowledge the funding sources that made my PhD work possible. I was funded by the Deutsche Forschungsgemeinschaft (DFG). My work was also supported by Hochschule Osnabrück.

Words cannot express how grateful I am to my family member Nazime, Hayal and Göksel Altundiş, for all of the sacrifices that they have made on my behalf. Their prayer for me was what sustained me thus far.



## Abstract

Over the past decade, new developed and refined titanium casting technologies make it possible to produce dental and medical implants. Avoiding impurities and changes of the surface layer by  $\alpha$  case formation are major challenges in titanium casting. In this context, the present results show the effect of four types of investments on the  $\alpha$  case layer of Ti67-castings. In brief,  $Y_2O_3$  based investment materials are a reliable and promising choice for the production of titanium castings compared to Invest-Ti-T,  $Al_2O_3$  and  $ZrSiO_4$  based investment materials, although the processing of this material is comparatively difficult.

It can be concluded that an  $\alpha$  case layer with a suitable thickness has a positive effect on titanium castings and can help to improve mechanical properties such as Young's modulus, flexure stress, and fatigue resistance. In the light of these results, 15  $\mu m$  was determined as a critical thickness value for an  $\alpha$  case layer.

The main objective of this study was to evaluate the implant stability numerically after four weeks and six months implantation time for rat and sheep implants, respectively. The FEA was performed to simulate biomechanical push-out tests.

The simulated average maximum push-out forces are higher than the experimentally measured values. Both 3D model curves reach the maximum push-out force at larger displacements. The computationally predicted stiffness values for both 3D models exhibited a high agreement with the experimentally calculated stiffness. The second stage of 2D model curves were similar to that of measured curves. However, no clear non-linear behavior was observed for both 3D model curves. Meanwhile, 2D models showed a uniform and continuous sliding stage, while implants eluding occurred faster and sliding stages curves were narrow in 3D models. Even though different stress magnitudes were obtained for both groups of rat and sheep implants, the stress distribution at the bone interface was similar.

It can be concluded that 3D simulations were more sensitive than the 2D FE analyses. It should be noted that a detailed bone model is crucial and unit cell assumptions enhances the accuracy of FE analyses. Elongated tetrakaidecahedron unit cells improved the prediction of cancellous bone behavior and the highest accuracy of FE prediction was also achieved.

FEA results allow to make statements about the average behavior of the implant bone interface. High correlations were found between push-out strength as estimated from FE and the experimentally measured push-out strength.



## Kurzfassung

In den letzten Jahrzehnten, ermöglichen neu entwickelte und verfeinerte Titan-Gusstechnologien die Herstellung verschiedenen Zahn- und medizinischer Implantate. Allerdings sind noch viele praktische Probleme zu lösen. Vermeidung der Verunreinigungen und Veränderungen der Oberflächenschicht durch  $\alpha$ -Case Bildung sind große Herausforderungen in Titanguss. In diesem Zusammenhang umfassen die vorliegenden Ergebnisse die Auswirkung von vier verschiedenen keramischen Formmaterialien auf die Entstehung der  $\alpha$ -Case-Schicht von Ti67-Gussteilen. In Kürze,  $Y_2O_3$ -basierte Formmaterialien sind eine zuverlässige und vielversprechende Wahl für die Herstellung von Titan-Gussteilen im Vergleich zu Invest-Ti-T-,  $Al_2O_3$ - und  $ZrSiO_4$ -basierten Formmaterialien, obwohl die Verarbeitung dieses Materials vergleichsweise schwierig ist. Es lässt sich feststellen, dass eine  $\alpha$ -Case-Schicht mit einer optimalen Dicke einen positiven Effekt auf Titan-Gussteile hat und dazu beitragen kann, die mechanischen Eigenschaften wie den Elastizitätsmodul, die Biegebeanspruchung und die Ermüdungsbeständigkeit zu verbessern. Angesichts dieser Ergebnisse wurden  $15\ \mu m$  als kritischer Dickenwert für eine  $\alpha$ -case Schicht bestimmt.

Das Hauptziel dieser Arbeit war es, die Implantatstabilität nach vier Wochen und sechs Monaten Implantationszeit für Ratten bzw. Schafimplantate numerisch zu bewerten. Die FEA wurde durchgeführt, um biomechanische push-out Tests zu simulieren.

Die simulierten durchschnittlichen maximalen push-out Kräfte sind höher als die experimentell gemessenen Werte. Beide 3D-Modellkurven erreichen die maximale push-out Kraft bei größeren Verschiebungen. Die rechnerisch vorhergesagten Steifigkeitswerte für beide 3D-Modelle zeigten ein hohes Übereinstimmung mit der experimentell festgestellten Steifigkeit. Die zweite Stufe der 2D-Modellkurven ähnelte denen der gemessenen Kurven. Für beide 3D-Modellkurven wurde jedoch kein klares, nichtlineares Verhalten beobachtet. Mittlerweile zeigten 2D-Modelle ein gleichmäßiges und kontinuierliches Gleitreibungsverhalten, während die Trennung der Implantate von Knochenaufbau schneller auftraten und Gleitreibungsverhaltenkurven in 3D-Modellen schmal waren. Obwohl für beide Gruppen von Ratten- und Schafimplantaten unterschiedliche Stressgrößen erhalten wurden, war die Spannungsverteilung an der Knochenoberfläche ähnlich.

Es lässt sich feststellen, dass 3D-Simulationen empfindlicher waren als die 2D-FE-Analysen. Es ist anzumerken, dass ein detailliertes Knochenmodell entscheidend ist und die Einheitszell Annahme die Genauigkeit von FE-Analysen erhöht. Langgestreckte Tetraikadehedron-

Einheitszellen verbesserten die Vorhersage des spongiösen Knochenverhaltens und die höchste Genauigkeit der FE-Vorhersage wurde ebenfalls erreicht.

FEA-Ergebnisse erlauben es, Aussagen über das durchschnittliche Verhalten der Implantat-Knochen-Grenzfläche zu machen. Es wurden hohe Korrelationen zwischen der von FE geschätzten Push-out Festigkeiten und der experimentell gemessenen Push-out Festigkeiten gefunden.

# Content

<b>Acknowledgements.....</b>	<b>i</b>
<b>Abstract.....</b>	<b>iii</b>
<b>Kurzfassung.....</b>	<b>v</b>
<b>Symbols and Abbreviations.....</b>	<b>ix</b>
<b>1 Introduction.....</b>	<b>1</b>
<b>2 Literature Review .....</b>	<b>4</b>
2.1 Natural Bone .....	4
2.1.1 Bone structure and composition.....	4
2.1.2 Mechanical properties of bone .....	8
2.1.3 Bone healing .....	13
2.2 Ti and Ti Alloys .....	17
2.3 Fabrication Methods of Cellular Metals.....	23
2.4 Surface Requirements of Biomaterials .....	30
2.4.1 Biocompatibility .....	30
2.4.2 Surface roughness .....	33
2.5 Properties of Cellular Materials .....	35
2.5.1 Fatigue properties .....	42
2.6 Biomechanical Tests .....	43
2.7 Finite Element Analysis .....	47
<b>3 Materials and Testing Methods .....</b>	<b>54</b>
3.1 Ti67 Material.....	54
3.2 Manufacturing of Samples .....	54
3.3 Surface Modification .....	56
3.4 Implantation of Samples .....	57
3.5 Biomechanical Push-Out Test Procedure.....	58
3.6 Determination of Biomechanical Parameters.....	59
3.7 Mechanical Testing .....	59
3.7.1 Rectangular samples .....	59
3.7. 2 Sponge samples .....	61
3.8 Heat Treatment.....	62
3.8.1 Determination of the $\beta$ -transus temperature.....	62

3.9 Hardness Measurement .....	63
3.10 Roughness Measurement .....	63
3.11 Morphological and Analytical Studies.....	64
3.12 Finite Element Modeling.....	64
<b>4 Results.....</b>	<b>73</b>
4.1 Investigation of $\alpha$ Case Formation.....	73
4.1.1 Invest-Ti-T .....	73
4.1.2 Al <sub>2</sub> O <sub>3</sub> -based investment .....	75
4.1.3 ZrSiO <sub>4</sub> -based investment .....	77
4.1.4 Y <sub>2</sub> O <sub>3</sub> -based investment.....	79
4.2 Influence of the $\alpha$ Case Layer on Mechanical Properties.....	82
4.3 $\beta$ -transus Temperature .....	88
4.4 Heat Treatment .....	89
4.5 Mechanical Behavior of Ti67 Sponge .....	96
4.6 Experimental Push-Out Test.....	100
4.7 Finite Element Analysis Results .....	103
4.7.1 Determination of shear strength for rat implants .....	105
4.7.2 2D results for rat implants .....	105
4.7.3 3D results for rat implants .....	106
4.7.4 Determination of shear strength for sheep implants .....	110
4.7.5 2D results for sheep implants .....	111
4.7.6 3D results for sheep implants.....	111
<b>5 Discussions.....</b>	<b>117</b>
5.1 Investigation of the $\alpha$ Case Formation.....	117
5.2 Effect of the $\alpha$ Case Layer on Mechanical Properties.....	121
5.3 Effect of Heat Treatment on the Cast Ti67 Specimens.....	125
5.4 Mechanical Properties of the Cast Ti67 Sponges .....	128
5.5 Properties of CaTiO <sub>3</sub> Reaction Layer on the Cast Ti67 Implants.....	130
5.6 Finite Element Analysis of Biomechanical Push-Out Tests of Porous Ti67 implants.....	132
<b>6 Conclusions.....</b>	<b>144</b>
<b>7 References.....</b>	<b>148</b>

## Symbols and Abbreviations

### Latin symbols

$C_1, C_2, C_3$	[--]	Geometry constants for cellular materials defined by Gibson and Ashby
$E$	[GPa]	Young's modulus
$E^*$	[GPa]	Young's modulus of an open cell foam
$E_s$	[GPa]	Young's modulus of the solid which make a strut
$E_0$	[GPa]	Initial Young's modulus
$F$	[N]	Force
$F_x$	[N]	Longitudinal force during push-out test
$F_y$	[N]	Lateral force during push-out test
$h$	[mm]	Height of a cell strut in a honeycomb defined by Gibson and Ashby
$HV$	[HV]	Vickers hardness
$I$	[kgm <sup>2</sup> ]	Moment of inertia
$l$	[mm]	Length of the cell strut
$M_p$	[Nm]	Plastic moment
$R$	[--]	Stress ratio
$R_a$	[ $\mu\text{m}$ ]	Arithmetic average of the absolute roughness (2D)
$R_{max}$	[ $\mu\text{m}$ ]	Maximum roughness
$R_q$	[ $\mu\text{m}$ ]	Root mean square roughness (2D)
$R_{sk}$	[ $\mu\text{m}$ ]	Skewness of the roughness profile (2D)
$S_a$	[ $\mu\text{m}$ ]	Arithmetic average of the absolute roughness (3D)
$S_q$	[ $\mu\text{m}$ ]	Root mean square roughness (3D)
$S_{sk}$	[ $\mu\text{m}$ ]	Skewness of the roughness profile (3D)
$t$	[mm]	Thickness of the cell strut
$t^2$	[mm <sup>2</sup> ]	Cross-sectional area of a cell strut

## Greek symbols

$\delta$	[mm]	Bending deflection
$\varepsilon$	[--]	Strain
$\varepsilon_D$	[--]	Densification strain
$\theta$	[°]	Angle of a cell strut in a honeycomb defined by Gibson and Ashby
$\rho^*$	[kg/m <sup>3</sup> ]	Density of the cellular material
$\rho_r$	[--]	Relative density
$1 - \rho_r$	[--]	Porosity
$\rho_s$	[kg/m <sup>3</sup> ]	Density of the solid
$\sigma$	[MPa]	Stress
$\sigma_{cr}^*$	[MPa]	Brittle crushing strength
$\sigma_{el}^*$	[MPa]	Elastic collapse stress defined by Gibson and Ashby
$\sigma_{fs}^*$	[MPa]	Rupture strength defined by Gibson and Ashby
$\sigma_{pl}^*$	[MPa]	Plastic collapse stress
$\sigma_{ult}$	[MPa]	Ultimate strength
$\sigma_y$	[MPa]	Yield strength
$\sigma_{ys}$	[MPa]	Yield strength of the solid which make the strut
$\nu^*$	[--]	Poisson's ratio for foam metal

## Abbreviations

bcc	Body centered cubic
BMPs	Bone morphogenic proteins
BSE	Back scattering electron
BSP	Bone sialoprotein
Ca-Ti	Calcium titanate
CE	Counting electrode
CTE	Coefficients of thermal expansion
CVD	Chemical vapour deposition
DIN	Deutsches Institut für Normung
DSC	Differential scanning calorimetry
EBSD	Electron back-scattered diffraction
ECM	Extracellular matrix
FGFs	Fibroblast growth factors
HA	Hydroxyapatite
hcp	Hexagonal closed packed
HD	High density
HDI	High-density inclusions
HIP	Hot isostatic pressing
IGFs	Insulin growth factors
LD	Low density
LDI	Low-density inclusion
LOF	Weld lack of fusion
MD	Medium density
MTD	Main trabecular direction
μCT	Micro-computer tomography
OCP	Open-circuit potential
OPN	Osteopontin
PCF	Powder compact foaming
PLGA	Poly (lactic-co-glycolic)
PMMA	Polymethyl metha crylat
ppi	Pores per inch
ppm	Parts per million

PSR	Pseudo saturation region
PTFE	Polytetrafluorethylene
RE	Reference electrode
rpm	Revolutions per minute
SB	Salt bath
SBF	Simulated body fluid
SCE	Saturated calomel electrode
SD	Standard deviation
SE	Secondary electron
SEM	Scanning electron microscope
TAT	Tensile adhesion test
TGF- $\beta$	Transforming growth factor beta
Tb.Sp.	Trabeculae spacing
Tb.Th.	Trabeculae thickness
TMT	Thermo mechanical treatment
UHMWPE	Ultra-high-molecular-weight polyethylene
WE	Working electrode
XRD	X-ray diffraction
ZTA	Zirconia toughened alumina

## 1 Introduction

Biomaterials are used to replace lost body structures and to assist or replace human organs, and meet the increased life expectancy of patients [1]. During the past decades, the use of biomaterials in medical technology has become one of the most promising research fields for improving life quality [2]. Materials used for biomedical applications cover a wide range of choices of materials that fall into four different groups: metals, ceramics, polymers and their composites [3]. Materials used for biomedical applications must exhibit specific properties. Most of the currently used biomaterials are not specifically developed for biological applications, and, hence, their effectiveness is questionable. Yet, there have been continuing improvements in biomaterials selection and treatment. Compatibility of the biomaterials with natural tissue has paramount importance for the acceptance of the material by the human body. Knowledge of the interactions between the materials and the body is essential for designing new biocompatible biomaterials [1, 4].

Biomaterials as a field of study and research has changed and improved continuously in combination with technological advances in medicine, biology, chemistry, materials science and engineering. Over the last two decades, interdisciplinary consortiums have had a sustainable impact on the development of various biopolymers, metal alloys and ceramics, and also their combination as utilized in medical devices and implants [5].

Pure titanium and some titanium alloys including Ti6Al7Nb (hereafter Ti67) have demonstrated success in both medical and dental fields, especially for bone-anchoring systems including orthopedic implants and osteosynthesis applications [6]. Nowadays, due to their excellent mechanical, physical and biological performance, titanium alloys are the most promising metallic materials for implant devices. They have been used to replace failed hard tissue including artificial hip joints, artificial knee joints, bone plates, screws for fracture fixation, cardiac valve prostheses, and artificial hearts [7].

It is known that bone replacement materials should not only provide adequate mechanical strength in order to sustain physiological loads, but also provide acceptable biological, chemical and physical properties to facilitate tissue attachment, regeneration and/or healing [8]. For instance, hydroxyapatite (HA) is known for its excellent biocompatibility and bioactivity. However, its usage as a bone replacement material has been hindered by the difficulty of matching the mechanical properties of bone tissue, due to its weakness and brittleness [9]. Therefore, new developments in the design of orthopedic implants have tried to aggregate

strong metallic and bioactive Calcium Phosphate (CaP) materials, which are meant to satisfy both mechanical and bioactive requirements [9, 10].

The most important limitation to Ti and its alloys used in clinical practice, orthopedics and dentistry is the difference in elastic modulus between the metallic implant of Ti and bone tissue [11]. For instance, the modulus of Ti67 alloy is 110 GPa, while the elastic modulus of a cortical bone is close to 18 GPa. In such a case, the high elastic modulus of the implant material leads to large stress-shielding from the surrounding bone tissues, and consequently to poor fixation between the implant and tissues, and thus an unsuccessful implantation procedure [12]. Nowadays, the low modulus alloys are preferred whose modulus are much more similar to that of bone and the fabrication of pores in the implant structure can be aided, thus solving of the modulus mismatch problem [13].

It is known that the usage of porous Ti implants solves the modulus mismatch problem. Not only does implant loosening decrease but implant life-time also increases due to the usage of porous metals with low elastic modulus as compared to those of bulk metals [14]. Apart from this, interconnected pores provide better interaction with bone, significant enhancement in the rate of bone formation and implant bone fixation through a higher degree of body fluid transportation. Furthermore, in order to shorten the bone fixation time, the surface of titanium implants can be coated with CaP materials, which are known for their excellent bioactive and osteoinductive properties. Recent studies have shown that coated implants lead to rapid implant fixation and a stable interface between bone and biomaterial surface [15].

*In vivo* researches have been performed to evaluate the osseointegration, response to the implant design parameters and assert how the material's characteristics may affect the short- and long-term stability of the metallo-biological interface [16]. Despite the technical difficulties of *in vivo* analysis and the limitations of current histological examinations and biomechanical tests, reliable computational models can be beneficial for decision-making in terms of implant treatments and design [17].

Finite Element Analysis (FEA) has been widely applied to the field of biomedical engineering in order to model and predict the biomechanical performance of various implant designs. Furthermore, the effect of clinical factors on implant success may be determined by means of these predictions. The analysis is based on a realistic theoretical model, whose structure and conditions are predetermined by some experimental results and assumptions depending on the physiologic condition. The stress and strain distributions in the model are usually presented as a result. For instance, the interface stress distribution in the area where the implants contact with bone, can be evaluated by using FEA [18]. FE modeling has become an

encouraging tool in dental and orthopedic biomechanics due to some critical advantages such as the possible determination of optimal implant shape and the implant treatment plan, which are essential to improve prediction of the long term survival of implants. Moreover, it allows the simulation of complex geometries. FEA has assisted researchers and clinicians in designing and has also brought researchers and clinicians closer together [19].

Within the framework of this PhD thesis, FEA was used to simulate biomechanical push-out tests and to evaluate the stress distribution at the bone implant interface. The FE results were verified through a comparison with push-out test results. This dissertation presents part of the results of research activities within the project "Manufacturing and Characterization of Open Cellular Metallic Implants with Biological Reaction Layer" (MEDFOAM) that was financially supported by Deutsche Forschungsgemeinschaft (DFG), as an interdisciplinary cooperation between four German project partners. MEDFOAM covers every obligatory step for the development of a new biomaterial: from production and modification up to the suitability testing of a novel material for medical applications.

The Foundry Institute of RWTH Aachen University was responsible for the development of the casting process and manufacturing of porous titanium structures. Methods for the application of bioactive coatings to raise the biocompatibility of these structures were investigated by The Federal Institute for Materials Research and Testing (BAM) Berlin. In order to analyze biocompatibility of the new implant material in detail, *in vivo* and *in vitro* test were carried out at The Laboratory for Experimental Accident Surgery of the Justus Liebig University (JLU) Giessen. Bone-implant fixation was investigated experimentally at the Institute of Material Technology of the University of Siegen and also theoretically by using FEA at the Institute of Materials Design and Structural Integrity at the University of Applied Sciences Osnabrück.

## 2 Literature Review

### 2.1 Natural Bone

Bone develops in a variety of shapes and has a highly organized hierarchical structure. It is a living, growing, unique tissue and serves multiple functions. Two main functions of bone are: providing structural support to maintain the shape of the body and protecting the internal organs i.e. skull (brain), ribs (lungs, heart) and pelvis viscera. Additionally, bones transmit the force of muscular contraction from one part of the body to another during movement. Apart from the mechanical function, bones act as a mineral, whereby endocrine systems regulate the level of calcium and phosphate ions in the circulating body fluids and also contribute to physiological functions such as formation of blood cells and storage of minerals. As a living tissue, bone should be well-adapted to changes in its biological environment in order to accomplish its functions continuously throughout its lifetime [20, 21]. The characteristics of bone's structural adaptation are determined by the hormonal changes and lifestyle. Experimental studies and computational models have been developed to understand the response of bone to different changes in its environment [22].

#### 2.1.1 Bone structure and composition

Bone is a composite material and consists of both an organic and inorganic phase. It contains different structures on different levels. These levels and structures are (i) macrostructure (continuum), (ii) microstructure (tissue), (iii) sub-microstructure (cellular), (iv) nanostructure (molecular), and (v) sub-nanostructure. These five structural levels of the hierarchy can be distinguished in adult human bone as seen in Figure 1 [23]. At the macrostructure level, the scale is 5 mm and higher. At this level, bone is composed of two main types of tissues: dense cortical bone and porous cancellous bone. This combination of trabecular and cortical bone has the form of a "sandwich-type" structure. At the tissue level, the scale of 100  $\mu\text{m}$  to 1 mm, the difference between two tissues is in geometrical arrangement of the microstructure and they are categorized according to their levels of porosity. The proportion of cortical and trabecular bone is different at various locations in the skeleton [20-23].

At the cellular level, on the scale of 5 to 50  $\mu\text{m}$  two types of bone can be found: non lamellar bone and lamellar bone. Major differences can be identified within the cortical and trabecular

structures at this level. Non lamellar bone is also known as immature or woven bone; lamellar bone is also known as mature. The bones are built by haversian system, osteons and single trabecular.

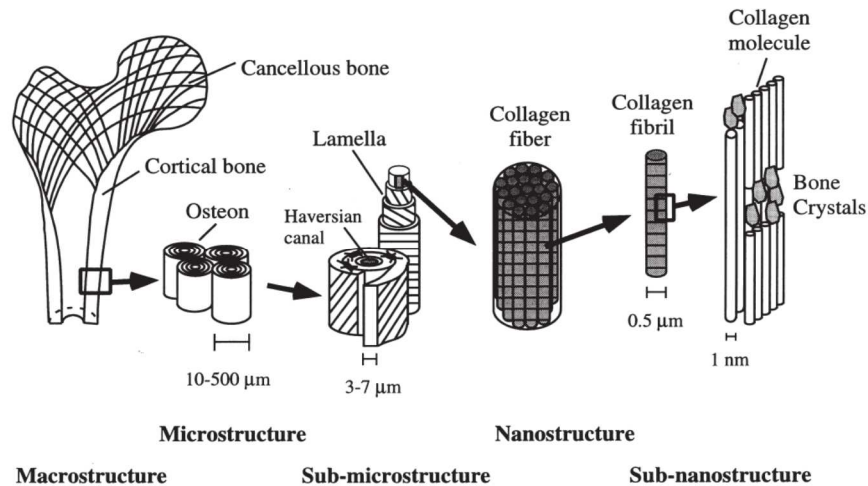


**Figure 1.** Hierarchical structural organization of bone [23].

The skeletal embryo consists of woven bone, which is later replaced by lamellar bone. There are many differences in composition, organization, growth and mechanical properties, between the two types of bone [20]. While woven bone is quickly formed and poorly organized with an arrangement of collagen fibers and mineral crystals, lamellar bone is slowly formed, highly organized and has parallel layers that make it stronger than woven bone [21].

Woven bone is the first bone that is formed during the embryonic development, and is typically seen in young individuals. As time passes, it is replaced by other bone types. Woven bone is also found at early stages of implant osseointegration or fracture healing [21-23]. On the other hand, almost all of the bone tissue in the adult skeleton consists of lamellar bone. At this hierarchical level, all bone tissue either lamellar or woven, is comprised of mineralized collagen fibrils. The nanostructural level bone stands for the molecular structure of constituent elements. The collagen fibers, surrounded and infiltrated by the mineral, are the most prominent structures seen at this scale [23].

Crystals, collagens, and non-collagenous organic proteins are the three main materials of the sub-nanostructures [24-26]. The various collagen forms are only a few nanometers wide (fibrils, 1.5-3.5 nm; fibers, 50-70 nm). Collagen plays an important role in the capacity of bone to absorb energy and on its toughness, due to a decisive influence of the mineral phase on the stiffness of the tissue. Furthermore, different mechanical responses of the collagen can be raised depending

on the spacing, orientation, length of collagen fibers and the strength of intermolecular interactions [22].

The crystals of bone, occurring within the discrete spaces within the collagen fibrils, are plate-shaped, with average lengths and widths of just tens of nanometers and some 2-3 nm thick [21-23]. The anisotropic properties of bone are achieved by the arrangement of bone crystals and the size, shape, and volume fraction of the crystals effect the mechanical behavior of bone [23].

Non-collagenous organic proteins, including phosphoproteins, regulate the size, orientation, and crystal habit of the mineral deposits, serving as a reservoir for calcium or phosphate ions for mineral formation [22, 23].

### 2.1.1.1 Cortical bone

The outer hard layer of bone tissue is called the cortical bone, known also as a compact or a dense bone (see Figure 2a). The porosity range of cortical bone is between 5% and 10% [25]. The internal table (inner) and external table (outer) of flat bones and along the exterior shaft section of long bones are formed by cortical bone, accounting for about 80% of the total skeletal mass of an adult skeleton. This part of the tissue gives bones their smooth, white, and solid appearance [27]. Well organized and repeated osteons are the primary structural unit of highly dense cortical bone. Their diameter ranges from 10 to 500  $\mu\text{m}$  and is also called haversian system. Cylindrical osteons run roughly parallel to the centerline axis of the bone. Osteons consist of cylindrical shaped lamellar bone that surrounds longitudinally haversian canals composing of blood vessels, nerves and loose connective tissue in parallel to the long axis of the bone. Haversian canals are typically 40 to 50  $\mu\text{m}$  in diameter and each canal is surrounded by 4-20 concentric lamellae of collagen fibres [21, 23, 26].

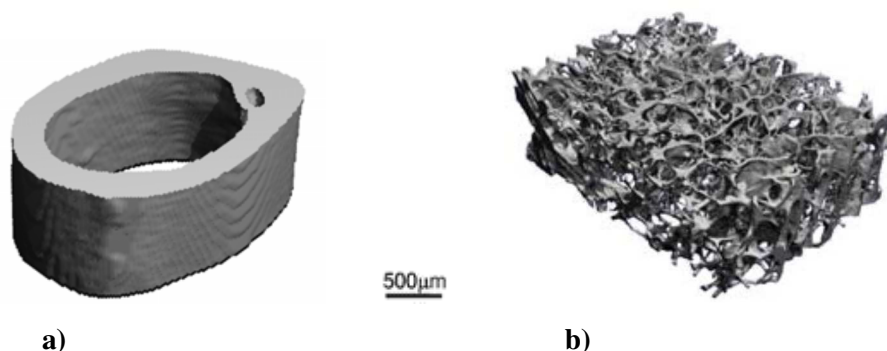


**Figure 2.** Computer tomography image of **a)** cortical bone and **b)** cancellous bone [25].

### 2.1.1.2 Cancellous bone

The interior of the bone is known as the spongy bone (or cancellous or trabecular bone). Unlike cortical bone, cancellous bone is highly porous and consists of an interconnected network of trabeculae, which is about 50-300  $\mu\text{m}$  in diameter (see Figure 2b) [25]. It is composed of plates and struts with a thickness of about 200  $\mu\text{m}$  and a variable arrangement of rod- and plate-like elements. Trabeculae are typically 100-200  $\mu\text{m}$  thick, and the spacing between them generally ranges from 500 to 1000  $\mu\text{m}$ . These make the tissue lighter and allow space for blood vessels and marrow [27].

The structure of trabecular bone is a latticework of struts (trabeculae) giving trabecular bone its distinctive and interesting mechanical properties. Spongy bone accounts for 20% of the total bone mass and it constitutes some 70% for the skeletal volume. It has nearly 10 times the surface area of compact bone and has a very high surface to mass ratio [28]. Trabecular bone has a porosity ranging from 75% to 95% and its three-dimensional structure consists of interconnected pores, much like a sponge, having varying diameters of 50-450  $\mu\text{m}$ . The non-mineralized spaces within trabecular bone contain bone marrow composed of blood vessels, nerves and various types of cells. Trabecular bone functions as a cushion against shock in the skeletal system because of its spongy structure providing a large surface area for metabolic activities of bone. By this means, mechanical strength increases without the disadvantages of undue weight [25, 28].

### 2.1.1.3 Composition of bone

Bone is made up of both organic and inorganic materials. Bone contains around 10% water by weight. A range from 60 to 65% of the weight of dry bone is composed of inorganic materials. Approximately 95% of the inorganic material is a calcium phosphate crystalline hydroxyapatite and the remaining 5% are various impurities such as carbonate, chloride, or fluoride as tabulated in Table 1 [23, 25, 28]. There are other mineral ions in bone structure such as citrate ( $\text{C}_6\text{H}_5\text{O}_7^{4-}$ ), carbonate ( $\text{CO}_3^{2-}$ ), fluoride ( $\text{F}^-$ ) and hydroxyl ions ( $\text{OH}^-$ ), which may bring subtle differences in the microstructural features of bone. Additionally, dry bone consists of organic matrix of fibrous protein and collagen (25-30%). A highly aligned type I collagen structure, which yields a very anisotropic structure, is the primary organic material in bone. Osteoid is the unmineralized organic matrix composed of 90% type I collagen and 10% ground substances, such as glycoproteins, peptides, carbohydrates and lipids. This organic component

of bone is predominantly responsible for its tensile strength. The mineralization of osteoid by inorganic mineral salts provides bone with its strength and rigidity [29]. Bones also contain small quantities of magnesium, fluoride and sodium [23].

**Table 1.** The overall composition of bone [23, 25, 28].

Inorganic phase	wt %	Organic phase	wt %
Hydroxyapatite	60	Collagen	20
Carbonate	4	Water	10
Citrate	0.9	Non-collagenous proteins	3
Sodium	0.7	(sialoprotein, serum proteins etc.)	
Other traces: Cl <sup>-</sup> , F <sup>-</sup> , K <sup>+</sup> , Sr <sup>2+</sup> , Pb <sup>2+</sup> , Zn <sup>2+</sup> , Cu <sup>2+</sup>		Other traces: Polysaccharides, lipids cytokines and primary bone cells	

### 2.1.2 Mechanical properties of bone

The mechanical properties of bone, changing permanently in terms of the mechanical environment, depend on several factors including, age, sex, anatomical location, load orientation, geometry/architecture, arrangement of collagen fibers and mineral particles, bone density and bone diseases. The mechanical properties of the cortical and cancellous bone are rather different, as illustrated in Table 2 [23-25]. Cortical bone works as the protective shell for trabecular bone, together providing resistance to bending, torsional and compressive forces. For instance, cortical bone suffer greater stress but less strain before failure since it is stiffer than cancellous bone. On the other hand, in comparison with cortical bone, cancellous bone has a greater energy absorption capacity [29, 30].

Cortical bone is semi-brittle, viscoelastic and anisotropic, and these material properties are influenced by porosity, mineralization level and the organization of the solid matrix. Its mechanical strength is directly dependent on the tight packing of the osteons [23-27, 31]. Its relative density or volume fraction, trabecular microstructure, and trabecular tissue properties indicate the mechanical properties of trabecular bone. Particular attention should be given to the understanding of the complex micro architecture of trabecular bone [31].

In detail, the inorganic components and the organic components have extremely different mechanical responsibilities and properties. The mineral phase, dominating the elastic behavior of bone, is approximately 100 times stiffer than the organic phase [32]. Consequently, inorganic components are mainly responsible for the compression strength and stiffness.

**Table 2.** The mechanical properties of human cortical and cancellous bone [24].

Properties	Measurements	
	Cortical Bone	Cancellous Bone
Young's modulus (GPa)	14-20	0.05-0.5
Tensile strength (MPa)	50-150	10-20
Compressive strength (MPa)	170-193	7-10
Fracture toughness (MPa m <sup>1/2</sup> )	2-12	0.1
Strain to failure	1-3	5-7
Density (g/cm <sup>3</sup> )	18-22	0.1-1.0
Apparent density (g/cm <sup>3</sup> )	1.8-2.0	0.1-1.0
Surface/bone volume (mm <sup>2</sup> /mm <sup>3</sup> )	2.5	20
Total bone volume (mm <sup>3</sup> )	1.4x10 <sup>6</sup>	0.35x10 <sup>6</sup>
Total internal surface (mm <sup>2</sup> )	3.5x10 <sup>6</sup>	7.0x10 <sup>6</sup>

In contrast, brittle organic components of bone provide the corresponding tension properties due to behaving as a compliant material with high toughness, which is much higher in the transverse direction than in the longitudinal one, and low modulus. The combination of the elastic-plastic behavior of the mineral with pure elastic deformation of the collagen matrix is assumed to be the macroscopic plastic deformation [28, 33].

The combination of the porous structure and the composite behavior of bone tissue is thought to be optimized to achieve a remarkable mechanical performance, resulting in several extraordinary mechanical properties including heterogeneity, anisotropy and asymmetry (different response in tension vs. compression) [29, 32].

Principally, the mechanical properties of bone vary with anatomical location and the loading direction because of its anisotropic structure. Anisotropy of cortical bone is mainly controlled by lamellar and osteonal orientation, while anisotropy of trabecular bone is determined by trabecular orientation [33]. It is known that structural anisotropy has a direct influence on stiffness properties as well as on strength. It is reported that the strength of cortical bone in the longitudinal direction is about 79-151 MPa in tension and 131-224 MPa in compression, respectively [25]. On the other hand, the tensile strength in the transverse direction is only between 51-56 MPa in tension and the compressive strength value ranges from 106 to 133 MPa [27]. The Young's modulus of compact bone in the longitudinal direction (17 to 20 GPa) is approximately 1.5 times its modulus in the transverse direction (6 to 13 GPa). Furthermore, the mechanical strength of cancellous bone is not a consistent and varies not only longitudinally but also from one bone to another [25, 29, 32]. Cancellous bone exhibits much broader

mechanical properties compared to those of cortical bone. It is widely accepted that each trabeculae follows the lines of stress, and can be realigned by changes in the direction of stress and the remodeling stimuli depends very strongly on the mechanical loading of the bone. In other words, the relative density of trabecular bone depends on the load that it suffers, with high density structures being developed where the stress is high. In this sense, if the loads are equivalent in the three directions of bone, a structure with equiaxed cells can be obtained. In contrast, the trabeculae tend to align in the load direction, adopting an anisotropic structure, if the load is higher in one direction [22, 24, 34].

### 2.1.2.1 Compression behavior

Healthy trabecular bone, whose compressive stress-strain curve is depicted in Figure 3, can be characterized by three distinct regions [27]. It behaves very similarly to porous metals and plastics. The initial is a stiff, non-damaging region of loading up to the maximum stress. The bending of trabeculae is responsible for this elastic regime. This is followed by a decrease in stress with applied strain to a minimum stress where the curve reaches a horizontal region. The second region is associated with elastic buckling, plastic yielding or brittle fracture of trabeculae. The trabecular bone absorbs large amounts of energy owing to the plastic behavior of the bone during pore collapse as well as fracture and buckling of individual trabeculae. The horizontal region of the stress-strain response is characterized by pore collapse. In the final part, significant deformation pore closure occurs and cell walls or trabeculae touch each other, thus increasing stiffness and raising the stress value until fracture [29, 32, 35].

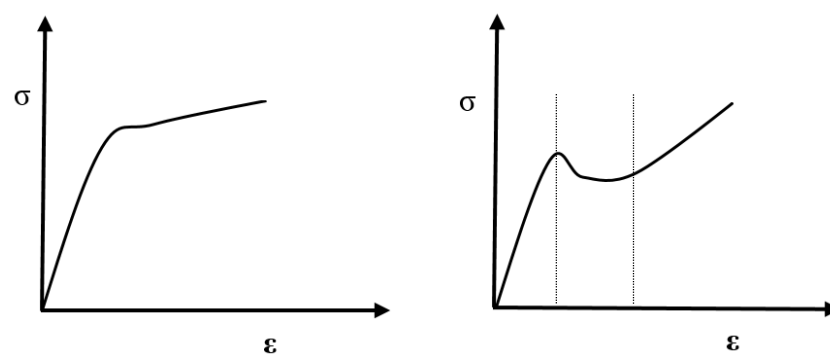


**Figure 3.** Compressive stress-strain curves along the axis of a long bone  
**a)** for cortical bone **b)** for trabecular bone [27].

When the crack morphology of the trabecular bone is investigated, it is observed that shear failure and complete fracture of individual trabeculae were only found in elements oriented transversely to the loading direction [34].

It is generally accepted that the mechanical properties of trabecular bone are related to their density. For example, the Young's modulus is proportional to the square of the relative density, while the tensile yield strain is independent from density due to axial yielding of trabeculae [29]. Moreover, the compressive yield strength and energy absorption increased with increasing apparent density.

### **2.1.2.2 Tension**

Tensile stress-strain curves for trabecular bone are generalized by an initial linear elastic stage, followed by a non-linear deformation until reaching a maximum stress value where crack initiation starts. In tension, the mineral content has an increasing effect on the Young's modulus of the compact bone. Trabecular bone has a higher strength in compression than in tension. Its tensile-compressive yield strength ratio is obtained around 0.6, which means that the strength is asymmetric [29].

### **2.1.2.3 Fatigue**

Bones are subjected to fatigue because of the action of cyclic loading resulting from daily activity or prolonged exercise. Fatigue loading is one of the primary causes of human bone failure. Cyclic loading causes damage and initiates crack, even though the load and stress amplitude is far below yield strength. Cyclic failures of bone due to accumulation of plastic strain is known clinically as overuse injuries or stress fractures. Accumulation of micro-cracks of bone structure results in fatigue damage. It has been suggested that this micro damage initiates remodeling processes. Micro-cracks should be repaired completely through bone remodeling, otherwise they accumulate and coalesce, which is the main reason for decreasing bone stiffness and increasing of fracture risk [34].

The fatigue behavior of trabecular bone is characterized by an increase of residual strain on unloading ( $\epsilon_{res}$ ), a broadening of the hysteresis loops, and by a decrease of the secant modulus. Although the cyclic deformation of trabecular bone can be affected by density and the anatomic position, the fatigue behavior of trabecular bone exhibits the common fatigue curve with three stages. Figure 4 shows the main phases of the cyclic deformation behavior [34]. It can be characterized by an initial increase of the strains with the number of cycles (the transient region), followed by a zone where the strain range is almost constant (the pseudo saturation region (PSR)) and finally a third zone which is characterized by a rapid increase of strains until failure [34, 35].

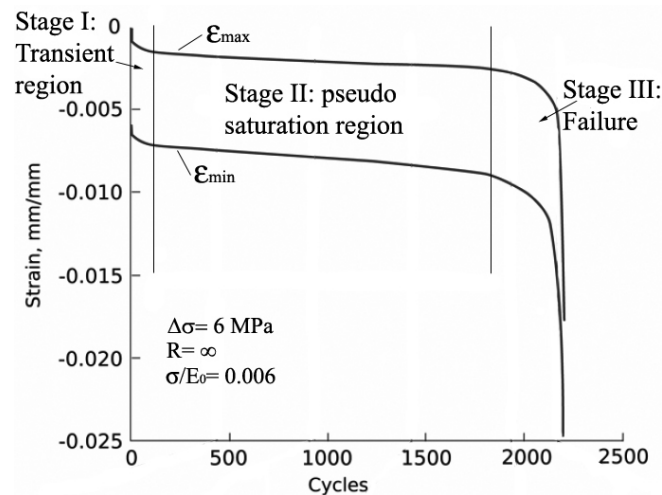


**Figure 4.** Strain evolution as a function of numbers of cycles of bovine cancellous bone [34].

If a trabecular fractures completely, stresses are redistributed to nearby trabecular, leading to greater damage rates, and then failure occurs rapidly. At a localized level, the peak tissue stresses are reduced because of the early load cycle's material degradation. However, in these high stress regions, significant modulus degradation and permanent strains are obtained during the fatigue life. On a global level, significant modulus degradation is observed after a fracture of trabecular. According to this micro damage evaluation in trabecular bone, a fatigue endurance limit at a normalized stress level of  $\sigma/E_0 = 0.0035$  has been reported. Also, the accumulated permanent strain at failure was typically 10 % of the initial applied apparent strain [34].

Although many recent studies suggested that creep effects are negligible in low-cycle fatigue tests, the exact influence of creep is controversial. Moore et al. [35] seem to think otherwise. Creep plays an important role on physiological load levels and a dominant on the non-traumatic bone fractures. According to Haddock et al. [36], a decreasing of the secant modulus and a broadening of the hysteresis loops can be associated with the cyclic creep effect. The moving of the stress strain hysteresis along the strain axis during cyclic compression is caused also by cyclic creep.

A reduction of the secant modulus was observed not only in cortical bone but also cancellous bone, as a result from the formation and growth of micro cracks. In the case of low-stress, high-cycle fatigue of trabecular bone, crack growth and propagation was observed as the primary failure mechanism. On the other hand, creep deformation and fracture were suggested for the primary failure mechanism for high-stress low-cycle fatigue [34-36].

### 2.1.3 Bone healing

All broken bones, whether a bone has been cut surgically or fractured through an injury, go through the same complex and multifactorial healing process, which differs in speed and success among individuals. The bone healing process is divided into three overlapping stages: inflammatory phase, repair phase and remodeling phase (see Figure 5). Generally, in six to eight weeks bone can be healed to a significant degree. The time required for bone healing depends on many factors, involving fracture type, patient's age, nutritional status and medical conditions [37].

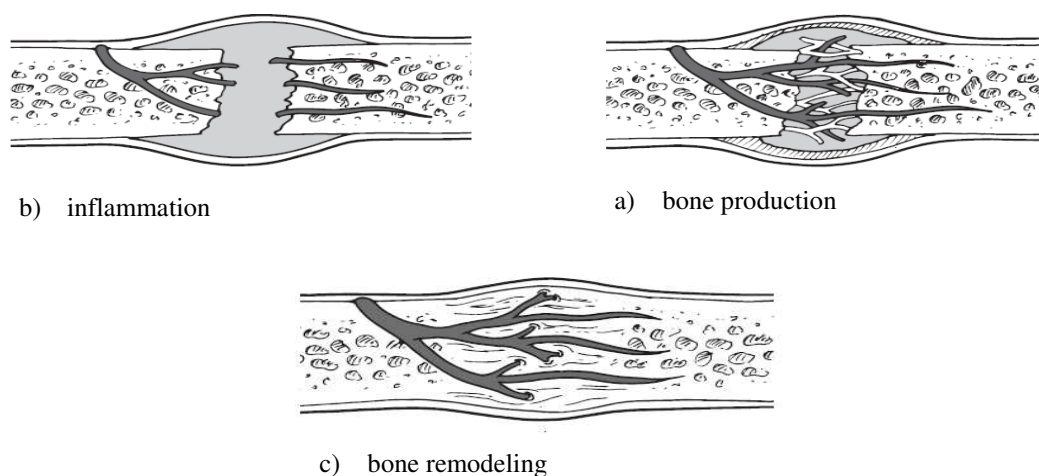


**Figure 5.** The three stages of the bone healing process [37].

#### 2.1.3.1 Inflammatory phase

The inflammatory phase is the first stage of healing and begins immediately after the bone is fractured. This phase should be completed within three to four days, unless the amount of force that caused the fracture is big. Following bone trauma, which occurs either from the implantation procedure or because of the fracture, numerous blood vessels are disrupted. This can be resulted in subsequent extravasation of blood, a damage on the cortical bone, periosteum and surrounding soft tissues. The blood loss is minimized by contraction and thrombosis of ruptured vessels. However the ischemic bone necrosis, which is the result of the traumatic interruption of the blood flow, cannot be prohibited. Blood rapidly coagulates to form a fibrin-rich clot at the fracture site, initiating spontaneous fracture healing. This clot acts as a scaffold for cells, and provides a source of growth factors, playing an important role in the healing process. The initial stage of bone regeneration and the inflammation phase starts in this way.

As a result of this the initial structural stability and framework for producing new bone may be provided. At the end of inflammation, cartilage can be formed or bone is initiated [37].

### **2.1.3.2 Repair phase**

The second stage, beginning approximately on the fifth day after injury and continues for four to six weeks, is characterized by an increased fibroblast activity. The body begins to proliferate cells for replacing the damaged cells and scar tissue becomes organized, leading to an increased connective tissue strength and formation of adhesion. The reparative stage can be separated into two sub phases: the soft and the hard callus phase [38].

Bone production begins with the soft callus phase in which the clotted blood that was formed by inflammation is replaced with fibrous tissue and cartilage. The soft callus is transformed completely into woven bone. The release of mineral compounds and mineralization of the soft callus subsequently transform into hard callus at the center of the fracture site, which can be seen on X-rays several weeks after the fracture. At the end of the repair phase, bone union is achieved and the injured bone has regained enough strength and rigidity to allow low impact exercise [37, 38].

### **2.1.3.2 Remodeling phase**

During the remodeling stage, which is the final phase of bone healing and lasts for several months up to more than half a year, bone continues to form [39]. It becomes compact, and eventually returns to its original shape. Woven bone is gradually replaced by a lamellar bone which is highly organized along lines of stress and turns out to be much stronger. Furthermore, the repaired tissue remodels itself and blood circulation in the area improves [38]. The remodeling phase can be characterized by a morphological adaptation of bone to regain optimal functionality and strength. This slow process represents 70% of the total healing time of bone fracture and may last for six to nine years in humans depending on several factors. The correlation of bone healing with time can be seen in Figure 6. Bone remodeling, repairs microscopical damage, prevents accumulation of fatigue damage and provides the fine tuning to obtain optimal mechanical efficiency. After completion of the healing process, the bone should be at least as strong as it was originally. Thus, to increase bone strength, weight bearing exercise might be encouraged at the bone remodeling stage of fracture healing [37-39].

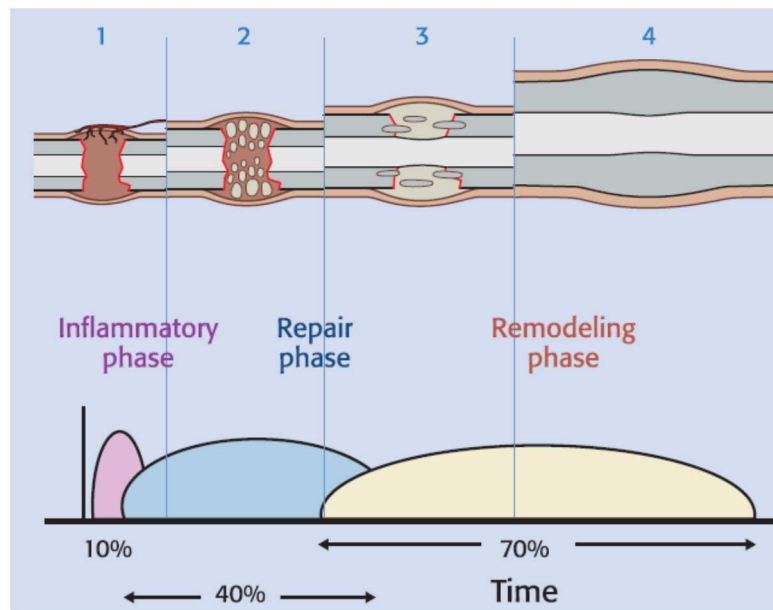


**Figure 6.** Correlation of bone healing with time [39].

### 2.1.3.3 Requirements for bone healing

Many variables, including mechanical stability, biochemical factors and vascular supply, have significant influence on fracture healing. Although many of the basic influences of these factors on connective tissue response during fracture healing are not completely understood, biochemical and mechanical interactions are recognized as most important [37-39].

### 2.1.3.4 Mechanical stability of bone-implant system

Stability can be classified into two different categories: primary stability and secondary stability [36]. Primary stability is a mechanical locking of the bone and implant and directly related to the quality and quantity of local bone. Secondary stability, by definition, is related to the changes which are occurring at the bone-implant interface due to the remodeling of the tissues and surrounding bone. Secondary stability cannot occur without accomplished primary stability, since poor primary stability does not allow for the necessary bone remodeling in order to achieve secondary stability. As a result, micro fracturing occurs and fibrous connective tissues thicken slowly around the implant and finally, the implant may fail owing to lack of bone to implant contact [36, 38]. Osseointegration occurs between bone and replacement material, in the case of achieved primary and secondary stability. Fractures can heal successfully not only under extremely rigid fixation but also under relatively flexible fixation.

While rigid fixation results in primary healing, more flexible fixation is better for indirect or secondary healing [38, 39].

The fracture magnitude and geometry, direction and history of the interfragmentary motion are known to be the most dominant mechanical factors determining the local strain field in the callus. A local strain distribution ensures the mechanobiological signal for the fracture repair process. External load and fixation stability determine the amount of interfragmentary movement whose direction influences the healing process (see Figure 7). Axial interfragmentary movement increases the rate of healing and it is widely accepted that it enhances fracture repair [39].

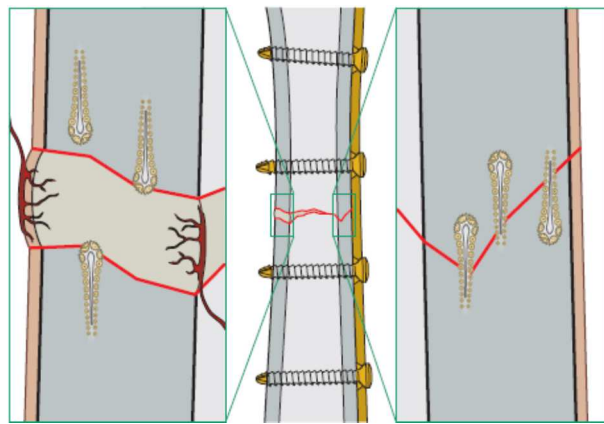


**Figure 7.** Fixation stability on the interfragmentary movement [39].

Some experimental studies have shown that shear movements at the fracture site decrease callus formation and inferior mechanical stability, compared to healing with axial movement. On the other hand, according to clinical studies, shear movement has to be compatible with successful healing. It is still uncertain how it translates to shear at the tissue and cell level [37].

### 2.1.3.5 Biochemical factors

Recent studies focused on obtaining the importance of restoration of the soft tissues surrounding the fracture. It has been found that restoration of blood supply is essential to provide the essential biological environment for fracture healing [39]. Metaphyseal vessels, the nutrient artery in the intramedullary canal and the capillary-rich periosteum, are all essential to provide new cells with oxygen, nutrients and biochemical factors [37].

The process of skeletal tissue repair and remodeling can be affected by several growth factors. However, many chemical factors, such as growth factors and cytokines, have been investigated in isolation [38]. Bone morphogenetic proteins (BMPs), transforming growth

factor (TGF)  $\beta$ , fibroblast growth factor (FGFs) and insulin-like growth factor (IGFs) exist during normal healing of bone fractures. Each growth factor family includes multiple related growth factor genes and has influence on osteoblast proliferation and differentiation [39]. They are also incorporated into mineralized bone matrix and retain activity when extracted from bone. TGF- $\beta$  is released from bone in a biologically inert state and during the immediate injury response is produced by platelets, inflammatory cells, osteoblasts, osteoclasts, and chondrocytes in the fracture site [37]. It has been reported that members of the TGF- $\beta$  supergene family control numerous processes during healing. TGF- $\beta$  is one of the key factors on bone resorption: it inhibits osteoclast formation and osteoclast activity. TGF- $\beta$  also has many other roles, stimulating bone formation by increasing proliferation and differentiation of mesenchymal cells into osteoblasts and inhibiting osteoblast differentiation and mineralization. Moreover, it also increases the production of other bone and cartilage components [39].

BMPs are the non-collagenous and water-soluble substances in bone matrix [38]. They activate genes for proliferation and differentiation. It has been confirmed that BMP-2 and -7 induce bone locally and speed-up skeletal defect repair. They are strongly present undifferentiated mesenchymal cells during the inflammatory phase and in newly formed trabecular bone. BMP-7 also stimulates normal human osteoblast proliferation [37-39].

FGFs are produced by inflammatory cells, osteoblasts, and chondrocytes within the fracture callus. The FGF-1 ( $\alpha$ ) and FGF- 2 ( $\beta$ ) are the most abundant in human tissue [36]. While the FGF-2 accelerates fracture healing directly, the FGF-1 provides cytotoxic resistance to inflammatory oxidants and therefore promotes an osteogenic response in progenitor cells. Furthermore, blood vessel formation, callus size and strength can be increased by FGFs [39].

IGFs produced by bone cells become incorporated into bone matrix and are released during resorption [38]. The IGF family stimulates activity of osteoblast and enhances bone formation by increasing proliferation of chondrocytes and osteoblasts, and stimulation of angiogenesis. Additionally, several cytokines play a critical role during the skeletal repairing process. For instance, prostaglandins decreasing osteoclast activity, thus limit remodeling and induce osteoblastic bone formation [37].

### **2.2 Ti and Ti Alloys**

At low temperatures, pure titanium crystallizes into a hexagonal close packed structure (HCP), called "alpha" ( $\alpha$ ) phase. At the  $\beta$ -transus temperature it exhibits an allotropic phase transformation from the hexagonal close packed structure ( $\alpha$  phase) to a body centered cubic structure (BCC,  $\beta$  phase) and remains in this crystallographic structure up to the melting point

at 1672 °C [40, 41]. The  $\beta$ -transus temperature is defined as the lowest equilibrium temperature at which the material is 100%  $\beta$  and 882±2 °C is given as a  $T_{\beta}$  for pure titanium [40]. The exact transformation temperature depends on interstitial and substitutional elements and, is therefore, strongly influenced by the purity of the metal.

Titanium can be alloyed to change its characteristics, primarily to improve its mechanical properties, such as strength, high temperature performance, creep resistance, and formability [42]. Basically, titanium alloys can be classified as  $\alpha$ ,  $\alpha+\beta$ , and  $\beta$  alloys (see Figure 8), with further subdivision into near  $\alpha$  and metastable  $\beta$  alloys [43].

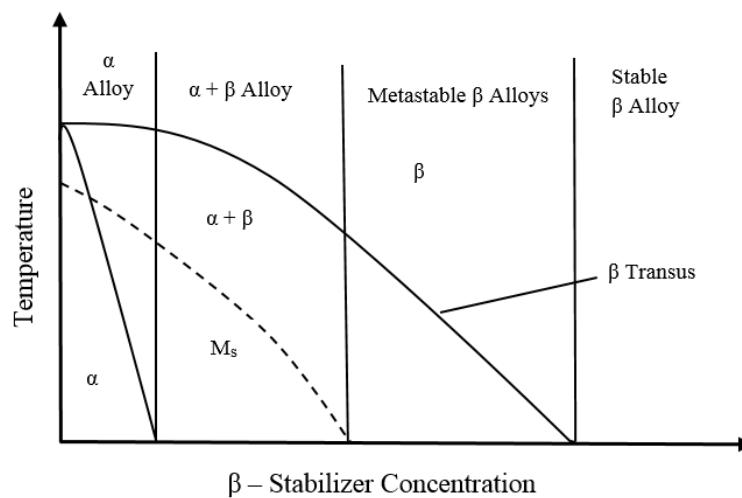


**Figure 8.** Schematic phase diagram of titanium alloys [43].

Alloying elements that are added to titanium are usually divided into two groups of  $\alpha$  stabilizers and  $\beta$  stabilizers, respectively, depending on their influence on the  $\beta$ -transus temperature changes. The substitutional element Al and the interstitial elements O, N, and C are strong  $\alpha$  stabilizers and increase the transus temperature with increasing solute content. In addition, an increase of room temperature strength and flow stress, high temperature strength and creep strength as well as weldability improvement are generally recognized by increasing the  $\alpha$  phase portion.  $\beta$ -stabilizing elements are mainly the transition metals, such as V, Mo, Nb, Ta, and Cr, which tend to reduce the temperature of the  $\alpha/\beta$  transformation. It is known that they improve heat treatment and forming capabilities, but increase strain rate sensitivity. In addition to extending the  $\alpha$  phase field to higher temperatures, the  $\alpha$  stabilizers develop a two-phase  $\alpha+\beta$  field which has the compositions of a mixture of  $\alpha$  and  $\beta$  phases and may contain between 10 and 40% of  $\beta$  phase at room temperature [40-43].

$\alpha$ -titanium alloys are preferred for high temperature applications and generally used in aerospace industries because of their higher oxidation-resistance, superior in high-temperature strength, high creep resistance and good weldability. However,  $\alpha$  is less ductile compared to the bcc  $\beta$  and is difficult to form or cold work at room temperature, because the deformation capability of HCP structures is limited [42, 44].

On the other hand,  $\beta$  titanium alloys have a good formability at lower temperatures and the  $\beta$  phase tends to exhibit a much lower modulus compared with  $\alpha$  phase. Because of their higher strength level, the usage of the  $\beta$  titanium alloys is increasing in the area of aerospace applications. The low modulus of elasticity of these alloys in combination with the relatively high yield stress is the primary reason for producing springs used in a large variety of shapes and sizes in airplanes. Furthermore, their good corrosion resistance in aggressive environments makes their application in oil and gas drilling and production, geothermal wells, etc. possible [45].

Owing to their higher yield stress and fatigue strength in comparison with other competing metallic materials, better corrosion resistance, higher modulus of elasticity and higher temperature capability,  $\alpha+\beta$  titanium alloys can be found in aerospace, power plants, sporting goods, automotive, orthodontic and orthopedic implants applications.  $\beta$ -titanium alloys are commonly strong, due to the duplex phase structure. They are more formable than  $\alpha$  alloys, yet slightly more difficult to weld [46].

The most popular alloy of  $\alpha+\beta$  titanium is Ti6Al4V (hereafter Ti64) which has become the most important medical titanium alloy [43]. However, it is well known that for better biocompatibility, it seems important to avoid the presence of V in the composition due to the possible toxic effect resulting from released vanadium. Recent studies [46, 47] have shown that releasing of V ions are associated with long-term health problems, such as Alzheimer disease and neuropathy. The Ti67 alloy belonging to the non-toxic group in tissue interaction was developed by replacing vanadium in Ti64 with the same atomic amount of niobium which exhibits excellent biocompatibility [48]. The heterogeneous Ti67 alloy with the optimal composition has the same  $\alpha+\beta$  structure like Ti64, with enrichment of Al in the  $\alpha$  phase and Nb in the  $\beta$  phase. Another development reason for this alloy is to improve the wear resistance and castability which can enhance the quality of dental prostheses. The strength of Ti67 alloy casting is slightly lower than that of Ti64 alloy, due to the negative effect of Nb on the modulus of elasticity, but the ductility and corrosion resistance were better than in Ti64 [47]. Furthermore, in comparison with commercially pure (CP) titanium, Ti67 alloy is easier to polish and has better finishing surface condition [49].

The size and arrangement of  $\alpha$  and  $\beta$  phases determine the microstructure which has a substantial effect on the properties of titanium alloys. Changing the alloy composition and processing modifies the microstructure [45]. The interaction between microstructural constituents and their fracture behavior designates the resultant mechanical properties [47]. Akahori et al. [48] reported that not only tensile strength and elongation of cast Ti67, but also its fatigue strength in both low- and high-cycle fatigue life regions are improved by thermochemical processing combined with a post-heat treatment.

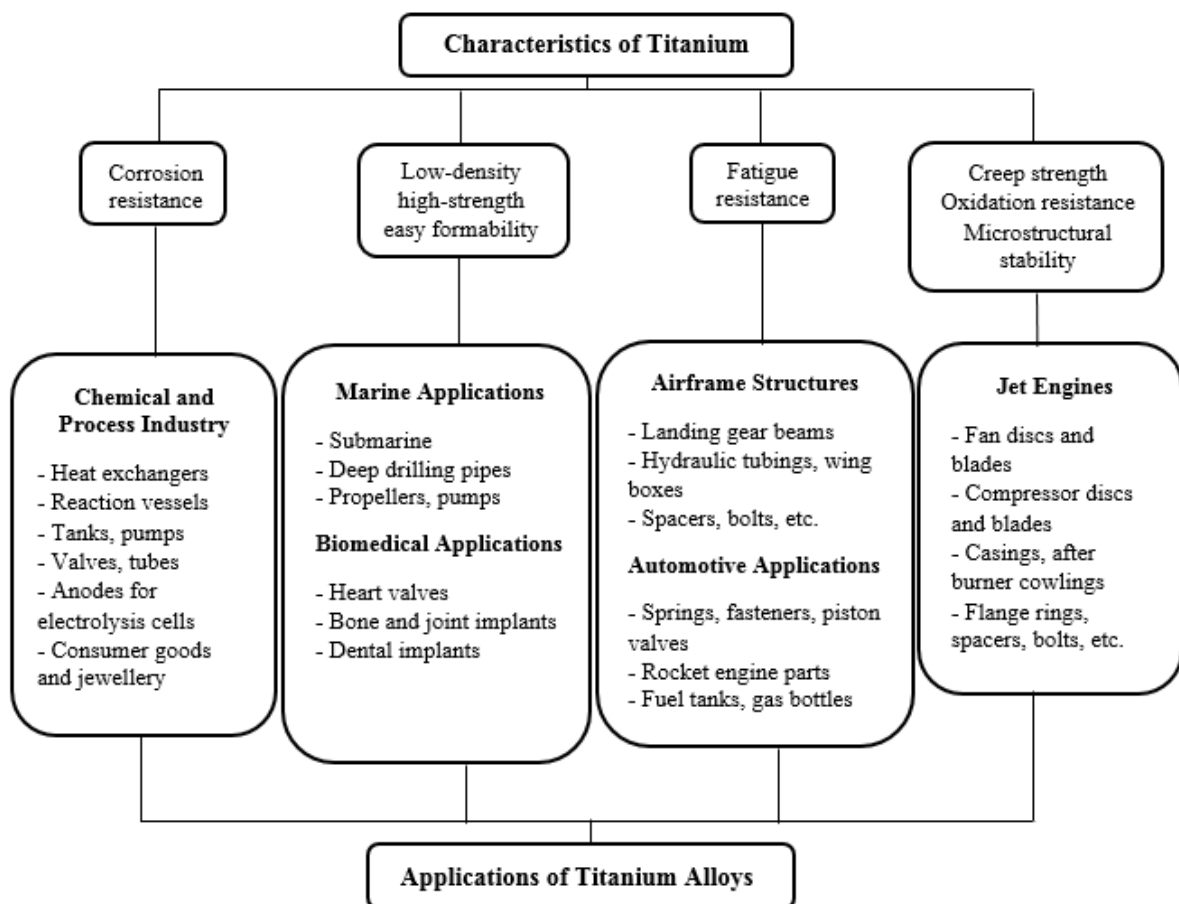


**Figure 9.** Typical applications of titanium alloys [49].

Microstructural variations and property combinations are attained either during the  $\alpha/\beta$  transformation in the alloy or through thermomechanical treatment (TMT) [44, 50]. In this way, the adaptation of properties to specific applications can be achieved [40, 42, 50]. Figure 9 illustrates typical applications of titanium alloys.

Different microstructures can be generated by using a combination of solution-heat treatment, deformation, recrystallization, aging, and annealing for stress relief as schematically outlined in Figure 10. Controlling the deformation rate at any particular temperature and at the

working temperature are important for achieving the desired microstructure after TMT. Moreover, the expected texture is very sensitive with working methods in TMT [49-54].

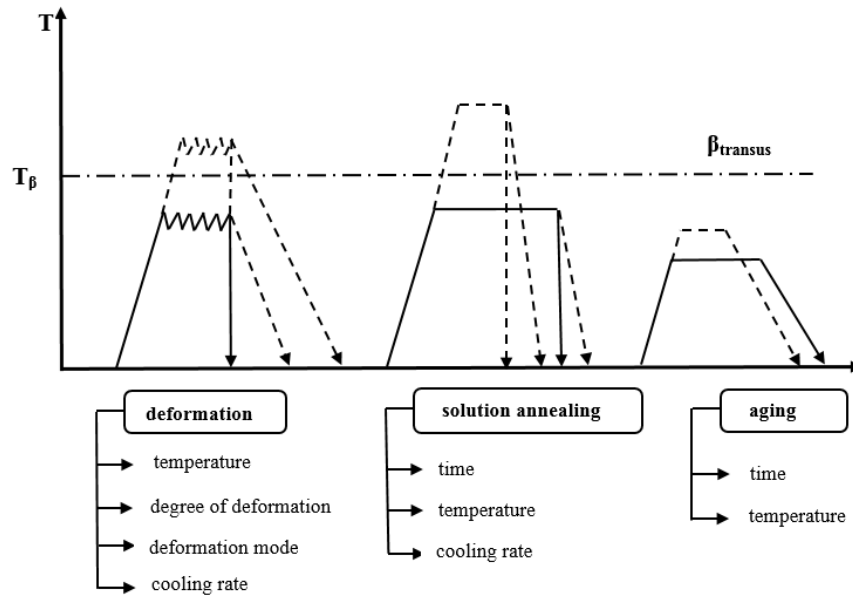


**Figure 10.** Thermomechanical treatment of titanium alloys [54].

The lamellar and the equiaxed microstructures are the two extreme cases of phase arrangements which are generated upon cooling from the  $\beta$  phase field, and a result of a recrystallization process respectively. Both types of microstructure can have a fine as well as a coarse arrangement of their two phases. The  $\beta$ -transus temperature is a central point in the evolution of microstructure and is of great technological importance in determining heat treatment and the processing schedule since it separates the single-phase  $\beta$  field from the two-phase  $\alpha + \beta$  field. The mechanism of the  $\beta$  phase transformation during cooling dominates the development of titanium microstructure. When titanium alloys are heat-treated above the  $\beta$  transus temperature they are in single-phase  $\beta$ . The  $\beta$  transus temperature is related to the alloy chemistry. Alloys heat treated above the  $\beta$  transus temperature result in acicular or lamellar structure, depending upon the cooling rate and alloying content. Below the transus temperature,  $\alpha$  nucleates at grain boundaries and then grows as lamellae into the (prior)  $\beta$  grain. Whereas pure lamellar microstructures are caused by slow cooling, the lamellae becomes coarser with a reduced cooling rate. Rapid quenching results in a very fine needle-like microstructure due to martensitic transformation of  $\beta$ . The transformation of the  $\beta$  phase during cooling dominates the microstructure in most of the commercially important titanium alloys [49, 52]. On slower cooling,  $\beta$  can transform by nucleation and growth to Widmanstätten  $\alpha$

phase of which morphology can change from a colony of similarly aligned  $\alpha$  laths to a basket weave arrangement because of the increasing of cooling rate or alloying content.

The equiaxed form is a result of a recrystallization process, while the lamellar one is generated upon cooling from the  $\beta$  phase field, and both structures have a fine as well as a coarse arrangement of their two phases depending on the cooling rate [44, 49]. Firstly, in the  $\alpha+\beta$  field, the alloy has to be highly deformed for achieving enough cold work into the material. A recrystallized and equiaxed microstructure is generated upon subsequent solution heat treatment at temperatures in the two-phase field. The volume fraction of the primary  $\alpha$  is determined by the solution heat treatment temperature. Bimodal microstructures consisting partly of equiaxed (primary)  $\alpha$  in a lamellar  $\alpha+\beta$  matrix is caused by solution heat treatment just below the  $\beta$ -transus temperature. Bimodal microstructures are a combination of lamellar and equiaxed microstructure.  $\beta$  transforms into martensite, with high cooling rates from temperatures above the martensitic start temperature (MS) that varies basing on the starting structure and the microstructural homogeneity, and through the two-phase field [50].

**Table 3.** Influence of microstructure on selected properties of titanium alloys [51].

<b>fine</b>	<b>coarse</b>	<b>Property</b>	<b>lamellar</b>	<b>equiaxed</b>
o	o	Elastic modulus	o	+/-
+	-	Strength	-	+
+	-	Ductility	-	+
-	+	Fracture toughness	+	-
+	-	Fatigue crack initiation	-	+
-	+	Fatigue crack propagation	+	-
-	+	Creep strength	+	-
+	-	Super plasticity	-	+
+	-	Oxidation behavior	+	-

Numerous previous studies [45-53] have focused on the investigation of the influence of the various microstructures on the mechanical properties of titanium alloys, thus some general statements can be made. Table 3 illustrates qualitatively how the size and the arrangement of the phases have an effect on some important selected mechanical behaviors [49]. Fine-scale microstructures, which are a prerequisite for superplastic deformation, increase the strength as well as the ductility and retard crack nucleation. On the other hand, resistance to creep and fatigue crack growth can be increased with coarse microstructures [50]. Equiaxed

microstructures, preferred for superplastic deformation, have high ductility and fatigue strength, whereas lamellar structures, showing high fracture toughness, have superior resistance to creep and fatigue crack growth. Bimodal microstructures exhibit a well-balanced property profile because of the combination of the advantages of lamellar and equiaxed structures [52].

During the selection of a manufacturing process, different aspects, such as the complexity of the implant, costs, final mechanical properties, etc. should be taken into consideration. A final decision is made mostly on the basis of manufacturing needs [50, 54].

The bone replacement material is expected to have a modulus equivalent to that of bone. However, the high elastic modulus of the current implant materials compared to bone leads to poor fixation between the implant and tissues, and unsuccessful implantation procedure. The implant transfers the major part of the load and this biomechanical incompatibility results in a large stress-shielding from the surrounding bone tissues, and consequently to poor fixation between the implant and tissues, and a subsequent loosening of the implant [12]. Thus, nowadays a material with an excellent combination of high strength and low modulus closer to bone has to be used for implantation, and the fabrication of pores in the implant structure can be aided thus solving the modulus mismatch problem and creating a longer service period by avoiding revision surgery [28, 52].

### **2.3 Fabrication Methods of Cellular Metals**

Over the years, numerous fabrication processes have been developed to produce cellular metals. The fabrication methods of open cell porous metal can be divided into four classes according to the state of matter in which the metal is processed: metal vapor, liquid metal, powdered metal or metal ions [43, 55]. Figure 11 shows the four main routes of making metal foams and the methods they use.

Powder compact foaming (PCF), based on the partial densification during sintering of metal powders, is the simplest fabrication technique for producing open cell metallic foam [55, 56]. A cellular structure is manufactured by compacting, binding, and sintering metal powders. In order to produce porous metal samples with greater porosity the space holder method can be suggested. This process starts with mixing the metal powders with space holders such as carbamide, ammonium hydrogen carbonate, sodium chloride and polymethyl-methacrylate and is followed by the compaction. Finally, a compacted green body is subjected to sintering [57].

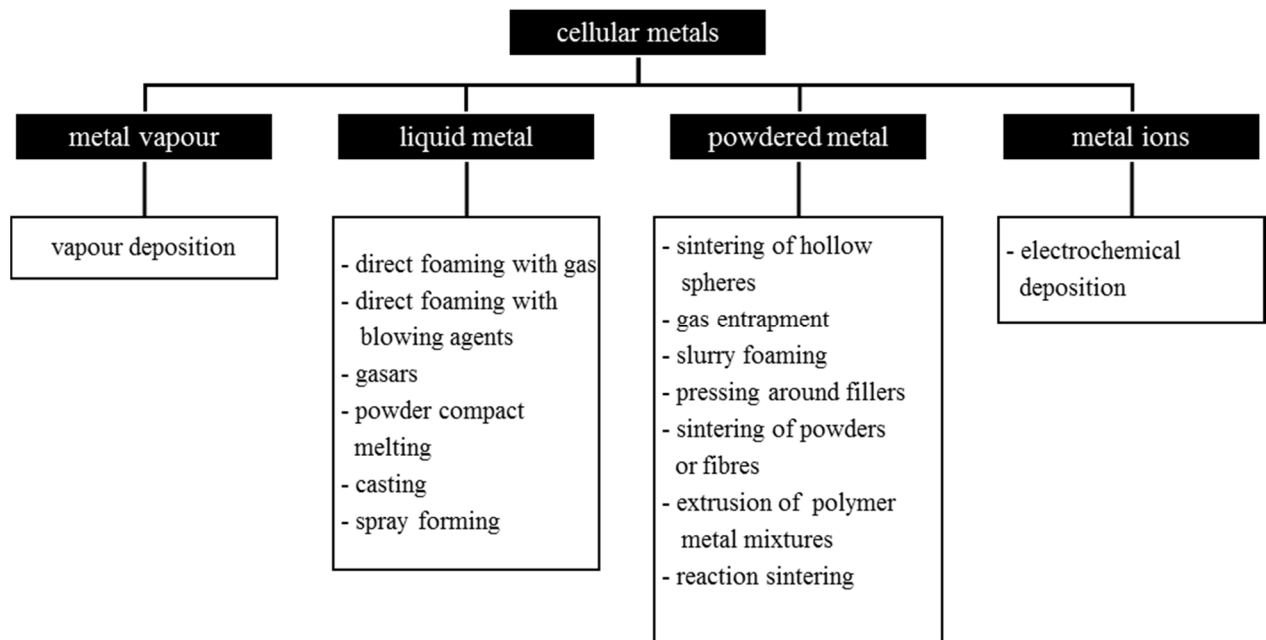


**Figure 11.** Fabrication methods of metal foams [57].

A broad range of different porous material can be fabricated by the replication method, which is based on powder metallurgical technologies. This method consists of three essential production steps: First, an open cell polymer foam (e.g., polyurethane) is coated by slurry infiltration. Following this, the template is thermally removed, heating up and melting the foam. In a final step, the debinded metal structure is sintered. The open network of the polymer foam can be transformed completely to the metal foam. Although the process is rather simple, every single processing step requires proper development which is a prerequisite for the production of defect-free structures with optimum properties [53-58].

Casting techniques are also applied in order to manufacture cellular metallic structure. Currently available Ti casting systems can be classified in three groups: i) pressure/vacuum casting systems with separate melting and casting chambers, ii) pressure/vacuum casting systems with one chamber for melting and casting, and iii) vacuum/centrifuge casting systems [53, 57, 58].

Investment casting is used in the automotive, aerospace and biomedical industries, owing to the advantages of reproducing complex shapes at relatively low cost, scalability from single items to large numbers of identical items, and low wastage of raw materials [57]. Almost all technical alloys, including the most common metallic biomaterials, such as titanium alloys, stainless steels and cobalt-chromium alloys, can be casted by using the investment casting method. The main advantage of the casting process compared to other procedures is the

treatment of the struts, which affects the mechanical and thermal properties of the foam [58-60].

The investment casting process consists of nine major steps is shown schematically in Figure 12. The production of a pattern of the desired castings, manufacturing out of paraffin/microcrystalline wax, or plastic, is the first step in investment casting. Depending on their size and complexity, a number of patterns are attached to a central wax stick to form a casting cluster, or assembly. For titanium casting, shrinkage of both the wax and the titanium alloy should be taken into account and the wax model must be bigger than the final titanium cast part. The wax pattern is dipped in a ceramic slurry, called the investment, which provides the opportunity to adapt the properties of the moulding material to the alloys needs. After multiple dipping in mixtures, once the investment is thick enough on the wax pattern, it is left to dry [61].

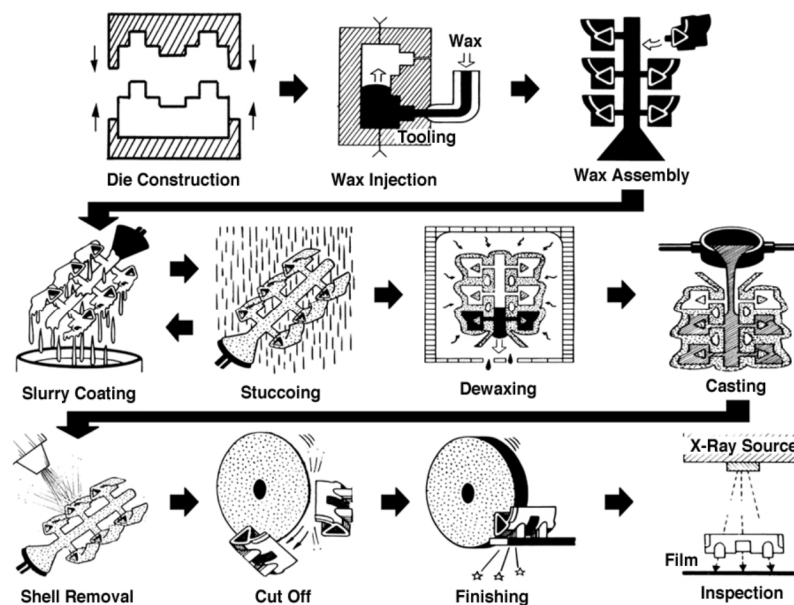


**Figure 12.** Schematic of the investment casting process [61].

The investment material is composed of fine ceramic particulates in a liquid binder. An ethyl silicate binder is often used in this process. The ceramic particulates have a low reactivity and the ability to withstand the thermal shock from contact with molten titanium, so this process is critical during titanium casting. The investment is then fired to achieve a cavity to pour in the metallic melt, and removed after solidification of the part [62, 63]. During this process, care must be taken to avoid mould cracking, resulting from the differences of thermal expansion coefficient between the pattern materials and the mould materials. Afterwards, the green mould

is fired and is ready for the addition of molten metal. When the part model is finished, the molten metal is poured in the investment and is drawn in through vacuum, positive air pressure or centrifugal casting procedures. Finally, when the titanium part is cooled and hardened, the investment is removed using vibrations, hammers, or a dissolving agent. The high flexibility of shape and the adjustability of mechanical properties of the moulds increase the applicability of the casting technologies [61-63].

From the viewpoint of cost efficiency, in comparison with permanent mould and vacuum die casting, the investment casting of titanium alloys is the most economic net-shape technology. Investment casting allows high dimensional accuracy because of the wax model, created in the exact size and shape of the final component [45].

One of the major difficulties in titanium casting is choosing the suitable investment material and the definition of its optimal curing cycle. In the case of titanium alloys, melting and casting have to be carried out in a highly pure vacuum atmosphere ( $1 \times 10^{-3}$  mbar) using inert ceramic moulds [64]. It is necessary for any investment to disallow the occurrence of any reaction with the surface of the titanium cast and the initial molten titanium at nearly 1700 °C. Furthermore, the ceramic moulds should be high temperature stable to withstand the high temperature of molten titanium. In addition, if the metal returns to room temperature after casting procedure, the investment material should have an ability to compensate for shrinkages of the titanium cast (typically 1.9-2.5%) [63-65]. Another difficulty in casting titanium is its small solidification range, i.e. the interval between molten and solid state, which is approximately  $\Delta T = 50$  K for Ti67. In addition, the usage of titanium and its alloys are restrained by a number of problems during casting process that are connected to their high melting point and highly reactive behavior with investment materials at high temperature [66].

Casting related defects have crucial effects on the design and lifetime of casting products [67]. Temperature distributions and moulds have a great influence on the quality of the investment castings [68]. Certain defects in the final product may result from the casting process, related to interaction of the melt with the shell mould and non-uniform properties due to usual solidification effects [61-67]. The degree of casting flaws indicates the mechanical properties and surface microstructure of casting specimens. Moreover, they increase the susceptibility to adhesion and corrosion, and also affect the biocompatibility and roughness [62, 69, 70].

Investment casting defects in titanium alloy systems may be classified into two types: voids and inclusions. Voids are the lack of solid material in the casting and include porosity defects which are caused by poor filling, volumetric shrinkage of the alloy during the solidification process, or dissolved gases. They are some of the most frequent defects in titanium casting and

weld lack-of-fusion (LOF) cavities [64, 66, 67, 70]. Three main reasons of high internal porosity in titanium castings during the casting procedure are: (i) a large pressure difference between the casting chamber and the mould chamber which leads to too high suctioning pressure, thus gas is introduced into the flowing melt, (ii) severe turbulence caused by too fast molten metal flowing, which could produce gas incorporation, and (iii) if the surface wettability of the mould is too great for the molten titanium, the metal flow becomes intermittent; the metal poured travels too promptly up to the end of the mould, immediately solidifying, and the metal following the first pour cannot catch up [67, 71]. A much higher hydrostatic pressure can be established in the melt by the centrifugal force which may help to decrease porosity defects and to enhance mould filling abilities [72].

In contrast to porosity defects, weld LOF cavities may develop after the casting process or during weld repair of the casting. Although they are generated during post-casting foundry processing, there are not truly casting defects. They are results of a poor surface preparation or inadequate heat delivered in the weld pool and rarely exceed 2 mm in maximum dimension [70].

Inclusions, which constitute any undesirable materials in the microstructure, can be separated into two main categories according to their source: high-density inclusions (HDI) and low-density inclusions (LDI). Ceramic shell from the invested mould is the main source of HDI. Ceramic mould fragments can spall and can be released into the metal, due to thermal and mechanical behavior of molten metal and its extreme flow rates during casting. If it occurs in the pour, these ceramics do not break down and can become inclusions. At the same time, the oxygen-rich ceramic shell particles can react with the titanium in its molten state, during solidification and heat treatment. Owing to the oxygen diffusion, generally, HDI are surrounded by the stabilization of a brittle oxygen-enriched reaction zone, typically 500  $\mu\text{m}$  thick [66, 70]. This diffusion zone causes some  $\alpha$  lamellae thickening and hardens the matrix [63, 67, 73].

The source of LDI inclusions is external contamination including hard  $\alpha$  (atmosphere stabilized  $\alpha$  phase titanium) and tungsten (welding electrodes). Up to now, numerous ways of origination have been identified, and, thus, LDI are a much greater problem for the producer than are HDI defects. However, the principal source for this form of the inclusions is extensive local stabilization of the  $\alpha$  phase (hard  $\alpha$ ) as a consequence of reactions between titanium and the oxygen/nitrogen in the atmosphere. The stabilized phase is very brittle and forms cracks after mechanical work [70]. A metallographic cross-section of hard  $\alpha$  inclusions is shown in Figure 13.

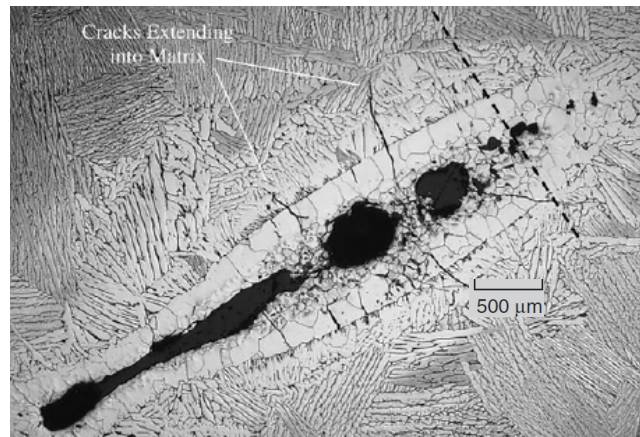


**Figure 13.** Metallographic cross-section of hard  $\alpha$  inclusions [70].

They are represented by the inclusion core which include  $\text{TiO}_2$ ,  $\text{TiN}$  phases often with  $\text{Ti}_3\text{Al}$ , and a measurable increase in hardness. The inclusions are surrounded by the porous, embrittled  $\alpha$  phase which is equiaxed by  $\beta$ -stabilizing elements into the matrix [70].

The ingot producer should take into account the reactive nature of all titanium alloys at high temperature and long-term homogenization treatments. Otherwise the inclusion problems explained above are experienced within the product [74].

In investment casting process, the reactivity of the metal with ceramic mould leads to a contamination between the surface regions of Ti alloys and oxygen. Due to the local increase of the oxygen concentration on the surface of the metal, an oxygen-rich Ti hexagonal solid solution ( $\alpha$  phase) becomes stable at the temperature where the bulk alloy would be single phase  $\beta$ , and also alters the  $\alpha/\beta$  structure near the surface during cooling to room temperature. As a result of interstitial oxygen diffusing through the titanium lattice from the reacted investment material during the period of the casting, solidification and cooling process, a hard and brittle surface layer is formed, that is commonly termed  $\alpha$  case [75]. Not only oxygen, but also other interstitial elements such as Si, N, C or Al from mould materials change the metallurgy of titanium [62, 76, 77].

Chan et al. [78] found that the thickness of the  $\alpha$  case layer changes between 50 to 500  $\mu\text{m}$ , whereby the thickness of the layer varies with the crystal orientation of the grains near to the surface. The thickness of this layer depends on the cooling rate, local cooling conditions at the mould wall, casting geometry, casting volume and the amount of oxygen at the mould/casting interface [78-80].

The  $\alpha$  case is characterized by a change in mechanical properties including  $E$ , yield strength, elongation, and hardness towards brittle, owing to a change in the microstructure. For instance,

the microhardness of the  $\alpha$  case is greater than that of bulk titanium [71, 80], and also fatigue strength and tensile ductility are lowered by this layer [81].

Figure 14 illustrates the microstructure of the  $\alpha$  case layer and a schematic drawing of a typical microhardness profile near the surface of cast Ti64, respectively.  $\alpha$  case layer and interstitial contamination especially reduce high-cycle fatigue properties dramatically [82]. The  $\alpha$  case promotes crack initiation and propagation, which occur with increasing intensity of the interstitial contamination. Furthermore, the mechanical properties of the surface of titanium castings will change during mechanical work [82-84].

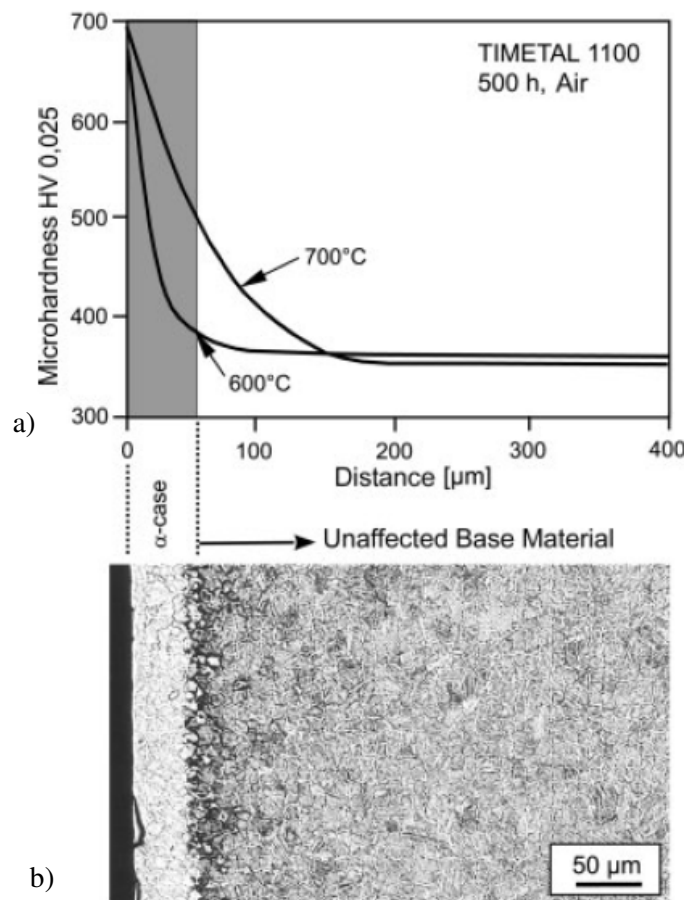


**Figure 14.** a) A schematic drawing of a typical microhardness profile near the surface of cast Ti64 b) Microstructure of  $\alpha$  case layer [54].

Thus,  $\alpha$  case formation should be prevented either during the casting process or removed from the castings before use. To prevent the formation of  $\alpha$  case layer during the casting process, ceramic investment materials such as  $\text{Al}_2\text{O}_3$ ,  $\text{MgO}$ ,  $\text{ZrO}_2$ ,  $\text{CaO}$ ,  $\text{Y}_2\text{O}_3$ , etc. whose standard free energies of the formation of oxides are much higher than  $\text{TiO}_2$ , have been introduced into the casting process of titanium. The ceramics are high temperature stable to withstand the high temperature of molten titanium and chemically inert to minimize reactions at the interface

between melt and mould [66, 68, 71]. In this way, a minimal reaction occurs between the mould wall and Ti as the liquid metal is poured into the mould [68, 69, 72].

If the  $\alpha$  case layer formation cannot be prevented during the casting process, it can be removed from the surface after the casting process by leaching/chemical milling or mechanical removal, e.g., by sand blasting or machining [77, 84, 85]. Mechanical milling and a water jet have been also used, but they are not applicable for complex-shape-cast specimens. Furthermore, these methods are not as effective as the chemical cleaning methods, based on considerations of their removal rate, surface integrity and tooling cost [70, 80, 81]. On the other hand, chemical milling is also costly and creates hazardous and unfriendly effects to the environments waste products including hydrofluoric acid (HF) [76, 81, 86]. Moreover, this destructive method can change sample dimensions: service materials whose dimensions must be maintained after the treatment could be destroyed completely by acid pickling [86].

## **2.4 Surface Requirements of Biomaterials**

### **2.4.1 Biocompatibility**

The performance of any biomedical material is controlled by two characteristics: its bio-functionality, which defines the ability of the device to perform the required function, and its biocompatibility, which determines the compatibility of the material with the body. Local tissue response to metal implants depends on the amount and toxicity of the corrosion products. To perform their functions metallic implants should firstly be accepted by the body [87]. Structural and functional properties are critical to the development of a rapid and reliable mechanically stable bone-implant interface and new remodeled bone tissue in direct contact with implanted material surface [88, 89].

Material surface topography and chemical characteristics play a key role in the osteointegration process and the long-term success of the implant. The tissue response of an implant involves physical factors depending on the implant design, surface properties like crystallographic structure, morphology and composition of surface layers, wettability surface topography, and chemical factors, associated with the composition and structure of the materials [87-89]. In this connection, an ideal implant surface should be able to induce osteointegration, independently of implant site, available bone volume or bone quality [90, 91].

Titanium loses its chemical reactivity with other materials at room temperature and become extremely inactive. In oxygen-containing environments, Ti is spontaneously covered with a thin oxide layer with the thickness of a few nanometers, which consists of mainly titanium dioxide

(TiO<sub>2</sub>), and it covers the surface of pure titanium. It appears amorphous, is insoluble and highly adherent to the metal surface over a wide range of pHs, potentials, and temperatures. The excellent biocompatibility and corrosion resistance of titanium are associated with the formation of this passive and protective oxide layer on its surface [92]. This oxide film serves as a protective barrier against further corrosion and is partially responsible for its outstanding biological properties. In addition, a low level of electronic conductivity and slightly negative charging of the passive surface film at physiological pH are also responsible for the biocompatibility of titanium [87-89, 93].

Despite its excellent corrosion resistance in mildly reducing, neutral, and highly oxidizing environments, including quite high temperatures, a passive oxide film breakdown and resultant corrosion can occur [94] when titanium is exposed to a highly reducing condition. When implanted, they form a morphological connection with living tissues (bioinert behavior), and also show some osteointegration ability with direct bone-implant contact. Although the minimal tissue reaction induced by titanium and the favorable tissue response by the passive oxide surface layer [91], the bioactivity of this surface layer is not sufficient when osteoporotic bone is present or when faster healing is required [95].

Over the last two decades, research in orthopedic and dental material science have brought major advances in developing surface-modifying techniques to be applied to biomaterials for improving the osteointegration properties of titanium and titanium alloys [96]. Various titanium surface treatments, such as surface machining, acid etching, anodic oxidation, sandblasting (with aluminum dioxide, titanium dioxide, HA, glass microspheres), plasma-spraying and biocompatible coating have been carried out to improve the quality and quantity of the bone-implant interface of titanium based implants. Furthermore, by means of these surface treatments, the biological processes in the bone-implant interface can be accelerated. The rapid attachment of osteoblasts results in the initial success of an implant [87-91, 94-96].

Coatings of HA have good potential since they exploit the biocompatible and bone bonding properties of the ceramic. There are many techniques that have been used for HA coatings on metallic implant materials such as pulsed laser deposition, sol-gel processing, thermal spraying and ion beam sputter deposition [92, 97]. In the last three decades, the plasma spray technique was most frequently used to achieve HA coatings for improving implant osteointegration because of their biological response, resulting in high bone apposition without fibrous tissue interposition at bone-implant interface and high short-term mechanical performance. On the other hand, plasma spray is an expensive technique and needs extremely high operation temperatures (10.000 to 30.000°C) [97, 98]. Moreover, it causes poorer long-term performance

owing to low adhesion of the coating to the metal, resorption or delamination of the coating layer, lower crystallinity of the apatite and non-uniformity of the thickness [99]. As a result, some simple chemical and thermal treatments have been developed and tested in order to alter the composition and morphology of surface layers, and to overcome the mechanical drawbacks observed for HA plasma spray coatings [92, 98].

The reactivity and bioactivity of Ti implants can be enhanced directly by subjecting the metal to a simple chemical surface treatment and subsequent heat treatments. Sul et al. [100] discovered that changed oxide crystallinity and surface porosity are responsible for fast and effective bone fixation to oxidized implants *in vivo* test. An additional TiO<sub>2</sub> layer can be used to improve the bioactivity of Ti implants. Anodic oxidation, alkali treatment, and sol-gel coating have been applied to create an additional TiO<sub>2</sub> layer. Furthermore, the bone like apatite forming ability of Ti induced by NaOH and heat treatment could be enhanced [101]. During the chemical treatment with NaOH, a sodium titanate hydrogel layer is formed at the surface. By means of heat treatment, this layer becomes stable after dehydration. It is accepted that this type of bioactive material is very useful as a load-bearing bone replacement due to its high fracture toughness and a bone-bonding ability [102]. The incorporation of calcium into the outer TiO<sub>2</sub> layer of medical implants has also many beneficial effects on increasing osseointegration. TiO<sub>2</sub> surfaces can be converted chemically into calcium titanate (CaTiO<sub>3</sub>) with various different coating methods like salt baths, hydrothermal-electrical treatment or sol-gel coating [103, 104].

Titanium implants can be bioactivated also by a biomimetic process based on ion precipitation and growth of a CaP film on a substrate after a certain period of immersion in a simulated body fluid solution (SBF), which has an ion concentration nearly equal to human body fluid at 37 °C [101]. Since the first studies of Kokubo [101, 105] on the SBF solution, the method has been modified by other researchers. If this method is combined with chemical and thermal treatments while the nucleation time decreases, the chemical adhesion of the CaP film tends to increase. The titanium specimen with sodium titanate layer on its surface created through NaOH coating and heat treatment, exchanges its Na<sup>+</sup> ion with H<sub>3</sub>O<sup>+</sup> ion in the SBF to induce the bone-like apatite nucleation. As a result, the titanium specimen bonds to living bone by the apatite layer [104-107].

Compared to the other processes, this method offers many advantages, such as the low process temperature, which allows the usage with any heat sensitive material, better control of the chemical composition of the coating, the possibility to prepare homogeneous films, control of the film microstructure, deposition on and into porous surfaces without changing the pore morphology, and good adhesion to the substrate [94-97, 101].

The biomimetic coating method is applied not only to smooth titanium surfaces, but also porous titanium substrates. It has been observed that these porous implants have shown to enhance the implant osseointegration. The porous titanium surface morphology also accelerated the biomimetic process due to its higher surface reactivity [14, 46, 98].

Biological tests used to measure the biocompatibility of a material can be classified as *in vitro* tests, *in vivo* tests and clinical tests. In terms of cost, simplicity and applicability, *in vitro* tests are commonly accepted as a first screening for checking the biological behavior and toxicity of newly developed materials. By using living organism, such as cells or bacteria, they simulate biological reactions to materials, when they are placed on or into tissues of the body [91, 92, 106].

The main advantages of *in vitro* biocompatibility tests are, being experimentally controllable, repeatable and fast. Another major advantage is that the ethical and legal issues are not compulsory. Cell death, reduced cell adhesion, altered cell morphology, reduced cell proliferation, and reduced biosynthetic activity parameters, which give warnings regarding material toxicity, are widely used to examine biocompatibility and toxicity. If these experiments and investigations show promising results, more comprehensive studies on small and big animals will be performed [46, 107].

In animal experiments (*in vivo*), the material is placed into small (e.g. rat, rabbit) or big (e.g. dog, pig, sheep) animals. *In vivo* tests allow long term evaluation of materials and after explantation, the implant-bone interface can be investigated by measuring the mechanical performance of this interface in various ways. Ethical concerns and animal welfare issues are very important in animal experiments [92, 93, 108]. However, the appropriateness of an animal species to represent the human response remains questionable.

The final step of this evaluation process are clinical tests which are essentially clinical trials of a material in which the material is placed into human patients. Clinical tests might be done only if satisfactory results are obtained in the *in vitro* and *in vivo* experiments [101-109].

### **2.4.2 Surface roughness**

It has been shown that roughness over a wide range of length scales affects the basic biological responses, like cell adhesion, spreading, proliferation and differentiation [110]. In addition, roughness on a micrometer and nanometer scale is an important parameter, influencing contact-related phenomena, such as tribology or adhesion [111]

The degree of roughness is determined either by the machining process during the preparation of the implant, or by the subsequent modification of the surface. Different implant surfaces, including turned surfaces, plasma sprayed surfaces, coated surfaces and acid etched surfaces, present an extremely varied topography [99, 102, 110].

It has been known that rougher surfaces promote faster, earlier bone healing and osseointegration, owing to enhancing the attachment of osteoblasts, and their subsequent proliferation and differentiation [2-4, 10, 110]. Conversely, recent studies have demonstrated that rougher surfaces may have theoretical clinical drawbacks, such as an increase of ion release and/or marginal bone resorption, and the effect of implant surface roughness on bone response are not as straightforward as suggested. Furthermore, a greater surface damage can occur due to a greater surface tissue contact caused by an increased surface area. In this sense, there is a lack of agreement in findings from *in vitro* and *in vivo* tests. In some *in vitro* studies, an improvement in cell adhesion and cell differentiation on the implant surface was noted with increasing surface roughness [110-113], while in other studies [114-117] a decrease was observed in cell adhesion and cell differentiation on the implant surface. Some researchers [105, 107, 108] have claimed that cell proliferation increases with increasing surface roughness whereas others [104, 106, 109, 110] have discovered that cell proliferation decreases with higher surface roughness. Lüthen et al. [113] and Kakei et al. [115] did not report any relation between cell proliferation and surface roughness. At the same time, some animal experiments [107, 109] have indicated a tendency for an increase of bone to implant contact with higher surface roughness. However, other studies either could not confirm positive effects [106, 108, 113] or could not find any effect at all [105, 114]. On the other hand, surface roughness affects the fatigue properties. Fatigue limit and crack initiation life decrease as the magnitude of surface roughness increases [105].

In previous studies [108-121], different methods and different roughness parameters including 2D parameters like  $R_q$ ,  $R_{sk}$ ,  $R_a$ , and 3D parameters like  $S_q$ ,  $S_{sk}$ ,  $S_a$  etc. were used and for *in vitro* tests different cells were chosen. Thus, it is not easy to obtain a roughness range for better biocompatibility. For instance, Wennerberg and Albrektsson [119] found out that only a very specific surface topography with a  $R_a$  value between 1 and 1.5  $\mu\text{m}$  provides an optimal surface for bone integration, while Rosa and Beloti [120] suggested that a roughness range ( $R_a$ = from 0.80  $\mu\text{m}$  to 1.90  $\mu\text{m}$ ) would optimize cellular response. However, Shalabi et al. [121] found that a positive effect on the bone response was seen from  $R_a/S_a$  of  $\sim 0.5 \mu\text{m}$  up to  $\sim 8.5 \mu\text{m}$ .

## 2.5 Properties of Cellular Materials

Natural cellular materials have been used throughout history. With the fast development of various processing techniques, a broad range of different materials with different designs can be fabricated. Thus, up to now synthetic cellular materials have been utilized in most aspects of modern life [122].

Cellular materials exhibit different attractive characteristics when compared with bulk materials owing to their porous structure. These revolutionary materials possess a set of unusual properties: they are crushable, they exhibit a plateau stress if compressed, and they exhibit a change in poisson ratio on deformation. Although most of the mechanical properties of cellular materials might be fulfilled with another materials, they are known to have many unique combinations of several properties that cannot be obtained in one conventional material at the same time, for instance, high stiffness combined with very low specific weight or high gas permeability in conjunction with high thermal conductivity. Furthermore, independent of the impact direction, they have higher impact energy absorption and are very efficient in sound absorption, electromagnetic shielding, and vibration damping. Extraordinary combinations of these properties may be adapted to a multiplicity of requirements and make them an attractive option for a variety of applications ranging from mechanical to thermal [13, 19, 122-125].

Recently, metallic foams are mainly being used in aerospace, filter and impact or insulation applications. In order to gain weight saving, cellular structures are generally used as lightweight structural components, because of their light weight and high stiffness characteristics. In terms of weight saving, they are often used as cores in sandwich plates and shells in a variety of applications as design options for structures [123-125].

The type of application of the cellular structure indicates the kind of material it is made of. For example, owing to their low thermal conductivity, polymeric foams and glass foams are useful for thermal insulation applications in food containers, in refrigerators, on the space shuttle booster rockets, etc. Low density composites with high temperature performance, which are ideal for applications in jet engine nacelles and rocket nozzles, can be manufactured with carbon foams and ceramic foams [125-127].

Their high surface area to volume ratio makes open cell metal sponges also ideal for usage in compact heat exchangers [122]. Cellular materials can also be used as acoustic materials not only for noise absorption, including, aircraft ventilation ducts, panels for automobiles, marine application, etc, but also for sound fidelity applications including earphones, microphone covers, and stereo speaker grilles [122-125]. Cellular materials also exhibit key benefits for

applications in the automotive industry, where high temperature resistant materials with high permeability and good strength for catalytic conversion are needed. Furthermore, they can be suggested for applications ranging from packing, cushioning to shock mitigation devices such as automobile bumpers and helicopter seats, since they absorb large amounts of energy at nearly constant pressure [122-124].

Whilst the morphological parameters of the open cell foams and the bone appear to be similar, the mechanical properties vary significantly between the foams and the bone. They allow the ingrowth of bone cells and blood vessels, which play a key role in assisting tissue regeneration and are necessary for bone growth. As permanent implants, cellular metals, based on biocompatible metallic material like titanium or tantalum are used to replace trabecular bone. It is expected that they provide better interaction with bone if porosity level, size and shape, strength and biocompatibility aspects satisfy the design specifications of implants [128].

It is known that implant porosity increases the contact area between the implants and bone tissue, open pores also allow the transportation of body fluid. By this means, implant stability can be improved and the process of osseointegration can be accelerated. Numerous studies have shown these positive effects of cellular biomaterials and emphasized that the percentage of porosity and pore size are key success factors for cellular implants [128, 129]. A high porosity level and increased pore size favor new bone growth, whereby providing sufficient space for cell adhesion and proliferation. On the other hand they make it difficult to provide adequate mechanical properties to withstand stresses during implantation. For this reason, when these two critical parameters are obtained, not only biological aspects but also mechanical requirements should be taken into consideration and equilibrium between the rate of porosity and the mechanical properties of the material should be maintained [130].

Xue et al. [131] reported that porous Ti samples with pores larger than 200  $\mu\text{m}$  have effects like increased cell attachment and differentiation. In another study, Karageorgiou and Kaplan [132] suggested that the minimum pore size should be 100  $\mu\text{m}$  due to cell size and the characteristics of cell migration and transport. It is also possible to correlate this data with the size of haversian channels of approximately 100-200  $\mu\text{m}$  in diameter. However, Itala et al. [129] investigated four different titanium plates, with different pore size (50, 75, 100, and 125  $\mu\text{m}$ ) in rabbit femoral defects under non-load-bearing conditions. They could not find any notable difference in bone ingrowth and proposed that 100  $\mu\text{m}$  may not be the critical pore size for non-load-bearing conditions. To sum up, the optimal pore size for bone ingrowth should be in the range of 50-400  $\mu\text{m}$ , and the pores must be interconnected to maintain the vascular system required for continuing bone development. Although Takemoto et al. [105] suggested that

porous Ti with 40% porosity could be an alternative for clinical use, the acceptable pore percentage range for Ti bone replacement materials is between 25 and 66%.

Not only the intrinsic material's microstructure but also the geometry and density of the cell walls (closed cell structures) and cell struts (open cell structures) have a determinative influence on the mechanical behavior of cellular materials [122-124]. Thus, giving a clear definition of the key mechanical data for cellular materials is more difficult than for bulk materials.

Three main factors dominate the mechanical properties of cellular materials, (i) the relative density

$$\rho_r = \rho^* / \rho_s \quad (1)$$

of the foam, where  $\rho^*$  is the density of the foam and  $\rho_s$  that of the bulk, (ii) the properties of the bulk materials of which the foam is made, and (iii) to a lesser extent the connectivity and shape of the cell structure [122-127].

Usually, the data of a cellular material are compared quantitatively by their relative density  $\rho_r$  and many researches performed have presented the mechanical properties of cellular structure as a function of the material's relative density, which directly affects the cell size, cell wall thickness and pore diameter [123, 124].

The compressive response of cellular solid is characterized by linear elastic behavior at low stresses, corresponding to partially reversible cell edge bending or face stretching up to a strain of approximately 1-5%. Then it is followed by an extended collapse plateau to strains typically above 50%. This behavior corresponds to progressive cell collapse by elastic buckling, plastic yielding or brittle crushing at a relatively constant stress. The slope and length of the plateau is related to the geometry of the cell walls. Finally, the stiffness increases sharply in the densification period, corresponding to collapse of the cells throughout the material and subsequent loading of the cell edges and faces against one another [123, 124, 126, 127].

The test and evaluation procedure of their compressive behavior is one of the key properties for engineering design, because of the increasing application of cellular materials. The inhomogeneity of most cellular materials, the structure-dependent stiffness and variations in the shape and length of the plateau regime in the stress-strain curve has to be considered [133, 134]. Recently, DIN 50134 was published as the standard method for the compression test of porous and cellular metals. This international standard specifies a testing method for compressive properties of porous and cellular metals with the porosity of 50% or more [123, 133].

Figure 15 illustrates a commonly observed compressive stress-strain diagram which indicates the specific regions of deformation. The area under the stress-strain curve represents

the amount of energy absorbed by the foam. Linear elastic behavior of open cell foams is caused by cell wall and cell struts deformation due to bending and axial forces.

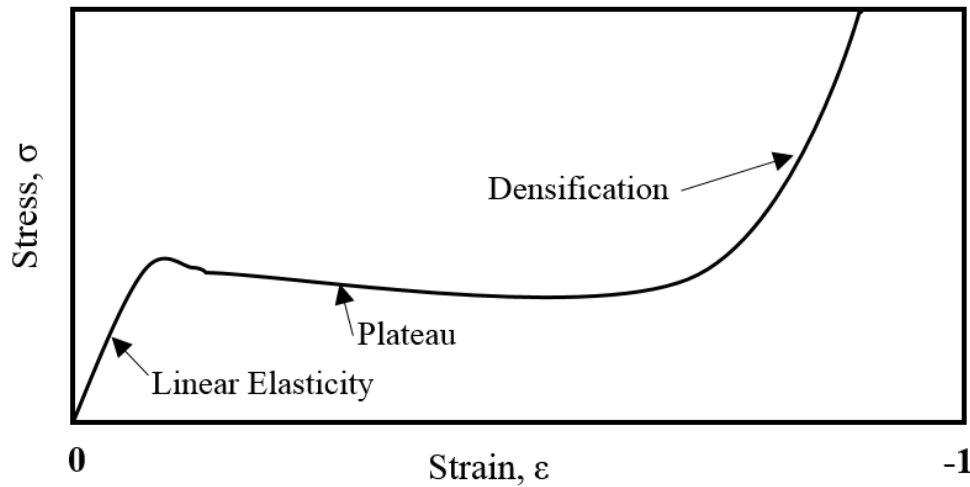


**Figure 15.** Compressive stress strain diagram of cellular materials [123].

However, local buckling and cracking of cell walls and cell struts results in increasing irreversibility of the linear regime. For this reason, the initial slope of the stress-strain curve is not straight and only a small part of the strain can be defined as purely linear-elastic. In contrast the Young's modulus  $E$  of foams should be measured either dynamically or into the plastic range, then unloading and determining  $E$  from the unloading slope [123-125].

Under compressive loading, the collapse of metal foams is caused by the formation of deformation bands, comprised of collapsed cells. Up to the peak stress, a perpendicular band having a width of one cell diameter and with the load increasing, propagates to the loading direction as the load increases. Initial deformations occur at the weakest region, followed by the next weakest, and in this way the process goes on until densification [124, 125].

In spite of their low relative densities, many cellular materials can be deformed up to large strains (70-80%) before densification occurs. It might be dependent on the ductility of the cell wall/strut material. It has been known that the brittle materials have strong scatter within the plateau regime owing to the formation and collapse of local deformation bands, while a continuous stress increases in the plateau regime with increasing relative density for the ductile materials [123-127, 133].

Gibson and Ashby [124] addressed the properties of three-dimensional (3D) foam networks in great detail and formulated the mechanical properties of foams based on the compressive behavior, since cellular structures are subjected to compressive loading in many applications. Basic mechanics and a cubic unit cell assumption were used to derive the expressions.

The dimensional arguments assume that the cells in foams of different relative densities are geometrically similar. A cubic unit cell with ligaments of length  $l$  and square cross-section of side length  $t$ , is represented in Figure 16.

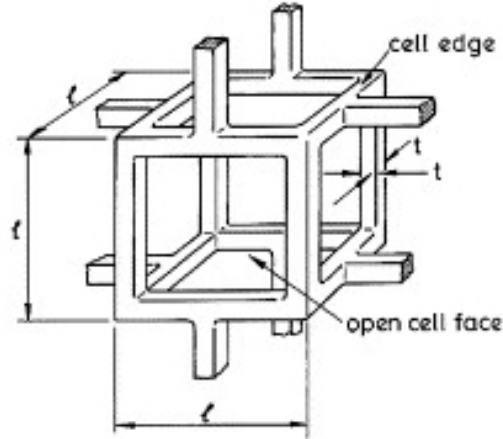


**Figure 16.** A cubic unit cell [124].

According to a unit cell assumption, the relative density  $\frac{\rho^*}{\rho_s}$  and the moment of inertia  $I$  can be related to these dimensions by

$$\frac{\rho^*}{\rho_s} \propto \left(\frac{t}{l}\right)^2 \quad (2)$$

$$I \propto t^4 \quad (3)$$

It is known that the deformation of most foams, whether open or closed cell, is bending-dominated. Therefore, besides the stress and strain relationship of the entire cell, Gibson and Ashby used the standard beam theory in order to derive their expressions. The Young's modulus  $E^*$  can be estimated as follows. Figure 17 a) and b) show that under a transverse load,  $F$ , the bending deflection,  $\delta$ , and cross-sectional area proportional to  $t^2$ , is given by:

$$\delta \propto \frac{Fl^3}{E_s I} \quad (4)$$

The stress acting on the cell is proportional to  $F/l^2$  and the strain is proportional to  $\delta/l$ . Expression for the elastic modulus can be determined by combination of these relationships

$$E^* = \frac{\sigma}{\varepsilon} = \frac{F}{l^2} \cdot \frac{l}{\delta} \quad (5)$$

$$E^* = \frac{C_1 E_s I}{l^4} \quad (6)$$

By substituting Equations (2) and (3) into Equation (6) obtains

$$\frac{E^*}{E_S} = C_1 \left( \frac{\rho^*}{\rho_S} \right)^2 \quad (7)$$

for open cell foams. The constant  $C_1$ , includes the constants of proportionality and is obtained from test data to be nearly equal to one. It is also related to the cell geometry; e.g.,  $C_1$  is 0.98 for a tetrakaidecahedral unit cell model [124, 127].

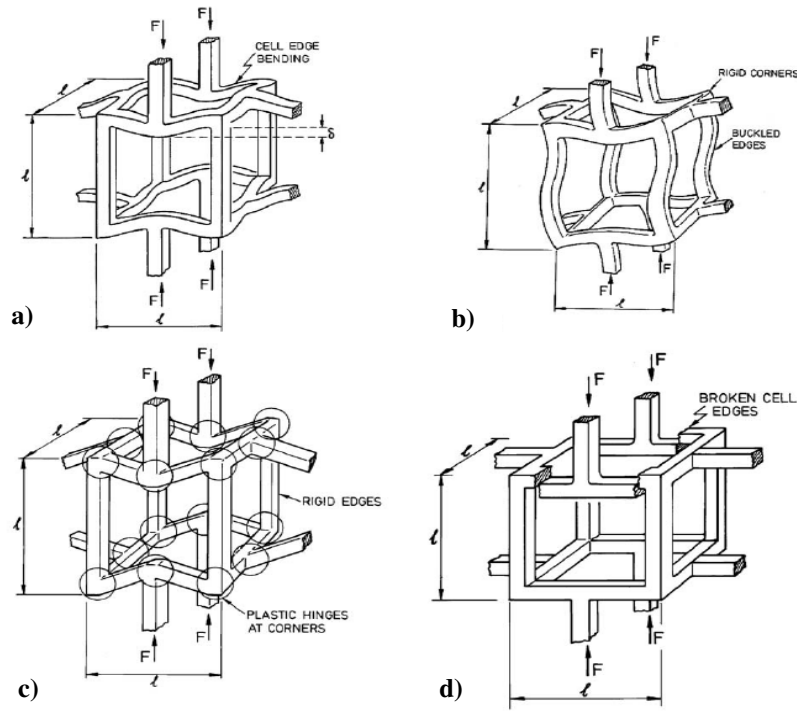


**Figure 17.** Dimensional analysis for an open cell foam **a)** linear elastic strut bending. Cell collapse by **b)** elastic buckling **c)** plastic yielding **d)** brittle crushing [124].

The shear modulus is derived similarly. It is assumed that cell wall bending occurs under an applied shear stress. The deflection,  $\delta$ , is proportional to  $F^3/E_S I$ , and the overall stress,  $\tau$ , and strain,  $\gamma$ , are proportional to  $F/l^2$  and  $\delta/l$ , respectively. The shear modulus can be written as

$$G^* = \frac{\tau}{\gamma} = \frac{C_2 E_S I}{l^4} \quad (8)$$

or

$$\frac{G^*}{E_S} = C_2 \left( \frac{\rho^*}{\rho_S} \right)^2 \quad (9)$$

Fitting Equation (9) to data suggests that  $C_2$  is approximately equal to 3/8. For a tetrakaidecahedral unit cell model  $C_2$  value is between 0.1 and 0.18 because of the different cross-section of the edges.

## 2 Literature Review

The Poisson's ratio of a foam,  $\nu^*$ , is defined as the negative ratio of transverse to axial strain, both of which are proportional to  $\delta/\rho$ . For this reason Poisson's ratio is a constant. The Poisson's ratio of foams depends only on cell geometry and is independent of the relative density of the foam. Material properties  $E$ ,  $\nu$  and  $G$  for an elastic isotropic material are connected by the relation

$$G = \frac{E}{2(1 + \nu)} \quad (10)$$

Poisson's ratio for foam material can be determined to be

$$\nu^* = \frac{C_1}{2C_2} - 1 \approx 0.33 \quad (11)$$

The plastic collapse stress,  $\sigma_{pl}^*$  can be determined as a function of the relative density by equating the applied moment,  $M$ , on a strut from a transverse force  $F$  to the plastic moment,  $M_p$ , required to form plastic hinges (Figure 17 c)

$$Fl \propto \sigma_{pl}^* l^3 \quad (12)$$

$$M_p \propto \sigma_{ys} t^3 \quad (13)$$

$$\frac{\sigma_{pl}^*}{\sigma_{ys}} \left(\frac{t}{l}\right)^3 = C_3 \left(\frac{\rho^*}{\rho_s}\right)^{3/2} \quad (14)$$

where  $\sigma_{ys}$  is the yield strength of the cell strut material. Fitting Equation (14) to data gives  $C_3 \sim 0.3$ .

Similarly, the brittle crushing strength can be formulated, with (Figure 17 d):

$$\frac{\sigma_{cr}^*}{\sigma_{fs}} = C_4 \left(\frac{\rho^*}{\rho_s}\right)^{3/2} \quad (15)$$

where  $\sigma_{fs}$  is the modulus of rupture of the solid cell wall material. Fitting Equation (15) to data gives  $C_4 \sim 0.2$ .

### 2.5.1 Fatigue properties

In many potential structural applications, foams would be subjected to cyclic loading. It is necessary to understand the fatigue behavior and failure of foams in order to translate their properties for use in applications in which fatigue is an issue. For instance, the capability of metal foams to absorb energy should be examined by their response under fatigue testing [134].

In contrast to bulk materials, foams show large strain accumulation prior to failure, which is a desirable quality in the absorption of energy since they undergo progressive collapse under compression-compression fatigue loading [122-127, 133].

Figure 18 illustrates strain vs. number of cycle curves for metallic foams under compression fatigue. This can be characterized by three stages. In the first stage, following the inelastic strain in the first cycle, only small additional strains occur in the next few decades which are caused by early formation of cracks. During the second stage, also known as the incubation period, there is only minimal strain accumulation. In this period, many cycles produce minimal further strain for crack growth. Thereafter, the strain rate increases rapidly, until the material attains its densification strain and finally failure occurs [123, 125, 135-137].

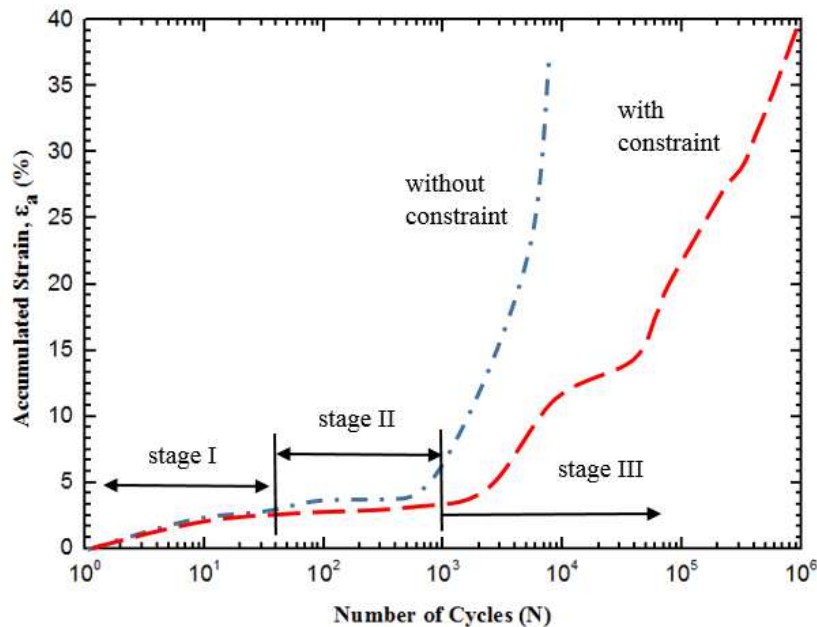


**Figure 18.** Cyclic deformation curve for compressive fatigue behavior [137].

This final stage can be explained by three potential failure mechanisms. The first type of failure, happening in a single and sudden step, occurs with uniform accumulation of strain throughout the foam. Neither formation of crush bands nor localized failures can be observed.

Commonly, this type of failure is observed in Duocel foams [122, 127, 136]. The second type and the third type of failure behavior are shown in Figure 19 a) and Figure 19 b), respectively.

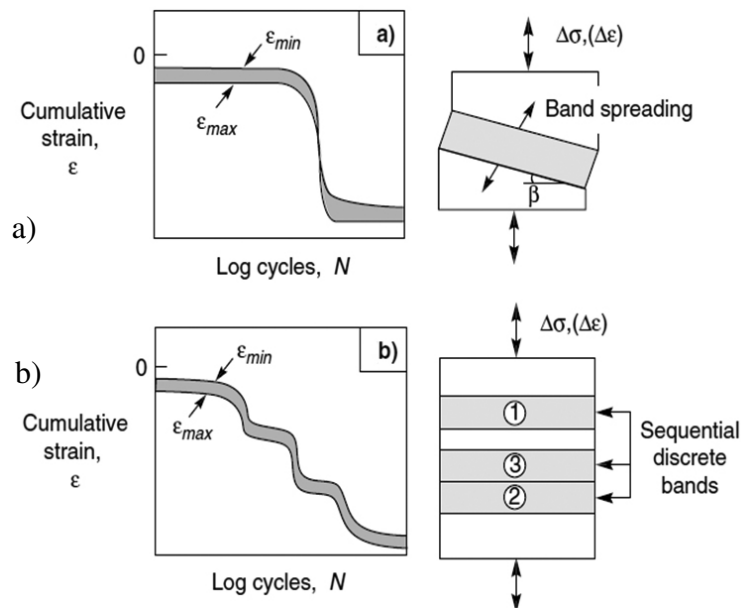


**Figure 19.** Failure behavior of metallic foams under compression fatigue [137].

The second type of deformation starts from the weakest cell wall/strut and with increasing fatigue cycle creates a deformation band which broadens and results in failure. This type of failure has been observed in Alulight foams [114, 124]. In this behavior, multiple crush bands form from the weakest sections of the foams. These bands fail one by one, when the strain accumulation increases up to failure of a single crush band. Each failure creates a strain accumulation step. This type of failure is observed in Alcan foams [122-124, 136].

## 2.6 Biomechanical Tests

Either destructive or non-destructive methods are widely used to investigate the characteristics of the bone-implant interface in a range of orthopedic applications. Destructive methods include histomorphologic research, tensional tests, push/pull-out tests and removal/insertion torque tests. Percussion tests, radiography, cutting torque tests while placing implants are classified as destructive methods [138-139].

Both method groups have their own advantages and disadvantages. The intact bone-implant interface cannot be examined after destructive tests. However, the ability to investigate the implant itself or the host bed is still possible. A non-destructive test would be helpful to characterize mechanical and morphological assays of the intact interface in the same specimen. In contrast to destructive methods, the strength of fixation cannot be determined non-

destructively. However, some previous studies [139] claimed that the shear modulus of the interface zone, which can be determined by using non-destructive methods, might be more suggestive about the type of tissues at the interface than the strength [38, 140]. Berzins et al. [141] developed such a test to determine the implant-bone interface shear modulus by measuring the shear deformation of a thin layer adjacent to the implant.

The *ex-vivo* mechanical properties of biological fixation of orthopedic and dental implants are commonly tested by push-out and pull-out tests, via quantitative evaluation of the shear strength of the bone-implant interface or the holding strength of orthopedic screws. The test protocols of these tests are relatively simple, usually requiring a uniaxial materials testing machine and a simple support jig for the push-out test or a hook-up system for the pull-out test so that it can be operated under displacement control. The effects of implant material, surface topography, implant geometry, porosity, and surface composition of the implant are examined by means of these tests. Moreover, implant stability and fixation strength of orthopedic devices, like artificial joint screws, can be obtained. Both types of tests are usually applied on cylindrical implants, which have been implanted *in vivo* and left *in situ* for various lengths of time. The specimens can be tested either in the fresh condition or after having been frozen. During the tests, the specimen should not be allowed to dry, since the mechanical properties of bone and soft tissue might be altered by histological processing methods [139-141].

Nowadays, mechanical torque systems, including reverse and insertion torque tests, are a common way to evaluate the implant stability and fixation successfully. A reverse torque analysis, known as torque-out, is also proposed for the assessment of implant stability at the time of bone-implant connection. Insertion torque is the decisive parameter to determine the bone quality in various parts of the jaw during implant placement and can be measured by a torque-in test [139]. The torque-in values represents a baseline for the stability of an implant at the time point of insertion [140]. This parameter can be affected by surgical procedure, implant design and bone quality at the implant site [139]. The secondary stability by new bone formation and remodeling around the implant can be investigated by both torque tests. Furthermore, with torque value, the initial stability at the time of implant insertion can be compared with the stability achieved at a certain time after implantation. However, a collection of continuous assessment of implant stability changes after placement is not possible. An increase in torque may indicate not only a rise in primary stability but also may be interpreted in the light of successful repair and remodeling around an inserted biomaterial or surface structure. It has been reported that the maximum torque is produced by the pressure of implant neck on the dense cortical bone [142, 143].

These tests may not provide a clear information about bone bonding and attachment, owing to difficulties in distinguishing biological effects from mechanical interlocking effects on implants attachments. The torque test results can be strongly influenced by friction and in-growth of bone tissue on the implant surface, and the implant surface may be damaged or even fractured under the applied torque stress [139]. Therefore, the push/pull-out tests have several advantages in comparison with the removal torque such as uniaxial strength application and controlled deformation rate of the bone-implant interface [139, 144].

In the push- or pull-out test, a cylindrical implant, which has been placed transcortically or intramedullarily in animal bone, is removed by applying force via a device connected to the crosshead of the materials testing machine. Load should be slowly applied by a calibrated machine, in the vertical direction along the long axis of the implant, until the implant is dislodged. Sudden displacements of the implant should be recognized. During the force application process on the implant, displacement occurs in a bone implant set up and is measured as a change in length or area. During push- and pull-out testing as well as in both torque tests, the failure point represents the breaking of the bone- implant/screw interface [138, 139].

A typical load-displacement curve from a push- or pull-out test can be recorded that illustrates the force along the vertical axis and the position of the crosshead along the horizontal axis shown as in Figure 20.

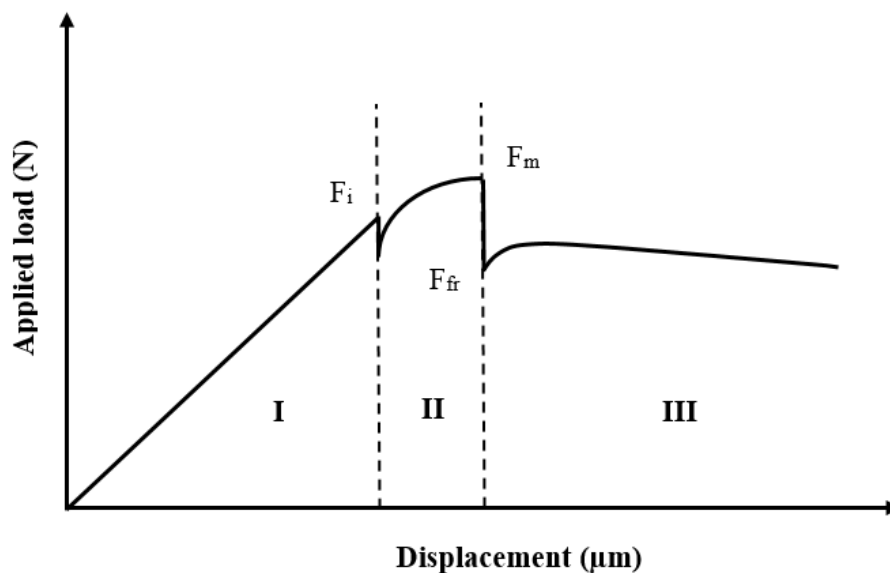


**Figure 20.** A typical load-displacement curve from a push-out or pull-out test [139].

The load-displacement curve could be generalized by three zones. In Zone I, the load increases progressively until the initiation of delamination ( $F_i$ ). A combination of partial

delamination and frictional sliding can be seen in zone II. Zone III corresponds to the onset of complete delamination in which there is a sudden drop in load ( $F_{fr}$ ). Finally, frictional forces resist to further movement of the implant [139].

The maximum load capability (or failure load) is defined as the maximum force  $F_{max}$  on the force-displacement plot and is used in the calculation of the interfacial strength. The interfacial shear stiffness is visualized as the slope of the load-displacement curve at the linear region of the force-displacement curve before the breakpoint [139, 145].

At the end of these tests, the ultimate shear strength of the interface ( $\sigma_u$ ) is commonly calculated. Its value is calculated by dividing the maximum push- or pull-out force ( $F$ ) by the nominal interface area ( $A$ ):

$$\sigma_u = F_{max}/A \quad (16)$$

For a cylindrical implant, the interface area is

$$A = \pi DL \quad (17)$$

where  $D$  is the outer diameter of the cylindrical implant and  $L$  is the length of the implant in contact with bone, while the value of  $L$  is measured at multiple points on the specimen for transcortical implants; for implants cut into slab sections, the thickness of the slab can be used as a  $L$  value. In the case of porous-coated implants, the length of the porous-coating region correspond to  $L$ . The results are usually reported in terms of force per unit area (i.e., the maximum shear stress). It has been reported that the amount of maximum force required to pull/push-out an implant is directly related to bone to implant contact [139]. In that respect two implants with the same test conditions, geometry, and nominal bone contact area can be compared simply by the use of  $F_{max}$ . Some experimental results [122, 139] were reported in terms of the yield strength.

If the interface is assumed to be infinitely thin, the "Young's modulus" or the "interface stiffness" have been calculated as either

$$\Delta F/d \quad (18)$$

or as

$$(\Delta F/A)/d \quad (19)$$

where  $d$  is the displacement. It was reported that the strain rate effect is small for variations between  $\dot{\epsilon} = 10^{-3}/s$  to  $10^{-1}/s$  (roughly, a displacement rate of 1 to 100 mm/min for the implants tested) [139].

It has been found that the diameter and length of implant affect the amount of bone to implant contact, and are important factors in determining the amount of maximum force. Huja et al. [146] obtained a correlation between cortical bone thickness and pull-out strength. Dhert et al. [147] tested the influence of the four parameters (clearance of the hole in the support jig, Young's modulus of the implant; cortical thickness; and implant diameter) on the interface stress distribution and it was reported that variation of the cortical thickness showed a reciprocal relationship between cortical thickness and interface shear stress. Furthermore, the Young's modulus of the implant materials also affects the interface shear stresses. Other factors, such as bone density and quality, possibly play further roles in determining pull/push-out strength [139].

In order to give an impulse to standardization and to gain more insight in the biomechanics of the push-out test, a finite element analysis of this test was performed [139, 141].

### 2.7 Finite Element Analysis

The computer-based numerical FEA is widely used for predicting the mechanical behavior of engineering structures and it can be applied to various structures having complex shapes, loads and boundary conditions. Either small or large scale deflection, stress, vibration, buckling behavior and many other phenomena can be analyzed by using FEA. Owing to the complexity and high cost of experimental measurements, such numerical FE approaches are well accepted. They allow the calculation the complex distributions of elastic and inelastic stresses in different applications. Very numerically accurate results have been produced with the help of this method and the results can be presented visually [17-19, 139, 147].

FEA becomes of important significance in biomechanical research and has many useful applications in the field of medical science to investigate the mechanical behavior of human organs like bones, not only under static loading, but also cyclic loading conditions. It is widely accepted as an ideal tool for biomechanics modeling with complex geometry and inhomogeneous material properties [17, 19, 139, 147].

The applications of FEA in the field of orthopedic biomechanics can be classified into two major numerical approaches: (i) musculoskeletal researches deal with multi-body-dynamics, based on the kinematics of the skeletal systems and muscle activity. (ii) structure mechanical research deals with stress and strain analysis of bone, load-bearing implants and bone-implant

interfaces. There are three main requirements for FEA of bone-implant constructs: geometry of the bone and implant should be modeled in detail, bone and implant material properties should be represented adequately and the boundary conditions of interface between bone and implant should be described appropriately [18, 139].

Recently, two-dimensional (2D) and three dimensional (3D) FE analyses have been used to investigate stress distribution in bone-implant fixation area correlated with implant design. Selection of either 2D or 3D analysis depends not only on the software capabilities, but also on the required accuracy of the results. If detailed stress information is required, then 3D modeling is necessary. On the other hand, a 2D analysis are more efficient in terms of computation time, as compared to a three-dimensional equivalent [17-19, 146-148]. FEA evaluates not only internal stress/strain visually but also provides detailed quantitative data anywhere within the 3D model. In the literature [17, 19, 146-149] the physical behavior of cellular materials has been modeled by different approaches that can be categorized into four directions: (i) phenomenological models, (ii) the application of equations which were developed for composite materials, (iii) model structures representative of the physical structure and (iv) the real structure model based on  $\mu$ CT images.

In previous studies [147-160, 181,183], several models either 2D or 3D were created based on the geometry and characteristics of bone (see Figure 21). Hammad et al. [150] set up constructed 3D models describing implants in blocks of cortical and trabecular bone to evaluate the effect of different implant cross-sectional designs on bone stress levels under vertical and horizontal loading conditions. Chen et al. [151] and Żmudzki et al. [152] simplified the bone geometry to a cylindrical shape surrounding area 3D for the carried out analysis. Eraslan and Inan [153] simulated four types of 3D mathematical models to evaluate the biomechanical influence of implant thread on stresses at implant-bone interface. Huang et al. [154] also created 3D bone-implant models via the computer aided design (CAD) software and used non-linear FEA. Akca and Cehreli [155] used 2D and 3D bone models to analyze the biomechanical effects of progressive marginal bone loss in the peri-implant bone. The model was centrally and vertically positioned into a cylindrical representative of cortical and trabecular bone. The solutions were performed on half of the 3D model, because of the symmetric geometry of the implant. Each model was subjected to a vertical static load of 100 N. As a result, stress distribution, displacement, and equivalent of elastic strain outcomes were compared.

Quaresma et al. [156] created a 2D finite element model based on the physical properties of the implant, prosthesis, and surrounding bone. To investigate the stress distribution in the bone surrounding an implant, a 3D model was generated by Fanuscu et al. [157] from its original

mechanical drawing. They assumed that the model was ideal osseointegrated (100% contact between bone and the implant). The thickness of the cortical bone and stiffness of the graft were varied in the models. Axial and lateral loads were considered. It was reported that the stress from the lateral load was higher than that of the axial load around the implant. The von Mises stress distribution indicated that the stress was highest in the cortical bone and stress was maximal around the top of the implant.

In another study, which aimed to explore the effect of different bone-implant contact on the density distribution of bone, Lian et al. [158] created a 2D model by using plane-strain elements. Cortical and cancellous bone are identified in the model. Van Staden et al. [159] modeled the complex material and geometric properties of the bone and implant by using 2D triangular and quadrilateral plane strain elements. In another study, Guan et al. [160] adopted the 2D representation of implant and bone structures based on either the assumption of axial symmetry of loads or geometry. They claimed that the translation of the clinical condition to a 2D model gives sufficient insight into the behavior of the bone around implants.

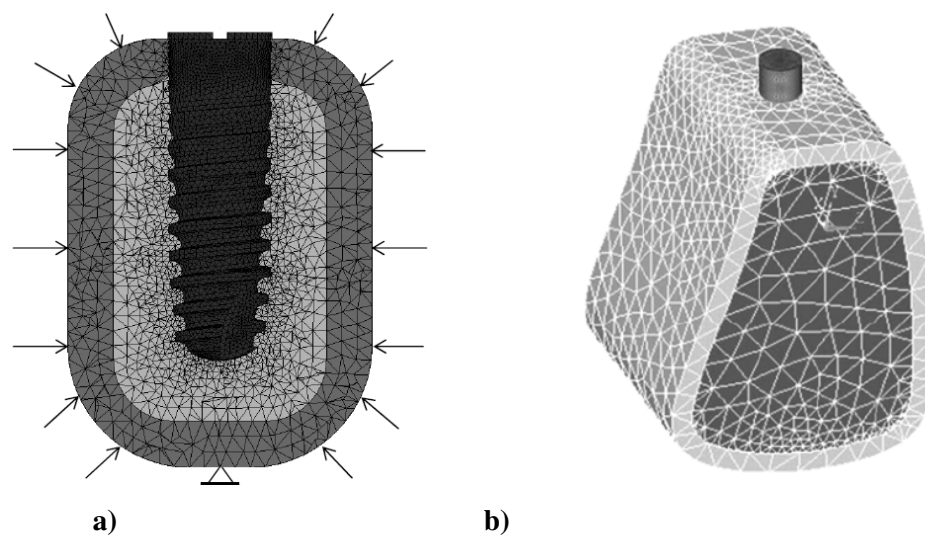


**Figure 21.**Types of finite element models **a)** 2D and **b)** 3D [141,151].

The major aim of the third approach is to create a model structure that strongly simplifies the real geometry. The model should represent characteristics of the real geometry and behave in a similar way to the real structure. With this approach the material behavior may be described by derivation of some equations. However, parameters, which are used in the equations, must be evaluated through experiments. According to the various unit cell forms, many kinds of 2D and 3D models are represented in the literature [161-181].

Mostly, the regular, irregular and inverted hexagonal structures were used for 3D idealization. Gibson and Ashby [123] applied cubic strut models for different types of cellular materials to investigate different macroscopic properties by consideration of beam bending of the struts.

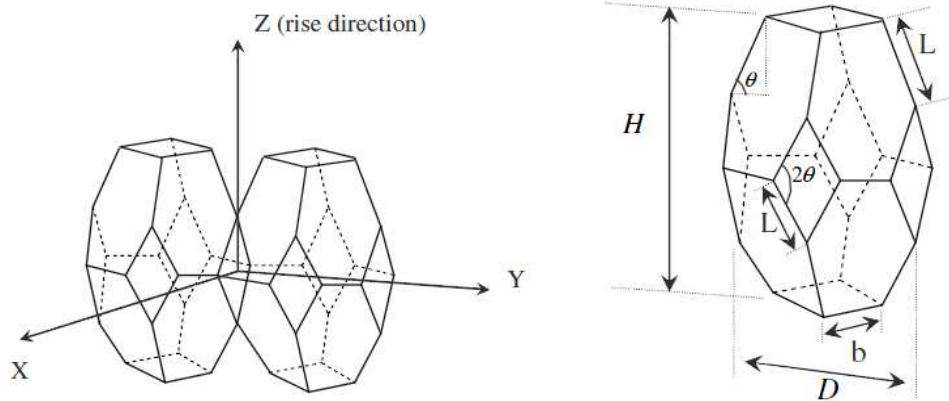


**Figure 22.** Sketch of an elongated Kelvin foam model repeating tetrakaidecahedron unit cell [169].

Fereidoon and Taheri [165] idealized the microstructure of open cell polymeric foams by a regular Kelvin cell. In a cubic strut model, anisotropy can be represented by uniformly stretching it in one of the principal directions. Gong et al. [166] found that the Kelvin cell model is an adequate method of replicating the initial elastic behavior of foams. A regular Kelvin cell is shown above in Figure 22.

Most available mechanical models are based on idealized unit cell structures. Equi-sided and Kelvin-elongated tetrakaidecahedron as unit cells are studied to idealize open cell foams and for predicting their orthotropic properties [166, 167]. An equi-sided tetrakaidecahedron consists of 24 vertices and 36 edges comprising eight six-sided polygons, and six four-sided polygons and has all edges of equal length. The principal directions X, Y, and Z are considered to be along the lines passing through the centers of the squares on the front and back, the left and right, and the top and the bottom, respectively [166-180]. The length of the strut of the unit cell ( $L$ ) and the side of the equilateral triangle ( $d$ ) are the required dimensions to completely describe an equi-sided tetrakaidecahedron unit cell, shown in Figure 22. Zhu et al. [168] used the foam modeled with equi-sided tetrakaidecahedron as a unit cell for predicting the elastic moduli, Poisson ratios, and shear moduli.

However, the unit cell modeling approach does not account for the natural variations in typical foam microstructure, because most real foams are characterized by a random cellular microstructure rather than a perfectly ordered periodic geometry [166, 169]. Gong et al. [166, 167] achieved results that most closely resemble experimentation by means of random foam

model. In another study, Sullivan et al. [169] compared the analytical model with the foam modeled construction with elongated tetrakaidecahedron unit cell which was previously developed by the authors and the equations which result from this model are summarized. For instance, the edge lengths  $b$  and  $L$  and the edge cross-section radius  $r$  can be predicted by using these equations. They concluded that the general elongated Kelvin foam model would be capable of predicting the foam modulus and strength in the principal material directions, if the modulus and strength of the solid material are known. Instead of modeling the complex internal structure of metal foam directly, an unit cell approach is often used [166, 170].

By means of X-ray tomography, Gong et al. [166, 167] determined that area variation in the Al foam ligaments and the cross-sections are different from those of polymeric foams. The concave shape in the polymeric foam templates has been replaced by one with convex sides. They indicated the importance of the variation of cross-sectional area of ligaments along their length on the mechanical properties of foams. It is accepted that the most open cell foam structure contains some level of anisotropy, commonly the elongation of cells in the vertical direction.

The tetrakaidecahedron unit cell includes the squares and the hexagons and is composed of 36 beam elements [169]. As well as continuum element based models, various beam element based models were employed for finite element modeling concepts and linear analysis of 3D cellular structures [166-171]. Because continuum element models imply highly detailed analyses, high modeling effort and can be computationally much more expensive. Analytical methods and finite element simulations based on beam elements were most frequently constructed with tetrakaidecahedral unit cells and Gibson-Ashby's cubic unit cells. A regular network of tetrakaidecahedrons of Kelvin foam gives quasi-isotropic elastic properties.

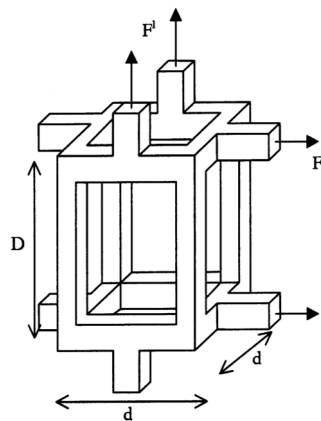


**Figure 23.** Elongated Gibson-Ashby unit cell [162].

Gibson and Ashby [123] considered an elementary cell of cubic or hexagonal form. Koudelka et al. [178] modeled the internal structure of the foam by using elongated Gibson-Ashby's cellular model (see in Figure 23), and performed mechanical behavior analysis in both elastic and plastic fields.

Figure 24 illustrates the cell network deformed under compressive loading. They reported that the considered discretization model can be used for numerical modeling of the deformation behavior of trabecular bone [178].

Straightforward discretization by beam elements is used for adaptation of the stiffness and the material distribution in the vicinity of the vertices. Furthermore, the beam element approaches employed 3D beam elements for modeling these structures [166]. Luxner et al. [180] employed continuum element based models and beam element based models to linear analyses of 3D regular cellular solids and compared to results of uniaxial compression tests of samples. They underlined that the mechanical behavior of cellular structure is represented very well by the beam models and, it follows that the beam element approach is suitable for modeling such structures.

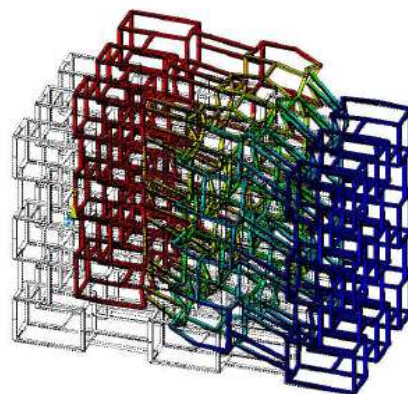


**Figure 24.** The cell network deformed under compressive loading [178].

Recently, finite element analysis has been used in combination with micro-computer tomography ( $\mu$ CT) imaging which indicates strong correlations between implant structural parameters and biomechanical investigations. It appears to be a promising method for determining the mechanical stability of implants and the local stresses, strains, and deformation behavior of the bone implant constructions [17-19, 159, 179-183]. Moreover, the randomness level of cellular structure and its effect on the elastic properties of the material can be determined thanks to the  $\mu$ CT technique.  $\mu$ CT scan data have been widely used to make accurate 3D finite element model of bones, because it provides the necessary detail to represent the

trabecular microstructure of bones and it can be assessed in a single measurement. Furthermore, this method is non-destructive, non-invasive fast and can be carried out completely automated. However,  $\mu$ CT images should be interpreted carefully due to the inability of eliminating radiographic artifacts. In the case of nonlinear material behavior, this method may give deficient results if  $\mu$ CT images have unsmoothed surfaces with sharp geometric discontinuities [179-183].

In previous studies [159, 179-183], data acquisition for the bone dimensions were carried out using CT scanned images. First these images were transformed into 2D and 3D FE models, then they were meshed and material properties were applied. Wirth et al. [181] designed pull-out tests with a microstructural finite element ( $\mu$ FE) approach that combined  $\mu$ CT with finite element analysis. Orthopedic screws inserting into the vertebral bodies of sheep were built and analyzed by using a large-scale linear FE solver. The according to  $\mu$ CT grayscale image and a 3D model representation can be seen in Figure 25 a) and b) respectively. The calculated pull-out strength, obtained from  $\mu$ FE calculation, agreed with the experimentally measured pull-out strength. They suggested that bone-implant constructs can be analyzed using  $\mu$ FE in a detailed and innovative way.

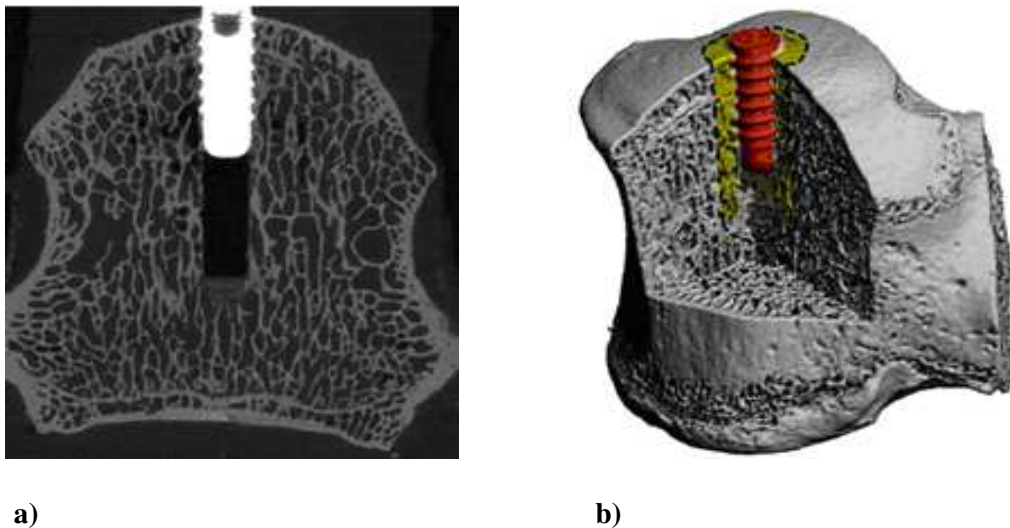


**Figure 25.** a)  $\mu$ CT grayscale image showing the thin trabecular bone structures, b) segmented 3D representation of the inserted screw into the sheep vertebra [181].

### 3 Materials and Testing Methods

#### 3.1 Ti67 Material

A Ti67 (ASTM 1295) alloy was selected for the manufacturing of the implant. According to the TIMET Savoie S.A. data specifications [184, 185], its chemical composition is given in Table 4. Ti67 ingots were hot rolled, annealed at 700 °C for 1 hour and cooled at air.

**Table 4.** Nominal chemical composition of the Ti67 alloy (weight percent) [184, 185].

Element	Nb	Fe	Al	C	O	N	Ta	H	Ti
(wt %)	6.5~7.5	0.25	5.5~6.5	0.08	0.2	0.05	0.50	0.009	Balance

#### 3.2 Manufacturing of Samples

Ti67 specimens used in this work were precision-cast at the Foundry Institute at RWTH Aachen. To prepare the test specimens, four types of investments were used for Ti67 castings: Invest-Ti-T, Al<sub>2</sub>O<sub>3</sub>, ZrSiO<sub>4</sub> and Y<sub>2</sub>O<sub>3</sub>. Invest-Ti-T, based on MgO + Al<sub>2</sub>O<sub>3</sub> + CaO is commercially available (Ti-Research GbR) and is used for dental or jewellery castings. It is mixed and poured into a metal ring that forms a cylindrical block of ceramic around the wax model by use of vacuum. The other three materials (Al<sub>2</sub>O<sub>3</sub>, ZrSiO<sub>4</sub> and Y<sub>2</sub>O<sub>3</sub>) are classical slurries for investment casting. They were dipped and sanded with the above mentioned ceramics and also placed in metal rings and poured with Invest-T-Ti to achieve a high strength of the moulds. Air bubbles and entrapments at undercuts are avoided by the use of vacuum. Casting of Ti67 specimens was carried out under inert argon atmosphere in a centrifugal casting machine (TiCast Super R, SelecCast), that is sketched in Figure 26.

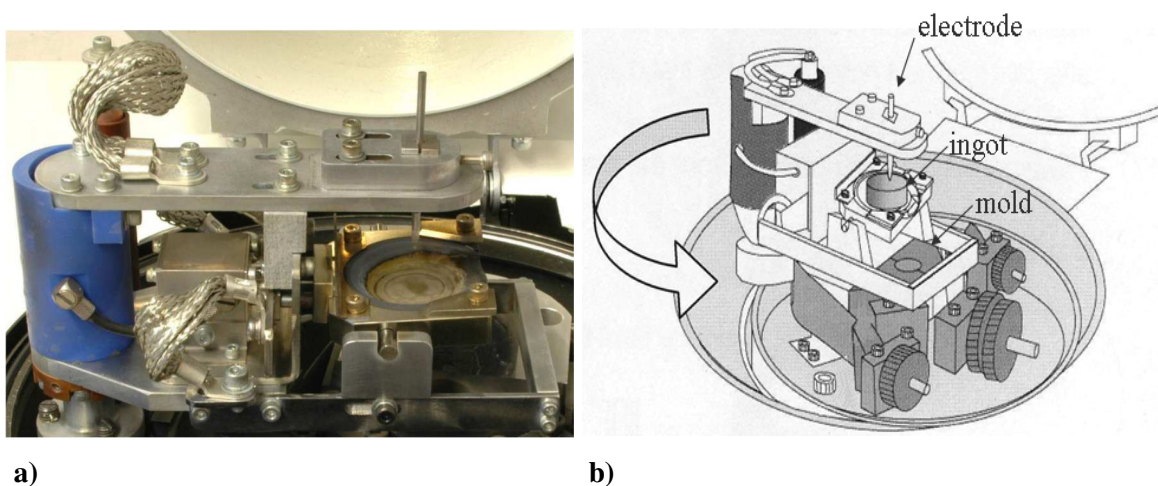


**Figure 26.** a) Centrifugal casting machine, b) schematic overview of the casting chamber [184, 185].

The desired final geometry of the samples was obtained by using reproducing polyurethane templates. Wax models were assembled and dipped into a liquid slurry of the particular ceramic. The layer was then sanded with the same material as the slurry, dried for six hours at a temperature of 21 °C and a relative humidity of 65%. The process was repeated for a second layer that should compensate irregularities of the first layer and enhance the strength of the coatings to withstand the thermal expansion of the different materials during dewaxing and firing.

The casting machine has a small electric arc furnace that produces a drop of molten metal lying on a skull of solid material that avoids the contaminations of melt by the graphite crucible. While melting the ingot material, the plate on which the mould is fixed accelerates to the final velocity of 3000 rpm before the tilting of the crucible.

The manufacturer specifies a theoretical pressure of up to 800 bar at mould filling times in the range of a few milliseconds can be achieved, depending on the design of the casting and the mass of molten metal. Casting of the Ti67 specimen was carried out under inert argon atmosphere at approximately 250 mbar.

In this study, rectangular samples with dimensions of 10 x 10 x 1 mm<sup>3</sup> were used to investigate the  $\alpha$  case formation, as well as to characterize the effect of the mould material on the surface and microstructure of the cast Ti67 samples, illustrated in Figure 27 a). This design was chosen to produce several test specimens with one single casting. Mounting of the samples that was necessary for coating experiments is done with a wire around the conical ingrate that is not removed after the casting process. Figure 27 b) illustrates the casted Ti67 sponge sample which was used to understand not only the fatigue behavior of the open cell structure but also the mechanical behavior of the cell struts.

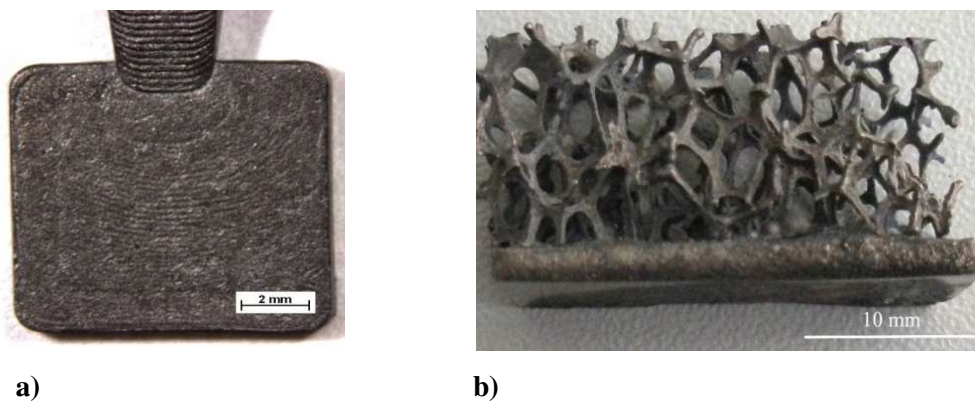


**Figure 27. a) rectangular cast specimen b) cast Ti67 sponge.**

The porous implants used for animal tests were cast with Invest-Ti-T investment, as illustrated in Figure 28. Cylindrical rat implants were fabricated with external diameter of  $3.0\pm 0.2$  mm and  $3.5\pm 0.3$  mm in length. These cylinders had four holes of approx. 1 mm of diameter located on the lateral surface and interconnected with a fifth hole on the bottom (Figure 28 a). The ovine implants were also cylindrical and initially cast with an external diameter of  $10.5\pm 1$  mm, internal diameter of  $8.6\pm 0.4$  mm and  $12.5\pm 1$  mm in length (Figure 28 b).

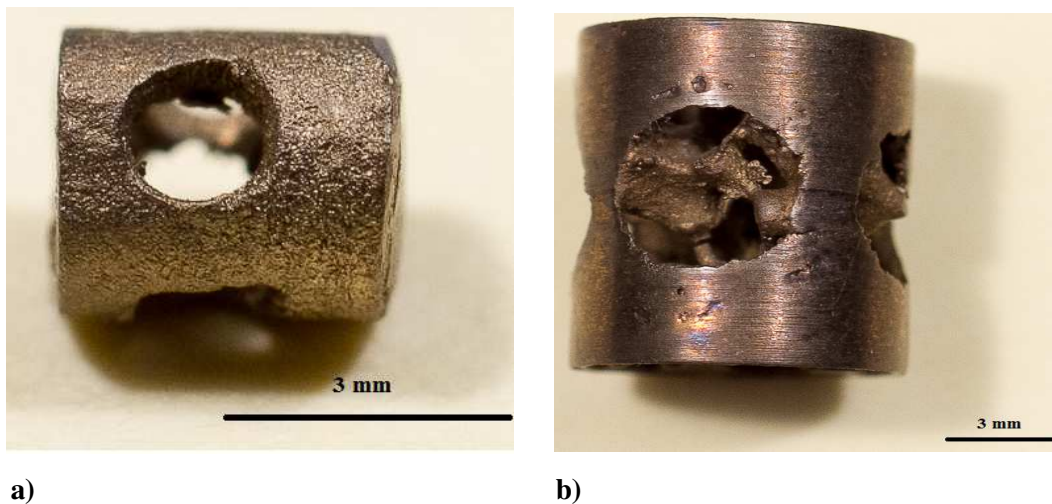


**Figure 28.** a) rat implant, b) ovine porous implant.

After the mechanical milling process, every implant had the same diameter (9.7mm). Inside of the implant, there was a porous structure with cell spacing of  $1674\pm 704$   $\mu\text{m}$  and strut thickness of  $595\pm 205$   $\mu\text{m}$ .

### 3.3 Surface Modification

To remove the brittle  $\alpha$  case from the surface of cast samples the pickling technique was chosen. After the casting process, all samples were attacked with an acid mixture of 70%  $\text{HNO}_3$ +10% HF and distilled water at a temperature between 30-40 °C at the Institut für Werkstofftechnik of the Universität Siegen [184].

In order to understand the effect of bioactive coating on the bone-implant fixation, some samples were coated with a  $\text{CaTiO}_3$  layer after the pickling process at BAM Berlin. The coating process was applied in two steps; in the first step, grid-shaped and plate samples were coated in different salt baths, which are described in Table 5. At the Institut für Werkstofftechnik of the Universität Siegen, the thicknesses of the reaction layers were measured by a cross-sectional examination in the SEM, and each coating was mechanically tested in Ringer's solution using cyclic bending and fretting testing. The same time, the cell culture analysis was carried out at JLU Giessen. The samples coated with SBI showed the best results not only for the mechanical

but also biological tests. In the second step of the coating process, the selected SBI coating was applied on a part of the rat and ovine implants.

**Table 5.** Chemical composition of the four different salt baths used at BAM [184].

Code	Composition [Mol- %]			Temperature [°C]
	Ca(NO <sub>3</sub> ) <sub>2</sub>	NaNO <sub>3</sub>	KNO <sub>3</sub>	
SBI	46	27	27	350
SBII	50	50	-	410
SBIII	60	40	-	450
SBIV	75	25	-	510

### 3.4 Implantation of Samples

In order to investigate the osseointegration process and the mechanical stability of the Ti67 implants in the cancellous bone, the implants were inserted into the metaphysis of the distal femur of rats and sheep (Figure 29 a and 30 a) at JLU Gießen.

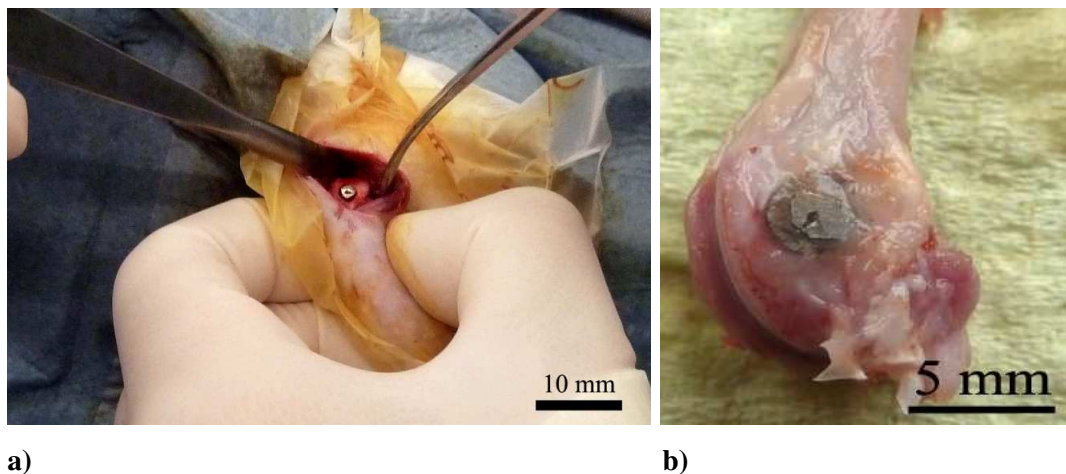


**Figure 29.** a) Implantation in a rat distal femoral metaphysis, b) extracted bone with implant after 30 days [184].

In total, 48 rats and 24 sheep were treated by implantation at JLU Gießen. Small and big animal tests were handled in accordance with the regional commission of Gießen and the regional commission of Darmstadt, respectively.

After 30 days, distal femoral metaphysis of 12 rats and, after 6 months, distal femoral metaphysis of 12 sheep with their respective implants (see Figure 29 b and Figure 30 b) were extracted and used for biomechanical push-out tests. Histomorphometric analysis was

performed on the rest of distal femoral metaphysis at JLU Gießen. Two rats did not survive the operation. They were used as a reference of bone-implant interface at zero days [184].

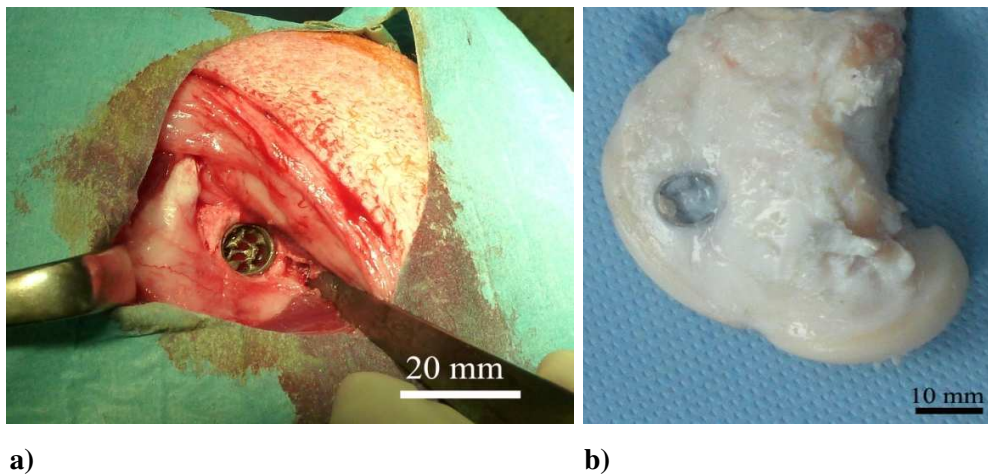


**Figure 30.** a) Implantation in an ovine distal femoral metaphysis, b) extracted bone with implant after 6 months [184].

### 3.5 Biomechanical Push-Out Test Procedure

Biomechanical push-out tests were carried out to analyze the mechanical stability of the bone-implant fixation of rats and sheep at the Institut für Werkstofftechnik of the Universität Siegen.

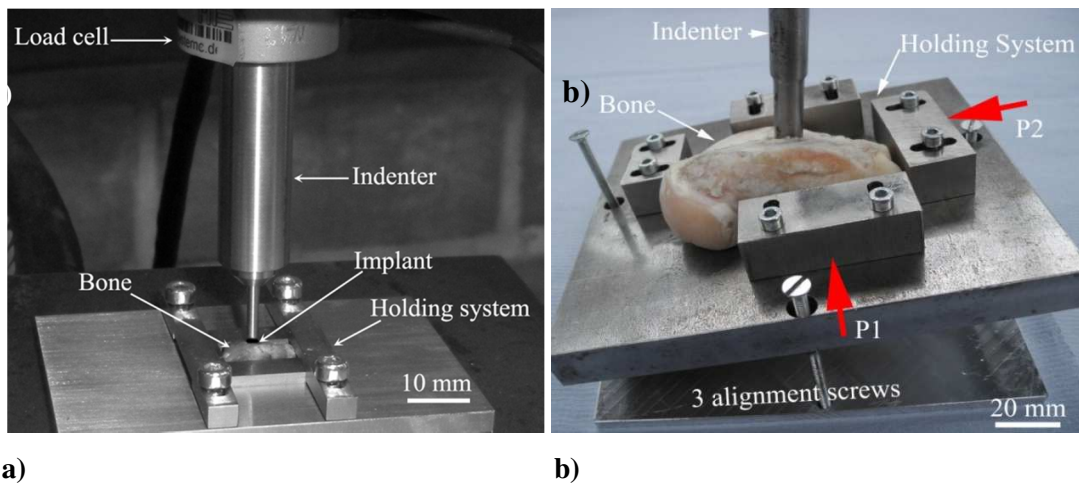


**Figure 31.** Push-out testing system used to analyze the bone-implant interface a) for the rats b) for the ovine bone-implant interface [184].

The push-out system for rat samples and sheep samples are shown in Figure 31 a) and Figure 31 b), respectively. The push-out systems, which were used for rat and sheep implants were nearly the same.

In a prior push-out test, the position of the sheep implants in the ovine distal femoral metaphysis was observed by means of X-ray analysis, in order to eliminate any misalignment of the implants inside the bones during the healing time.

### 3.6 Determination of Biomechanical Parameters

The following essential biomechanical parameters were identified by means of a push-out test to assess and compare biomechanical properties of the bone-implant interface of two different implant types tested in the present study:

The maximum push-out force ( $F_{max}$ ) [N] (also referred to as "peak force" or "ultimate load") was determined as the maximum load recorded during mechanical testing regardless of implant displacement. The implant is pushed-out from the surrounding bone and the measure of the highest force applied before the implant fails is recorded.

The ultimate shear strength of the interface ( $\sigma_u$ ) [N/mm<sup>2</sup>] (also referred to as "maximum shear stress" or "ultimate shear stress") was calculated by dividing the maximum push-out force ( $F_{max}$ ) by the nominal interface area ( $A$ ) (Equation (16))

For a cylindrical implant, where  $D$  is the outer diameter of the cylindrical implant and  $L$  is the length of the implant in contact with bone Equation (17) was used to calculate the nominal interface area.

The interface stiffness [N/mm] (also referred to as "interface elastic modulus") was measured as the slope of the load-displacement curve in its linear region; and calculated according to Equation (18-19), where  $d$  is the displacement. Equation (16-19) were given in the biomechanical tests part of this thesis.

Energy absorption to failure ( $EA$ ) [Nmm = mJ] was calculated as the area under the load-displacement curve until failure (i.e. maximum push-out force) using the ORIGIN PRO 9 software package (OriginLab Corporation, Northampton, USA).

### 3.7 Mechanical Testing

#### 3.7.1 Rectangular samples

Both static and fatigue tests were performed through a three-point bending testing fixture device shown in Figure 32. Such a device was designed and built for these tests according to ASTM E 855 [186].

The monotonic three-point bending tests were conducted by means of a displacement controlled Zwick tension-compression test machine (with a maximum load of 50 kN) with a

displacement rate of 1 mm/min. Five rectangular specimens with dimensions of 10 x 10 x 1 mm<sup>3</sup> were tested for each investment material. Three-point bending fatigue tests were carried out in a DynaMess pneumatic testing system (with a maximum load of 5 kN).

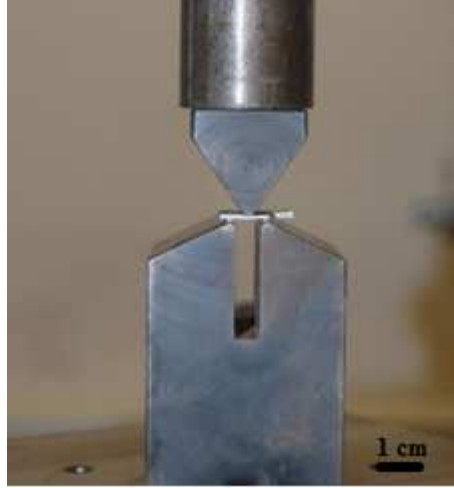


**Figure 32.** Three-point bending testing fixture device.

Tests were performed at a room temperature under direct load control, while the load cycling amplitudes were chosen according to the monotonic three-point bending tests results. The test load was sinusoidal with a frequency  $f = 10$  Hz and a constant amplitude loading with a load ratio of  $R = 0.1$ . Tests were continued until specimen failure occurred.

Elastic modulus, flexural stress and flexural strain (in %) values were calculated according to ISO 178 Standard [187]. In the case of simply supported beams, the maximum flexural stress,  $\sigma_{max}$ , and flexural strain can be determined as follows:

$$\sigma_{max} = \frac{(3FL)}{2bh^2} \quad (20)$$

The flexural strain parameters can be defined by the following equation:

$$\varepsilon_f = \frac{6sh}{L^2} \quad (21)$$

In equations (20) and (21)  $F$ ,  $L$ ,  $h$ ,  $b$ , and  $s$  are referred, applied load (N), span length (mm), thickness of the specimen (mm), width of the specimen (mm) and the deflection (mm) of a rectangular cross-section, respectively.

After the mechanical tests, the microstructure, composition, and thickness of the  $\alpha$  case layer were characterized by optical microscopy and SEM with EDS analysis. All specimens were mounted in epoxy resin for grinding and polishing. They were grinded and polished until the

plane of interest is ready. After that, all of them were etched with Kroll's reagent (100ml H<sub>2</sub>O, 6ml HNO<sub>3</sub>, 3ml HF) for 15 seconds. The fracture surfaces after monotonic and cyclic bending tests were observed by SEM.

### 3.7.2 Sponge samples

To investigate the mechanical properties of individual cell struts, three-point bending tests were applied on the cell struts of Ti67 sponges. A special bending system was constructed and used to test cell struts of the Ti67 sponges. Figure 33 shows the bending system. Monotonic bending tests were performed on a Zwick/Roell Z 2.5 Universal test machine with a maximum load of 2.5 kN and a displacement rate of 0.05 mm/sec.

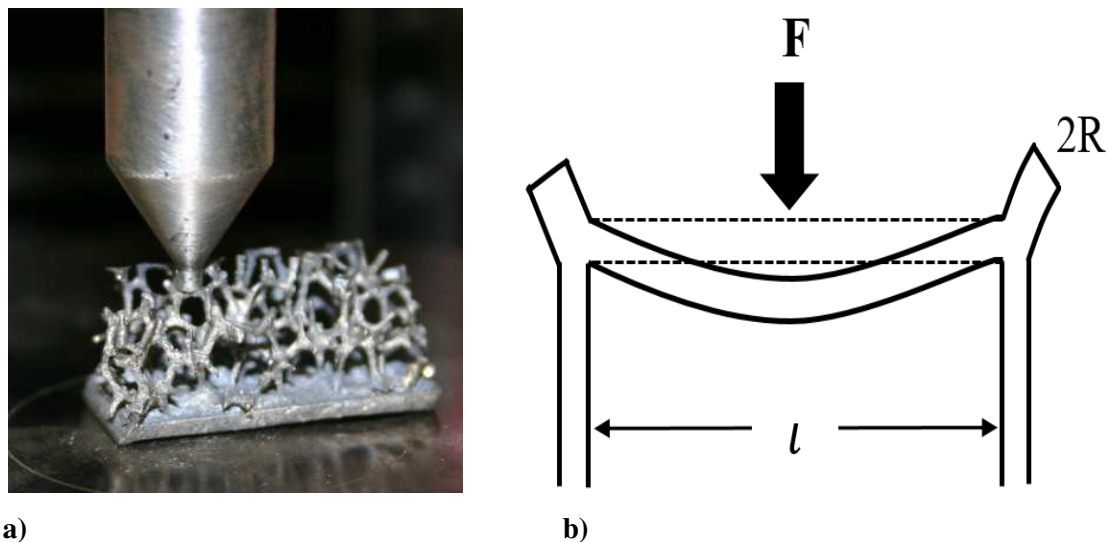


**Figure 33.** Bending test of Ti67 sponges **a)** test system **b)** parameters.

The maximum bending stress,  $\sigma_{max}$  was calculated according to;

$$\sigma_{max} = \frac{FL}{\pi R^3} \quad (22)$$

with:  $\sigma_{max}$  = maximum bending strength,  $F$  = applied load (N),  $L$  = span length (mm),  
 $R$  = radius of beam (mm)

Mechanical testing of the Ti67 sponge specimens was performed under fatigue loading conditions using a DynaMess pneumatic testing system (with a maximum load of 5 kN). Compression-compression fatigue tests were performed at a room temperature under direct load

control, while the load cycling amplitudes were chosen on the basis of the static test result. The test load was sinusoidal with a frequency of  $f = 10$  Hz and a load ratio of  $R = 0.02$  and a constant amplitude loading.

### 3.8 Heat Treatment

In this study, different ways of heat treatment were carried out on commercial Ti67 rectangular (20 mm x 15 mm) samples in order to observe the microstructure evolution as well as the mechanical properties of the Ti67 alloy. These samples were solutionized for 1 hour at temperatures below (950 °C) and above (1050 °C) the  $\beta$ -transus temperature in a horizontal tube furnace flowing by a high purity (99.998%) Ar atmosphere.

The Ti67 samples were inserted into the furnace at room temperature inside an enclosed Ti box on a graphite plate which prevented the bonding between the Ti box and specimens. Three different cooling processes were applied on the samples: air cooling (AC), water quenching (WQ) and furnace cooling (FC) (5 °C/min). A part of the samples were aged at 550 °C for 4 hours. The heat treated samples summarized in Table 6 were characterized by means of metallography and hardness.

**Table 6.** Heat treatment conditions.

<b>commercial Ti67 samples</b>	<b>solution treatment</b>	950°C-1h AC	950°C-1h WQ	950°C-1h FC	1050°C-1h AC	1050°C-1h WQ	1050°C-1h FC
	<b>solution treatment + aging</b>	950°C-1h AC + 550°C-4h	950°C-1h WQ + 550°C-4h	950°C-1h FC + 550°C-4h	1050°C-1h AC + 550°C-4h	1050°C-1h WQ + 550°C-4h	1050°C-1h FC + 550°C-4h

In addition, Ti67 sponge samples were subjected to two different heat treatments to determine the effect of different heat treatments on microstructure and mechanical properties of cell strut. Samples were heated to 950 °C in a tightly enclosed horizontal tube furnace under high purity (99.998%) Ar atmosphere and cooled with different cooling processes; WQ and AC. All samples were aged at 550 °C for 4 hours.

### 3.8.1 Determination of the $\beta$ -transus temperature

A Bähr-Thermoanalyse horizontal DIL 802 difference dilatometer was used to determine the  $\beta$ -transus temperature. Dilatometers provide the measurement of the thermal change of length of a body as a function of the temperature. Differential dilatometers measure the difference between the sample and the inert reference materials [188]. A schematic overview of DIL 802 differential dilatometer is depicted in Figure 34. In this study, cylindrical commercial Ti67 samples with 3 mm diameter and 25 mm length were used and  $\text{Al}_2\text{O}_3$  was chosen as a reference material. All tests are carried out with a temperature range from room temperature to 1100 °C and under vacuum conditions.

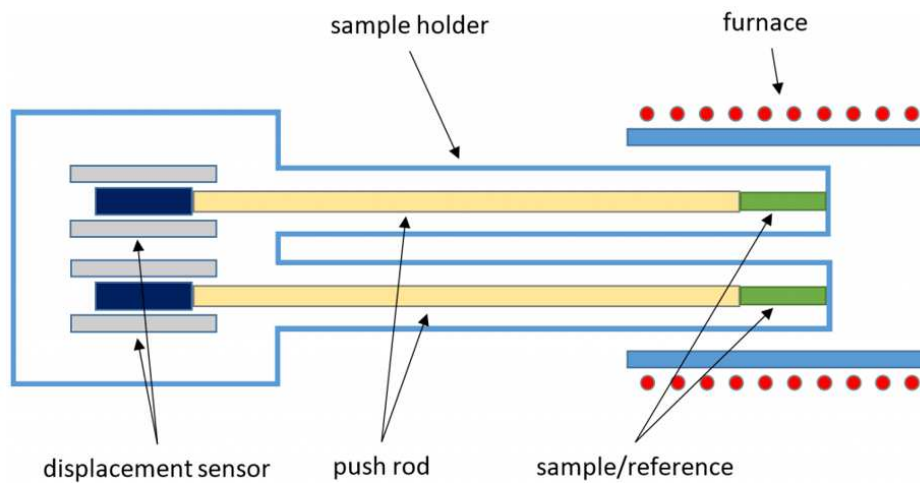


**Figure 34.** DIL 802L differential dilatometer [188].

### 3.9 Hardness Measurement

Microhardness measurements were performed by using a Zeiss AxioVision Vickers microhardness device. Microhardness profiles in each  $\alpha$  case specimen were recorded by means of Vickers microhardness indentations to measure changes in hardness in relation to the depth from the surfaces of the specimens. The stated values are the averages of three measurements at three different positions. Measuring points were arranged in a line at length intervals of 20  $\mu\text{m}$  ranging from 0 to 100  $\mu\text{m}$  and in a line at length intervals of 50  $\mu\text{m}$  from 100  $\mu\text{m}$  to 500  $\mu\text{m}$  depth. The hardness of three different points were measured and averaged for each depth in each specimen.

### 3.10 Roughness Measurement

A Laser Scanning Microscope (Zeiss 700) was used to study the surface roughness of the samples. In this present study, a comparison of the results for roughness parameters was obtained

by using two different methods to evaluate the quality of the finished surfaces: 2D profilometry and 3D profilometry. 2D and 3D surface roughness were determined by characterising  $R_a$ ,  $R_z$  and  $S_a$ ,  $S_z$  respectively. The surface roughness was measured in five locations on one specimen from each of the four material groups.

#### **3.11 Morphological and Analytical Studies**

A Zeiss AURIGA scanning electron microscope (SEM) with energy dispersive X-ray spectroscopy (EDS) was used to carry out morphological and analytical investigations. Metallographical observations were performed by using light microscopy (Zeiss Axio Imager).

To determine the crack depth, mechanical test specimens were sectioned after testing, polished, and etched to reveal the microstructure. The specimens were placed in a light microscope to characterize the microstructure after mechanical deformation, and numerous micro-cracks were observed on the specimen surfaces. The crack depth of the individual micro-cracks was measured. The fracture surfaces were examined by means of SEM in combination with EDS.

O<sub>2</sub> concentration profiles across the  $\alpha$  case region were measured by using line scan analysis and EDS analysis on repolished and unetched samples by SEM.

Prior to microstructural investigations, all Ti67 samples, for  $\alpha$  case layer investigation, were cleaned ultrasonically in ethanol and distilled in water for 20 min. The microstructure, composition, and distribution of the elements in the  $\alpha$  case layer were characterized by using hot epoxy-mounted samples.

Bone specimens were dehydrated before placing the specimen in the SEM sample chamber by passing the specimens through a graded ethanol series from water through 30%, 50%, 70%, 90%, and 100% ethanol, each for 15 minutes, respectively. Then, the samples were dried at room temperature for 24 hours in air. Finally, the dried bones were stored for several days in a desiccator.

#### **3.12 Finite Element Modeling**

In this study, FEA was chosen to examine the quantitative evaluation of stresses on the implant and its surrounding bone. The 2D and 3D models of the designed implants and surrounding bones were constructed and the FEA's were carried out using MSC. Marc and Mentat (MSC Software Corp., Santa Ana, CA, USA). To provide design guidelines for the

development of new implants, the stress distributions on the implant-bone interface were investigated under static loading conditions.

The first step of the modeling is to define the bone and implant geometry. This is followed by specifying the material behavior in terms of the Young's modulus, Poisson's ratio and density for various bone components and the implant. The boundary conditions were described, e.g. with respect to the directions and magnitudes of the forces and displacements acting on the construct.

The 2D FE model was established with two bone blocks the cortical and cancellous bones, and a parallel-side cylindrical rat and sheep implant whose dimensions were given above.

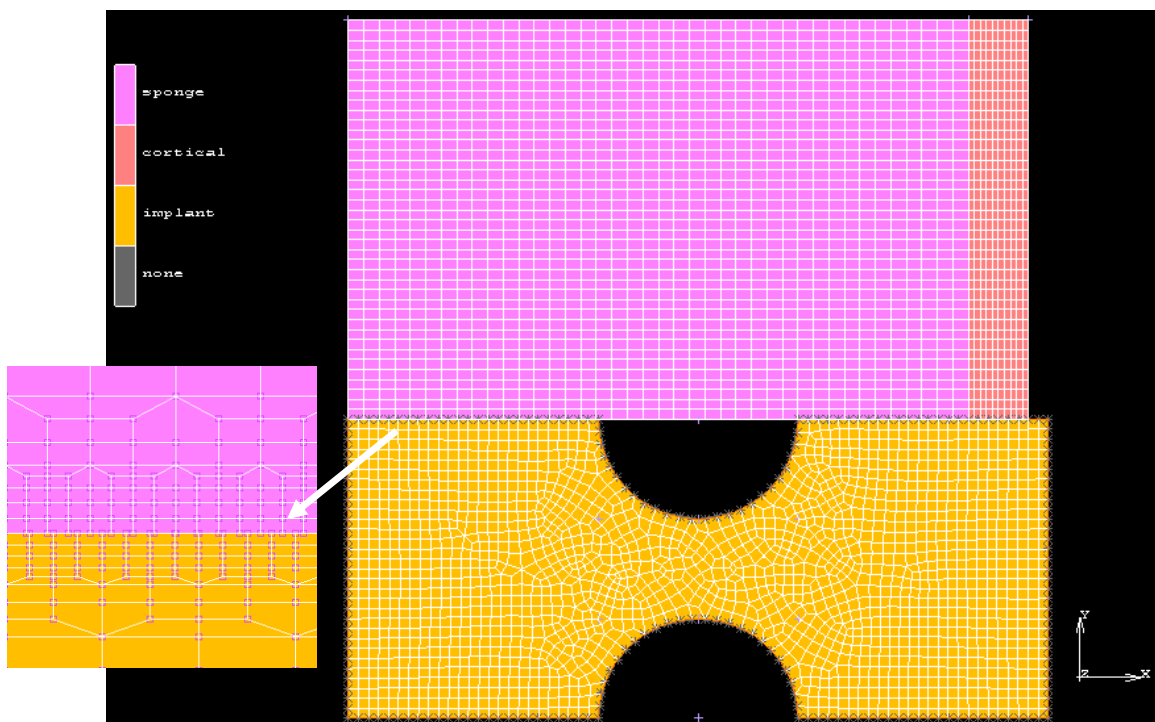


**Figure 35.** 2D Finite Element model.

The bone was modeled as a cancellous core surrounded by a cortical layer with various thickness values measured by means of SEM investigation. In this case, both bones were modeled as a bulk material without any geometrical porosity. In this study, an axisymmetric model was used to study the bone loading patterns in terms of implant displacement. A similar 2D model construction with different dimensions were used for rat and sheep push-out tests. The general 2D model is illustrated in Figure 35. A quadrilateral axisymmetric element type 10 was selected for the 2D model. Element type 10 has four nodes. Although the elements with

eight nodes provide more realistic results, an adequate number of quadrilateral elements could also converge to the similar results that were obtained.

On the other hand, two approaches, in which the detailed micro-architecture including the actual porous cancellous network is incorporated, were mainly followed in modeling cancellous bone for a 3D model. In the first approach, a set of elongated tetrakaidecahedrons (seen Figure 36) was selected for cancellous bone modeling, whereas the elongated Gibson-Ashby's cellular model (seen Figure 37) was used in the second approach. In both approaches, the unit cells were joined together in a repeating pattern in all three directions (left and right; up and down; forward and backward) to form a cancellous bone structure. For elongated tetrakaidecahedrons unit cell, the struts of the cells joined those of the other cells, out of the 6 squares (3 pairs of squares - the top and bottom pair, the left and the right pair and the front and the back pair).

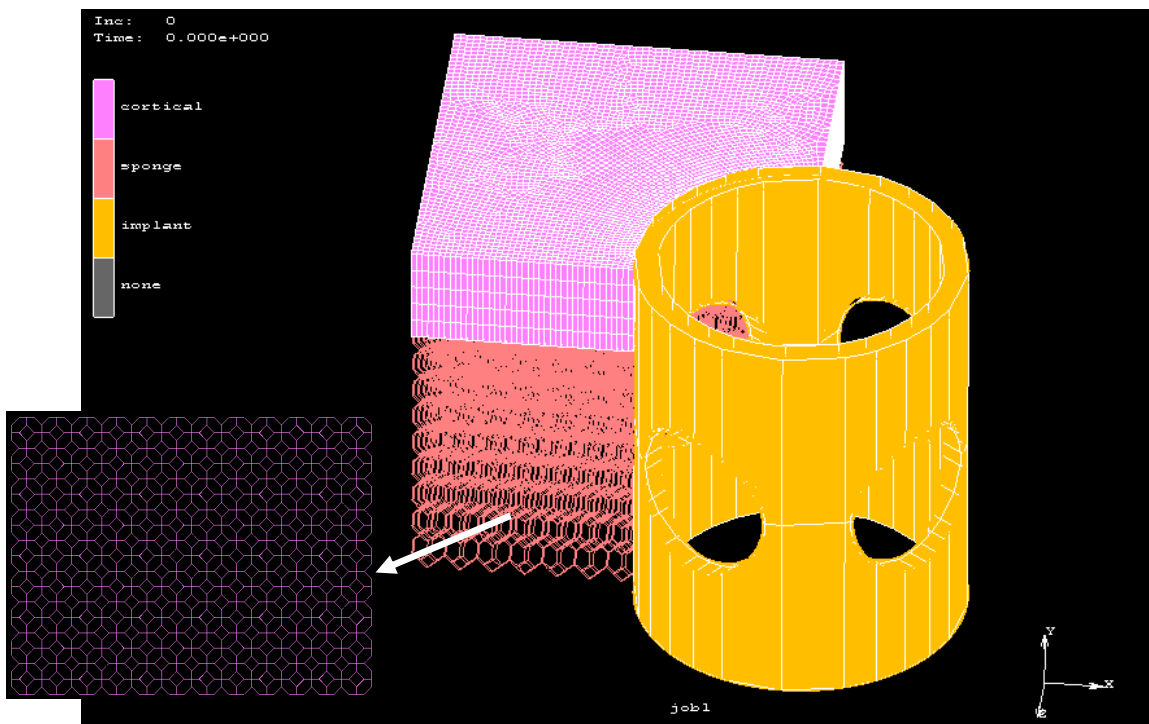


**Figure 36.** 3D model with an elongated tetrakaidecahedron unit cell.

Thus, a more realistic deformation mechanism of cancellous bone was achieved and load-transfer mechanisms can be represented in much more detail with these geometrical assumptions. Furthermore, the direction-dependent, anisotropic behavior of the bone tissue is automatically taken into account. Both models were originally developed for discretization of open cell foams. The beam discretization with cubic cells and tetrakaidecahedron is intentionally used to investigate whether it is suitable for modeling of cancellous bones.

The real geometric parameters of rat and sheep cancellous bones such as cell size, cell anisotropy, strut thickness and ligament length were defined by considering SEM microscope images. The geometry of cancellous bone was modeled by using constant cell dimensions in the proposed 3D beam model, where beams were considered as foam struts. Thereby, deduction of macroscopic characteristics is done by studying the bending of a beam.

For a more realistic representation, geometries of two 3D FE models with the measured dimensions, were generated with a CAD Program (Catia V5) and imported into the FE program.

The material properties of all three materials in this model are considered to be homogeneous, isotropic, and linearly elastic. The Young's modulus and Poisson ratio for the materials are presented in Table 7 [177-181, 189-192].

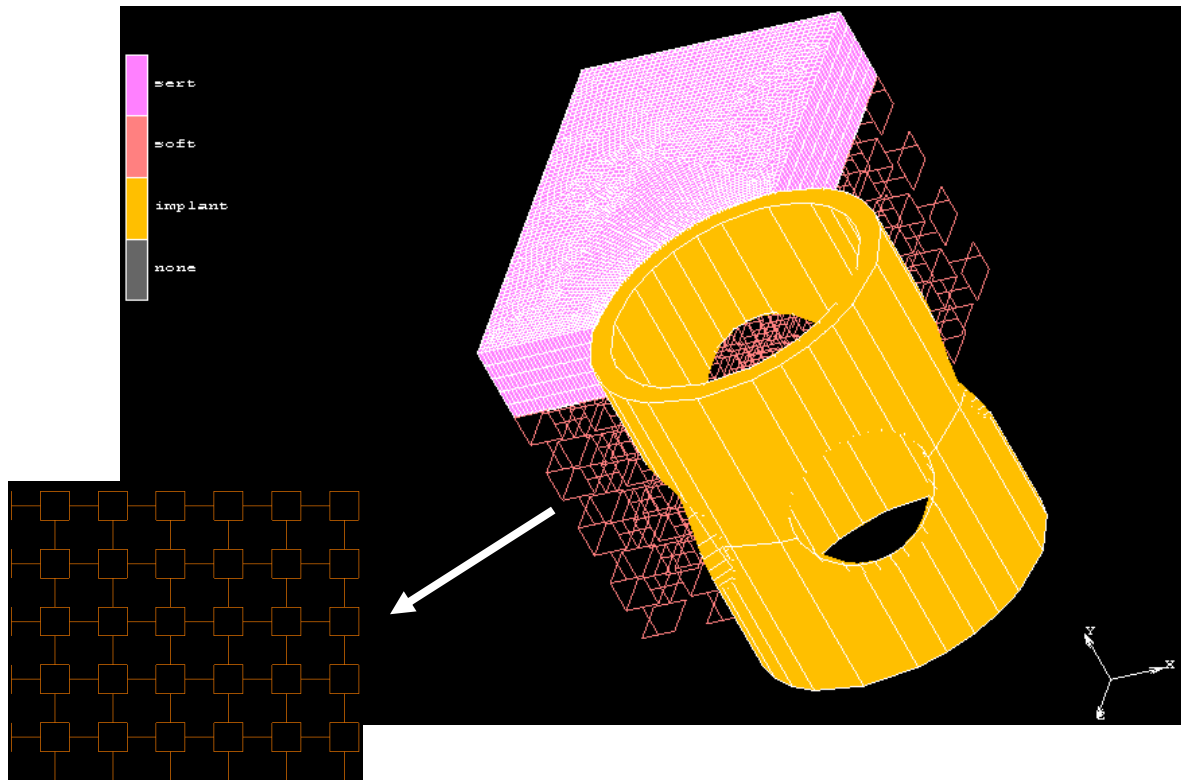


**Figure 37.** 3D model with an elongated Gibson-Ashby's cell.

The main area of analysis and investigation was the contact region between the implant and bone. Hence, the models are constrained in the X, Y, Z directions at the nodes of outer border of the bone surface so that the degrees of freedom in all directions are zero. The von Mises stresses and shear stresses were utilized as bone damage indicators to measure stress levels and evaluate the stress distribution at implant-bone interface as well as the maximum applied load values on implants.

**Table 7.** The material properties of all three materials used within the study [177-181, 189-192].

	<b>Young's Modulus</b>	<b>Poisson ratio</b>
<b>Rat cancellous bone</b>	13700 MPa	0.33
<b>Rat cortical bone</b>	1370 MPa	0.3
<b>Sheep cancellous bone</b>	44000 MPa	0.33
<b>Sheep cortical bone</b>	4400 MPa	0.3
<b>Ti67 implant</b>	110000 MPa	0.3

Bone and implant model were meshed separately and a quadrilateral mesh was constructed. When the models were meshed, the areas with high stress and strain gradients were identified and given a finer mesh. That was particularly important for lateral contact points between implant and bone, in other words, around the point of application of concentrated force (see Figure 35). In this way, the accuracy of the numerical solution was improved. The analysis of mesh convergence was performed. Resulting from an optimization process the ideal mesh size was determined for each model individually. At the bone-implant interface the element size was refined. The meshing process was performed using MSC PATRAN (MSC Software Corp., Santa Ana, CA, USA) due to its high meshing sensitivity. Because of the symmetric geometry of the implant and bone model, the solutions were performed on quarters of the 3D models with proper boundary conditions.

For the 3D models, element type7 and type98 were used for solid cortical bone and for cancellous bone structure, respectively. Element type7, which is hexahedral solid has eight nodes, whereas element type98, which has thick elastic beam elements has two nodes. The robustness of the models was controlled with a sensitivity analysis. The convergence tolerance was defined, as being 0.01. In addition, the use of a bias factor is recommended in presence of frictional contact. The contact bias factor specifies the position of the contact tolerance zone and is essential to precisely capture the touching and separation of the nodes from the contact surface. The Bias factor can have a value in the range of [0-1), in this study, it was assigned a value of 0.9.

The analysis of contact behavior is complex, and the ability to model the contact phenomena plays a crucial role in the simulation of many physical problems. Besides the movement of multiple geometric bodies, the interaction of these bodies after contact should be simulated accurately.

The FE software Marc allows contact analysis to be performed automatically without the use of special contact elements. The numerical capability of Marc makes it possible to detect the motion of the bodies, without any penetration, and apply appropriate boundary conditions to simulate the frictional behavior. Non-penetration constraints are automatically imposed by the program in order to describe the contact between bone and implant. Using the contact option is related to certain rules, (i) at least one deformable body is needed in contact, (ii) the deformable bodies must be defined before the rigid bodies (iii) one node or element can be defined only for one contact body, and (iv) a coordinate axis transformation is not allowed in a contact node. There are two types of contact bodies in Marc; deformable and rigid. Implant and bone were defined as rigid and deformable body, respectively.

FEA programs provide several types of contact algorithms for simulation of contact situations. Three different contact types are defined in Marc: (i) no-contact, (ii) touch, and (iii) glue are used to describe the integration quality at the implant-bone interface. The perfect osseointegration was simulated by glue type contact in which the implant and the surrounding bone and neither sliding nor separation in the implant-bone interface is possible if a glue separation value is not given. The touch type indicates an imperfect osseointegration in which sliding between the implant and bone may take place and separation at the contact interface is allowed. Three contact groups were defined: cancellous bone cortical bone, implant cancellous bone and implant cortical bone. Contact condition needed to be imposed with no penetration of one material into the other. 3D beam elements can be used for the contact analysis in 3D methods. The nodes of the beams can come into contact with rigid bodies composed of surfaces. The normal is based upon the normal of the rigid surface.

For the initial stability, the interfaces between the implant and bone blocks were assumed to be not fully osseointegrated. Therefore, the touch contact option was assigned rather than a glue contact option. The touch contact make sliding of contacting body surfaces along as well as to separate each other possible. The first model configuration represents the situation immediately after implantation. In the second model, it was assumed that osseointegration was complete when the implant was totally surrounded by cancellous bone. Glue type contact was selected for the interfaces between the implant and bone blocks. The breaking options of the glue contact was activated. After the breaking of glue contact, touch contact was activated automatically. For both assumptions, the contact status between cancellous bone and cortical bone was defined as a glue contact which was not allowed to break contact.

In the present study, contact is defined in Marc by using the "node to segment" contact control method. This method provides more accurate stress and pressure results than the

"segment to segment" method. A contact table model option was used to modify the order in which contact is established.

The contact option offers the following three global contact search controls: (i) single-sided, (ii) double-sided, and (iii) optimized contact constraint equations. The double-sided contact option was entered as a global contact search control. Marc offers four ways to prescribe the motion of rigid surfaces: prescribed velocity, prescribed position, prescribed load and prescribed scaling. In this study, prescribed position was taken for the motion of rigid surfaces. Displacement of implant was designated for rat implants; at 2.5 mm, and for sheep implants; at 4.5 mm. At the beginning of the analysis, bodies were in contact. For contact between implant and both bone parts, the size of the contact distance tolerance (i.e. the distance limit below which a node is assumed to be touching a surface) was set to a value of 0.01 mm after a couple of analyses showing its significant impact on the computational time and the accuracy of the solution. While too small contact distance tolerance leads to higher costs, too large contact tolerance results in a loss of accuracy.

To simplify the friction phenomena between bone and implant, a Coulomb friction model was chosen since the Coulomb friction model is more appropriate than the shear friction model. The Marc software requires the input of the friction coefficient ( $\mu$ ) as well as a SL parameter, which describes the non-linear friction characteristics of the interface and determines a smoothing of the step-function of the Coulomb model. Shirazi-Adl et al. [193] investigated the finite element predicted curves for various settings of SL and reported that setting of SL= 0.1 predicts the experimental curve well. Hence, in this study, this setting was used.

It was assumed that the friction coefficient is constant in the slip zone. For solving the numerical difficulties of friction phenomena, three different approximations of the step function for the Coulomb friction model have been implemented in Marc: (i) arctangent model, (ii) stick-slip model, and (iii) bilinear model. The Arctangent model approximation, based on a continuously differentiable function in terms of the relative sliding velocity, was selected so that a true moment carrying glued connection was ensured. The breaking glue contact, in which a user-defined criterion can be given, was activated and the glued connection was broken up using a stress criterion.

Because of loading, stresses were generated during push-out test at the interfaces between implant and bone. If the interface stresses exceed the strength of the bonding, local disruption or debonding will occur. As a result, the interface conditions change and a new stress distribution is appeared at the interface. The debonded implant can now move at the locations where interface disruption occurred [19, 138,142]. In order to evaluate the locations where the

bone-implant interface would debond, the Hoffman's failure criterion was used in this study, depending on the local normal and shear stresses. A multi-axial Hoffmann's failure criterion was assumed for the implant/bone interface and can be described by an ellipsoid for three-dimensional or an ellipse for two-dimensional cases [194, 195]. Figure 38 shows an ellipse describing the interface strength of the implant/bone interface.

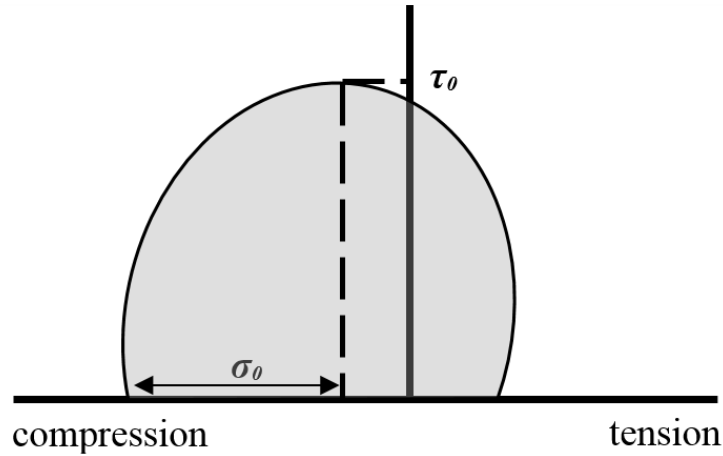


**Figure 38.** Failure criterion for the implant-bone interface [195].

There are few experimental validations in support of the Hoffman's criterion [195-197] and it has been used to evaluate not only cemented implant-bone interface failure but also uncemented implant-bone interface failure. Weins et al. incorporated this failure criterion in a FE model simulating the process of implant-bone disruption [195].

Hoffman's criterion approximates potential interface failure by using a quadratic relation based on the static strength of the interface in normal and shear direction in Equation 23. A combination of interface normal and shear stress values outside ellipse provokes a failure of the bond [195, 196]

The interface stresses and a Hoffman number (FI) can be calculated at each interface nodal point an interface in mathematical terms. This method ensures equilibrium of stresses at the material interface. The FI describes the risk of interface failure and a high value of FI indicates a high risk of failure of the interface. Static interface debonding is expected to occur in case  $FI \geq 1$ .

It was considered that each glued contact nodes should separate if

$$FI = \left(\frac{\sigma}{\sigma_0}\right)^2 + \left(\frac{\tau}{\tau_0}\right)^2 \geq 1 \quad (23)$$

with  $\sigma$  and  $\tau$  the actual normal and shear stresses, respectively, and  $\sigma_0$  and  $\tau_0$  constants as shown in Figure 38.

When a node is released after the breaking of the glue, the contact status changes from being glued to standard contact which permits separation and friction (touching contact). After applying the appropriate restraint conditions, contributions of different parameters on the stress profile in the bone-implant interface can be evaluated.

The interfacial conditions between the rat implants and the bone were determined according to a reference rat (hereafter ref.rat) sample's result such as the friction coefficient. On the other hand, two push-out curves, which reveal very low push-out force values were used as a reference for each sheep implant groups. For the interface between implant and bone, a constant finite shear strength was implemented. Pistoia et al. [198] developed a structural hypothesis for  $\mu$ FE models of human distal fore arms. In this study, the strength was estimated based on this hypothesis. According to this concept, failure is expected to occur as soon as the effective strain level (deformation / length of bone implant interface) exceed a certain critical threshold. Previous biomechanical studies [193, 196-199] suggested that failure occurs as soon as the effective strain levels in a characteristic fraction of the bone volume exceeded a critical threshold. In this study a critical threshold was accepted as 0.7%. The effective strain threshold was set to 7000 microstrain based on literature values [194-198]. Until this strain values, separation of bone and implant was not allowed in order to determine maximum push-out force. The Pearson correlation coefficient was used between FE-calculated maximum push-out forces and mechanically measured push-out forces.

The effective interference approach was used to simulate the biomechanical behavior of the CaTiO<sub>3</sub> coated implants. The effective interferences at the coated implants interface are 0.5  $\mu$ m and 1.5  $\mu$ m for rat and sheep implants, respectively. These effective interference values were based directly on measurements of the thickness of the CaTiO<sub>3</sub> coating layer.

## 4. Results

### 4.1 Investigation of $\alpha$ Case Formation

The distribution of the  $\alpha$  and  $\beta$  phase gave nearly identical values for the Ti67 samples (see Table 8). Only  $Y_2O_3$ -investment cast samples have a slightly higher content of the  $\beta$  phase than  $\alpha$  phase in their microstructure. On the other hand, the samples prepared with  $Y_2O_3$  as the investment material had the smallest grain size in comparison with the other materials (Invest-Ti-T,  $Al_2O_3$ ,  $ZrSiO_4$ ).

**Table 8.**  $\alpha/\beta$ -phase distribution (in %) and grain size of the casted Ti67 samples by using different investment materials.

	Invest-Ti-T	$Al_2O_3$	$ZrSiO_4$	$Y_2O_3$
<b><math>\alpha/\beta</math>-phase distribution (%)</b>	52/48	51/49	54/46	48/52
<b>Grain size (<math>\mu m</math>)</b>	167	143	133	124

#### 4.1.1 Invest-Ti-T

The microstructure and the element mapping by means of EDS of the interfacial reaction region between Ti67 and the investment material Invest-Ti-T are shown in Figure 39 and Figure 40, respectively. It was found that the  $\alpha$  case reaction layer of titanium castings fabricated with the Invest-Ti-T investment was approximately 35  $\mu m$  thick and could be divided into two layers.

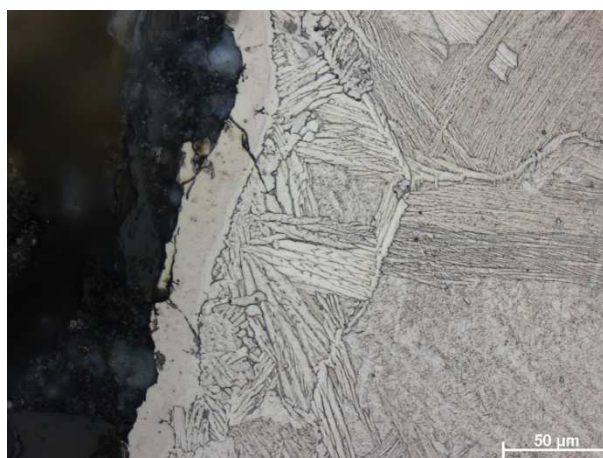


**Figure 39.** Microstructure of a cast Ti67 sample with Invest-Ti-T investment.

#### 4 Results

Elemental mapping reveals the presence of aluminum, calcium and oxygen, all of which were also detected by EDS chemical composition measurements on the surface of the sample.

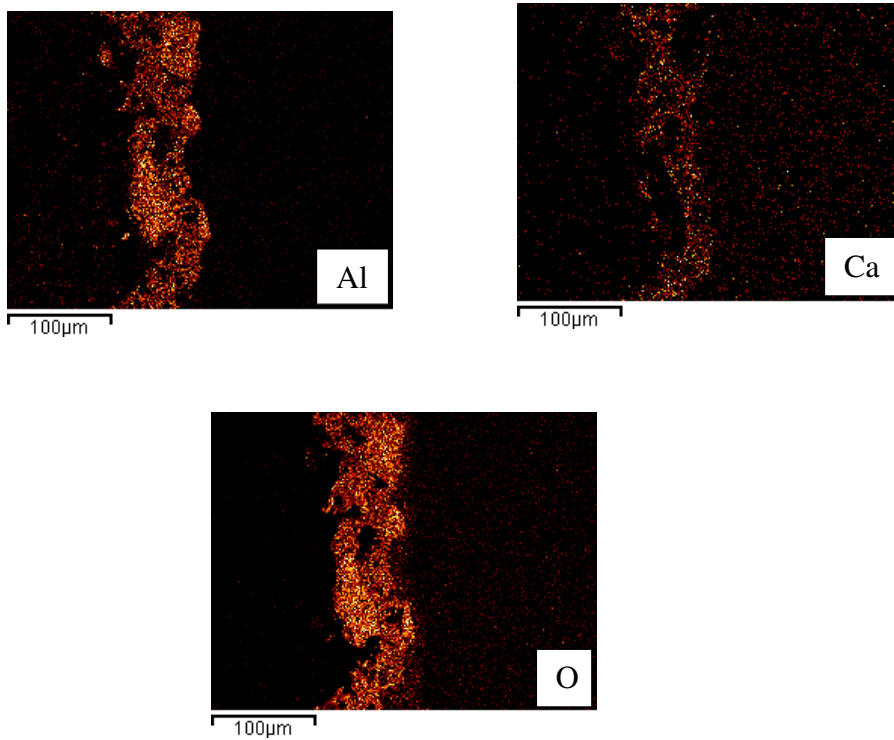


**Figure 40.** Element mapping image of Al, O, and Ca in Ti67 casting with Invest-Ti-T investment.

The two layers are represented in back-scattered electrons micrograph image in Figure 41. The outer layer is an oxide layer with a thickness of approximately 25µm and the inner layer is the so-called alloy layer, which was approximately 10 µm thick.

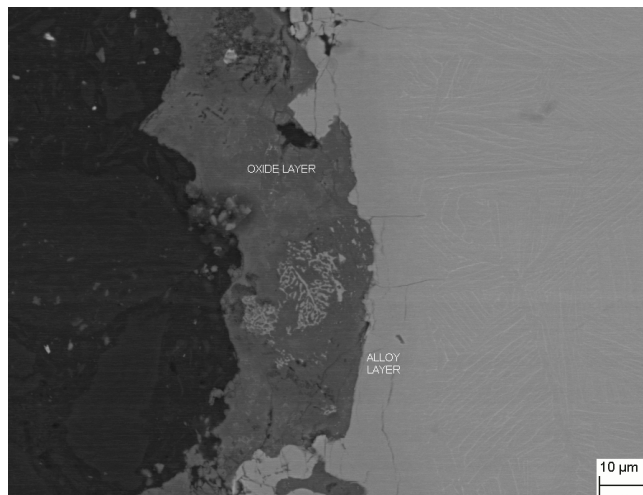


**Figure 41.** SEM micrograph of the  $\alpha$  case layer of a Ti67 casting made with Invest-Ti-T investment.

Table 9 shows the typical composition of the constituents of the  $\alpha$  case layer. According to EDS measurements, it was found that the oxide layer includes  $\text{Al}_2\text{O}_3$ ,  $\text{CaO}_2$  and  $\text{TiO}_2$ , whereas the alloy layer consists of Ti, Al, and a small amount of Ca. Additionally, a fine-grained outer zone of hexagonal  $\text{Ti}_3\text{Al}$  corresponding to the  $\alpha$  case layer was obtained thanks to analysis of the crystallographic structure of the surface layer by using automated electron back-scattered diffraction (EBSD) [184]. It can be clearly seen that the formation of a hardening layer did not result from the reaction between molten titanium and investment.

**Table 9.** EDS measurements at the chemical composition of the  $\alpha$  case layer of Ti67 casting in Invest-Ti-T.

layer	Element ( wt% )				
	O	Al	Ca	Ti	Nb
oxide	63±6.7	21±3.4	8±1.6	8±2.3	0
alloy	0	18±2.1	4±0.6	76±4.2	2±0.3
hardening	0	11±1.7	0	84±3.8	5±0.8

#### 4.1.2 $\text{Al}_2\text{O}_3$ -based investment

Figure 42 and Figure 43 show the microstructure and the EDS element mapping of the interface between the alloy and an  $\text{Al}_2\text{O}_3$ -based investment, respectively. It was found that the reaction layer of Ti67 castings fabricated with the  $\text{Al}_2\text{O}_3$ -based investment was approximately 25  $\mu\text{m}$  thick.



**Figure 42.** Microstructure of a cast Ti67 sample in  $\text{Al}_2\text{O}_3$  based investment.

## 4 Results

The reaction layer can also be separated into two different layers which can be clearly seen in the BSE micrograph image in Figure 44. The thicknesses of the outer layer, an oxide layer, and the inner layer, an alloy layer, were obtained to be approximately 10  $\mu\text{m}$  and approximately 15  $\mu\text{m}$ , respectively.

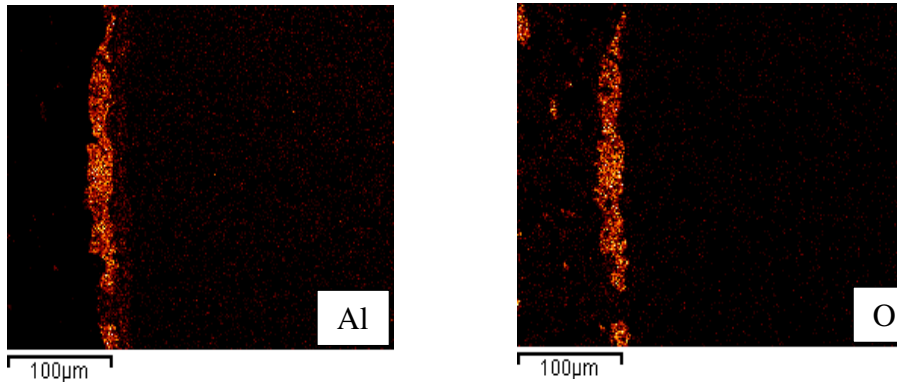


**Figure 43.** Element mapping image of Al and O, in Ti67 casting in  $\text{Al}_2\text{O}_3$  based investment.

According to EDS measurements, it was determined that the outer oxide layer may include  $\text{Al}_2\text{O}_3$  and  $\text{TiO}_2$ , whereas the alloy layer consists of Ti, Al, and O. Table 10 shows the typical composition of the  $\alpha$  case layer. It can be clearly seen that the formation of a hardening layer did not result from the reaction between molten titanium and investment. The thickness of the hardening layer primarily depends on the temperature of the molten titanium during casting and the cooling rate after casting [69, 72, 80].

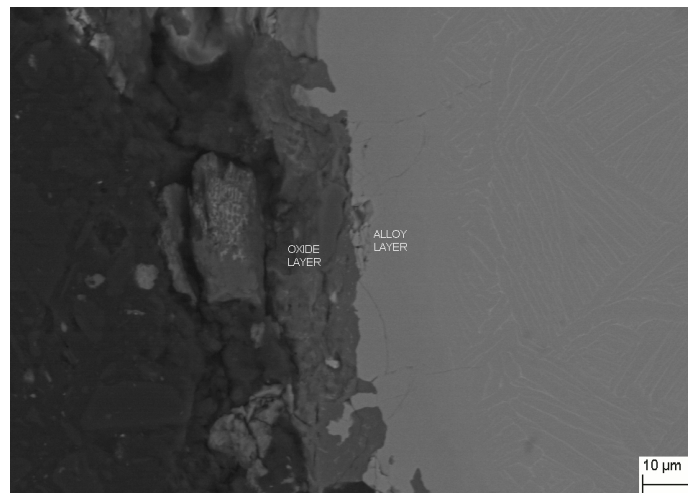


**Figure 44.** SEM micrograph of  $\alpha$  case layer of Ti67 casting made in  $\text{Al}_2\text{O}_3$  based investment.

In accordance with the results of EDS analysis of the chemical composition of the  $\alpha$  case layer, the presence of the oxygen aluminum and titanium was observed. The results of EDS chemical analysis indicate that the Al and Ti are rich in the oxide layer.

**Table 10.** EDS measurements at the chemical composition of the  $\alpha$  case layer of Ti67 castings in  $\text{Al}_2\text{O}_3$  based investment.

layer	Element ( wt% )			
	O	Al	Ti	Nb
oxide	64±5.88	21±3.11	15±1.33	0
alloy	0	19±1.88	78±4.11	3±0.5
hardening	0	9±0.88	85±4.44	6±0.8

#### 4.1.3 ZrSiO<sub>4</sub>-based investment

The microstructure and the EDS element mapping of the interface between Ti67 and the ZrSiO<sub>4</sub> based investment are presented in Figure 45 and Figure 46, respectively. It was shown that the reaction layer of titanium castings fabricated with the ZrSiO<sub>4</sub> investment was approximately between 20-25  $\mu\text{m}$  thick.

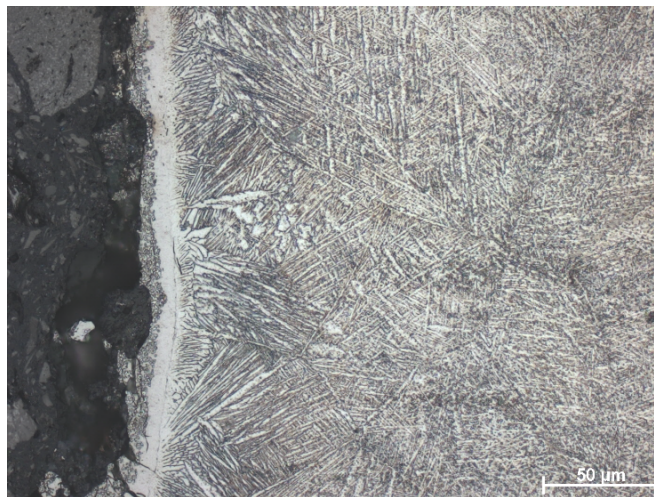


**Figure 45.** Microstructure of a cast Ti67 sample with ZrSiO<sub>4</sub> based investment.

Elemental mapping reveals presence of silicium, zirconium and oxygen, all of which were also detected by EDS chemical composition measurements on the surface of the sample.

#### 4 Results

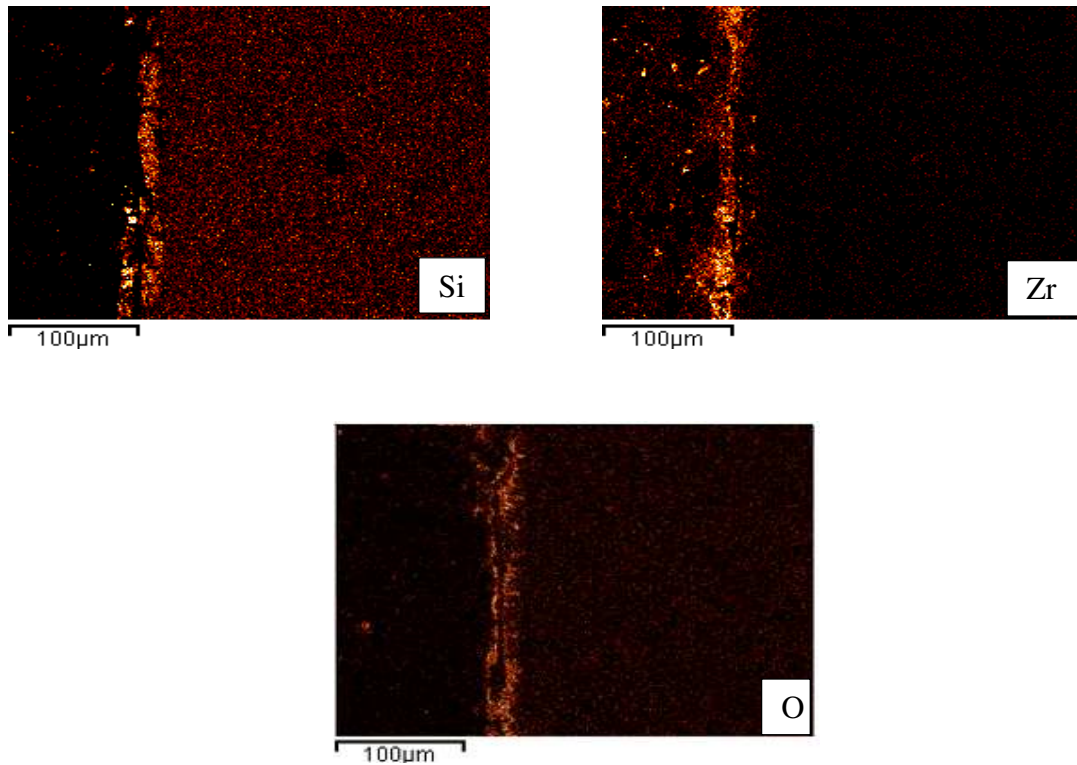


**Figure 46.** Element mapping images of Zr, Si and O in Ti67 casting with ZrSiO<sub>4</sub> based investment.

Figure 47 shows the back-scattered electrons micrograph image. The reaction layer could be divided into two layers. The outer layer is an oxide layer with a thickness of approximately 10 µm that may include SiO<sub>2</sub>, ZrO<sub>2</sub> and TiO<sub>2</sub>. The inner layer is the so-called alloy layer, which was approximately 15 µm thick, consisting of Ti, Zr and a small amount of Si. Table 11 shows the typical composition of the  $\alpha$  case layer. It can be clearly seen that the formation of a hardening layer did not result from the reaction between molten titanium and investment.

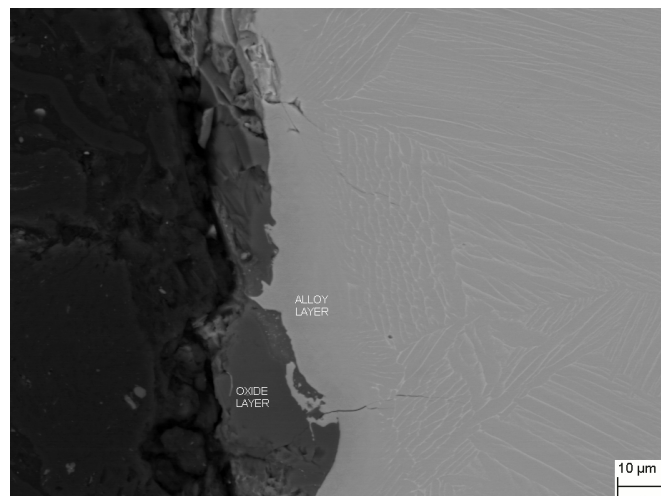


**Figure 47.** SEM micrograph of  $\alpha$  case layer of the Ti67 casting using a ZrSiO<sub>4</sub> based investment.

The results of EDS analysis of the chemical composition of the  $\alpha$  case layer indicate that the Zr and Si are rich in oxide layer, but poor in reaction layer.

**Table 11.** EDS measurements at the chemical composition of the  $\alpha$  case layer of Ti67 casting in ZrSiO<sub>4</sub> based investment.

layer	element ( wt% )					
	O	Zr	Si	Ti	Al	Nb
oxide	62±4.1	12±1.6	9±0.8	10±1.7	7±0.9	0
alloy	0	7±1.2	4±0.7	75±3.4	10±1.2	4±0.8
hardening	0	0	0	85±5.1	7±0.4	8±1.2

It was confirmed that the  $\alpha$  case layer on titanium castings invested with Invest-Ti-T, Al<sub>2</sub>O<sub>3</sub>, and ZrSiO<sub>4</sub> based investments consisted of three layers- namely, the oxide layer, the alloy layer, and the hardening layer. An EDS elemental mapping analysis demonstrated that the alpha case layer was not only composed by interstitial oxygen but also by substitutional elements dissolved from mould materials. Therefore, the oxide layer and alloy layer were called the reaction layer.

#### 4.1.4 Y<sub>2</sub>O<sub>3</sub>-based investment

According to the microstructure and the elemental mapping of the interfacial reaction region between Ti67 and an Y<sub>2</sub>O<sub>3</sub> based investment, obviously no surface reactions between metal and mould took place as it can be seen in Figure 48 and Figure 49, respectively.

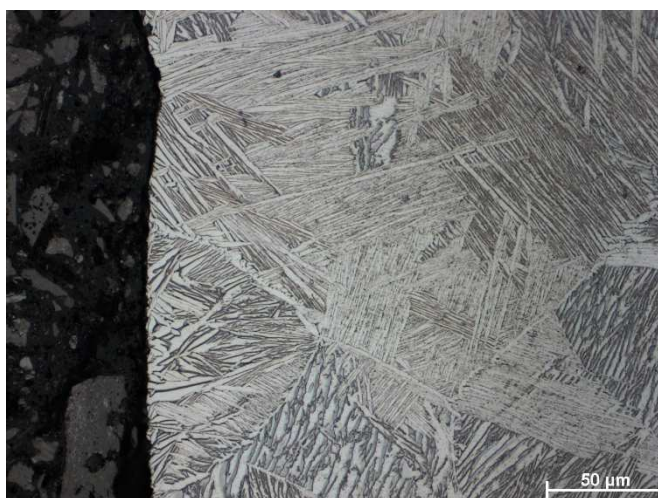


**Figure 48.** Microstructure of a cast Ti67 sample with Y<sub>2</sub>O<sub>3</sub> based investment.

#### 4 Results

The EDS measurements revealed a chemical composition of the interfacial reaction region of approx. 86 wt % Ti, 6 wt % Al, 6 wt % Nb and 2 wt% Y.

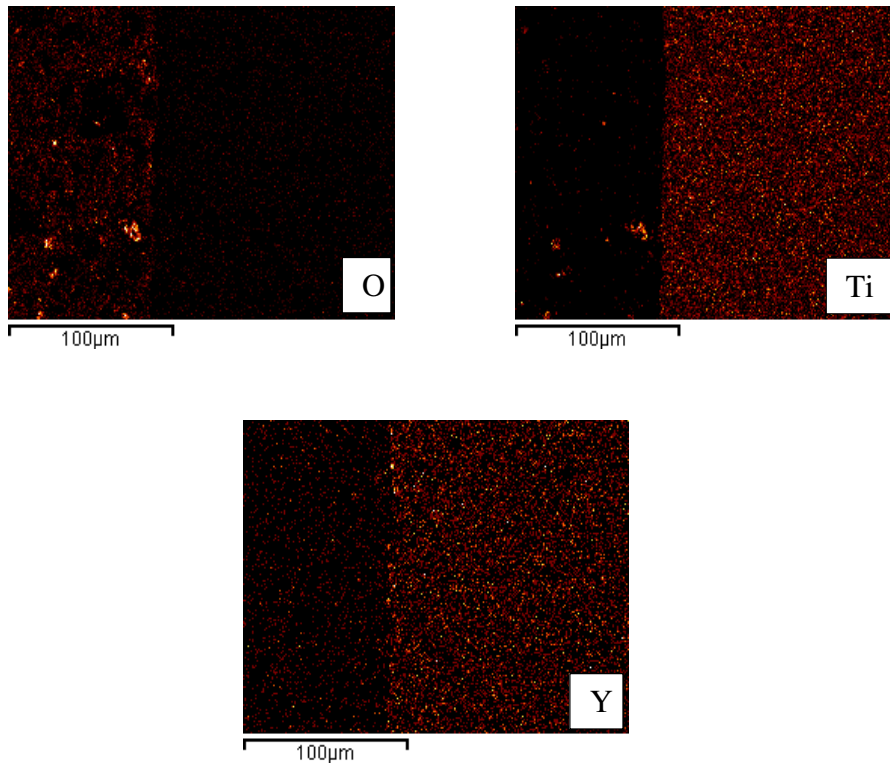


**Figure 49.** Element mapping image of Y, Ti and O in Ti67 casting in  $Y_2O_3$  based investment.

Figure 50 presents a back-scattered electron SEM micrograph of a cast Ti67 sample in  $Y_2O_3$  based investment. Neither oxide layer nor reaction layer were observed in the interfacial reaction region between Ti67 and the  $Y_2O_3$  based investment.

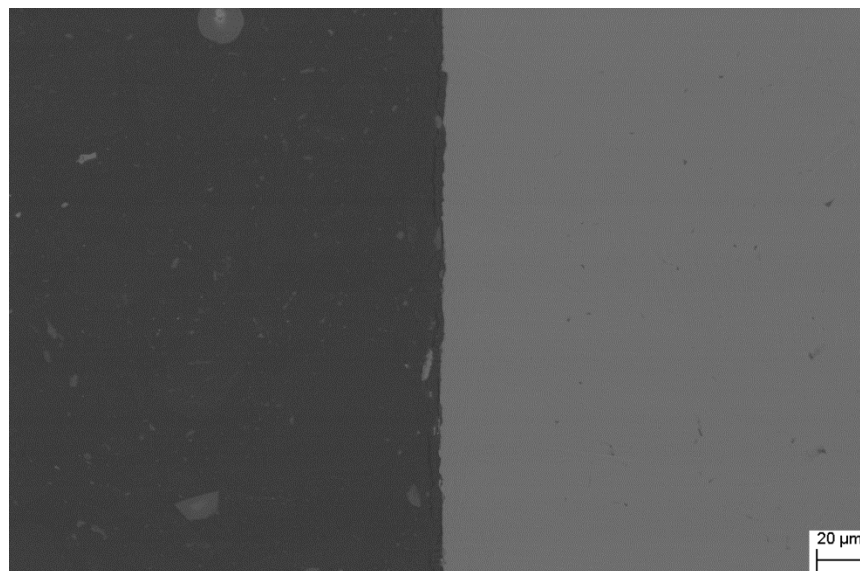


**Figure 50.** SEM micrograph of  $\alpha$  case layer of the Ti67 casting using a  $Y_2O_3$  based investment.

In Figure 51 the microhardness profiles across the surface layer of Ti67 castings made with Invest-Ti-T,  $\text{Al}_2\text{O}_3$ -,  $\text{ZrSiO}_4$ - and  $\text{Y}_2\text{O}_3$ - based investments are compared as a function of the depth from the outermost surface to the interior of the castings.

The hardness profiles of the samples are in good agreement with the illustrated results from light microscopy. The first three samples, cast with Invest-Ti-T,  $\text{Al}_2\text{O}_3$ - and  $\text{ZrSiO}_4$ - based investment, represent nearly the same properties. In contrast, the  $\text{Y}_2\text{O}_3$ - investment cast sample showed no increase in surface hardness.

The surface microhardness of sections of Ti67 castings produced with Invest-Ti-T investments was the highest (520 HV) and decreased rapidly from the surface to an approximate depth of 30  $\mu\text{m}$  (452 HV), and then reduced slowly to a depth of 100 (372 HV). Below that hardness remains nearly constant of 120  $\mu\text{m}$ . The surface microhardness of titanium castings produced with  $\text{ZrSiO}_4$ -based investment and with  $\text{Al}_2\text{O}_3$ -based investment were 490 and 505 HV, respectively. The hardness of these samples decreased rapidly from the surface to a depth of 15  $\mu\text{m}$ , and then decreased to a depth of 80  $\mu\text{m}$  slowly, whereas the surface microhardness profile of titanium castings made with  $\text{Y}_2\text{O}_3$  based investment material showed a smooth distribution with values in the range of 370 HV throughout the complete cross-section.

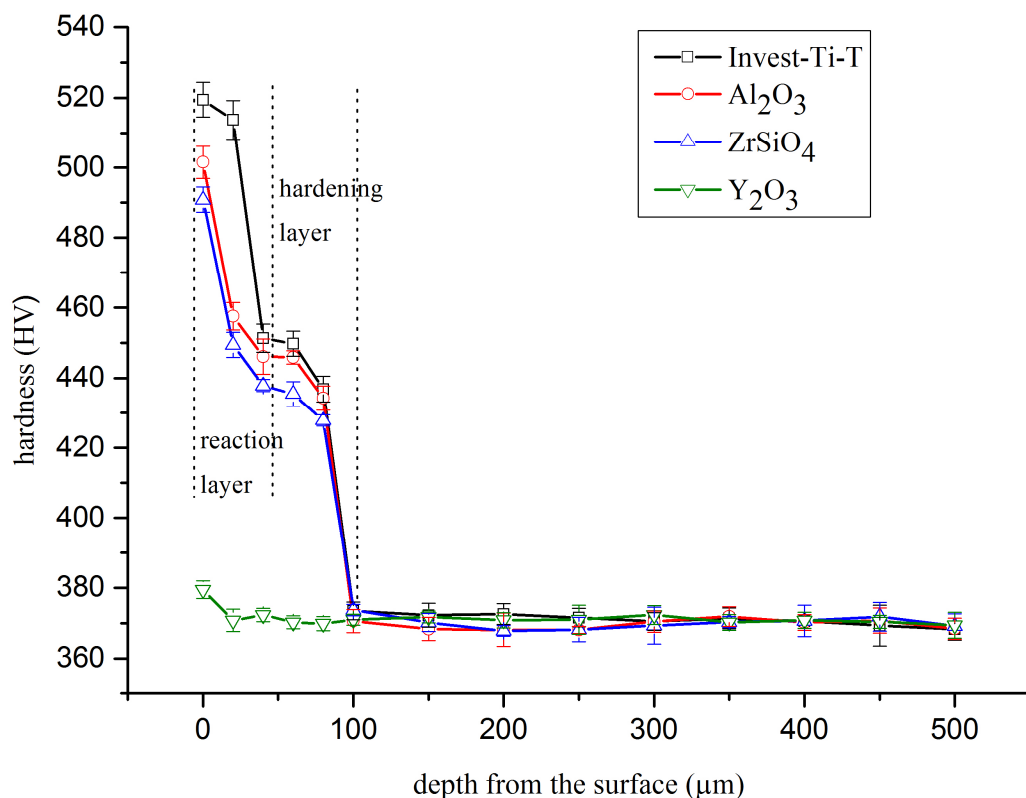


**Figure 51.** Microhardness profiles of four samples cast with different investments.

Obviously, the phase composition of the reaction layer has an influence on the surface microhardness of Ti67 castings. The elemental composition measurement of  $\alpha$  case layer, EDS elemental mapping analysis and EBSD investigation [184] demonstrated that the oxide layer does not only consist of pure oxides, but also of an oxide and titanium mixture. Particles are wetted by titanium that penetrates the surface of the mould. Such a composite of oxide and titanium has been termed technically cermet [70, 74]. In this study, it includes  $\text{TiO}_2$ ,  $\text{ZrO}_2$  and  $\text{Al}_2\text{O}_3$ . The hardness profile of the oxide layer on titanium castings behaves as follows: The hardness of this layer increases direct proportional compared to the increase of the ceramic content in the composite.

For all samples, except for them cast with  $\text{Y}_2\text{O}_3$ -investment, the depths of areas with the higher hardness are deeper than those of the reaction layers and two different regions can be separated in the microhardness profile. Thus, there is another layer between the surface reaction layer and Ti67. According to the EDS element mapping results, it was found out that this layer does not include investment material. The formation of this layer does not result from the reaction between Ti67 and investment material, but possibly rather from cooling molten Ti67 rapidly.

#### 4.2 Influence of the $\alpha$ Case Layer on the Mechanical Properties

The microstructures of the interfacial reaction region between Ti67 and the different investment materials are shown in Figure 39, Figure 42, Figure 45, and Figure 48, respectively. The specimens can be gathered into three groups, one without an  $\alpha$  case layer, one with  $\alpha$  case layer smaller than  $15\ \mu\text{m}$  and one with  $\alpha$  case layer thicker than  $15\ \mu\text{m}$ .

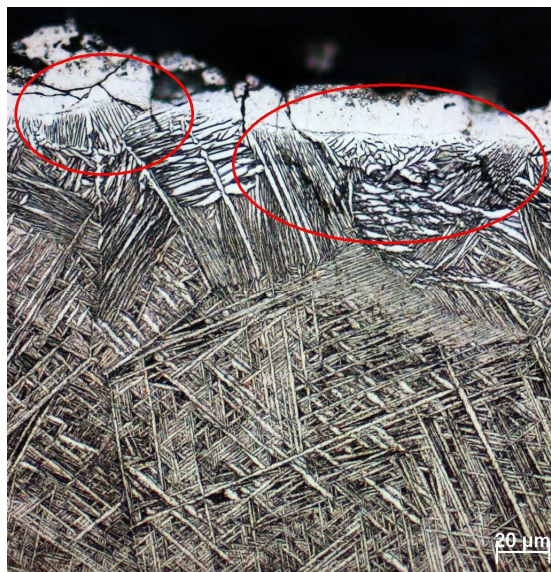


**Figure 52.** Micro-cracks in the  $\alpha$  case of a Ti67 casting specimen after fracture.

Figure 52 shows a micrograph of micro-cracks, which nucleated in the  $\alpha$  case on the sample surface perpendicular to the tensile loading axis of a Ti67 monotonic three-point bending sample after fracture. For thick  $\alpha$  case specimens, the average crack depth was 23  $\mu\text{m}$  with a standard deviation of  $\pm 5$   $\mu\text{m}$ , while the mean crack depth was 11  $\mu\text{m}$  with a standard deviation of  $\pm 3$   $\mu\text{m}$  for thin  $\alpha$  case specimens.

In Figure 53 the oxygen concentration and the microhardness profile across the surface layer of Ti67 castings are compared as a function of the depth from the outermost surface to the interior of the cast samples. The hardness profiles of the samples are in good agreement with the occurrence of the  $\alpha$  phase as illustrated in Figure 39, 42, and 45.

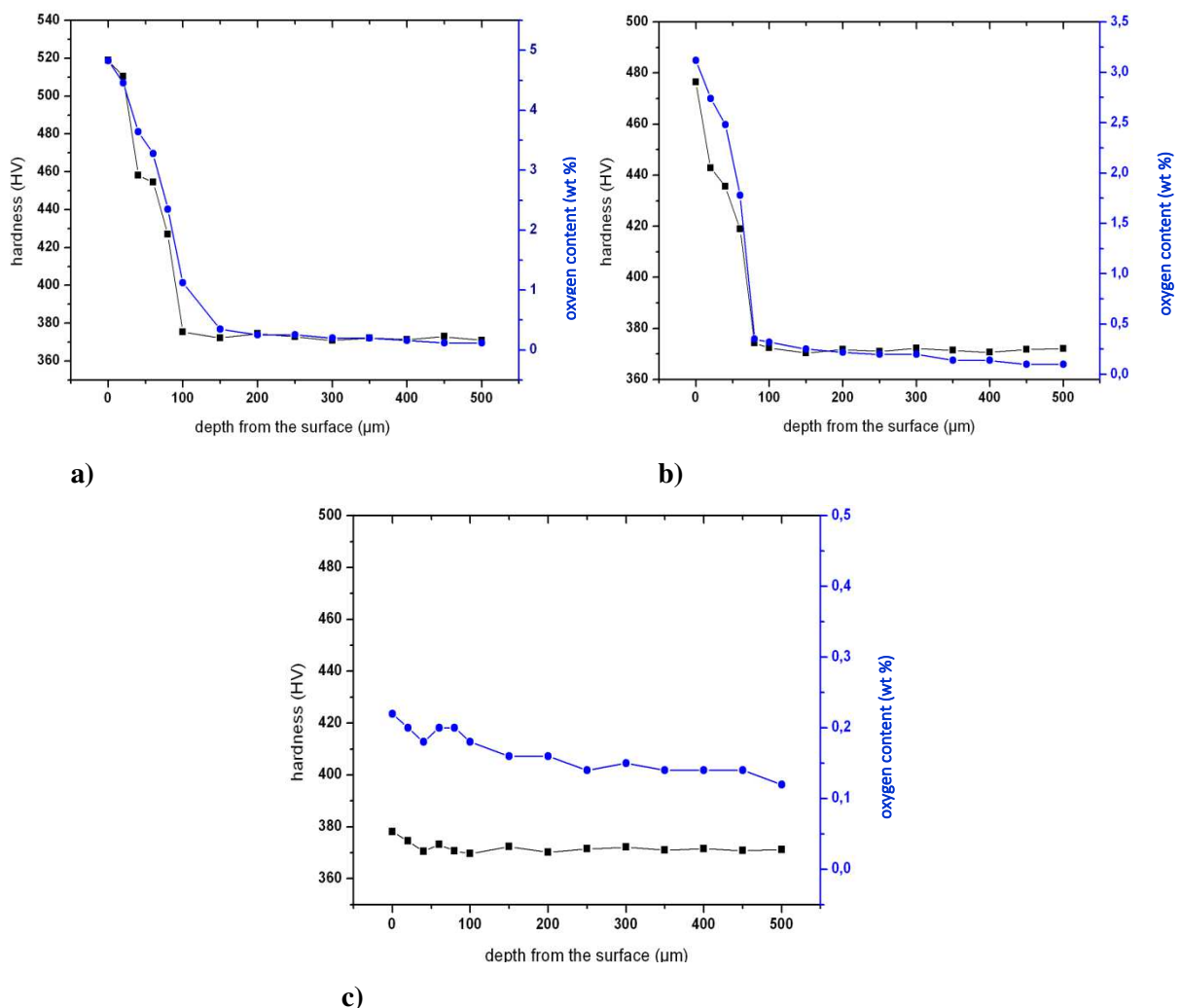


**Figure 53.** Oxygen concentration and microhardness profile of specimens.  
 a) with  $>15$   $\mu\text{m}$   $\alpha$  case layer, b) with  $<15$   $\mu\text{m}$  c) without  $\alpha$  case layer.

The surface microhardness of sections of Ti67 castings with thick  $\alpha$  case layer was the highest (518 HV) and decreases rapidly from the surface to approximately a depth of 30  $\mu\text{m}$  (458 HV), and then reduces slowly to a depth of 100  $\mu\text{m}$  (375 HV). At a depth of 120  $\mu\text{m}$ , the

## 4 Results

microhardness profile reaches a constant value. The surface microhardness of titanium castings with a thin  $\alpha$  case is 477 HV. The hardness of these samples decreases rapidly from the surface to a depth of 15  $\mu\text{m}$ , and then decreases slowly to a depth of 80  $\mu\text{m}$ . The non  $\alpha$  case sample showed no increase in surface hardness and its microhardness profile shows a smooth distribution with values in the range of 370 HV throughout the cross-section. It can be seen that the microhardness and the oxygen concentration profiles are quite similar.

The oxygen concentration was measured throughout the  $\alpha$  case region in a Ti67 (wt %) by EDS line scan analysis. The measured interface oxygen concentration ranges from  $1.5 \pm 0.3$  to  $4.9 \pm 0.7$  wt %. The concentration of oxygen at the limit of the  $\alpha$  case is indistinguishable from the concentration of the bulk alloy. The highest oxygen concentration measured has a value of  $4.9 \pm 0.7$  wt % on the thick  $\alpha$  case layer and  $3.3 \pm 0.4$  wt % for the thin  $\alpha$  case layer samples. On the other hand, the oxygen content was found to be no more than 0.12 wt % above the level of oxygen in the bulk alloy on the surface of the non  $\alpha$  case samples.

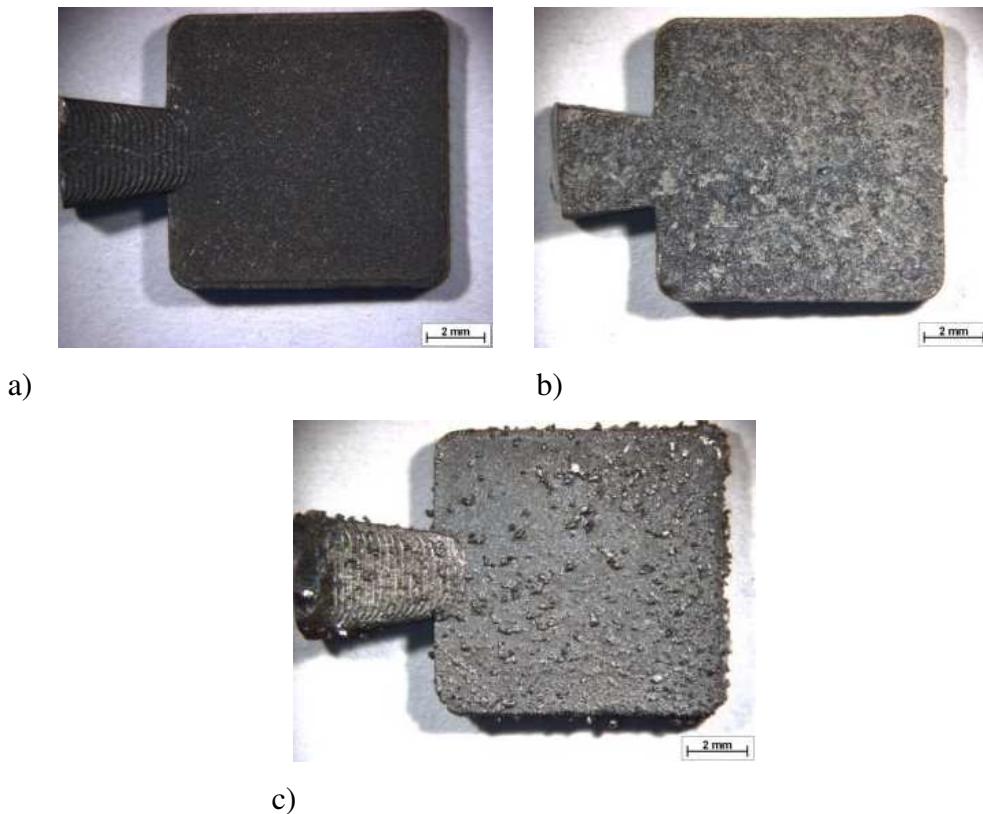


**Figure 54.** Surface images of cast Ti67 specimens **a)** without  $\alpha$  case layer, **b)** with  $<15 \mu\text{m}$  **c)** with  $>15 \mu\text{m}$   $\alpha$  case layer.

Figure 54 illustrates the surface morphology of cast Ti67 samples without  $\alpha$  case layer, with  $<15 \mu\text{m}$  and with  $>15 \mu\text{m}$   $\alpha$  case layer. The surface differences can be seen clearly.

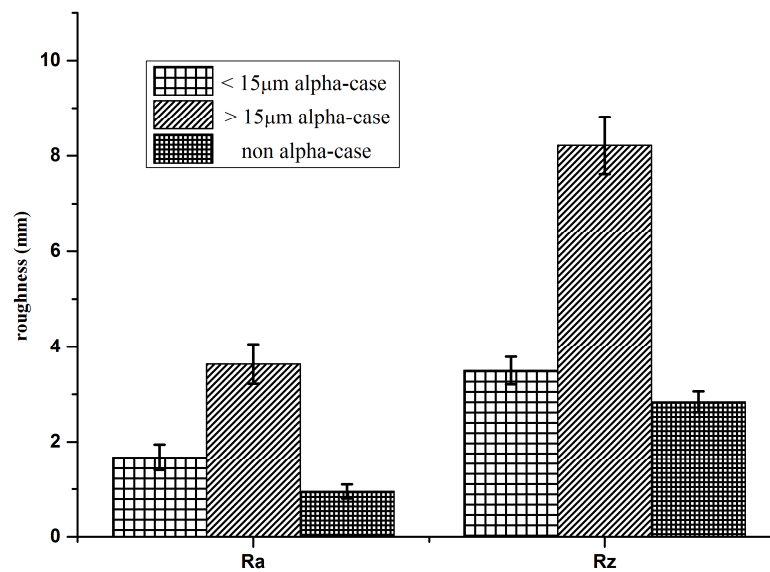


**Figure 55.** Surface roughness of Ti67 casting samples.

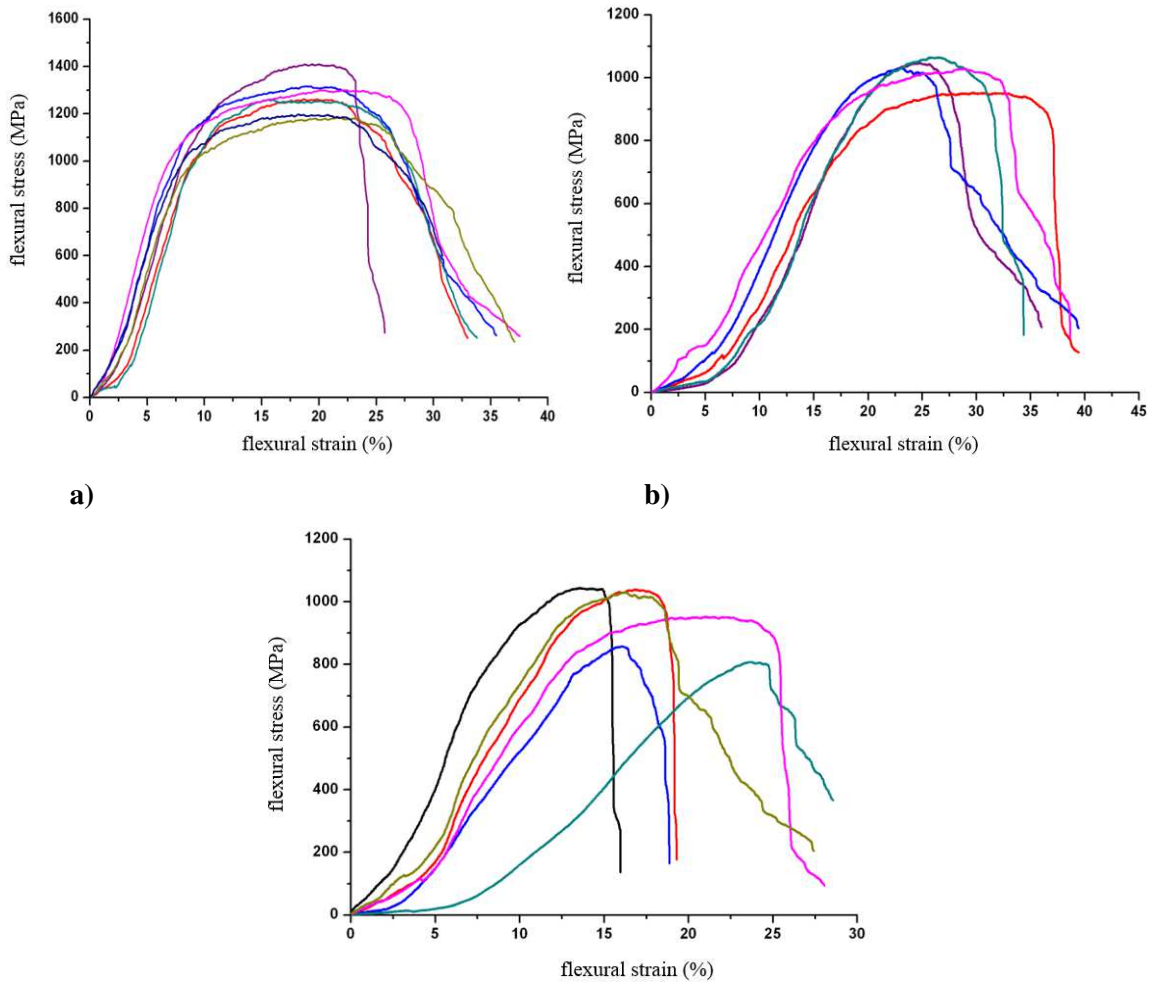
The average surface roughness ( $R_a$ ) and the average maximum height of the profile ( $R_z$ ) were determined from the surface profile.  $R_a$  and  $R_z$  values are plotted in Figure 55. The specimen with a thick  $\alpha$  case layer showed the highest roughness values for  $R_a$  (~4.21  $\mu\text{m}$ ) and  $R_z$  (~8.49  $\mu\text{m}$ ), while the samples without  $\alpha$  case showed the lowest  $R_a$  (~2.04  $\mu\text{m}$ ) and  $R_z$  (~3.74  $\mu\text{m}$ ) values. Between the specimens with a thin  $\alpha$  case layer and those without  $\alpha$  case, there were no significant differences in surface roughness. For the specimens with a thin  $\alpha$  case layer,  $R_a$  and  $R_z$  values were measured to be approximately 2.18  $\mu\text{m}$  and 3.87  $\mu\text{m}$ , respectively.

Monotonic three-point bending test results in the term of stress-strain curves are shown in Figure 56. Elastic modulus, flexural stress and elongation (in %) values were calculated according to ISO 178 Standard [187] which was given in detail in the materials and testing methods section of this thesis. Monotonic three-point bending tests showed that increasing the thickness of the  $\alpha$  case layer (> 15  $\mu\text{m}$ ) decreased the elastic modulus, flexural stress and elongation of Ti67 castings.

The reduction in elongation could be explained by the increased hardness of the casting surface resulting from metal-mould reactions. In addition, it is possible that an increased roughness contributes to this reduction. However, the specimens with a thin  $\alpha$  case layer (< 15  $\mu\text{m}$ ) showed improved mechanical properties as compared with non-  $\alpha$  case Ti67 castings. Although the flexural stress increased by 25% for specimens with a thin  $\alpha$  case (Figure 56 a), this value decreased by 15% for specimens with > 15  $\mu\text{m}$   $\alpha$  case (Figure 56 c). Furthermore, flexural strain decreased down to 20%, when the thickness of  $\alpha$  case layer increased. There were no substantial differences in elongation between non-  $\alpha$  case specimens (Figure 56 b) and

#### 4 Results

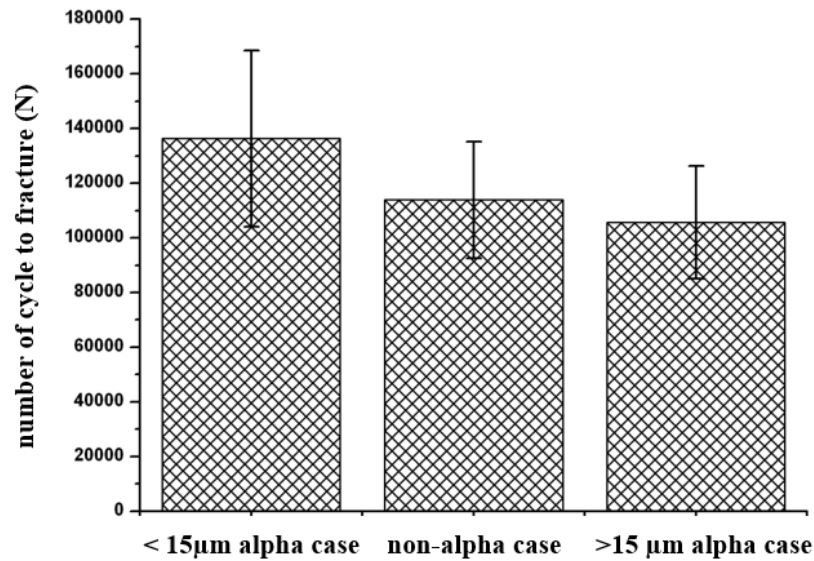
those with thin  $\alpha$  case specimens (Figure 56 a). However, it was determined that the elongation reduced rapidly (25%) when the flexural strength reaches 1400 MPa. The elastic modulus was calculated 117 GPa, 108 GPa and 97 GPa for the specimens with  $<15 \mu\text{m}$   $\alpha$  case , non-  $\alpha$  case and with  $>15 \mu\text{m}$   $\alpha$  case respectively.



**Figure 56.** Monotonic three-point bending test results as stress-strain curves.  
a) with  $<15 \mu\text{m}$  b) without  $\alpha$  case layer c) with  $>15 \mu\text{m}$   $\alpha$  case layer.

Figure 57. shows the cyclic three-point bending test results of cast specimens prepared through using different mould materials specialized for titanium casting. 'N' represents the number of cycles to failure. The lowest durability was observed for specimens with a thick  $\alpha$  case layer.

In this study, no distinct decrease in fatigue life of the specimens with an  $\alpha$  case thicker than  $15 \mu\text{m}$   $\alpha$  case layer was observed. However, specimens with an  $\alpha$  case layer thickness  $< 15 \mu\text{m}$  exhibited better durability when compared with non-  $\alpha$  case specimens. The thin  $\alpha$  case layer, thus, enhanced fatigue life by nearly 20%.



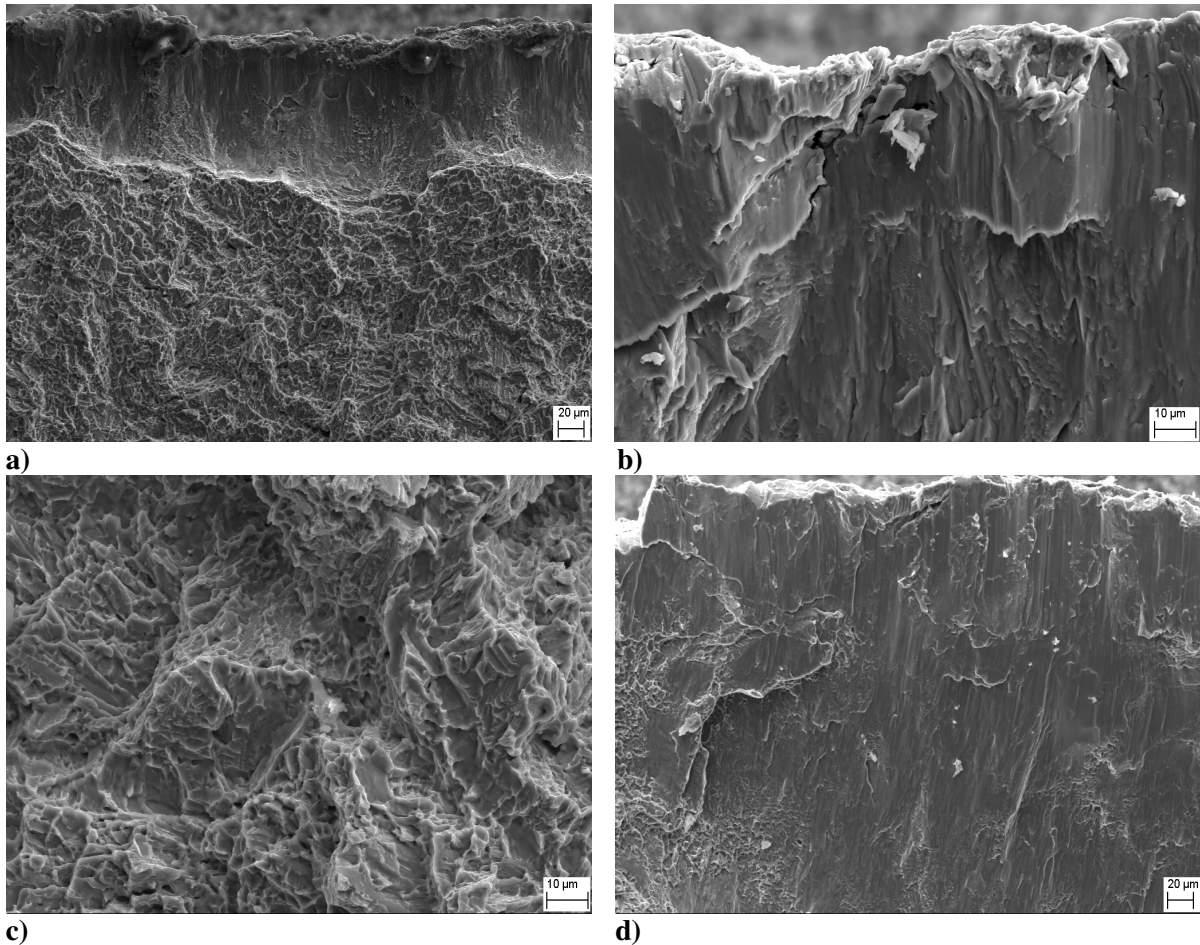
**Figure 57.** Effect of alpha case layer on fatigue life.

Figure 58 a)-c) shows SEM photographs of the fracture surfaces after monotonic three-point bending tests. Near the cast surfaces of all specimens with  $\alpha$  case layer, the typical fracture mode was observed as to be brittle fracture of titanium. The  $\alpha$  case layer region shows smoother fracture with cleavage facets (Figure 58 c).

The  $\alpha$  case layer and the second layer with coarse acicular Widmanstätten microstructure can be seen clearly in Figure 58 a). The interior region of fracture surfaces consist of dimples (Figure 58 c) which indicated ductile rupture. The observed fracture modes are in good agreement with the shape of the microhardness profiles in Figure 53 b)-c): harder surface regions brittle fracture and softer interior regions ductile fracture. Whilst at the outer layer oxygen concentration is in the range of 2.5 to 5 wt %, it was reduced to 1.5 wt % at the second layer. These results overlapped with the oxygen concentration profile as depicted in Figure 53.

Topographically, the fracture mode was brittle on the  $\alpha$  case layer and ductile in the bulk of the material. For thick  $\alpha$  case samples, brittle fracture was detected in greater depths than in thin  $\alpha$  case samples.

Figure 58 d) shows a SEM photograph of the fracture surfaces after cyclic three-point bending tests. Albeit, fatigue fractures have similar structures with monotonic test samples near the casting surfaces, the interior region showed no ductile fracture properties. The fracture surfaces after cyclic three-point bending tests can be characterized flat fracture propagation with some fatigue striations.



**Figure 58.** SEM photographs of the fracture surfaces after monotonic three-point bending tests (a-c) and after cyclic three-point bending tests (d).

### 4.3 $\beta$ - Transus Temperature

Thermal expansion vs. temperature curves for Ti67 are illustrated in Figure 59. The transformation from the  $\alpha+\beta$  to the  $\beta$  phase resulted in a volume contraction change in the slope of the thermal expansion vs. temperature curve.

The as-received Ti67 specimens experienced a contraction at  $\sim 900^\circ\text{C}$ , where the  $\alpha+\beta$  to the  $\beta$  phase transformation starts. The specimen then expands from  $990^\circ\text{C}$  and was described as the end of the  $\alpha+\beta$  to the  $\beta$  phase transformation and expands up to  $1050^\circ\text{C}$ . In the Ti67, the coefficients of thermal expansion (CTE) values increased up to approximately  $880^\circ\text{C}$  and exhibited a minimum near  $990^\circ\text{C}$ , at which a balance between thermal expansion and contraction appears. Above  $900^\circ\text{C}$ , the CTE increased with an increase in temperature.

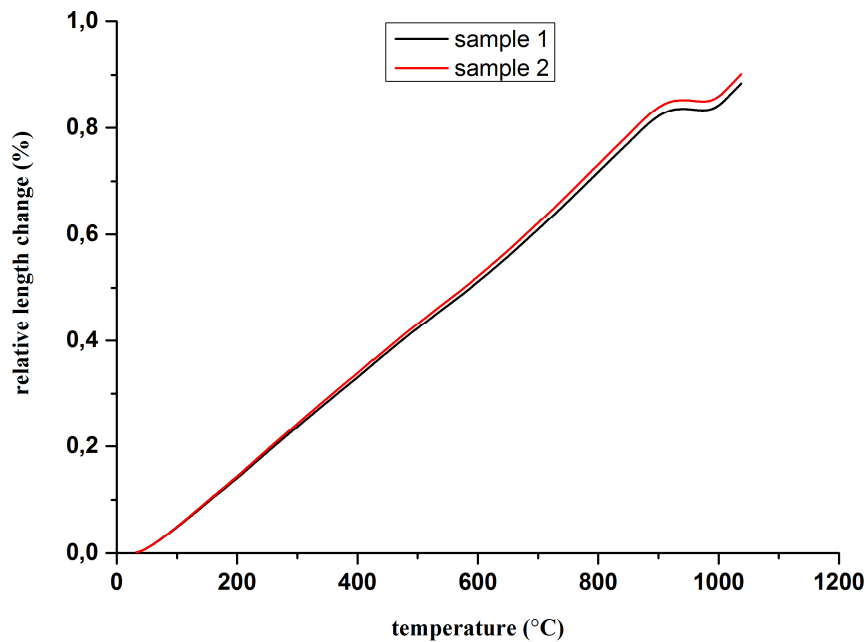


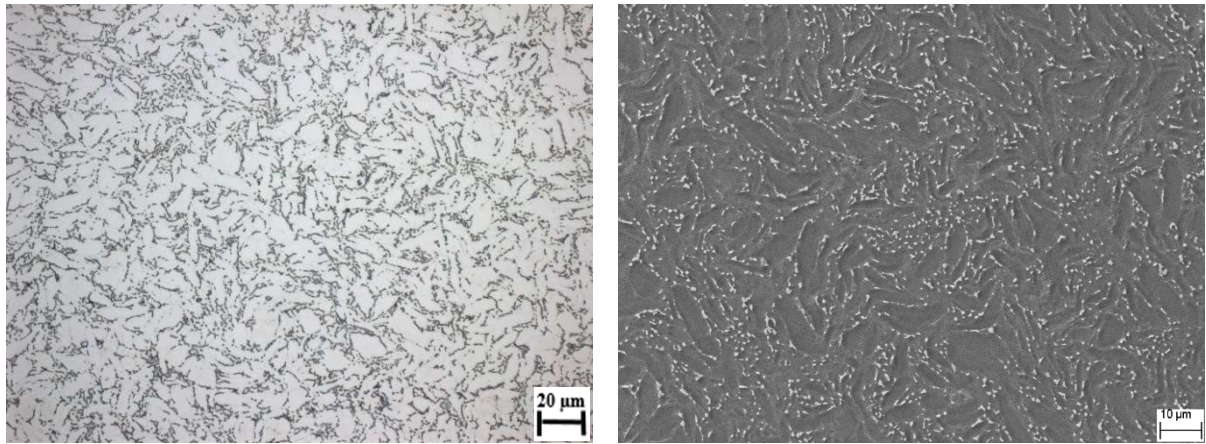
**Figure 59.** A thermal expansion vs. temperature curves for Ti67.

The start of the transformation was observed between 880-905 °C, while the volume decreased in this temperature range. As another crucial parameter, differential thermal expansion was also observed. Up to 880 °C, differential thermal expansion was approximately 1.5  $\mu\text{m}/\text{min}$ . After that, this value started to decrease sharply and was recorded at -0.6  $\mu\text{m}/\text{min}$  at ~990 °C. Finally, at 1050 °C, the value reached 1.5  $\mu\text{m}/\text{min}$ , just like at the beginning. As a result, the  $\beta$  transformation temperature was obtained between 980°C to 990 °C.

#### 4.4 Heat Treatment

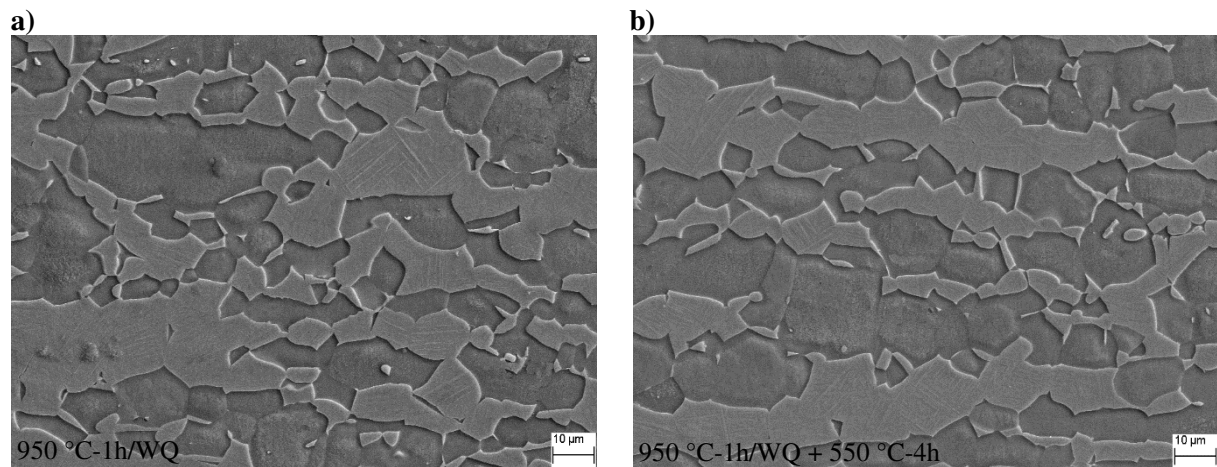
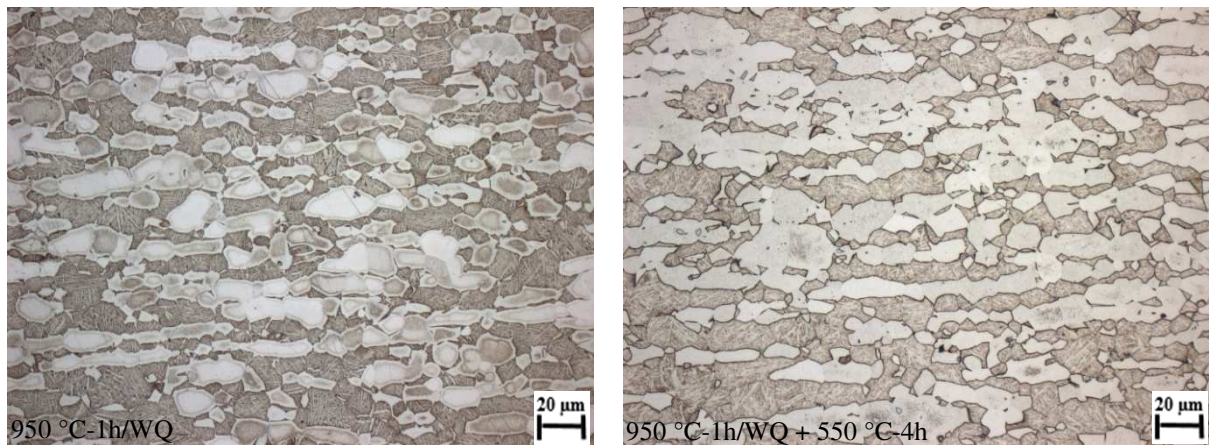
The microstructures of the samples were examined after a solution treatment below and above the  $\beta$ -transus temperatures, followed by various cooling processes: air cooling (AC), water quenching (WQ) and furnace cooling (FC) (5 °C/min). Some samples were subjected to an aging process at 550 °C for 4 hours to investigate its influence on the microstructure. After these heat treatments, the Ti67 samples exhibited different microstructures.

The initial microstructure and SEM micrograph of a Ti67 sample is shown in Figure 60. Ti67 samples were cut from Ti67 ingot which was hot rolled, annealed at 700 °C for 1hr and cooled in air. Fine coarse globular forming by equiaxed  $\alpha$  grains appeared with an average size of about 7.8  $\mu\text{m}$  (dark areas in Figure 60 b). The  $\beta$  phase is present in the  $\alpha$  grain boundaries (bright spots in Figure 60 b). The microstructure of samples after heat treatments below the  $\beta$ -transus temperature with various cooling processes: AC, WQ, and FC are shown in Figures 61-63.



a) b)  
**Figure 60.** a) The initial microstructure and b) SEM micrograph of a Ti67 sample.

When the Ti67 sample underwent heat treatment processing at temperatures below the  $\beta$ -transus and water quenching (see Figure 61), it showed a bi-modal microstructure, which consisted of interconnected equiaxed primary  $\alpha$  grains dispersed within lamellar  $\alpha+\beta$  colonies. The fine  $\alpha$  laths are separated by  $\beta$ . The average grain size was found to be  $\sim 20 \mu\text{m}$ .



a) b)  
c) d)  
**Figure 61.** Microstructure a) 950 °C-1h/WQ b) 950 °C-1h/WQ + 550 °C-4h.  
SEM micrograph c) 950 °C-1h/WQ d) 950 °C-1h/WQ + 550 °C-4h.

Optical micrograph of the Ti67 sample heat-treated at 950 °C for one hour and then slowly cooled down in air (see Figure 62) shows an equiaxed  $\alpha$  and a transformed  $\beta$  microstructure.

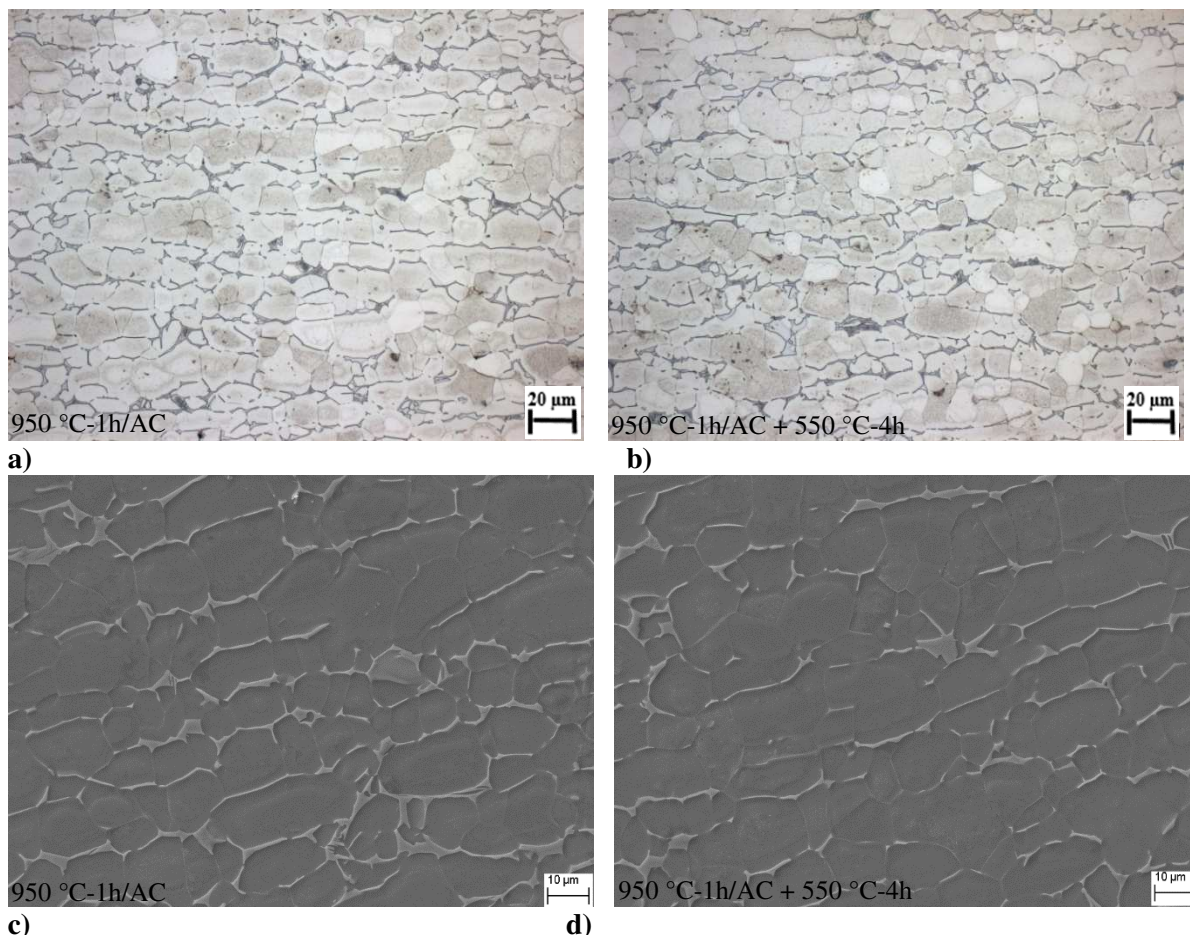


**Figure 62.** Microstructure **a)** 950 °C-1h/AC **b)** 950 °C-1h/AC + 550 °C-4h.  
SEM micrograph **c)** 950 °C-1h/AC **d)** 950 °C-1h/AC + 550 °C-4h.

The volume fraction of  $\alpha$  increased with a decrease in cooling rate and the transformed  $\beta$  becomes coarser. The obtained microstructure can be described as grains consisting of pure  $\alpha$  phase surrounded by a mixture of  $\alpha$  and small amounts of  $\beta$ -phases.

During the furnace cooling process from 950 °C (see Figure 63), only the  $\alpha$  grains grow and no  $\alpha$  lamellae are formed within the  $\beta$  grains. The metallographic figures of slowly cooled specimens show  $\beta$  as a small seam around the coarse  $\alpha$  lamellae (dark areas in Figure 63 c and d). The equilibrium volume fraction of the  $\beta$  phase is located at the triple-junctions of the  $\alpha$  grains.

Not only for air cooled samples, but also for furnace cooled samples, there were no significant differences observed in the grain size after the aging process.

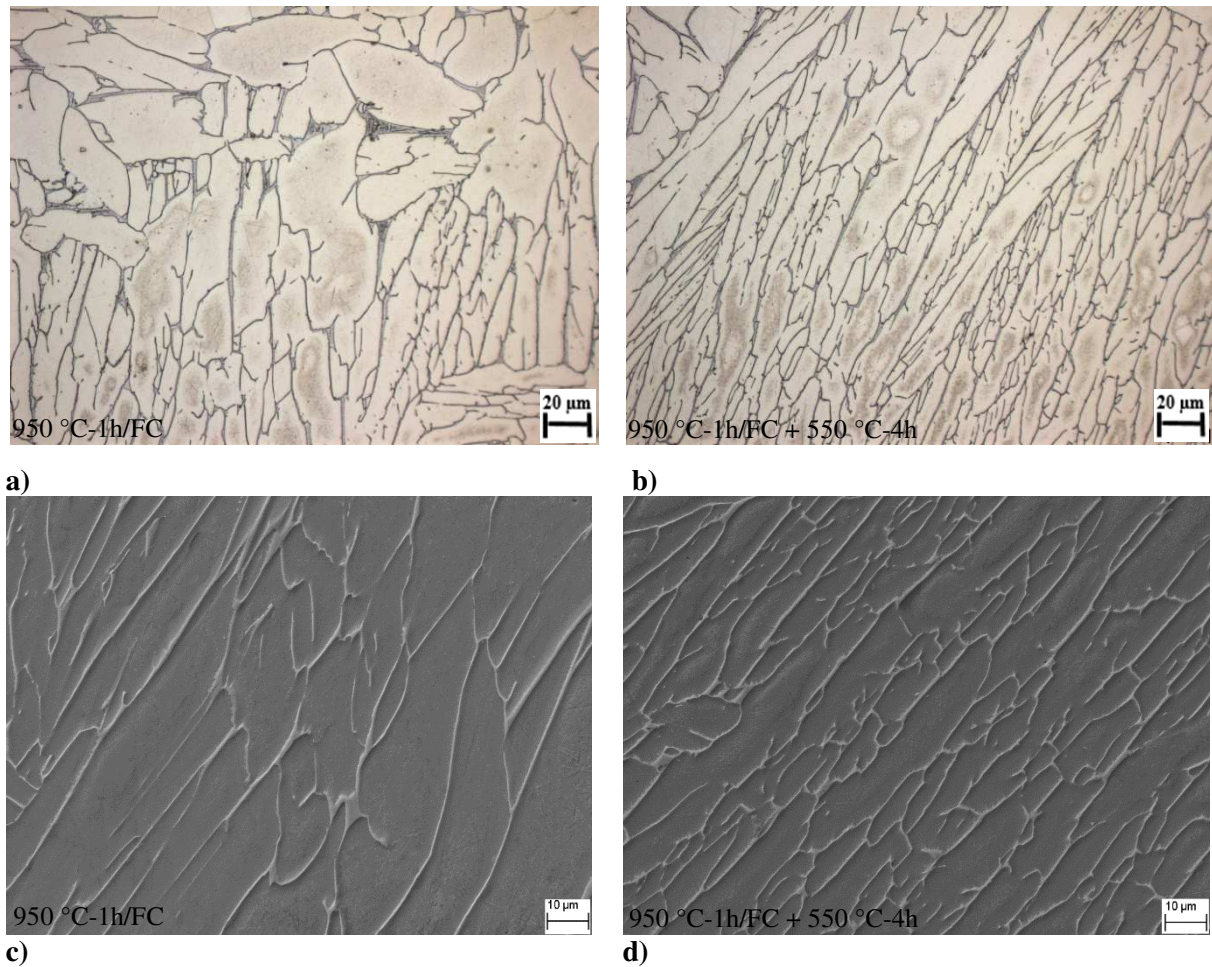


**Figure 63.** Microstructure **a)** 950 °C-1h/FC, **b)** 950 °C-1h/FC + 550 °C-4h.  
SEM micrograph **c)** 950 °C-1h/FC, **d)** 950 °C-1h/FC + 550 °C-4h.

Microstructures of Ti67 after heat treatments above the  $\beta$ -transus temperature with various cooling processes: AC, WQ, and FC are shown in Figure 64-66. The fastest cooling rate from  $\beta$ -transus temperature exhibited acicular-like martensitic transformation as seen in Figure 64 a). This microstructure is known as  $\alpha$  martensite structure. The remaining  $\beta$  phases can be seen between martensitic laths, no precipitation of grain boundary  $\alpha$  was recognized. During aging of the martensitic structure at 500 °C, a variation in the size of the martensite plates was observed (in Figure 64 b).

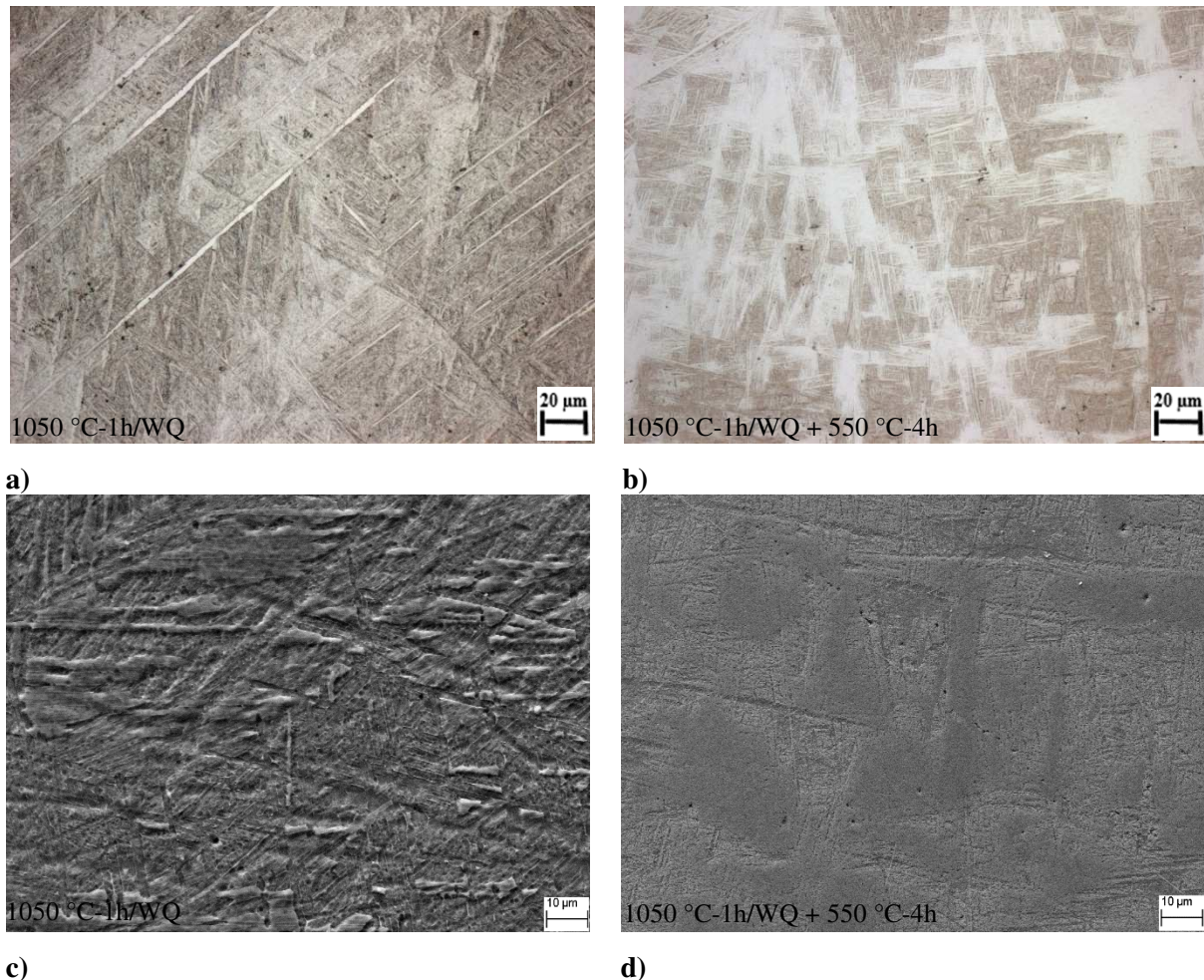


**Figure 64.** Microstructure **a)** 1050 °C-1h/WQ, **b)** 1050 °C-1h/WQ + 550 °C-4h.  
SEM micrograph **c)** 1050 °C-1h/WQ, **d)** 1050 °C-1h/WQ + 550 °C-4h.

Air cooling from  $\beta$ -transus temperature led to a refinement of the microstructure and both  $\alpha$  colony size and  $\alpha$  lamellae thickness were increased (see Figure 65). Additionally, new colonies tend to nucleate not only on  $\beta$  phase boundaries but also on boundaries of other colonies, growing perpendicularly to the existing lamellae. This caused the formation of a characteristic micro structure that is called "basket weave" or Widmanstätten microstructure.  $\beta$  can be transformed by nucleation and growth to Widmanstätten  $\alpha$  phase. In this heat treatment, during cooling from  $\beta$  solutionizing temperature nucleated inside the  $\beta$  grain. Moreover, the  $\beta$  phase is also continuously formed parallel to the  $\alpha$  phase. Given the low cooling rate, no  $\alpha'$  martensite was formed.

A fully lamellar microstructure was obtained by solution heat treatment at 1050 °C for 1 hour, followed by controlled cooling from the  $\beta$  single phase field to room temperature. A further decrease in the cooling rate induces a volumetric growth of the  $\alpha$  phase. Its morphology changed from needle-like to equiaxed (see Figure 66).

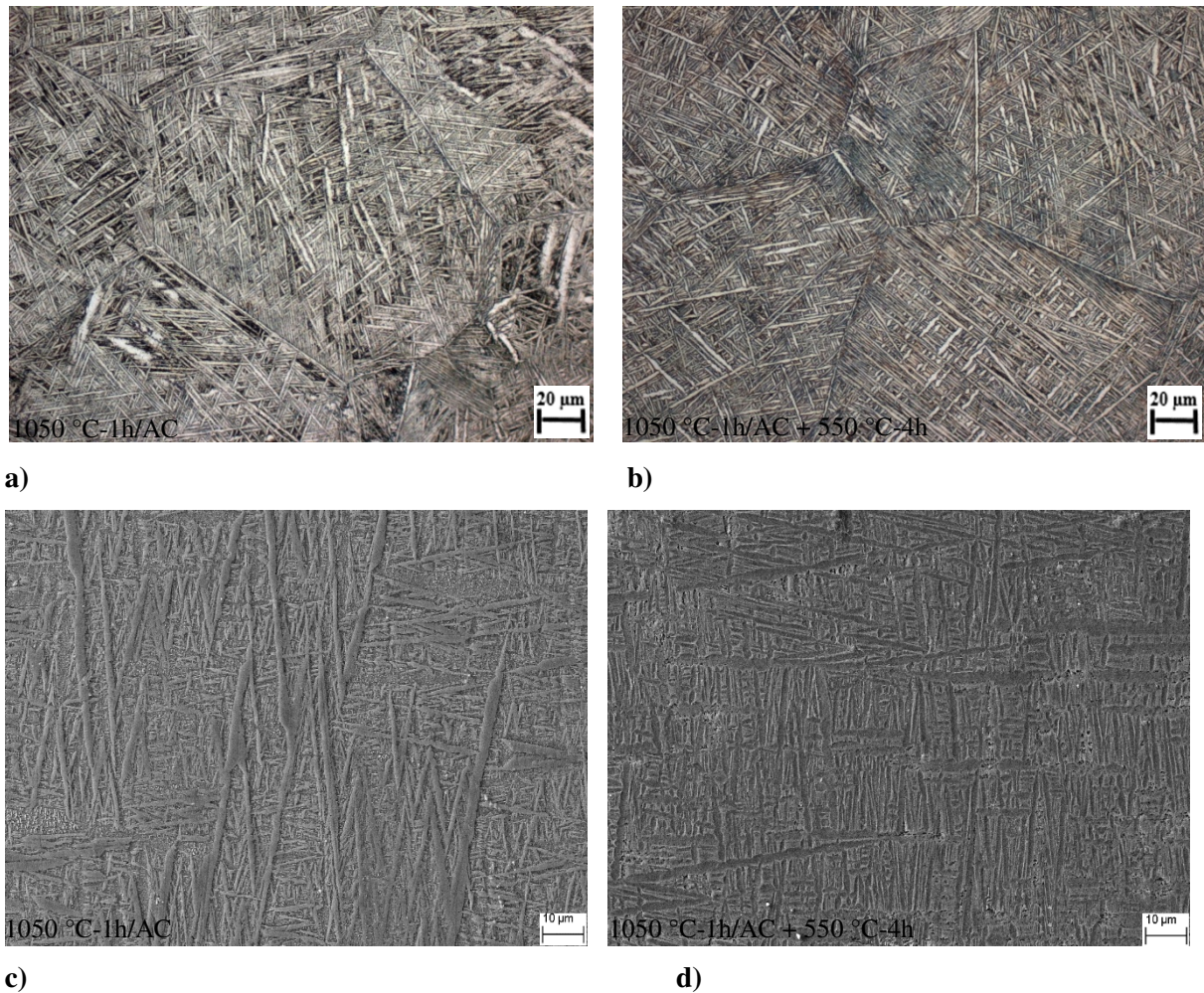


**Figure 65.** Microstructure **a)** 1050 °C-1h/AC, **b)** 1050 °C-1h/AC + 550 °C-4h.  
SEM micrograph **c)** 1050 °C-1h/AC, **d)** 1050 °C-1h/AC + 550 °C-4h.

On furnace cooling,  $\alpha$  phase was also presented on prior  $\beta$  grain boundaries. However, on slow cooling, the  $\alpha$  phase can precipitate out of the grain boundaries and within the grain.

The character of the formed microstructures has not basically changed after the aging treatment at 550 °C.

Heat treatment results were analyzed by means of microhardness testing. The results of the hardness tests after different heat treatments are shown in Figure 67.

These results were compared with the hardness of the samples without heat treatment. The initial hardness of the commercial Ti67 was 327 HV. After every complete heat treatment process (solution and aging treatment), an increase in hardness was observed in comparison with the initial cast state. Furnace cooling did not have any crucial influence on the initial hardness of the alloy.

Volume fraction of  $\alpha$  and  $\beta$  phase can be predicted by the hardness values presented in Figure 67. It was reported that  $\beta$  possesses a higher hardness than the  $\alpha$  phase [200, 201].

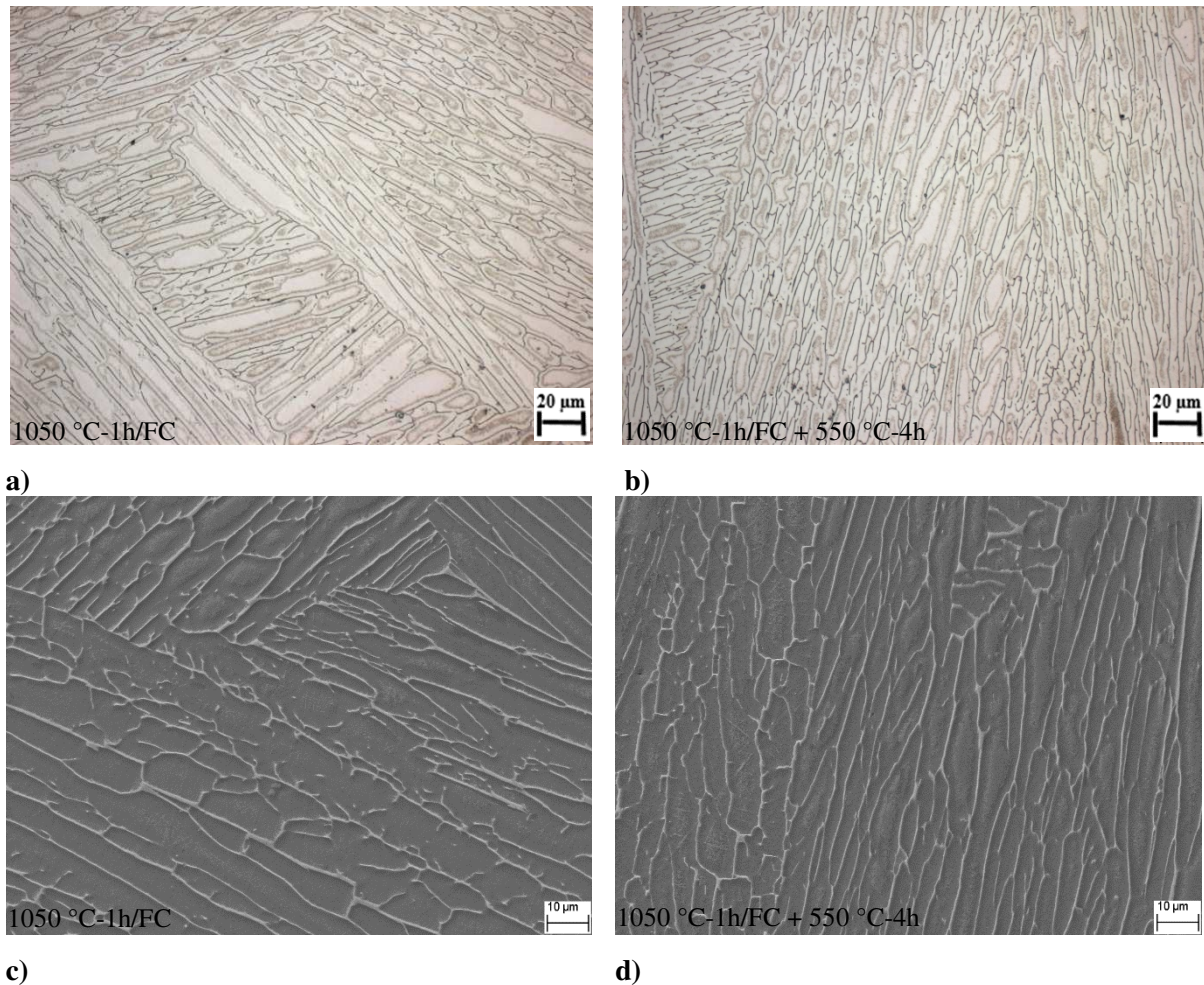


**Figure 66.** Microstructure **a)** 1050 °C-1h/FC, **b)** 1050 °C-1h/FC + 550 °C-4h.  
SEM micrograph **c)** 1050 °C-1h/FC, **d)** 1050 °C-1h/FC + 550 °C-4h.

The highest hardness was obtained by water quenching which suggests that the hardness increases with higher  $\beta$ -martensite phase in the alloy. Quenching from 950 °C and 1050 °C resulted in harder samples with 397 HV and 416 HV hardness, respectively. The amount of  $\beta$  phase trapped during quenching increases the hardness.

Slow cooling of Ti67 samples from 950 °C and 1050 °C resulted in more  $\alpha$  than  $\beta$  phases of lower hardness than water quenched samples. The minimum hardness values were measured for furnace cooled specimen that consists of  $\alpha$  and  $\beta$  phase in equilibrium. After furnace cooling, hardness values were measured to have a value of 340 HV and 355 HV for below and above the  $\beta$ -transus temperature samples, respectively. Hardness of water cooled specimens increased by nearly 7%.

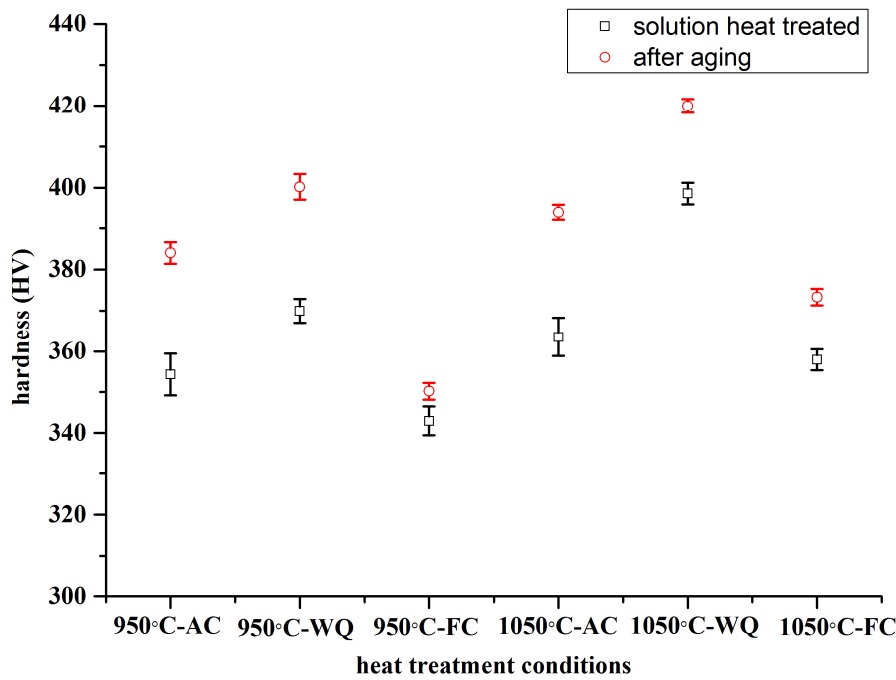


**Figure 67.** Hardness values of heat treated specimens.

In the case of cooling in air above the solution temperature and in the case of cooling into water below the solution temperature, the increasing of hardness value was more significant (approximately 10%) than within the other heat treatment conditions. After the subsequent ageing treatment, an increase of hardness was registered at 550 °C in comparison with the solution treated state. It is obvious that aging of martensite results in higher hardness values than ageing quenched specimens. The highest hardness was detected after the treatment at 1050 °C/WQ+550 °C-4h. The increase in hardness was measured to be 90 HV as compared to the original hardness value of the Ti67 sample.

#### 4.5 Mechanical Behavior of Ti67 Sponge

Compression tests were performed on Ti67 sponges by the project partner Siegen University [184]. It was reported that the structure behaved quite brittle with a steep load drop after reaching the upper compressive yield strength of about 8.3 MPa. Moreover, the clear stress-plateau regime was not observed in the stress-compression curve which was different from the general compression behavior of open cell foam structures. Figure 68 shows the compression behavior of a cast Ti67 sponge.

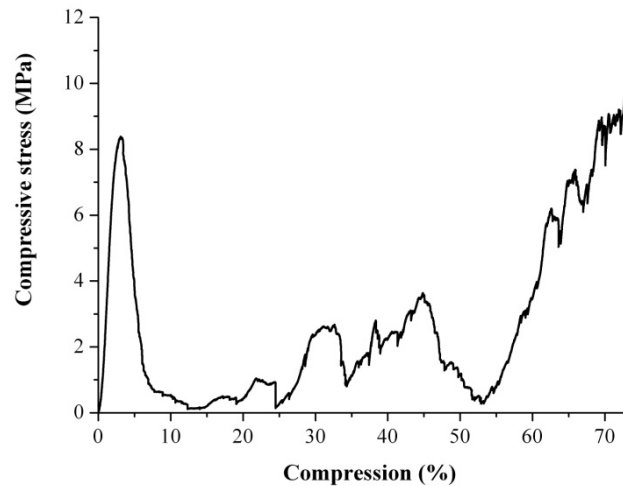


**Figure 68.** Stress vs. compression curve of Ti67 sponge [184].

However, the results of such tests are an important source of information that are helpful in the attempt to improve strength and ductility of the cell struts. The influence of the heat treatment on the mechanical behavior was also investigated. A commercial Ti67 sample with solution treatment above the  $\beta$ -transus (1050 °C) for 1 hour supplemented by water cooling and aging at 550 °C for 4 hours showed the highest hardness result. For this reason, this heat treatment process was applied to the Ti67 sponge. After the heat treatment process, the hardness value of the Ti67 sponge increased from 383 HV to 432 HV.

To examine the cell strut behavior, monotonic three-point bending tests, described in Chapter 3.7, were carried out and the compression bending behavior of cell struts with and without any heat treatment was examined. Cell strut examinations presented a maximum compression force of approx. 4.3 N for received Ti67 sponge. Cell strut compression behavior showed after a compression of approximately 0.3 mm a plastic deformation-like behavior.

Whilst the heat treatment process had a positive influence on the maximum compression force and reached 5.6 N, heat treated cell struts did not show pronounced plastic deformation. The compression behavior of both material variants of the cell struts was associated with a brittle behavior of the Ti67 sponges. The maximum bending stress,  $\sigma_{max}$ , was determined for both Ti67 sponges by using Equation (20). For the sample without treatment, the maximum bending stress was measured to be 0.46 MPa, whereas the value reached 0.54 MPa for the heat treated sample. The stress-strain relationship turned out to be nearly linear in both cases as shown in Figure 69 a) and b). Thus, solution heat treatment increased elongation values by a factor of two.

## 4 Results

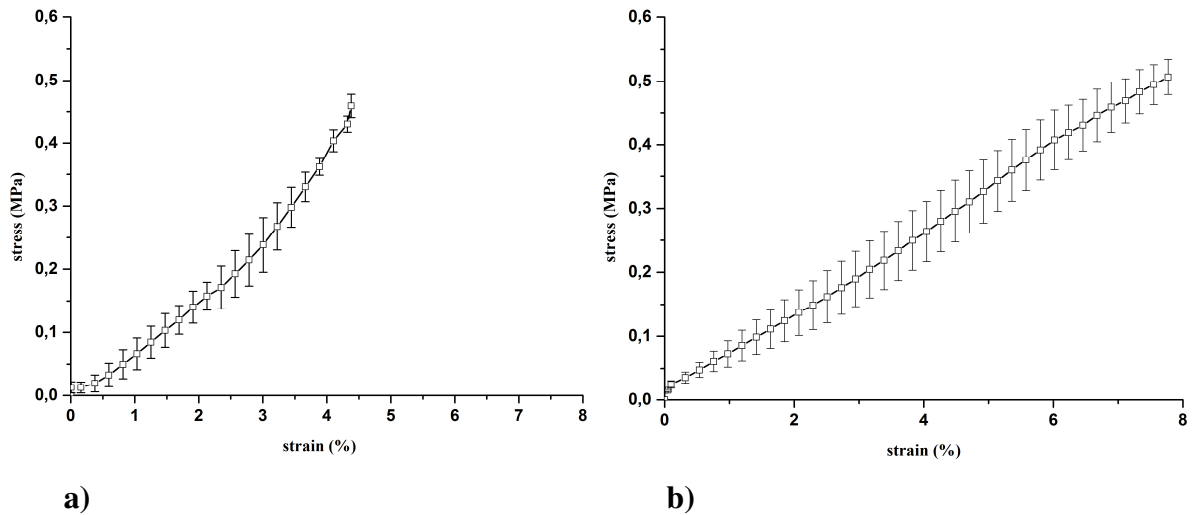


**Figure 69.** Bending behavior of cell struts **a)** as received **b)** heat treated.

The Ti67 sponge reveals a characteristic basket weave microstructure, which can be seen in Figure 70 a). The grain boundaries in the microstructure are clearly visible and the grain size was determined by line intercept method. The specimens exhibit a grain size of  $157 \pm 18 \mu\text{m}$ .  $\alpha/\beta$  phase distribution was measured to be 52/48 (in %). WQ from  $\beta$ -transus temperature  $1050^\circ\text{C}$  and aging at  $550^\circ\text{C}$  leads to an acicular  $\alpha$  martensite structure in which the  $\beta$  phase can transform to martensite and no  $\alpha$  precipitation was observed on the grain boundaries.

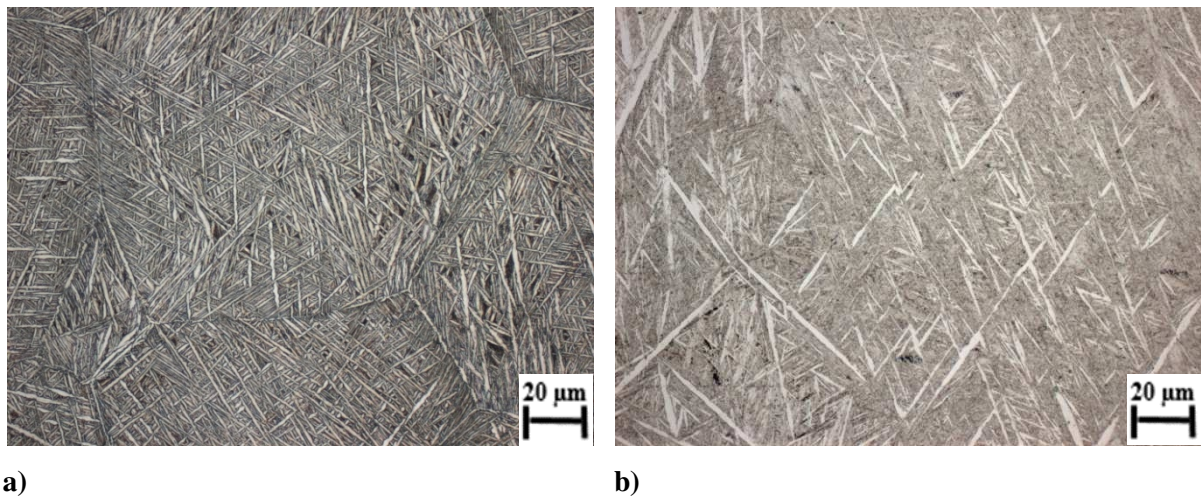


**Figure 70.** Microstructure of cell struts **a)** as received **b)** after heat treatment.

The resulting microstructure is shown in Figure 70 b). The  $\beta$  phase content and the grain size decreased by 44% and  $118 \pm 22 \mu\text{m}$ , respectively.

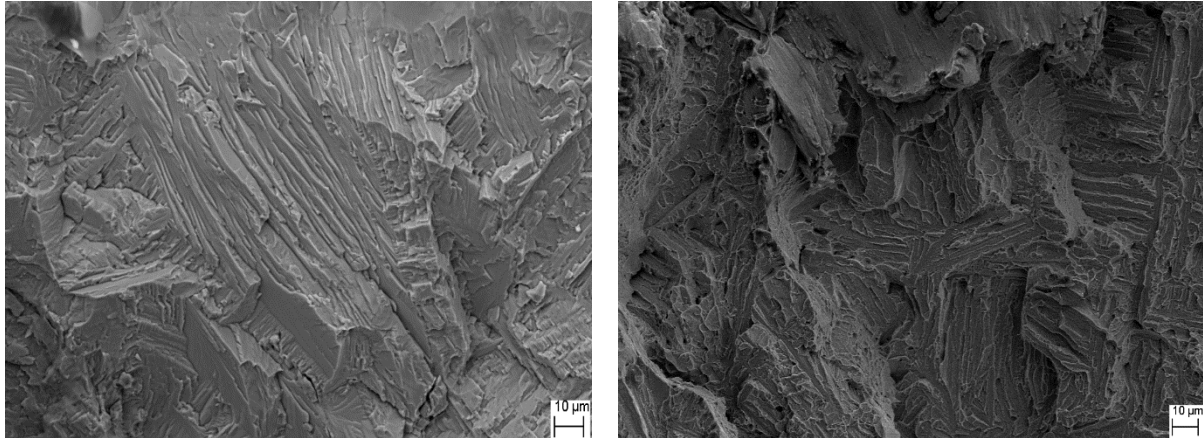


**Figure 71.** SEM fracture micrograph of Ti67 sponge after compression test.

Typical SEM photographs of the fracture surfaces of the broken cell struts after compression bending are shown in Figure 71 for as-received (Figure 71 a) and heat-treated (Figure 71 b) conditions. Brittle fracture was observed on both fracture surfaces, yet fracture surface of heat treated sample appears flatter. The water-quenched and aged strut (Figure 71 b) exhibited a lower fracture surface roughness compared to non-quenched case, due to more cleavage cracking in conjunction with some dimple. This is attributed to the presence of martensite arising with the WQ.

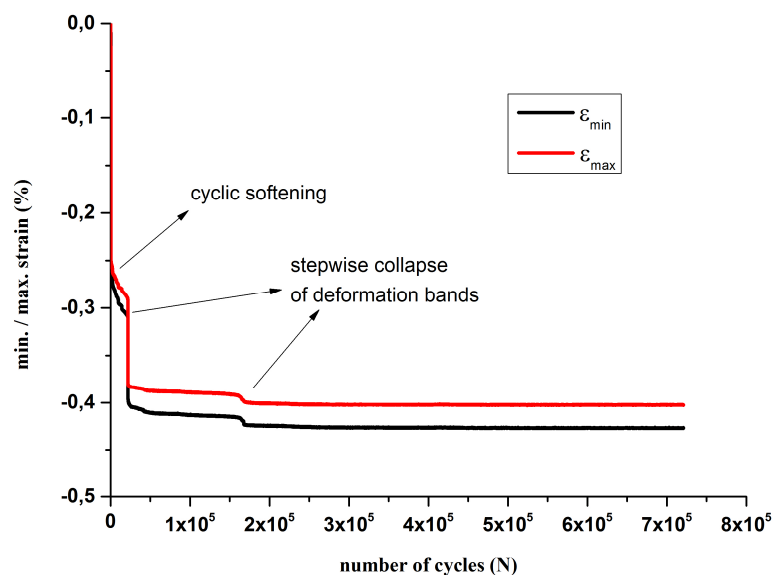


**Figure 72.** Cyclic deformation curve in compression-compression fatigue of an open cell Ti67 structure.

Figure 72 shows a cyclic deformation curve (min. and max. strain values) for stress-controlled fatigue ( $\sigma/2 = 1.1$  MPa). The main feature of the compression fatigue behavior is a

strong cyclic softening during the initial 20000 cycles. This softening is followed by a stepwise collapse of the structure in a similar way as it was observed by Ohrndorf et al. [133].

#### 4.6 Experimental Push-Out Test

The experimental tests were successfully performed by Girón [184] at Siegen University and resulted in similar force-displacement curves consisting of three characteristic zones, which were explained in detail in Chapter 2. The failure load is visible in the force load graphs. In addition to the failure load, displacement up to the failure point and interface stiffness were calculated from the graphs. The total bone-implant contact area was determined prior to mechanical testing.

Two rats died immediately after implant-placement surgery. The initial implant stability of rat implant was measured by applying the push-out test on this sample. The ref.rat specimen shows a push-out force of  $F_{\max} = 57$  N and the absorbed energy of it was calculated to have a value of 28.3 mJ.

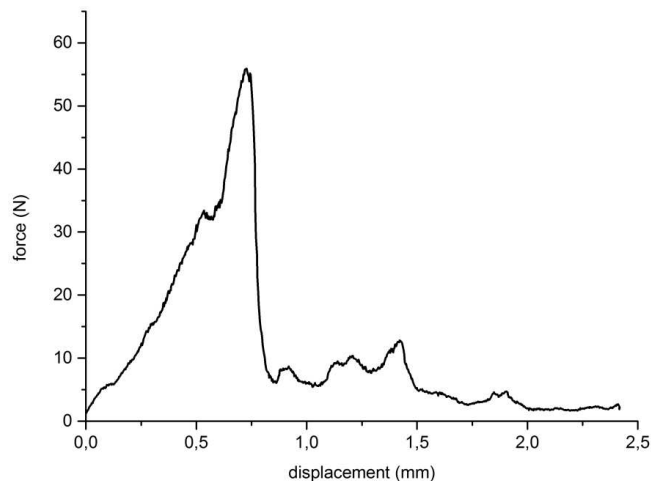


**Figure 73.** Force displacement curve of the ref.rat sample [184].

It was used as a reference for initial stability not only for coated rat implants but also for uncoated rat implants. Initial stability values were compared to secondary stability values of the other rats which recovered for 30 days for obtaining success of the healing process after implant placement surgery. Figure 73 shows the push-out force-displacement behavior of the ref.rat sample.

Average force-displacement curves for rat implants, including standard errors, are shown in Figure 74. Four and six push-out test data were used for average displacement-force curves for uncoated and coated rat implants, respectively. The graph shows in comparison with ref.rat samples an improvement in the implant fixation and stability. This indicates the

osseointegration and bone ingrowth, which was observed for both uncoated and coated implants after 30 days of healing.

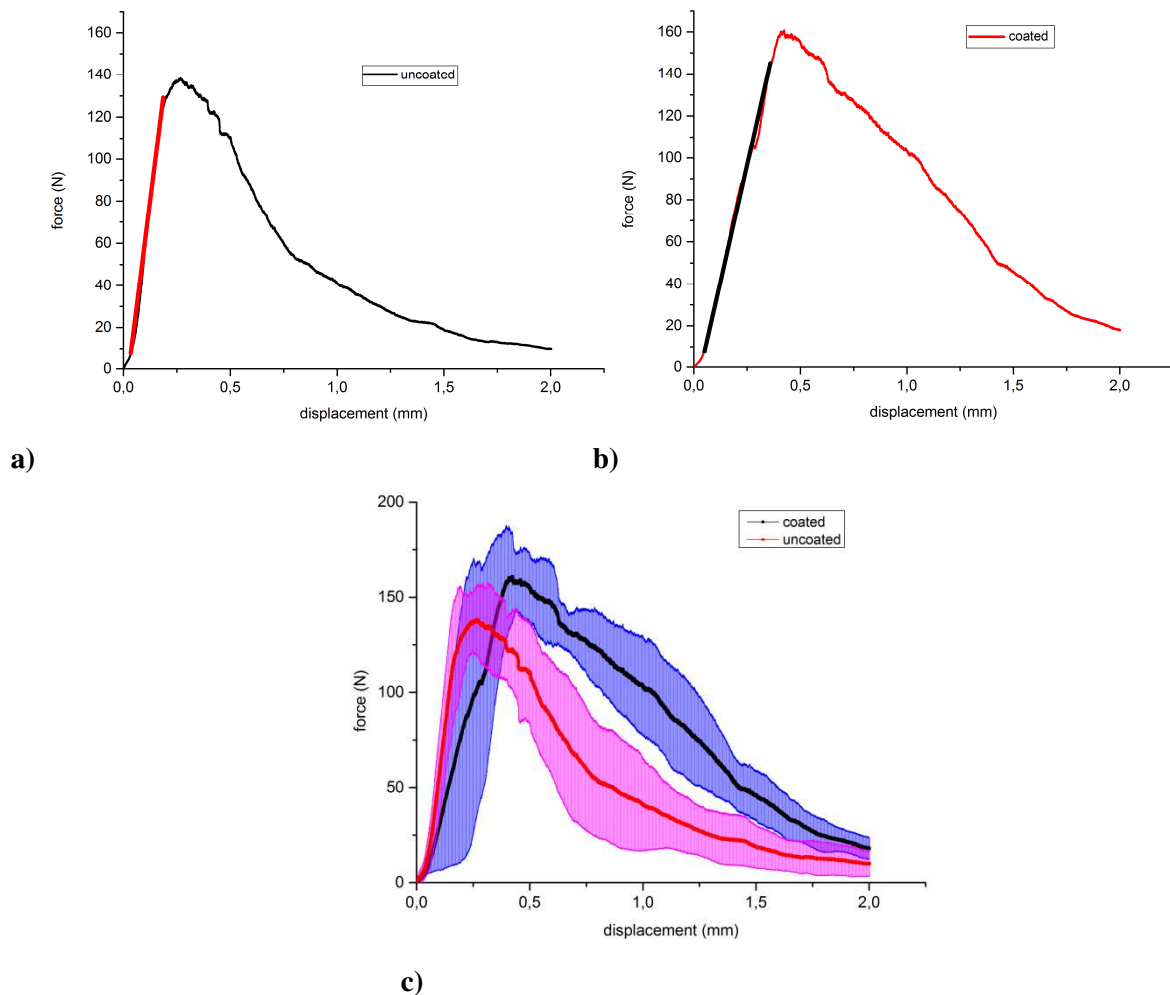


**Figure 74.** Average force-displacement curve **a)** for all six uncoated rat samples. **b)** for all four coated rat samples. **c)** including standard errors.

For uncoated rat implants, push-out forces ranged from  $F_{\max} = 124$  up to 156 N and the average push-out force was  $140 \pm 14$  N. The ultimate displacement values lay between 0.18 and 0.42 mm. The slope of the force-displacement graph, which is the push-out stiffness, was calculated to be 590 N/mm, by finding the longest linear portion of the average force-displacement graph slopes. The results of the push-out tests of coated implants demonstrated that after 30 days of implantation, the maximum force ranged from 126 up to 179 MPa. The investigated coated rat implants yielded a slightly higher average maximum push-out force of  $160 \pm 26$  N.

Energy absorption of coated implants was higher than the uncoated implants. The absorbed energy values of  $101 \pm 25$  mJ and  $147 \pm 17$  mJ were calculated for uncoated and coated implants, respectively. In comparison with ref.rat samples, uncoated samples and coated samples

## 4 Results

absorbed 3.6 times and 5.2 times higher energy during push-out tests, respectively. Furthermore, an apparent decrease in stiffness of the coated samples can be seen in force-displacement curves which show a decrease in slope towards 415 N/mm. Ultimate displacements ranged from 0.24 mm up to 0.47 mm. A relatively good correlation between the push-out force and the ultimate displacement was found for both uncoated ( $r^2 = 0.9972$ ) and coated samples ( $r^2 = 0.9914$ ).

After 30 days of implantation, the shear strengths of the bone-implant interface were calculated using push-out results averages of  $3.24 \pm 0.4$  MPa for uncoated rat implants, while this value increased to  $3.65 \pm 0.6$  MPa for  $\text{CaTiO}_3$  coated rat implants

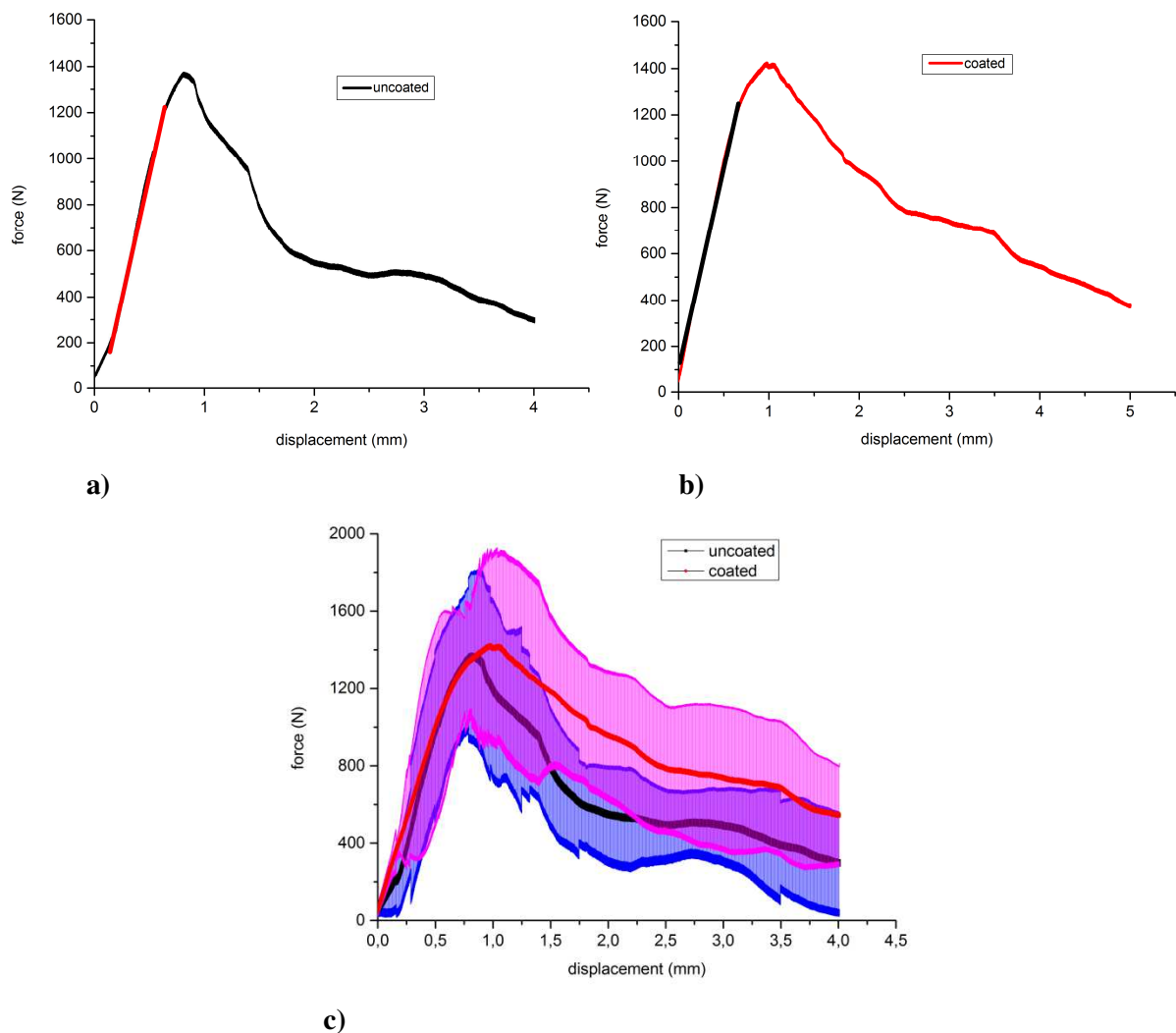


**Figure 75.** Average force-displacement curve **a)** for all four uncoated sheep samples. **b)** all six coated sheep samples **c)** including standard errors.

Average force-displacement curves for sheep implants, including standard errors, are shown in Figure 75. Six and four push-out test data were used for average displacement-force curves for uncoated and coated sheep implants, respectively. For uncoated sheep implants, push-out forces ranged from 674 up to 1816 N, and ultimate displacements from 0.76 up to 1.12 mm.

The average push-out force for all four specimens was recorded at  $1362 \pm 529$  N and the average absorbed energy was calculated to be  $3614 \pm 1556$  mJ.

No significant difference was observed for coated sheep implants, and  $1419 \pm 494$  N and  $3993 \pm 2274$  mJ were obtained for an average push-out force and an average absorbed energy values respectively. The ultimate displacement values lay between 0.72 and 1.47 mm for coated implants. Furthermore, a slight difference in stiffness of 1938 N/mm can be seen in force-displacement curves of coated samples.

A relatively good correlation between the push-out force and the ultimate displacement was found for both uncoated ( $r^2 = 0.9951$ ) and coated samples ( $r^2 = 0.9982$ ). Average force-displacement curves for sheep implants, including standard errors, are shown in Figure 75 c).

#### 4.7 Finite Element Analysis Results

The material and bone characterization was performed on rat and sheep bones using SEM microscope images and reported geometric characteristics of a bone included cell size, cell anisotropy and ligament length.

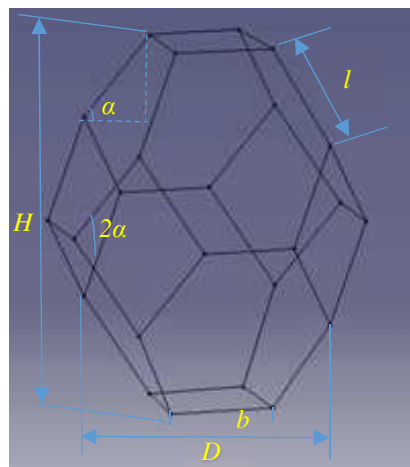


**Figure 76.** Geometric parameters of unit cell [170].

Figure 76 shows geometrical parameters of the unit cell and Table 13 summarizes the measured geometric parameters of the two bones.

SEM images showed that both rat and sheep bone are composed of unidirectionally elongated cells. Microstructural anisotropy is adopted to the Kelvin cell model in the manner of previous assumptions [167, 168]. The cell size is defined by the average height of the cells in the rise direction ( $H$ ) and the average width of the cells ( $D$ ). An anisotropy parameter  $\lambda$  was calculated using Equation (24)

$$\lambda = H/D = \tan \alpha \quad (24)$$

The average height of the cell was 0.32 mm and the average width of the cell was 0.23 mm for rat cancellous bone, whereas these values were calculated as 0.82 mm and 0.56 mm. for sheep cancellous bone. The mean values of  $\lambda$  reported in Table 13 ranges from about 1.21 to 1.42 and 1.24 to 1.57 for rat and sheep bone, respectively.

**Table 13.** Geometric parameters of rat and sheep cancellous bones.

	$h_1$	$h_2$	$\lambda$	$\alpha$	Tb.Sp ( $\mu\text{m}$ )	Tb.Th ( $\mu\text{m}$ )	cortical thickness
<b>Rat bone</b>	0.32	0.23	1.39	55	234±131	90±78	0.35-0.5
<b>Sheep bone</b>	0.82	0.56	1.46	58	532±232	120±50	3.2-3.5

The ligament length  $l$  is defined to be the distance between the centers of nodes. The ligament lengths were calculated to have a value of 0.0125 mm and 0.028 mm for rat and sheep bone, respectively. The cortical thickness measured for each bone sample at four locations was required to obtain the mean cortical thickness. The bone is modelled as a cancellous core surrounded by a cortical layer with thickness range for rats from 0.35-0.5 mm, and for sheep from 3.2-3.5 mm, respectively.

The interfacial conditions between both implants (rat and sheep implants) and the bone were determined according to the experimental results. For the interface between implant and bone, a finite shear strength was implemented from each push-out tests. For this reason for uncoated and coated rat implants, four and six different analyses were made, respectively. On the other hand, six and four different analyses were performed for uncoated and coated sheep implants, respectively. Displacement of implant was designated for rat implants at 2.5 mm, and for sheep implants at 4.5 mm. The occurrence of relative motion between implant and bone can change the contact conditions. According to FEA results, the simulated average force-displacement curves for rat implants and sheep implants were plotted and for comparison, the experimental average curve was also illustrated. The effective interference approach was chosen to simulate the effect of the  $\text{CaTiO}_3$  coating on the biomechanical behavior of implants. The effective interferences at the coated implants interface are 0.5  $\mu\text{m}$  and 1.5  $\mu\text{m}$  for rat and sheep implants, respectively.

### 4.7.1 Determination of shear strength for rat implants

All three FE models were successfully created and analyzed for four uncoated and six coated rat implants. The computational results are higher than the measured maximum push-out force. The highest maximum push-out forces are obtained with the 2D FEA. Both 3D FE models show nearly similar maximum push-out forces.

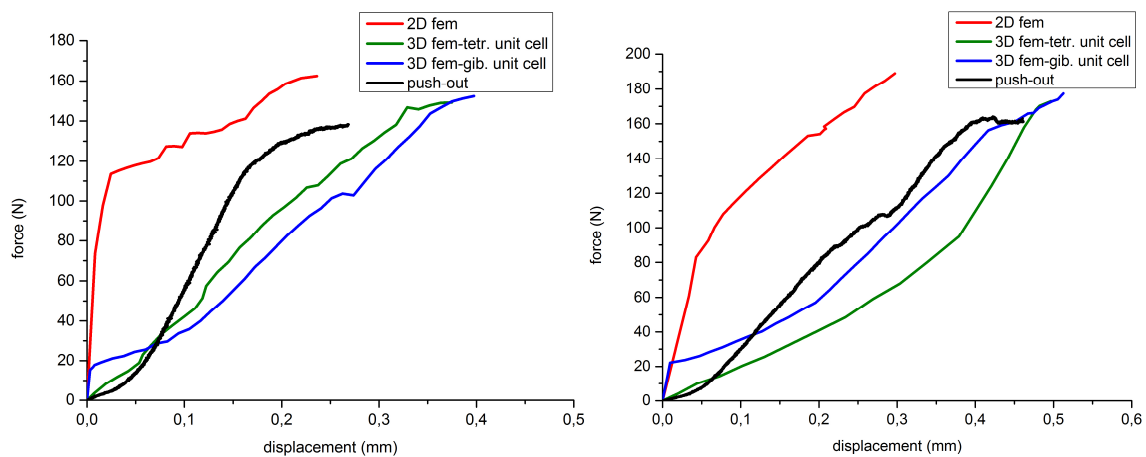


**Figure 77.** Comparison of the maximum push-out force obtained from the 2D model and two different 3D models for **a)** uncoated **b)** coated rat implants.

The best correlation for uncoated and coated rat implants was found for the tetrakaidecahedron unit cell ( $r^2 = 0.72$ ) and Gibson-Ashby's unit cell ( $r^2 = 0.76$ ) model, respectively. Average force-displacement curves for uncoated and coated rat implants from all FEA are shown in Figure 77 a) and b) respectively. On the other hand, the 2D FE results have a higher value than the measured stiffness. 2D FE-derived and measured stiffness did not correlate, whereas 3D FE- stiffness did not show the high correlation to experimentally measured stiffness. In the light of these results and in order to determine the shear strength of bone-implant interface for uncoated and coated rat implants, the average maximum push-out force was selected from the tetrakaidecahedron unit cell model and Gibson-Ashby's unit cell model results, respectively.

### 4.7.2 2D results for rat implants

Figure 78 a) and b) show the 2D FEA results of the push-out tests for uncoated and coated rat implants, respectively. Both FEA results for uncoated and coated implants show similar force-displacement curves with the experimental results of push-out tests. Not only for uncoated

## 4 Results

but also for coated implants, higher maximum push-out forces were observed. While for coated implants the maximum push-out forces were obtained nearly at the same displacement with test results, uncoated implants reached the maximum force at a smaller displacement and the analysis finished at approximately 1 mm. Average force-displacement curves for rat implants with standard errors, from 2D FEA are shown in Figure 78 c) In comparison with test results narrower standard error range calculated.

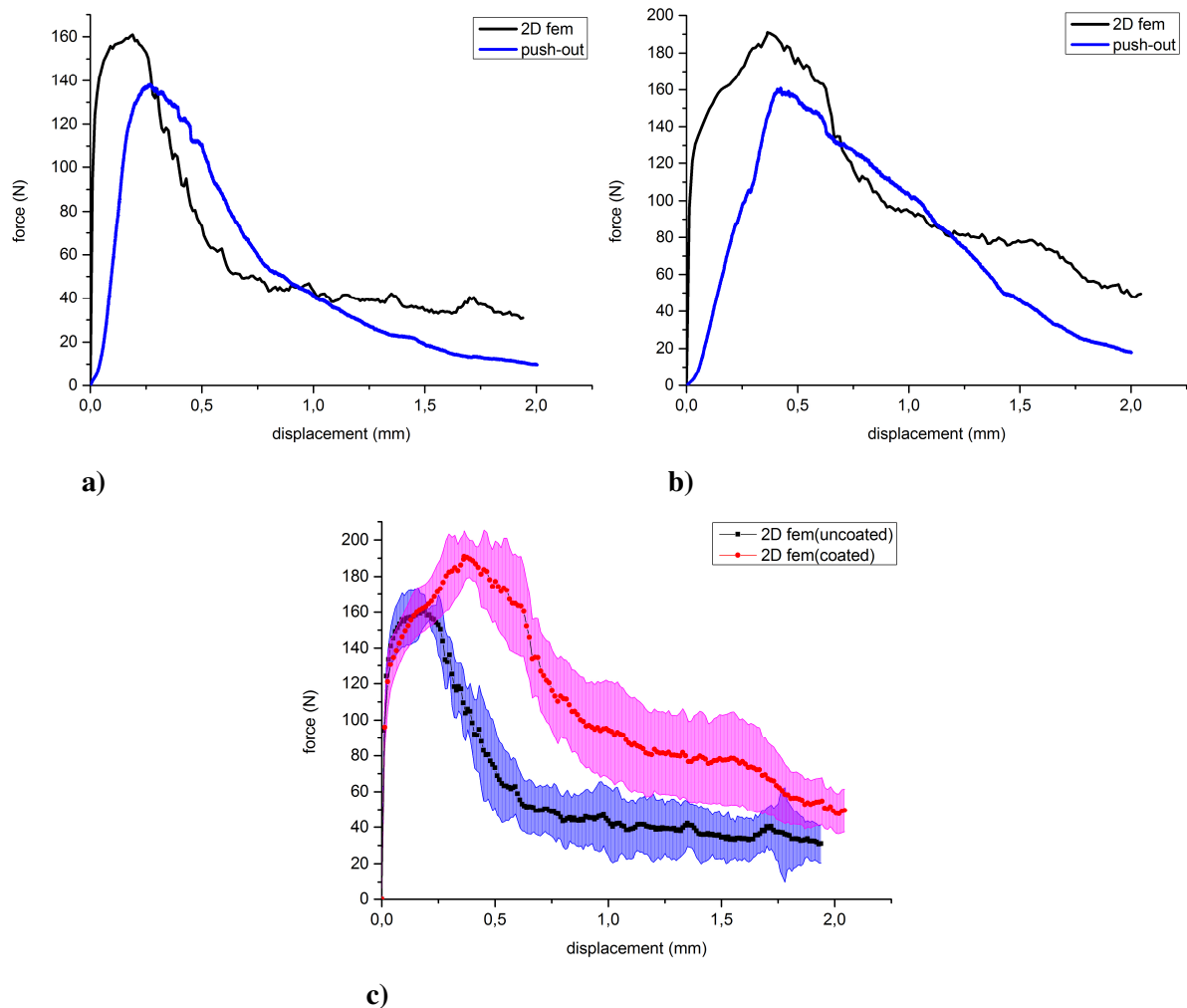


**Figure 78.** The 2D FE analysis results of the push-out tests for **a)** uncoated and **b)** coated rat implants **c)** average force-displacement curves for rat implants from 2D FEA, including standard errors.

### 4.7.3 3D FEA results for rat implants

#### Tetraprism unit cell

By means of 3D FEA, the results of the push-out tests for uncoated and coated rat implants were calculated and plotted in Figure 79 and 80.

The tetrakaidecahedron (tetra) unit cell based 3D model results of the push-out tests for uncoated and coated rat implants are plotted in Figure 79 a)-b). According to the 3D FEA with a tetra unit cell model, the average maximum push-out force was calculated to be 155 N and 183 N for uncoated implants and coated implants, respectively. Average force-displacement curves consist of three characteristic zones. Especially, the linear region of the force-displacement curves before the maximum push-out force correspond well to the test results and the slopes of the load-displacement curve at the linear region are in considerable agreement. While implant bone separation completed in 1.5 mm sliding movement for uncoated implants, coated implants separated from bone completely in 2 mm. This can be explained by a combination of partial separation and frictional sliding for coated implants.

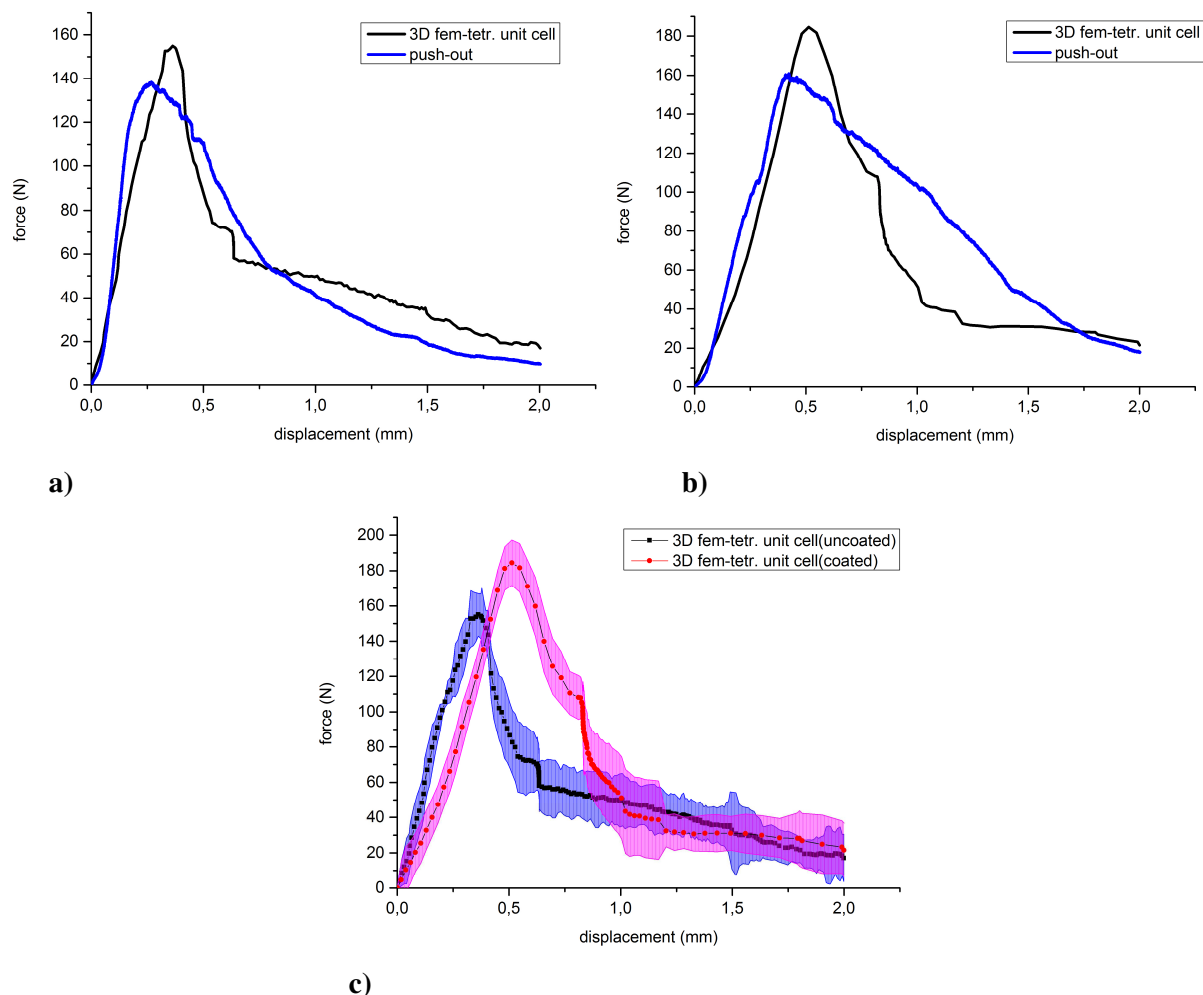


**Figure 79.** The results of the 3D-FEM analyses with the tetrakaidecahedron unit cell model for **a)** uncoated and **b)** coated rat implants **c)** average force-displacement curves with standard errors for rat implants from tetrakaidecahedron unit cell based 3D model.

The average push-out curves of both uncoated and coated rat implants with standard errors are plotted in Figure 79 c). Up to 0.8 mm displacement, the highest standard errors value of  $\pm 15$

## 4 Results

and  $\pm 23$  N were calculated for uncoated and coated implants. After that, the standard error range is wider for both types of implants. However, standard error values for FEA results were smaller than the test results and error bounds were more uniform.

### Gibson-Ashby's unit cell

The force and displacement results of the 3D Gibson unit cell model are illustrated in Figure 80 a) and b) for uncoated and coated rat implants, respectively. Both curves are in good agreement with the experimentally measured force displacement curves.

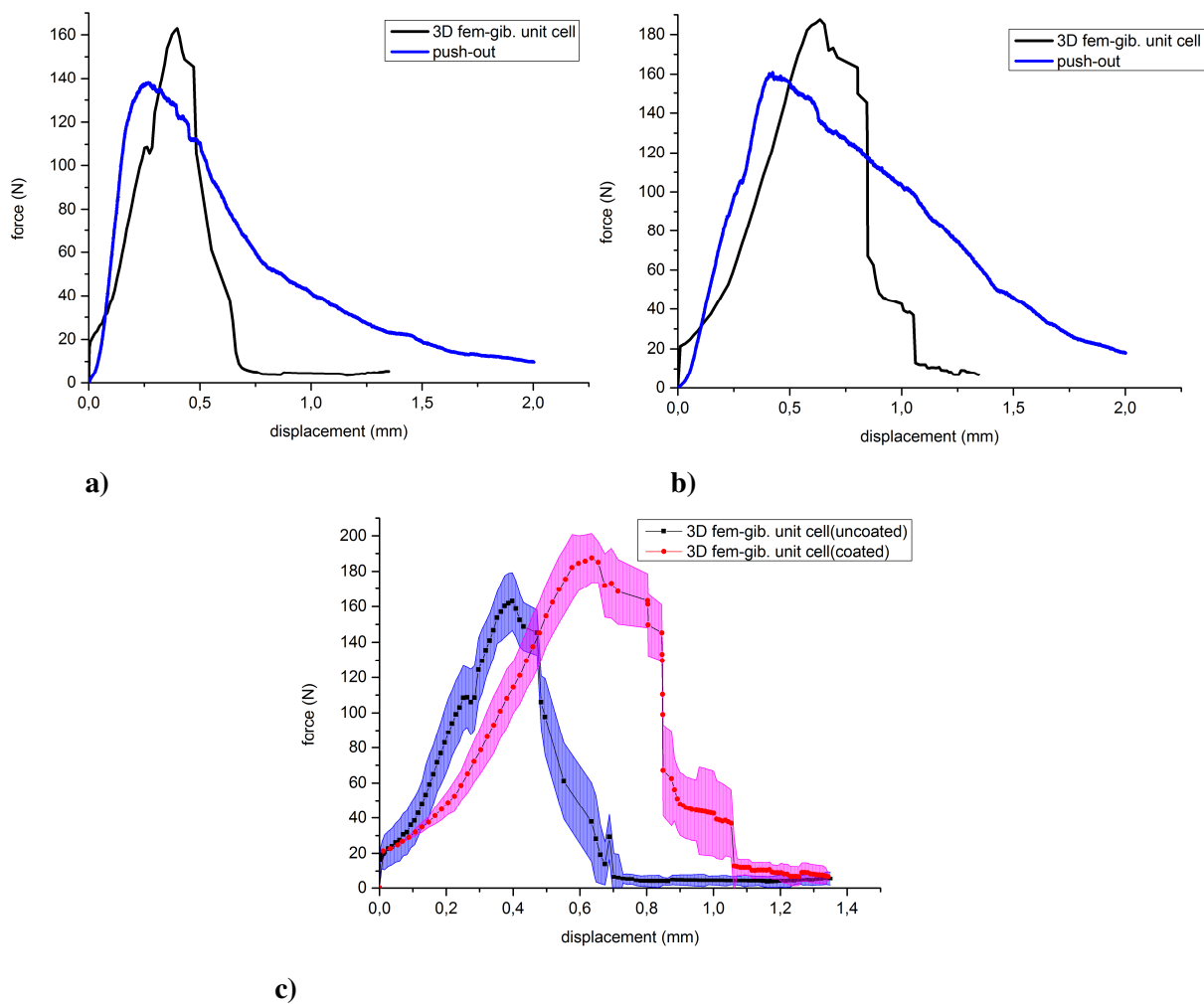


**Figure 80.** The results of Gibson unit cell based 3D model for a) uncoated and b) coated rat implants average force-displacement curves for rat implants with standard errors, results of Gibson unit cell model.

The average push-out forces of the uncoated and coated implants were approx. 24 N higher as compared to the test results. While the uncoated implant reaches peak load at 0.4 mm displacement, for the coated sample this value is 0.6 mm. Despite of the similarity of the linear

behavior between simulated and measured curves, after reaching  $F_{max}$  at the simulated curves, the push-out forces diminished significantly. This corresponds to the onset of complete separation.

Average force-displacement curves for rat implants with standard errors as results of the Gibson unit cell model are shown in Figure 80 c). While the standard errors are larger than for the tetrakaidecahedron unit cell model, the results of Gibson unit cell model have smaller standard errors, in comparison to test results.

In order to compare the results of the different models, the force-displacement curves are presented for comparison in Figure 81. All simulated force-displacement curves consist of three distinct stages. Initially, a linear response was observed corresponding to perfect implant bone bonding. For the 2D model, this elastic stage is shorter compared to the measured, and 3D simulated curves.

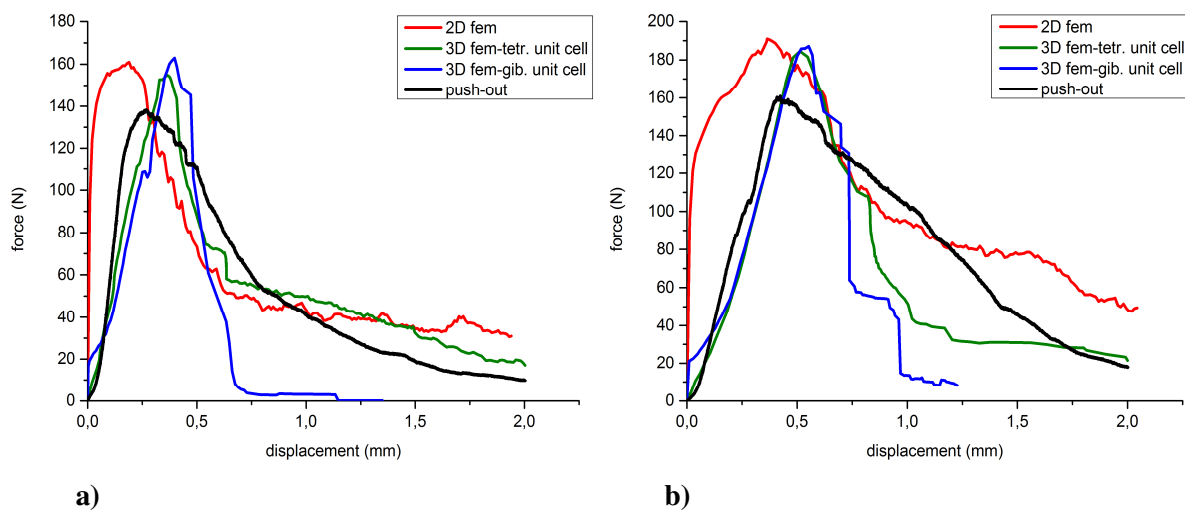


**Figure 81:** Comparison of the force-displacement curves obtained from the 2D model and two different 3D models (tetrakaidecahedron and Gibson unit cell) for **a)** uncoated **b)** coated implants.

While the computationally analyzed stiffness values for both 3D models correspond closely to the experimentally estimated stiffness, the computational 2D results are by a factor of 13 times higher than the measured interface stiffness. Both 3D model curves reach a maximum push-out force at larger displacements.

For all simulations, the average maximum push-out forces are higher than the experimentally measured values. At the second stage, a nonlinear load displacement curve is observed when the load increases. It can be concluded that the bonding between bone and implant becomes unstable and leads to separation, when the load reaches a critical value. Both 3D model curves did not show a remarkable nonlinear behavior at the second stage. On the other hand, the 2D

model curves are in good agreement with the measured curves. The last characteristic stage of curves corresponds to the sliding of the implants out of the surrounding bones. Whilst the sliding events at both 2D model curves were uniform and gradual, the sliding stage is quite different for 3D simulations, especially with Gibson unit cell assumption.

#### 4.7.4 Determination of shear strength for sheep implants

All three FE models were successfully created and analyzed for six uncoated and four coated sheep implants. The computational results are higher than the measured maximum push-out force, see in Figure 82. The highest maximum push-out forces are obtained with the 2D FEA. Both 3D FE models show nearly similar maximum push-out forces. The best correlation for uncoated and coated sheep implants was found for the tetrakaidecahedron unit cell with  $r^2 = 0.75$  and  $r^2 = 0.78$ , respectively. For coated and uncoated sheep implants, a comparison between the results of FE simulation and push-out tests is shown in Figure 82 a) and b), respectively.

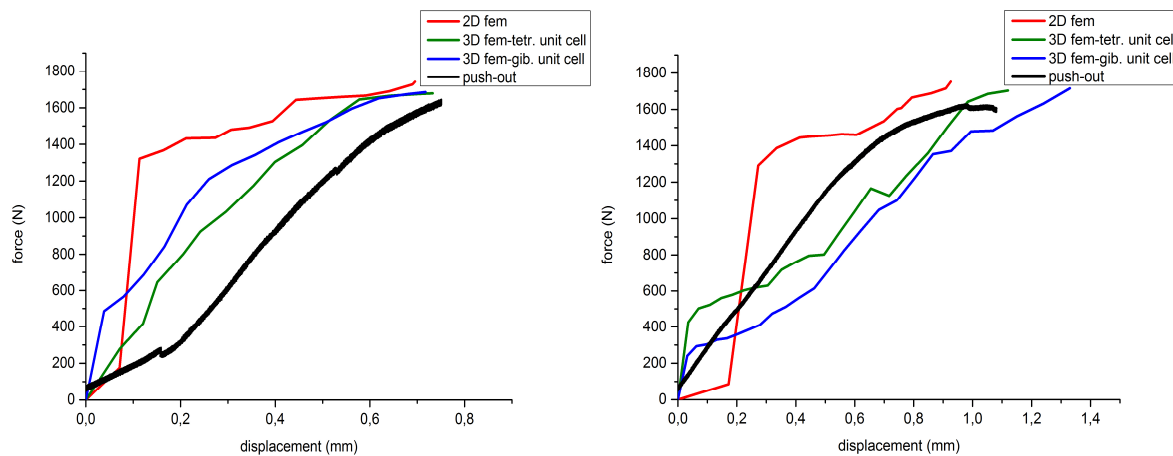


**Figure 82.** Comparison of the maximum push-out force obtained from the 2D model and two different 3D models for a) uncoated b) coated sheep implants.

On the other hand, the 2D FE results are higher than the measured stiffness. 2D FE-derived and measured stiffness did not correlate, whereas 3D FE- stiffness did not show the high correlation to experimentally measured stiffness.

In the light of these results, in order to determine the shear strength of bone-implant interface for uncoated and coated sheep implants, the average maximum push-out force was selected from tetrakaidecahedron unit cell model results.

### 4.7.5 2D results for sheep implants

Figure 83 a) and b) show the 2D FEA results of the push-out tests for uncoated and coated sheep implants, respectively.

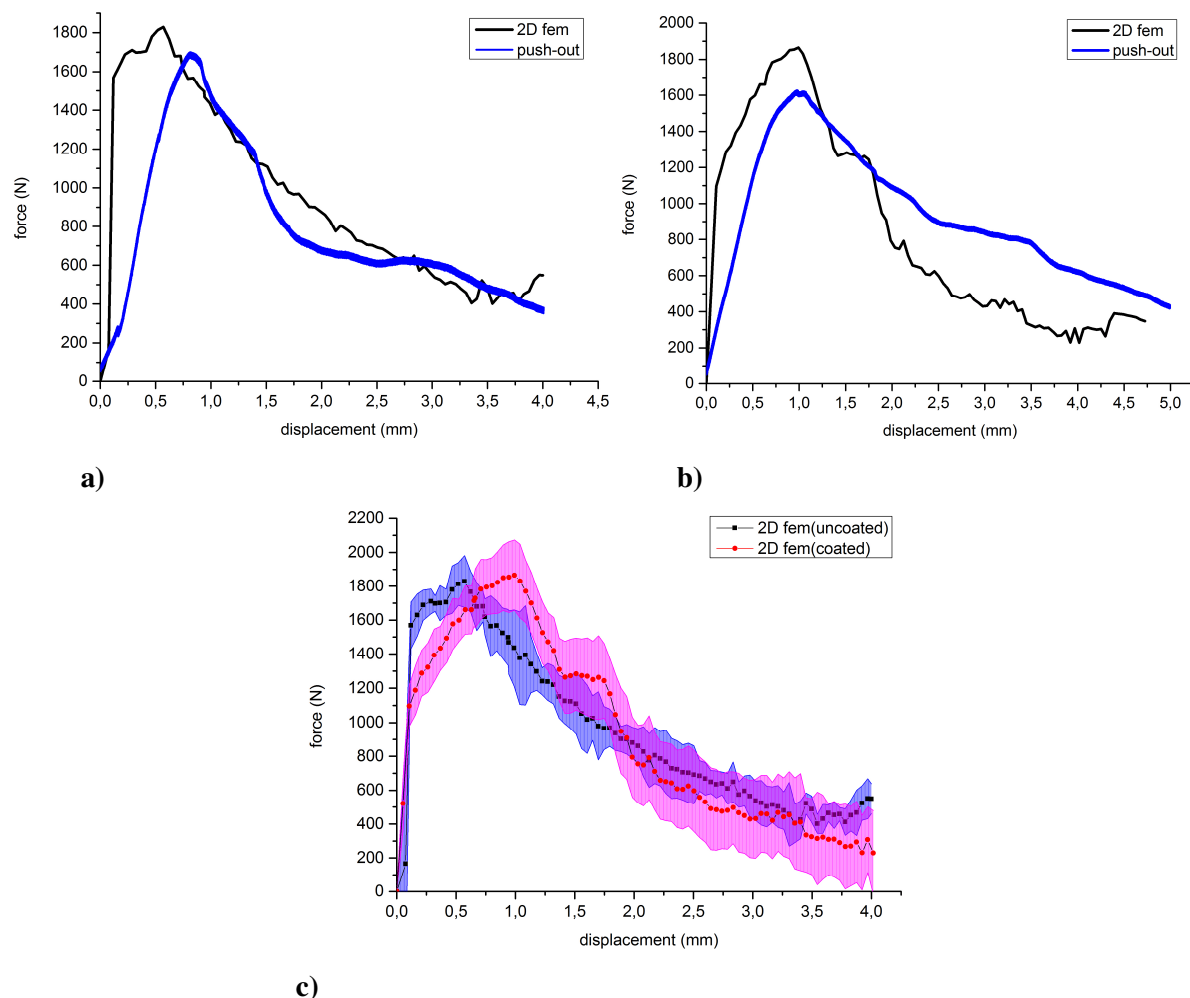


**Figure 83.** The 2D FEA results of the push-out tests for **a)** uncoated and **b)** coated sheep implants **c)** average force-displacement curves for sheep implants from 2D FEA, including standard errors.

The curves show an initially linear-elastic response, however, elastic behavior proceeds only small displacement values, which are 0.65 mm and 1.2 mm for uncoated and coated implants respectively. Both simulated curves reach the peak point at a smaller displacement than the measured curves. At the same time, a higher average maximum push-out force was found. After the break point the simulated curves became highly compliant with test results.

### 4.7.6 3D results for sheep implants

The 3D FEA results of the push-out tests for uncoated and coated sheep implants are shown in Figure 84 and 85 for two different types of unit cells.

### Tetrakaidecahedron unit cell

The force and displacement curves of the 3D tetrakaidecahedron unit cell model for uncoated and coated sheep implants are illustrated in Figure 84 a)-b).

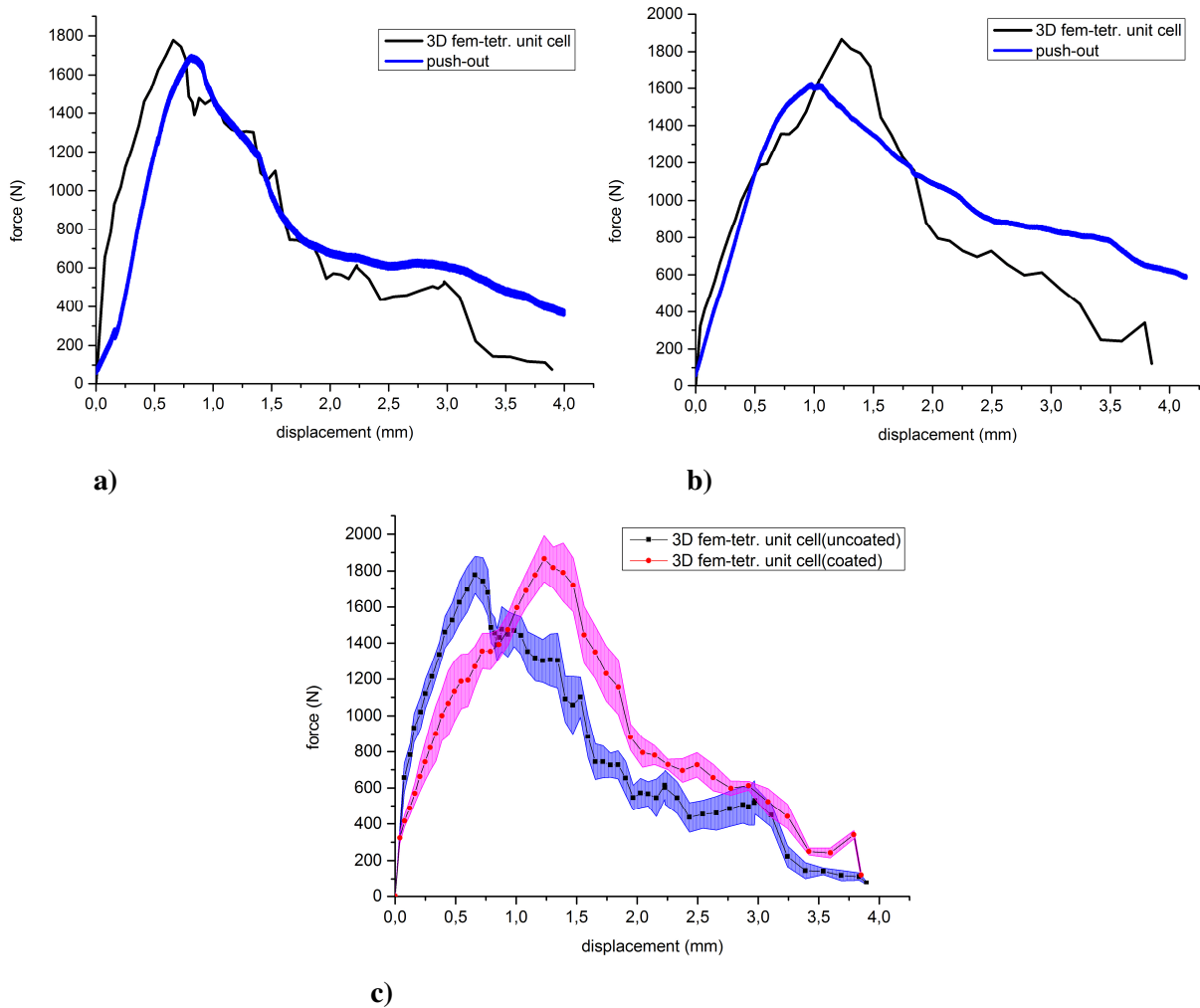


**Figure 84.** The results of the 3D FE analysis with the tetrakaidecahedron unit cell model for **a)** uncoated and **b)** coated sheep implants **c)** average force-displacement curves with standard errors for sheep implants from the tetrakaidecahedron unit cell based 3D model.

For uncoated implants, the maximum average push-out force was observed nearly at the same displacement values as those of the measured curve. However, an apparent increase in stiffness can be seen in force-displacement curves for coated implants with a maximum reached at 1832 N. The simulated maximum push-out forces for both the uncoated and the coated implants were higher than the measured maximum push-out forces.

The simulated force-displacement curves of coated implants showed virtually the same elastic behavior as the measured force displacement curve. Average force-displacement curves for rat implants with standard errors, for the tetrakaidecahedron unit cell model are shown in

Figure 84 c). Although no significant differences were observed between uncoated and coated sheep implants after push-out tests, the FEA results indicate that coated implants have a higher push-out force and the separation of implants from bone occurred at a larger displacement than the uncoated implants.

### Gibson-Ashby's unit cell

The force and displacement results of the 3D Gibson unit cell model are represented in Figure 85 a) and b) for uncoated and coated sheep implants, respectively.

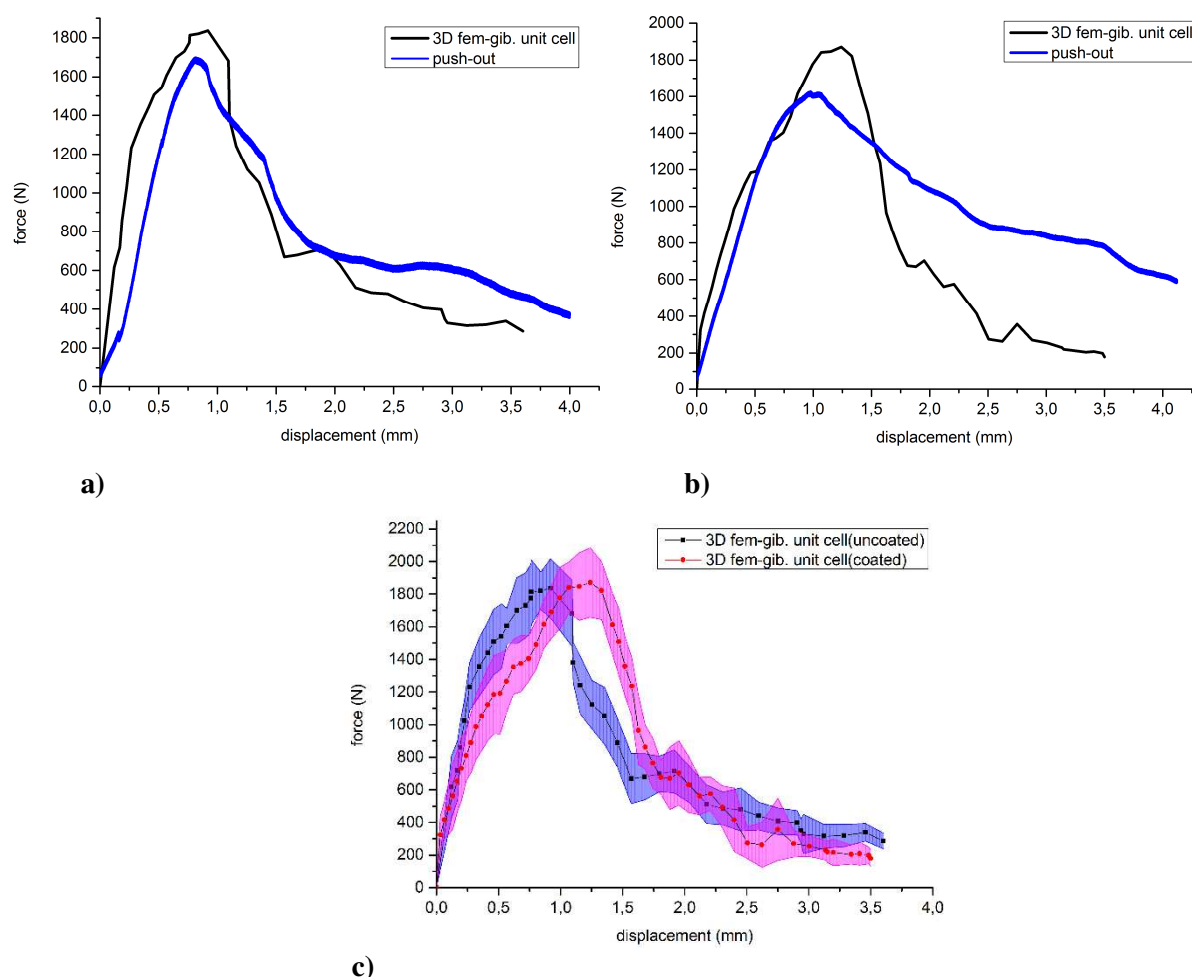


**Figure 85.** The results of Gibson unit cell based 3D model for **a)** uncoated and **b)** coated sheep implants **c)** average force-displacement curves for sheep implants with standard errors, results of Gibson unit cell model.

Both curves are in good agreement with the experimentally measured force-displacement curves. The average push-out forces of the uncoated and coated implants are approximately 200 N higher as compared to the test results. The uncoated implant reaches the maximum push-out

## 4 Results

force at a similar displacement value to the measured value, for the coated samples nearly a 0.5 mm increment was obtained.

Furthermore, a reduction of interface stiffness can be seen clearly between bone and coated implants. Average force-displacement curves for sheep implants with standard errors as results of the Gibson unit cell model are shown in Figure 85 c). While the standard errors are smaller than test results, they are in the same range as those achieved for the tetrakaidecahedron unit cell model.

For coated and uncoated sheep implants, a comparison between the results of FE simulation and push-out tests is shown in Figure 86 a) and b), respectively. Three characteristic regions can be seen clearly on all simulated force-displacement curves. The elastic region is narrow for the 2D model results compared to the measured and the 3D simulated curves.

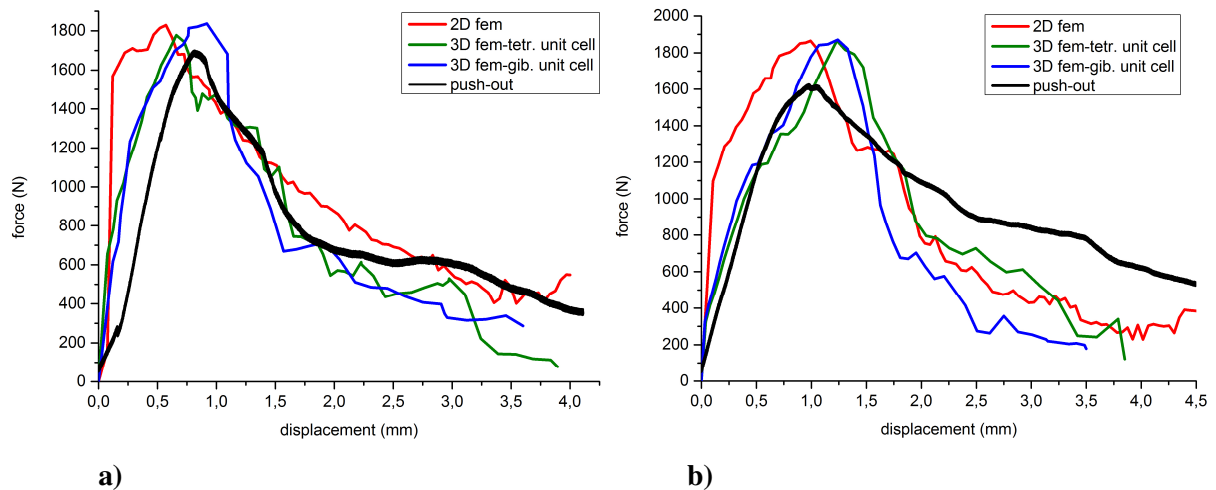


**Figure 86.** Comparison of the force-displacement curves obtained from the 2D model and two different 3D models (tetrakaidecahedron and Gibson unit cell) for a) uncoated b) coated implants.

For both 3D models, the computationally analyzed stiffness values correspond closely to the experimentally calculated stiffness for coated sheep implants, whereas the calculated stiffness is higher than the measured value. Not only for uncoated but also for coated implants, the interface stiffness of the 2D FE results are higher than the measured interface stiffness.

Higher average maximum push-out forces than experimentally measured values were simulated for all models. At the second region, a remarkable nonlinear behavior was observed for uncoated and coated implants according to both 3D model results. The sliding of the implants out of the bones occurs gradually on the 2D model curves. On the other hand, a fairly different sliding behavior was observed for 3D model simulations. Especially on the Gibson unit cell model curves, implant sliding concludes at a smaller level of displacement in

comparison with the results from experiment and other models. With uncoated implants, the peaks points of all curves were observed at nearly the same displacement value compared to that of the measured curves. Both 3D model curves for coated implants attain the maximum force at larger displacement levels compared with test results.

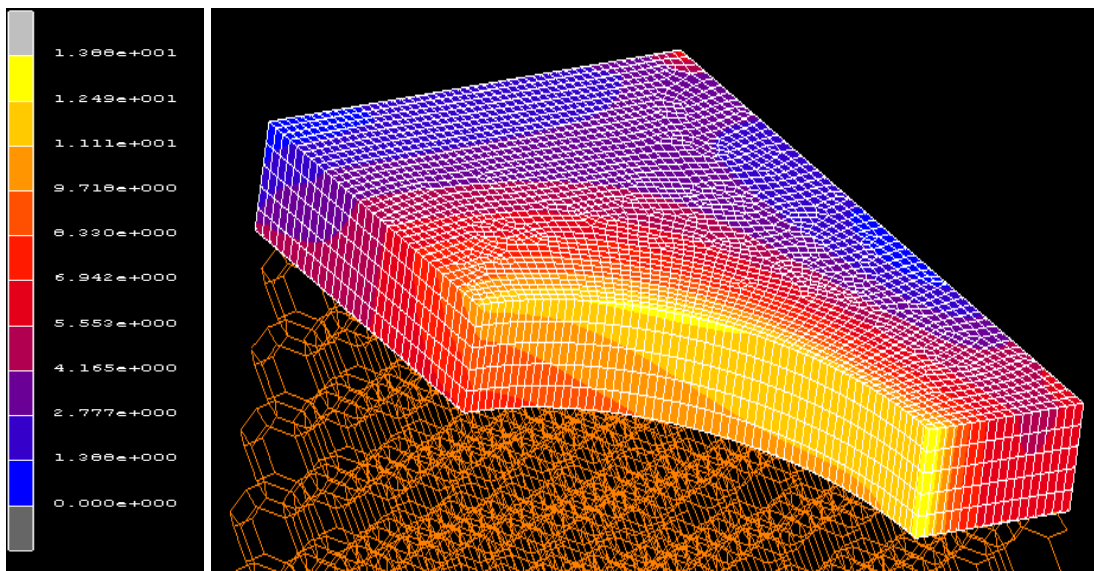


**Figure 87.** Von Mises stress distributions on bone-implant interface for rat implants.

All results of the numerical analysis were represented with Von Mises stresses. Eight different colours were selected for the indication of specific values of Von Mises stress. Rotationally symmetric stress distributions were observed for the rat and sheep implants (see in Figure 87 and Figure 88, respectively).

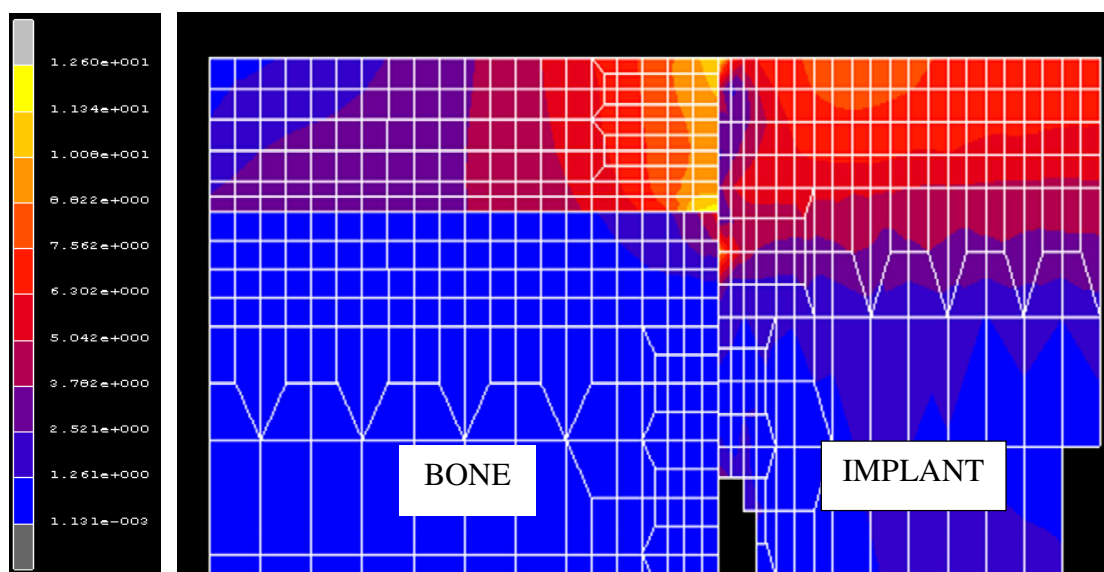


**Figure 88.** Von Mises stress distributions on bone-implant interface for sheep implants.

#### 4 Results

Coated and uncoated implants represented similar stress distribution in bone. The maximum Von Mises stress was the highest among those generated in the compact bone for all models (2D and 3D). The maximum Von Mises stresses were generated at the top of the compact bone region and decreased gradually towards the bottom of the implant. Significant reduction in Von Mises stress for all implant system was observed at the boundary between compact and cancellous bone because of the low elastic modulus of cancellous bone. Additionally, while the highest intensity of the mechanical stress is visible in the areas of bones which are closer to the implant, it decrease in magnitude towards the outer region.

## 5 Discussion

In the range of this study, every obligatory step for the development of the cast porous Ti67 implants as a new biomaterial, from the production and modification of the porous implant structure up to the suitability testing of a novel material for medical applications, was taken into consideration.

In this study, a precision casting process for the manufacturing of the complex porous implants was selected. The major advantages of the precision casting are the relative reduction of the overall cost, the production of the great variety of structure parameters and the precise dimension control it offers, giving designers and engineers more flexibility.

During the development of the cast porous Ti67 implants, rectangular samples with simple morphologies specimens were manufactured and used for the examination of the microstructure and mechanical properties. Thus, the manufacturing process of the cast porous Ti67 implants was optimized. Furthermore, the analysis of these samples plays a crucial role in predicting the microstructure and mechanical properties of thinner sectioned structures such as the cell struts of the implants.

### 5.1 Investigation of the $\alpha$ Case Formation

In previous studies [66-85], several types of casting-related defects were defined, such as shrink porosity, gas pores, chemical segregation due to the physical chemistry of solidification, and contamination due to mould-casting interactions. Microstructural analysis and mechanical testing of cast Ti67 samples revealed various defects associated with the casting process.

As a result of interstitial oxygen diffusing through the titanium lattice from the reacted investment material during the period of the casting, solidification and cooling process, a hard and brittle surface layer occurs, as commonly referred to as  $\alpha$  case layer [66, 68-70, 72-80, 83-85]. To prevent the formation of  $\alpha$  case during the casting process, investment materials such as  $\text{Al}_2\text{O}_3$ ,  $\text{MgO}$ ,  $\text{CaO}$ ,  $\text{ZrO}_2$ ,  $\text{Y}_2\text{O}_3$  etc. were introduced into the casting process of titanium [68, 69, 73, 81]. For the choice of investments for the casting of reactive metals, the following general thermodynamic rule is valid: the higher the standard free energy of the formation of oxides, the more stable is the ceramic with respect to the casting process. This is due to the fact that the usage of a thermodynamically ore stable ceramic leads to the formation of a thinner layer, and thus to a smaller depletion of reactive elements.

The present study summarizes experimental results on the effect of the mould composition on the surface quality and the  $\alpha$  case layer formation of Ti67 castings. To obtain the best conditions for Ti67 castings, four different investment materials were compared: Commercial Invest-Ti-T,  $\text{Al}_2\text{O}_3$ ,  $\text{ZrSiO}_4$  and  $\text{Y}_2\text{O}_3$ . The  $\alpha$  case formation was examined through microstructure analyses, hardness profiles and element mapping by EDS.

The microstructure of titanium castings produced with Invest-Ti-T,  $\text{Al}_2\text{O}_3$ , and  $\text{ZrSiO}_4$  based investments consisted of three different regions. The observation of the microstructure of plate structures of cast Ti67 indicated that a thin pure  $\alpha$  phase region is typically observed on the sample side of the interface. Further away from the investment material, an  $\alpha$  plate structure is clearly seen within large prior  $\beta$  grains. The  $\alpha$  plate size decreases and reaches the plate size of the bulk metal with distance increasing from the sample surface. The bulk microstructure consists of  $\alpha$  laths embedded in primary  $\beta$  phase. On the other hand, these kinds of microstructural differences were not observed for the cast Ti67 sample with  $\text{Y}_2\text{O}_3$  investment.

During the cooling process, the metal temperature will drop below the  $\beta$ -transus temperature. Oxygen is an  $\alpha$  stabilizer, and for this reason, the  $\beta$ -transus temperature increases with increasing oxygen content. As a result the  $\alpha$  phase first nucleates near the mould surface and grows inwards to form an  $\alpha$  layer [76]. Guillen et al. [201] found out with EBDS analysis that a fine-grained outer zone of hexagonal  $\text{Ti}_3\text{Al}$  corresponds to the  $\alpha$  case layer. The inner layer, which consists of coarse acicular Widmanstätten or plate-like crystals, corresponds to the second layer. The third layer, the bulk microstructure with fine plates, follows the acicular layer [66, 72, 78, 201]. According to previous studies [68, 81, 202-207], the investment material, the mould temperature, and the casting volume determine the size of the acicular layer. Increasing the mould temperature and the casting volume increased the thickness of the acicular layer and makes the acicular grains coarser [76, 78, 201].

The hardness profiles of the samples are in good agreement with the microstructural investigations. The strong dissimilarities between these three regions is seen clearly on the hardness profile. The  $\alpha$  case layer exhibits a nearly one and a half times higher hardness than the bulk Ti67 material. The relatively brittle behavior of the cast structures during mechanical testing can be related with the  $\alpha$  case and to the inhomogeneous internal microstructure. Hardness measurements revealed that, except from  $\text{Y}_2\text{O}_3$  investment for investment casting, the depths of areas with higher hardness are deeper than those of the reaction layers and the hardness profile of the oxide layer on Ti67 castings consisting of two different regions. Therewith, the element mapping results showed that the inner region does not include

investment material. In other words, there should be another layer between the surface reaction layer and Ti67. The formation of this layer might be the outcome of the rapid cooling of molten Ti67.

The microscopic examination showed that the thickness of the  $\alpha$  case layer on the casted Ti67 sample surfaces ranged from 10 up to 35  $\mu\text{m}$ . It was recognized that the commercial Invest-Ti-T investment causes the thickest reaction layer and the highest surface microhardness. The  $\alpha$  case layer of the samples which were cast with  $\text{Al}_2\text{O}_3$  based investment material and  $\text{ZrSiO}_4$  based investment has nearly the same thickness value. However,  $\text{ZrSiO}_4$  based investment produced less surface hardness compared to the  $\text{Al}_2\text{O}_3$  based investment material.

In the literature, there are several studies about the  $\alpha$  case formation [78, 80, 81, 85] and it was reported that the  $\alpha$  case reaches a thickness between 50 to 500  $\mu\text{m}$ , whereby the thickness of the layer varied with the crystal orientation of the grains near to the surface. In addition, it is basically associated with the energy content of the system such as preheating and temperature of the melt. In comparison with our rectangular samples with dimensions of 10 x 10 x 1  $\text{mm}^3$ , relatively thick specimens were used in previous studies [76, 78, 80]. It should be considered that a cooling rate of thin specimens is higher than that of thicker specimens [203].

On the other hand, present results show that not only the thickness of  $\alpha$  case layer but also the phase composition of the reaction layer obviously affects the surface microhardness of Ti67 castings. Furthermore, the thickness of an  $\alpha$  case layer is also dependent on investment materials [68, 73, 74]. Due to these effects, some differences are recognized between microhardness values of the samples which were cast with different investments. Chan et al. [78] claimed that the higher microhardness exhibited by the thicker plates lead to a greater penetration distance of Zr or Al and the formation of intermetallics in the  $\alpha$  case.

In the present study, it was confirmed that the  $\alpha$  case layer on titanium castings invested with Invest-Ti-T,  $\text{Al}_2\text{O}_3$ , and  $\text{ZrSiO}_4$  based investments consisted of three layers- namely, the oxide layer, the alloy layer and the hardening layer, whereby the oxide layer and alloy layer were called the reaction layer. In addition, an EDS elemental mapping analysis demonstrated that the  $\alpha$  case layer was not only composed of interstitial oxygen but also by substitutional elements dissolved from mould materials. Based on microstructural investigations, microhardness profiles and element analysis of titanium castings, it can be concluded that, the  $\text{Y}_2\text{O}_3$  based investment material provides the most reliable choice for the production of titanium castings compared to Invest-Ti-T,  $\text{Al}_2\text{O}_3$  and  $\text{ZrSiO}_4$  based investment materials and is beneficial for the casting of Ti67 because no  $\alpha$  case formation is occurring.

Sung et al. [68, 80] carried out a study on  $\text{Al}_2\text{O}_3$  investment material and divided the  $\alpha$  case into two zones: the reaction and the hardening layer. They distinguish an  $\alpha$  case formation mechanism and the  $\alpha$  case layer can be formed by not only interstitial oxygen atoms but also substitutional metal atoms which were dissolved from the investment material mold.

Guilin et al. [208] studied the reaction between titanium and  $\text{SiO}_2$ ,  $\text{Al}_2\text{O}_3$  and  $\text{MgO}$  based investments and their role in the  $\alpha$  case formation mechanisms. They characterize the reaction layer with the oxide and the alloy zone. The oxide zone also consists of cermet, a mixture of ceramic particles surrounded by metal. Furthermore, the area with increased microhardness was designated as a hardening layer [61, 80, 205]. Interstitial oxygen diffuses through the titanium lattice from the reacted investment material not only during the casting but also during the period of solidification and cooling process [201]. Therefore, the mould temperature, the casting temperature, casting volume and the cooling rate after casting are important parameters which affect the extent of surface hardening beneath the investment-casting interface [74, 76, 78, 80, 82, 85].

The oxide layer consists not only of pure oxides but also a mixture of oxides and titanium. The ceramic particles are wetted by the liquid titanium and can be penetrated by the melting titanium from the mould surface. Such a composite of oxide and titanium has been termed cermet [74, 78]. In this study, it may consist of  $\text{TiO}_2$ ,  $\text{ZrO}_2$ ,  $\text{Al}_2\text{O}_3$ , and Ti. Cruz [73] reported that Ti and its alloys are very sensitive to the ceramic mould chemical composition during investment casting. They found four types of oxide, namely  $\text{TiO}$ ,  $\text{Ti}_2\text{O}_3$ ,  $\text{Ti}_3\text{O}_5$ , and  $\text{TiO}_2$ . Lin et al. [206] also found  $\text{Ti}_3\text{O}$  and  $\text{Ti}_2\text{O}$  in the reaction layer and claimed that the titanium oxides formed in the reaction layer was  $\text{Ti}_2\text{O}$  rather than  $\text{TiO}$  because  $\text{Ti}_2\text{O}$  is more stable than  $\text{TiO}$  [207]. Watanabe et al. [72] and Guilin et al. [208] observed that a cross-section of CP Ti and Ti67 cast specimens show a three-layer structure. The outer layer was identified as  $\alpha$  case. This outer  $\alpha$  case layer is formed by a reaction between the Ti67 alloy and the Al, Si, O, and P from the investment mould material. It is known that, depending on the kind of mould material, the  $\alpha$  case layer in cast Ti structures consists of  $\text{TiO}_2$  and  $\text{Ti}_3\text{Al}$ . Guillen et al. [201] observed that a very brittle intermetallic  $\text{Ti}_3\text{Al}$  surface layer occurs during the casting process.

In previous studies [68, 80, 208], it was found that the  $\alpha$  case formation by interstitial oxygen cannot occur spontaneously. Thermodynamic calculations, which utilized the joint of army navyair force (JANAF) thermochemical tables, supported the assumption that the  $\alpha$  case is formed not only by interstitial oxygen atoms but also by substitutional atoms dissolved from mould materials. The consideration of heat capacities, enthalpies and entropies are not required to use JANAF Tables [68, 80]. From Table 9, 10, and 11 it becomes obvious that in the oxide

layer, not only oxides of titanium but also residues and reaction products of mould materials are existing. It seems that Invest-Ti-T,  $\text{Al}_2\text{O}_3$  and  $\text{ZrSiO}_4$  react with the molten titanium during the casting, while  $\text{Y}_2\text{O}_3$  does not show these changes.

In a previous study, Chan et al. [78] focused on the  $\alpha$  case formation of titanium alloys casting. They found for CP-Ti and Ti64, that the  $\alpha$  case thickness increases with increasing casting size because of decreasing cooling rates and more time for oxygen to diffuse from the surface to the interior of the casting. In another study, Boettinger et al. [76] found that the  $\alpha$  case thickness decreases with increasing cooling rate. They investigated the oxygen and hardness profiles of Ti64 cast specimens with three thickness values 6, 13 and 32 mm. The microhardness profiles for the 6 mm plate was found to be higher than that for 13 and 32 mm plates, because of slower cooling rates of the thicker plates.

The cooling rate of Ti castings also affects the penetration depth of substitution elements. An inverse proportion was reported between the cooling rate and penetration depth of substitution elements [76, 204]. Results of our study about the  $\alpha$  case formation show that in thin Ti67 castings, the  $\alpha$  case layer contains Zr, Si and Al. However, the penetration depth of these elements is smaller than in thick samples. In addition, the hardness of the oxide layer increased with a rising amount of ceramic content in the composite. Sung et al. [80] observed that thick Ti castings, depending on the mould materials, contain Zr and Al in addition to oxygen in the  $\alpha$  case, due to a slow cooling rate and more time for diffusion of Zr and Al into Ti during the reaction between molten Ti and the mould. The hardness of the  $\alpha$  case can increase with the formation of Zr- and Al- based intermetallics above that of an  $\alpha$  case with oxygen only [80, 81, 201, 206, 208]. Chan et al. [78] and Boettinger et al. [76] claimed that the higher microhardness exhibited by the thicker plates is caused by a greater penetration depth of Zr or Al and the formation of intermetallics in the  $\alpha$  case.

On the other hand, the heat transfer coefficient, the heat capacity of the investment material and possible reactions in the investments have an important effect on the cooling rate [208]. Due to these effects, some differences are recognized between microhardness values of the samples which were cast with different investments.

## 5.2 Effect of the $\alpha$ Case Layer on Mechanical Properties

The present study also summarizes the experimental results on the effects of the  $\alpha$  case layer on the mechanical behavior of Ti67 castings. Monotonic and cyclic three-point bending test were applied to the rectangular plate specimens. Additionally, the surface roughness was

investigated as a potential cause for reduced fatigue life. Furthermore, the fractured surfaces were examined by SEM.

In previous studies [82, 209], the most dramatic effect of  $\alpha$  case and interstitial contamination can be seen in correlation with the high cycle fatigue properties. It has been known that titanium materials with  $\alpha$  case fail at less than half of the life of titanium material without  $\alpha$  case. Furthermore, the  $\alpha$  case layer is an important limitation to the production of prostheses such as crowns and bridges because it reduces the elongation and fatigue limit of removable partial denture frames and clasps. Kikuchi et al. [203] investigated wedge-shaped casting specimens and observed that the  $\alpha$  case thickness increases with increasing wedge thickness. The  $\alpha$  case layer could result in premature failure because of brittleness. Furthermore, it makes final machining more difficult, which is necessary to remove the oxygen-enriched layer. The hardening effect should be considered in the design process. Therefore an aim of this study was the elimination of the  $\alpha$  case to improve the ductility of the samples.

On the other hand [210], a hardened surface layer of optimized thickness may increase wear and fatigue resistance. Carburizing and nitriding are widely used to create hard surfaces for improving wear and fatigue resistance in industrial machineries. In a theoretical analysis, Chan et al. [78] found out that an  $\alpha$  case with a thickness range of 10-30  $\mu\text{m}$  may provide adequate tensile ductility (plastic strain at fracture) and wear resistance in both CP-Ti and  $\alpha+\beta$  Ti alloy castings. The benefit is reduced quickly for thickness values greater than 50  $\mu\text{m}$ . Because of these opposite effects, the  $\alpha$  case with suitable thickness can be used in order to achieve durability of Ti casting [78, 207, 210]. Atwood et al. [66] suggested that the hardening effect of the  $\alpha$  case layer caused by oxygen can be beneficial along the wear surface of casting samples.

After monotonic three-point bending tests, it was observed that increasing the thickness of the  $\alpha$  case layer ( $>15 \mu\text{m}$ ) decreased the elastic modulus, flexural stress and elongation of Ti67 castings. This can be associated with the increasing of the hardness value on the  $\alpha$  case layer forming on casting surface and high surface roughness. For specimens with a thick  $\alpha$  case ( $>15\mu\text{m}$ ), a 15% reduction was obtained in the flexural stress compared to specimens without an  $\alpha$  case. On the other hand, the flexural stress increased by 25% for specimens with a thin  $\alpha$  case ( $<15 \mu\text{m}$ ), and no significant decline was observed in elongation. Moreover, the highest elastic modulus value was calculated for a thin  $\alpha$  case specimens. The specimens with a thin  $\alpha$  case also show better fatigue durability. In addition, the increasing of the thickness of the  $\alpha$  case layer has a negative effect on flexural strain, though no substantial differences were observed between non-  $\alpha$  case specimens and with thin  $\alpha$  case specimens

Eliopoulos et al. [81] investigated two different types of investment material. The  $\alpha$  case layer thickness was measured to extend from 50 to 80  $\mu\text{m}$  and from 15 to 20  $\mu\text{m}$  for cast samples with a phosphate-bonded silica-based investment material and with a magnesia-alumina investment, respectively. According to mechanical test results, they reported no significant difference as for the modulus of elasticity. On the other hand, the yield strength of thin  $\alpha$  case layer samples was observed to be higher than that of thick  $\alpha$  case layer samples, meanwhile the increasing of the layer thickness affected percentage elongation positively. In another study, for Ti samples with an  $\alpha$  case layer, Pitt and Ramulu [82] calculated 23% reduction for the maximum stress compared to Ti samples from which the  $\alpha$  case had been removed. Removal of the  $\alpha$  case layer restores the durability to be within 11%

The  $\alpha$  case is characterized by a change in mechanical properties towards brittle due to a change in the microstructure. The  $\alpha$  case leads to easy crack initiation and propagation during mechanical loading and will change the mechanical properties of the surface of titanium castings. The brittle intermetallic layer promotes micro-crack formation and micro-cracks easily occur with increasing intensity of the interstitial contamination. Chan et al. [78] investigated the crack depth of CP Ti and Ti64 casting samples after tensile test to calculate tensile ductility. They found out that the crack depth was about 0.84 to 0.93 of the  $\alpha$  case thickness for CP-Ti and Ti64, respectively along the gage length of a CP-Ti tensile specimen after fracture. For modeling of  $\alpha$  case effects on the mechanical properties of titanium alloy castings they used 0.9 as a constant to relate between crack depth and  $\alpha$  case thickness. ( $a = 0.9 t_\alpha$ ;  $a$  = crack depth,  $t_\alpha$  =  $\alpha$  case thickness). In this study, after a monotonic three-point bending test numerous micro-cracks were determined on the specimen surfaces. These micro-cracks nucleated in the  $\alpha$  case on the sample surface along the perpendicular to the tensile loading axis of a Ti67 samples. For thick  $\alpha$  case specimens, the mean crack depth was  $23 \pm 5 \mu\text{m}$ . For comparison, an average crack depth of  $11 \pm 3 \mu\text{m}$  was obtained for thin  $\alpha$  case specimens. These results correspond with previous thickness constant assumptions.

According to EDS line scan analysis, the oxygen concentration is higher near the surface of the cast Ti samples than in the central region of samples and the oxygen concentration measurements show perfect agreement with the distribution of Vickers hardness. The oxygen content on the casting surface with an  $\alpha$  case layer was between  $1.5 \pm 0.3$  and  $4.9 \pm 0.7 \text{ wt } \%$ .

In a previous study, Kikuchi et al. [203] reported a similar oxygen distribution on the cast Ti samples and the same relationship between oxygen concentration and hardness value. Boettinger et al. [76] detected the oxygen content on the titanium casting surfaces, which were

fabricated with the  $ZrO_2$  investment, between 5 and 9.5 wt % and measured no more than 0.02 wt % above the level of oxygen in the bulk alloy at the limit of the  $\alpha$  case region.

Chan et al. [78] have reported a linear dependency between microhardness and oxygen concentration. Their model prediction and experimental data show that the oxygen content and the hardness value are considerably decreased and the local ductility is not significantly reduced at a distance of  $0.9 t_\alpha$  below the surface. They found that the oxygen content and the penetration depth of oxygen diffusion during casting determines the  $\alpha$  case hardness on the thin Ti samples. By contrast, according to experimental study results, Bumps et al. found a parabolic relationship. In another study, Atwood et al. [66] found that the depth of the reaction layer and the proportion of intermetallic precipitation depends on the oxygen concentration. The depth of  $\alpha$  case formation significantly increases, thereby increasing the oxygen pickup. This is due to the fact that, oxygen pick-up during casting results in a surface structure composed predominantly of  $\alpha$  phase.

Apart from the metallographic structure, the mould temperature affects the mechanical properties of cast titanium. This is one of the most important factors for durability of titanium castings, even more important than the mould composition. It has been reported that if casting is carried out at lower temperature, the fatigue characteristics of titanium castings can improve. Furthermore, high temperature casting results in an increase of thickness of the  $\alpha$  case layer and hardness of the casting surface [202, 205]. Therefore, in our study, the temperature of molten titanium and the moulds was constant for the sample production in order to not changing its influence on all Ti67 casting specimens.

Previous studies [66, 68, 70, 78, 80, 201, 203] have pointed out that titanium alloys are very sensitive to surface defects and flaws, including surface roughness, which can cause crack initiation. Moreover, surface roughness is a potential cause for reduced fatigue life. The surface roughness values of  $ZrO_2$  and  $Al_2O_3$  investment cast samples were nearly the same. Conversely, for casting with Invest-Ti T investment material, approximately a two times higher  $R_a$  value and a nearly three times higher  $R_z$  value were measured in comparison with  $Y_2O_3$  investment casted samples. In addition, the highest surface roughness values were measured for the specimen with a thick  $\alpha$  case layer sample, and these values decreased with decreasing  $\alpha$  case thickness. The lowest roughness values were obtained for the specimens without  $\alpha$  case, while there were no significant differences in surface roughness between the specimens with a thin  $\alpha$  case layer and without  $\alpha$  case specimens. It can be claimed that the surface roughness is enhanced with increasing thickness of the  $\alpha$  case layer. It is very probable that increased roughness also contributed to reduction in elongation values during mechanical tests.

In fact, smooth fracture has been observed near the cast surfaces of all specimens after both monotonic and cyclic tests. However, dimples were observed in the interior region on fracture surfaces of monotonic test specimens. These fracture modes can be explained by the brittle fracture of titanium in the outer region and ductile fracture in the interior region. Watanabe et al. [72] reported a similar fracture behavior of a cast titanium sample with an  $\alpha$  case. The sensitivity of titanium to oxygen dissolved in the lattice was recognized as a potential reason for cleavage fracture mode near the surface. Furthermore, the shape of the microhardness profiles gave hints for these fractures.

### 5.3 Effect of Heat Treatment on the Cast Ti67 Specimens

The mechanical properties of the titanium alloys, such as strength, ductility, toughness, fatigue and crack propagation resistance, are strongly dependent on the microstructure of the material and this dependence should be taken into account for the efficient processing of cast Ti67. The microstructure can be controlled by using a suitable heat treatment. In this manner, the balance of strength, ductility, elongation and fatigue strength and some other mechanical properties can be controlled. In all these respects, an understanding of the phase transformations during thermomechanical processing is essential for achieving the optimal mechanical performance of  $\alpha+\beta$  titanium alloys [50, 54, 211, 212]. The heat treatment processes are designed with reference to some point of above and below the  $\beta$ -transus, which is why the determination of the  $\beta$ -transus temperature plays a key role in the evolution of microstructures in titanium alloys.

In this study, dilatometry was used to determine the critical  $\beta$ -transus temperature. The evolution of transformation was monitored through using a real-time dilatometric curve, which presents the specimen's change in volume during heating and cooling. It should be noted that on pure Ti, the  $\beta$ -transus occurs at 882 °C. Our results indicated that addition of alloying elements increased the  $\beta$ -transus temperature in Ti67 to a temperature between 980 and 990 °C. DSC (Differential Scanning Calorimetry) measurements, applied by our project partner RWTH Aachen, supported these results. According to DSC results, the  $\beta$ -transus temperature ranges from 974 to 985 °C [185].

The  $\alpha$  to  $\beta$  transformation temperature of pure titanium either increases or decreases depending on the nature of the alloying elements. The addition of  $\alpha$  stabilizers raises the  $\beta$ -transus temperature of the alloy so that the  $\alpha$  phase is stable at higher temperatures with

increasing solute content, while elements that stabilize that  $\beta$  phase depress the  $\beta$  transus temperature. [50, 213]

On the other hand, some of the elements can be classified as a neutral (such as Sn Zirconium), because they neither raise nor lower the  $\beta$ -transus when present in titanium alloys.  $\beta$  stabilizers lower the  $\beta$ -transus temperature by making the  $\beta$  phase stable at lower temperatures. Furthermore, the  $\beta$ -transus can be lowered to room temperature by adding enough concentration of these elements to the matrix of a titanium alloy [50, 213- 215].

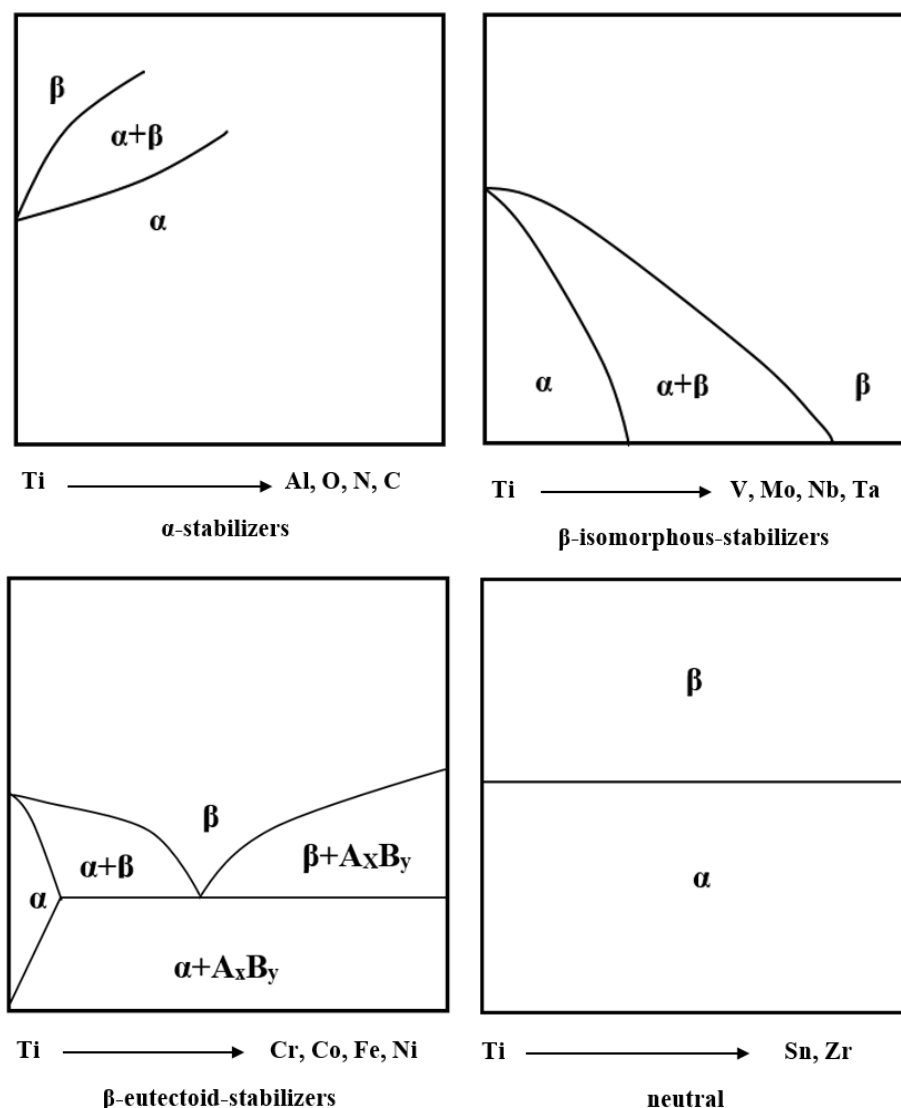


**Figure 89.** Effects on beta transus temperature of titanium alloys with the addition of  $\alpha$  and  $\beta$  stabilizers [215].

The addition of different  $\alpha$  and  $\beta$  stabilizers has a different effect on the  $\beta$ -transus temperature which is illustrated in Figure 89 by four phase diagrams. Isomorphous  $\beta$  stabilizers consisting of vanadium, molybdenum, niobium, tantalum, and rhenium, are entirely soluble in

the  $\beta$  phase, whereas eutectoid  $\beta$  stabilizers such as iron, chromium, and silicon form eutectoid systems with titanium.

On the other hand, because of its large solubilities in both the  $\alpha$  and  $\beta$  phases, aluminum is the most widely used alloying element in titanium alloys to raise the transition temperature. Some other  $\alpha$  stabilizers include B, Ga, Ge which have much lower solid solubilities as compared to aluminum, and none of these elements is used commonly as an alloying element [50]

A sensitivity of dilatometry measurement is associated with certain heating and cooling rates. At higher heating rates, the change in sample expansion is difficult to observe [216]. The cooling rate and the heating rate have a similar crucial effect on the dilatometry technique [217].

The morphology of particular phases has a distinctive effect on mechanical properties of two  $\alpha+\beta$  titanium alloys. It is known that depending on the heat treatment history, several  $\alpha$  morphologies may emerge. Each microstructure has different effects on the mechanical properties of titanium. For instance, good strength is obtained from a fine equiaxed, and because of grain refinement and increased dislocation density, martensitic microstructure increases the strength [50, 218].

Previous studies [7, 12, 50, 219] have shown that coarse lamellar structures offer soft, ductile properties, whereas the greatest ductility is seen in large equiaxed  $\alpha$  grains. On the other hand, the best combination of tensile properties can be attained by a bimodal distribution of equiaxed and lamellar structures.

It has been demonstrated that tensile strength and elongation of cast Ti67 can be improved through heat treatment processing. Akahori et al. [220] combined thermochemical processing with a post heat treatment and obtained an increase by around 10 and 40 % in tensile strength and the fatigue limits of cast Ti67, respectively, as compared with those of both as-cast alloys.

The volume fraction of each phase,  $\alpha$  lath thickness and the diameter of its colonies have the most significant influence [12, 193, 195, 197-199]. Akahori et al. [220] found that increasing the volume fraction in the primary  $\alpha$  phase had a positive influence on the short fatigue crack propagation resistance. In this way, the fatigue life of Ti67 alloy increases.

The cooling rate after solutionizing is a crucial parameter, and when it is increased, fatigue strength is increased as well [7, 50, 221-225]. The slowing down of cooling rates results in an increase of not only the thickness of the individual  $\alpha$  phase lamellae, but also in the size of the colonies of parallel  $\alpha$  lamellae. As a result, the yield stress and tensile strength of the alloys decline. If the microstructure contains too large  $\alpha$  phase lamellae, their colonies behave as a singular element, and thin layers of  $\beta$  phase cannot absorb large amounts of energy and prevent

the crack propagation [12, 50, 224-226]. In addition, Lütjering [227] reported that the yield strength and HCF strength can be improved by decreasing the  $\alpha$  colony size, which depends on the cooling rate from the  $\beta$  phase field.

In the light of these findings, the influence of different heat treatment conditions on the mechanical behavior was evaluated by Vickers hardness measurements and microscopic investigations. In conclusion, the optimum results were obtained from the solution treatment at 1050 °C with water cooling and 4h aging at 550 °C. In the literature, some studies examined the effect of heat treatment thanks to monotonic and cyclic mechanical tests, and reported an improvement of strength, ductility, fatigue life and fracture toughness when they selected the similar heat treatment conditions with our results. Moreover, it was emphasized that the selection of the correct combination of aging temperature and time is essential in order to optimize strength and ductility combination in titanium alloys.

Equation (25) has been widely used to state the relationship between the hardness HV and yield strength  $\sigma_y$ , approximately [225].

$$HV \approx 3 \cdot \sigma_y \quad (25)$$

On the other hand, the grain size, grain shape, and their arrangements influence the mechanical behavior. According to the Hall-Petch relationship, which is given by Equation (26) (where  $\sigma_y$  represents the yield strength,  $d$  is the grain diameter, and  $\sigma_0$  is the friction stress below which dislocations will not move in a single crystal, and  $k_y$  is the Hall-Petch coefficient), the yield strength is inversely proportional to the square root of the grain diameter. The small grain sizes improve the yield strength due to inhibiting the movement of dislocations during deformation.

$$\sigma_y = \sigma_0 + \frac{k_y}{\sqrt{d}} \quad (26)$$

#### 5.4 Mechanical Properties of the Cast Ti67 Sponges

The mechanical properties of open cell metallic foams depend strongly on the properties of the foam struts [18, 57, 133, 134, 228]. For example, the plastic collapse strength of a foam is a function of the strut yield strength, as well as its relative density. In Chapter 2, the strong relation between foam strength and strut strengths was explained with Equation (14). The

measurement of mechanical properties of individual cell strut can be helpful for the prediction of foam strength [228].

In this study, the maximum bending stress of cell struts was measured and for this purpose, a special compression bending system was designed. Bending tests were performed on struts in the as-fabricated and heat treated conditions. The bending behavior of the cell struts showed a similar brittle behavior of the Ti67 sponges. The fracture surface investigation supports the brittle behavior of the Ti67 sponge. Furthermore, an improving effect of heat treatment on the bending stress was obtained.

Ohrndorf et al. [228] evaluated the relationship between the cell strut properties and the mechanical behavior of metallic foams by using both monotonic and cyclic mechanical tests. The ductility of cell strut materials affects not only the tension behavior but also the compression behavior of metallic foams. An increase in ductility results in strongly plastically deformed cells. The stress plateau region in the stress-strain curve corresponds to the cell strut ductility, as well as to the homogeneity of the cell structure. In case of fatigue behavior, the formation of a macroscopic fatigue crack occurs as a result of the fatigue cracking of cell struts.

Zhou et al. [229] investigated the cell strut mechanical properties of aluminum foams by using a micro tensile technique. They evaluated the heat treatment effects by comparing the strut strength with the bulk aluminum subjected to the same heat treatment conditions. The annealing process or the strengthening was applied on the as-fabricated foams. They observed that annealing reduces the strut strength, but improves the strut ductility. In the case of the strengthening process (solution treatment + WQ + ageing), struts had significantly higher UTS (ultimate tensile strength) but strengthening is not associated with degradation in strut ductility.

Generally, the nominal strengths of the corresponding bulk alloys from which foams are fabricated is used to estimate the foam strength. However, previous studies [228, 229] demonstrated that the strength of struts can be notably different from bulk materials. For instance, Zhou et al. [229] reported that a significantly greater strut tensile strength and ductility was measured for heat treated open cell foam, compared to those of the corresponding bulk alloy subjected to the same heat treatment conditions. The cell struts have a different microstructure and composition from bulk materials because of the fabrication method.

An accurate prediction of the foam strength is required in the case of directly measured mechanical properties of an individual strut. Only a limited number of struts were tested in this study. Therefore, multiple tests are needed in a future study to provide a statistical understanding of the mechanical behavior of individual struts in open cell foams. Furthermore, bending tests on single struts may provide more information to assist in the understanding of

foam deformation in comparison with tensile test. Because the deformation of struts is mostly caused by compression or bending. Deformation occurs on numerous struts, and deformation of these struts would affect each other. Thus, the difficulty of bending tests is how to mimic real boundary conditions of foam struts during deformation.

### **5.5 Properties of CaTiO<sub>3</sub> Reaction Layer on the Cast Ti67 Implants**

In the framework of this project, the suitable application methods were analyzed for the coating of the cast Ti67 implants with the reaction layer, and the biocompatibility properties of a new implant material were examined in detail by using *in vivo* and *in vitro* tests. Animal models were used to investigate bone-implant fixation experimentally. Therefore, the effect of the porous structure of implants by bone ingrowth and the influence of bioactive coatings in the osseointegration process were evaluated.

Several types of biological surface treatment were applied on the test implants, with the aim of providing an accelerated and enduring bone integration. In this project, the chemical conversion of the naturally existing TiO<sub>2</sub> surface layer into CaTiO<sub>3</sub> was chosen as a coating technique in order to exclude the risk of loosening or flaking of surface coatings from the implant body [103]. Even though, beneficial effects of CaTiO<sub>3</sub> coating on the bone regeneration and the primary stabilization of the implant have been proven in the literature [95, 98, 230], no remarkable improvement was observed in bone fixation and in biomechanical properties of the bone-implant interface. According to the experimental push-out test results, it was reported that slightly better biomechanical results were obtained for the coated rat implants compared to those of the uncoated rat implants. On the other hand, for sheep implants, coated and uncoated implants show nearly similar push-out values [184]. Even though SEM analysis exhibited a higher amount of bone tissue bonded to the implant surface in comparison with the uncoated implants, it cannot be claimed that the CaTiO<sub>3</sub> coating has a strong influence on the osseointegration and the bone ingrowth [184]. Furthermore, there were no significant differences in surface roughness measured among the coated and uncoated implants.

Some potential sources for this observation were identified. First of all, the pickling process, applied on the uncoated implant surface in this project, may have a positive effect on bone-implant fixation. The general opinion is that a rougher implant surface can stimulate differentiation, growth and attachment of bone cells, and increases mineralization. Furthermore a rougher implant surface can induce faster bone integration and accomplished fixation. On the other hand, in some previous studies [66, 88-90] machined or etched titanium surfaces were suggested for good bone-implant contact. Etching of titanium in concentrated acid [88-90, 139,

231-234] is another attractive method for modifying the surface of titanium for biological applications, and various acids have been used to modify the titanium [231-233]. It has been reported that, in comparison with machined surfaces, etched surfaces lead to more bone apposition and enhance the interfacial strength as measured by various biomechanical tests [88-90, 139, 234, 235]. Roughening prior to etching, acid mixture, bath temperature, and etching time are the main parameters determining the topography of etched implants. It is known that the bone-implant interface strength increases in relation to the increase of the bone-implant contact. In a rabbit study by Baker et al. [232], a dual acid etched implant showed a higher degree of bone-implant contact than the machined, titanium plasma sprayed, and blasted implant surface in early time periods. It has been demonstrated that a minimum of 50% bone-implant contact is necessary for long term success of the implant [103]. In another study, Severson et al. [233] found that dual acid etched implants had met this criterion four weeks after implantation. This might be explained by an increased cellular proliferation in a shorter period of time [95, 234]. Yet, there was no specific relationship between bone quality and reduced implant success observed for the dual acid etched implants. In another study by Zhang et al. [235], an  $H_2O_2/HCl$  etched titanium surface without subsequent heat treatment was recommended in order to improve osseointegration response. Furthermore, the acid etching treatment of sandblasted surfaces had beneficial effects on bone formation around the Ti implant [98, 234, 235].

The insufficient healing time can be the second reason. The push-out test were carried out followed by a healing time of four and 24 weeks for rats and sheep, respectively. Haenle et al. [103] compared  $CaTiO_3$  coated titanium implants with an untreated sample at three different healing times. They reported an increase of the pull-out forces for untreated and treated implants with longer healing. However, no significant difference between treated and untreated implants could be observed after four weeks. On the other hand, after 12 weeks, a significantly higher pull-out force was measured for the treated implants, whereas the pull-out forces for treated and untreated implants became equal again after 36 weeks. Hayashi et al. [236] and Renz et al. [237] demonstrated that four weeks are insufficient to determine achievement of surface modification on osseointegration. Beneficial effects of  $CaTiO_3$  coating may be appear after a longer healing time.

As a third aspect, the thickness and morphology of the coatings are determinative to the effect of the bioactive coating on the bone osseointegration. The optimum thickness of the coating should be obtained by using a set of experimental conditions. For example, the HA coating is insufficient to clinical application, if the thickness of coating is  $>150 \mu m$ . The

optimum range was obtained for thicknesses at 60 to 120  $\mu\text{m}$ . The thickness of coating and/or morphology of coated surface are decisive [95, 230].

Shear strength of the bone-implant interface and the success of implants also depends on surface characteristics such as roughness. It can be expected that rough surfaces increase the contact area between implant and bone, and thus improve the bone osseointegration. Renz et al. [237] reported that the ultimate stress on the bone-implant interface changes by the different surface roughness and  $R_a=0.53 \mu\text{m}$  was obtained as an optimum roughness value for the best condition for the tissue formation. Hayashi et al. [236], considered that there was no influence of the surface roughness on the shear strength of the implants in the range of  $R_a=1-8 \mu\text{m}$ . In another study three different surface morphologies with different roughness properties were evaluated by Kim et al. [238]. Although they observed the highest bone to implant contact ratio for the roughest surface, the difference between that and the smooth surface was not remarkable. In the present study, there were no significant differences in surface roughness measured among the coated and uncoated implants.

### **5.6 Finite Element Analysis of Biomechanical Push-Out Tests of Porous Ti67 Implants**

A wide range of biomechanical tests are carried out for the examination of mechanical properties at the bone-implant interface [139]. In this study, the biomechanical behavior of the bone-implant interface was evaluated by using push-out tests. Owing to the relative simplicity of the test procedure, push-out tests are one of the most common methods to measure the shear strength of the bone-implant interface. The push-out test requires only a uniaxial material testing machine and a simple support jig to displacement control [139,184]. This test allows an accurate analysis of the shear strength without the interference of the tensile component and permits a more reliable stress analysis generated at the bone-implant interface [139].

In order to evaluate the behavior of the cast Ti67 implants in small and big animals, rats and sheep were chosen, respectively. Rat and sheep bones have been widely used as a model for human bone for *in vivo* tests. Morphological similarities between sheep and human bone has been reported and the distal femoral metaphysis of sheep is suggested as a good model for the examination of bone implants [138]. Easy and safe handling, availability issues and the low cost of acquisition make laboratory rats preferable for small animal experiments.

Investigation of the mechanical responses in bone and their relation to different parameters of implant and bone is important for understanding the success of implantation. Yet, clinical observations and experimental studies are not adequate to evaluate biomechanical aspects

because of limited information and sample variations. A computer-based numerical simulation technique, namely the FEA, has begun to be an alternative to *in vivo* tests. FEA has much potential in addressing questions of biomechanical applications [19].

Despite of the consideration of some axisymmetric or bidimensional simplified models in previous studies, studies [154,166, 167, 189, 239] suggest a 3D simulation in order to get more realistic results. A more detailed modeling of bone and implant, as well as suitable boundary conditions, do not affect the local stress distribution at the bone-implant interface.

In this study, the 2D model and 3D models of the designed implants and surrounding bones were constructed and the FE analyses were carried out in order to evaluate the biomechanical success of Ti67 bone implants. The mechanical properties of bone-implant interface and the stress/strain distributions in the bone were analyzed using three different FE models and their predictions were compared with measured results [240]. Not only all critical dimensional parameters which are crucial in order to set up realistic bone models but also the anisotropy of bone were measured directly from rat and sheep bone.

To reach good levels of accuracy, a contact non linearity of the bone-implant interface should be taken into account for the FEA [166-168, 170]. Although in many previous studies [159, 170, 176, 179] a node to node contact approach has been used, in the case of the large sliding situation node to face or face to face contact definitions were considered to be more accurate [155, 162, 165-167, 169]. In addition to the material properties and the coefficients of friction, it is necessary to define several numerical parameters, such as contact stiffness and, convergence tolerance. However, these parameters cannot be determined experimentally. Convergence tolerance is the most sensitive parameter and has a notable effect on the accuracy of the FEA [160]. In this study, a FE model was fully qualified. For this purpose, the levels of mesh refinement and convergence tolerance were determined on the basis of multiple exploratory runs. Previous independent experiments and studies were used as a reference to obtain physical parameters [157, 168-173, 175].

In the literature a few researchers [168, 170, 182] used an interference fit calculation to simulate the contact behavior of bone interface. However, the critical interface should be obtained carefully according to detailed experimental measurements for interference calculation. Before and after the push-out test, the diameter of bone holes was not measured. For this reason, in our FEAs, the hole diameters were assumed to be constant (for rat and sheep) and contact bodies were defined as not being of penetrating character. Because of glue contact and separation, the close nodes appear and each contact node is checked to see whether it is near a contact segment. In some cases, this allowed a contact body to contact itself. Entering a

bias factor is crucial in order to avoid this problem. The recommended value for the bias factor ranges from 0.0 and 0.99. In this study the value of 0.9 was entered for all 2D and 3D simulations.

A critical combination of normal and shear stress values of the interface was explained in MSC Marc by using Equation (23). with the following mathematical equation [241]:

$$\left(\frac{\sigma_n}{S_n}\right)^2 + \left(\frac{\sigma_t}{S_t}\right)^2 > 1 \quad (27)$$

In this study, the breaking up of the glued connection was determined by using a stress criterion according to Equation (27). The glue contact release occurred when this contact criterion was fulfilled at a node.

The first aim of the FEA was to determine how well stiffness and strength of bone-implant constructs can be determined from three different FE models. FE models of the same bone-implant constructs were built and solved. FE calculated maximum push-out force and push-out strength correlated highly with the experimentally measured values ( $r^2$  is ranging between 0.72 and 0.78) thereby statistically supporting the FE approach.  $S_n$  and  $S_t$  are user-defined parameters.  $S_t$  is obtained from FE results which were illustrated in Figure 77 and 82, and  $S_n$  values were defined from previous studies [195-198, 243-246]. They were given with the user subroutine. After the releasing of a node due to breaking glue, its status changes from being glued to touching contact and friction and start the sliding.

Bone-implant interaction involves frictional phenomena and it is not applicable to ignore the frictional effects. Better definition of frictional contact approach leads to closer results to the realistic situation. Huang et al. [154] found out that increasing the value of the frictional coefficient of the bone interface may be beneficial in enhancing the implant stability and success of osseointegration. Furthermore, decreasing the micromotion between bone and implant improves the peak stress at the surrounding bone [218].

Recent studies [165, 241] have indicated that the assumption of a fully bonded interface entails attention to frictional phenomena. Interlocking between implant and trabecular bone dominates the friction at the bone-implant interface. The effect of the friction has been evaluated in several previous studies [139, 140, 142]. Two different assumptions have been widely used: some researchers considered the same friction coefficient for implant-cortical bone and implant- cancellous bone [139, 148, 154, 160], whereas different friction coefficients were defined for the contact of implants with two different bones of other studies [139, 160,

181, 190, 193, 246]. When the common friction coefficient is applied, the cortical bone stress increases corresponding to the increase of the friction coefficient, meanwhile the cancellous bone stress decreases. The second assumption provided more elaborate results. Increasing the friction coefficient of cancellous bone resulted in a decrease of stress in both bones. On the other hand, if the cortical bone friction coefficient increases, the stress of the cortical bone increases whereas the cancellous bone stress decreases. It was concluded that changing the cancellous bone friction coefficient has more significant effect on the stress value and stress distribution [245].

During a push-out test, the horizontal displacement is resisted by a frictional force between the specimen and bone. In our study, the friction phenomena between implant and bone was not examined experimentally and the friction coefficients were not measured during the original experiments. Therefore, initially the friction coefficients for implant-cortical bone and implant-cancellous bone were determined according to previous studies [148, 151, 193], then sensitivity analysis were carried out in order to improve the accuracy of the simulation. For this aim, initial stability specimens were used as a reference and simulation results were compared with measured results for these specimens. Two different friction coefficient assumptions were chosen for FEA and the friction coefficients were assumed constant during simulation. A change of the friction coefficient, which occurs during the healing process, was neglected.

Helgason et al. [246] simulated the push-out test with friction coefficients ranging from 0.2 to 2.0. Higher values for the friction coefficient caused a difference of almost 10% in slope and maximum push-out force compared to using the selected value. Even if it was not higher than 5%, the same differences were observed in this study. This may result from the assumed constant friction coefficient. Accuracy of simulation results may be increased by applying a denser meshing process. However, it has been reported that this might only result in less than a 2% change in slope and peak force. When inner region of bone is subjected to high stress magnitude where it is closer to implant, stress magnitude decrease towards the outer region of bone [176-181, 246].

Surface roughness is also an essential parameter of a complex friction phenomenon. Whereas roughening the implant surface could diminish the interface sliding, long or wide implants cannot reduce the sliding between implant and bone [106-107]. According to LSM measurements, there was no big difference in surface roughness between coated and uncoated samples, which is why the roughness effect was not taken into account in the definition of friction.

The FE software Marc offers two idealistic concepts for the modeling of friction: the shear friction model and the Coulomb friction model. The second model has been widely used not only for bone-implant interface simulation but also in various engineering applications.

Coulomb 's law states that [241]

$$\|\sigma_t\| < \mu\sigma_n \text{ (stick) and } \sigma_t = -\mu\sigma_n \cdot t \text{ (slip)} \quad (28)$$

where  $\sigma_t$  is the tangential (friction) stress,  $\sigma_n$  is the normal stress,  $\mu$  is the friction coefficient and  $t$  is the tangential vector in the direction of the relative velocity.  $t$  is associated with the relative sliding velocity by

$$t = \frac{v_r}{\|v_r\|}, v_r \text{ is the relative sliding velocity}$$

In this study, the sliding velocity was used as a constant parameter and the increase of sliding velocity associated with magnitude of the frictional coefficient was ignored.

Correspondingly, the Coulomb's model which is outlined in Figure 90 a), can be written by using nodal forces [241] with

$$\|f_t\| < \mu f_n \text{ (stick) and } f_t = -\mu f_n \cdot t \text{ (slip)} \quad (29)$$

where  $f_t$  is the tangential (friction) force and  $f_n$  is the normal force. When the tangential stress is smaller than critical stress, no relative motion occurs [241].

Because of discontinuity in the friction value, some numerical difficulties may easily occur, which can be minimized through the implementation of arctangent model approximations of the step function. A graphical representation of the arctangent model is illustrated in Figure 90 b).

The correlation rate of rat implants simulation with measured results is higher than that of sheep implants simulation with measured results. This can be explained by the fact that increasing the normal force and stress decreases the correlation rate of the Coulomb friction model with experimental observations.

In the FE models used in this study, a small element edge length was used. It was as small as a fraction of a millimeter. It was assumed that the same average behavior of bone applies to

all elements. However, at this scale, cancellous bone shows in reality an inhomogeneous behavior.

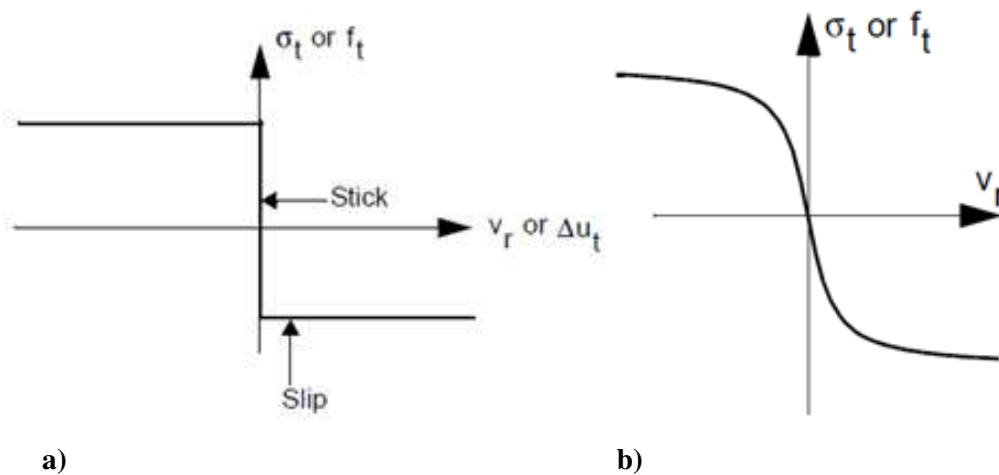


**Figure 90.** a) Coulomb friction model b) arctangent model [241].

2D models did not include the heterogeneous cellular structure of bone. Hence, the porous structure of cancellous bone could not be modeled in a two dimensional model. On the other hand, 3D models were created by taking into consideration the different characteristics of cortical bone and cancellous bone. It was assumed that both kind of bone were isotropic, homogeneous, and linearly elastic. Using such 3D models, it was possible to investigate the stress around the implant in a more detailed manner. Sufficient data concerning the formation of bone at the implant-tissue interface is still unavailable. Initial stability and bone ingrowth are influenced by biological as well as mechanical factors. For this reason, experimental validation of numerical models is difficult [16-18,129, 238, 247, 248].

High correlations were found between push-out strength as simulated from all three FE models and the experimentally measured push-out strength. When 2D predicted push-out strength correlated well to measured strength, the 2D predicted stiffness did not show the same high correlation to measured stiffness. A neglect of the cellular microstructure of cancellous bone can be a potential reason for this behavior. Bulk material assumption restricted the elastic behavior of cortical and cancellous bone and enhanced the influence of friction. Furthermore, in this study, the identical bone properties were assumed for all rat and sheep bones, whereas the actual material properties may have varied from bone to bone. For example, the usage of different bone elastic moduli would have changed the absolute values for bone-implant stiffness. However, it could not have had a significant effect on the correlation between experimentally determined stiffness and stiffness as derived from FEA.

The difference in interface shear strength and the error bars on the load displacement curves can be explained by the different degree of bone-implant contact. For 2D models, the ratio between the simulated shear stiffness and shear strength is higher than the same ratio for measured values, while for 3D models no remarkable differences were observed for the ratio between simulation and experimental results.

Successful implant osseointegration can be defined by measuring implant stability. While the mechanical engagement of an implant with surrounding bone is designated as the primary stability, regeneration and remodeling of bone refers to the secondary stability. The primary stability of an implant is positively related with a secondary stability. The accomplishment of primary stability is affected by various factors like the density and quality of the bone surrounding the implant, the implant design, and surgical techniques used [39, 153, 247].

It has been reported that implant dimensions play a critical role in the bone stress and it can be reduced by an average of 20% by increasing the length or diameter of implants [249]. Girón [184] observed some irregularities in shape and surface for the rat implants and reported a difference of nearly 6.7% of implant diameter. Dimensional differences were also observed on implant length.

Baggi et al. [250] demonstrated that the implant length affects stress values and distribution at the cancellous bone-implant interface, while the stress peak at the cortical bone is influenced by the implant diameter. The implant length was designated as a more effective parameter than implant diameter for implant design. Figure 91. shows clearly that the top surface of the implant is not smooth and during push-out tests, the indenter contacted with this rough surface.



**Figure 91.** Implant length difference.

This roughness affects the displacement on the force-displacement curve. To simulate this effect in the FE model, the tops of the rat and sheep implants were positioned 0.1 mm and 0.3

mm above the cortical bone. Furthermore, the dimensions of implants were also assumed to be constant.

The stiffness of the implant in the surrounding bone tissue is the main factor determining implant stability. The bone and implant stiffness should be taken into account as well as the stiffness of the implant bone interface [182, 184, 249].

The importance of initial bone quantity and quality has been indicated in the literature and poorness of these factors was reported as the main risk factor for implant failure, owing to excessive bone resorption and impairment in the healing process [9, 28, 74, 183].

In the case of the primary stability of implants in low density bone, surgical techniques and roughness of implant surface are distinctive factors. Rao and Gill [251] suggested that the undersized drilling technique, i.e., a smaller drill diameter than the implant diameter, should be chosen in order to optimize local bone density and improve the primary stability.

Because of manual implantation, the implants were found at varied position of the distal femoral metaphysis. It can result in some differences in the amount of cancellous bone surrounding the implants (bone quality, initial stability). Furthermore, Girón [184] reported an implant misalignment and observed that some implants lost their initial position. They were positioned below the cortical bone, having no contact with the cortical bone. In this instance it can be a possible explanation that there has been some slipping between the implant and the surrounding bone because of early loading which was applied during the healing period from implantation to bone fixation. It may be the reason for very low peak force values, which were observed in the load displacement curve for one sample from each group of sheep implants. The experimental results from these samples were used as a reference in order to obtain initial stability and friction coefficients for both groups of sheep implants.

From the experimental literature [138-142], it appears that it is not the absence of loading per se that is critical for osseointegration, but rather the absence of excessive micromotion at the implant bone interface. Not every micromovement was detrimental to implant integration; excessive movements were deleterious. Micromovements of 50 micrometer were tolerated, and it is anticipated that micromovements up to 100 micrometer may be tolerated for implants with a bio inert surface. The tolerated micromotion threshold varies according to the surface state and/or implant design. The *in vivo* literature [141, 142] suggests that implant design, loading mode, and the prosthetic reconstruction scheme play important roles in converting mechanical stresses into micromotion at the interface. It also suggests that under optimized circumstances, involving screw type implants and splinting, a long, stress free healing period is not mandatory in the achievement of direct bone apposition. One week of delayed loading was sufficient to

achieve osseointegration in a dog mandible model involving occlusal or functional loading [138].

Although a positive influence of a well-controlled micromotion on bone formation especially in early healing periods was proven in previous studies, it was also reported that if the level of micromotions was above 100 $\mu$ m, bone formation and remodeling can be negatively affected [252].

A mechanical interaction of implant with cortical bone is crucial for the primary stability of an implant. Migliorati et al. [248] and Lian et al. [158] demonstrated a significant correlation between pull-out force and cortical bone structural parameters, such as thickness and density of cortical bone. Migliorati et al. [248] claimed that a high value of interconnection was observed on a mechanical interlock between implant and high density cortical bone. Moreover, they obtained a higher pull-out force for thicker cortical bone, and concluded that the thickness was more associated with initial stability of implants than the cortical density [184, 237]. On the other hand, the density of the cortical bone seems to be a more essential sensitive parameter for implant stability [248, 253].

The influence of test conditions on the push-out results was not evaluated in detail in this study. However, different cortical thickness was measured for each bone and used to react like realistic bone geometry. Dhert et al. [147] investigated the four parameters, (i) design of the support jig, (ii) Young's modulus of the implant, (iii) cortical thickness, and (iv) implant diameter, which can have a considerable effect on the interface stress distribution.

It was found that the occurrence of peak stresses in the interface has a strong relationship with the distance between the implant and support jig. When the hole in the support jig is slightly oversized, high stress appears at the jig edge supports the bone. A more uniform stress distribution was observed at the bone-implant interface with increasing diameter differences between bone and jig hole [138]. On the other hand Shirazi-Ad [193] recently suggested that if the bone is supported by the bone around the implant instead of the bone under the implant, a uniform stress distribution along the interface can be seen. In this study, not only around the bone but also under the bone through the orifice of the holding system platform were used to support the bone surrounded implant samples.

Range and distribution of interface stress are associated with variations of the Young's modulus of the implants. For instance, a less uniform stress distribution can be observed at the interface if the implant has a low Young's modulus [247]. As the bone implants used in this study were fabricated from the same material, this effect was not taken into consideration.

Even though the cortical thickness affected the calculated shear stiffness and strength considerably, the ratio between calculated stiffness and strength was almost constant. A reciprocal relationship between the cortical thickness and interface shear stress was indicated. On the other hand, the cortical thickness does not strongly affect the stress distribution [247].

Furthermore, another potential lack in the experimental system could have been responsible for the differences between measured and simulated stiffness, as these effects could not be simulated in the FEA [181].

Seebeck et al. [254] found out that the amount of bone in the vicinity of an implant and local bone density should be transferred in the simulation to improve the predictability of bone-implant interface biomechanics. The arrangement of the trabecular microarchitecture and microarchitectural parameters, such as trabecular thickness, are important for implant stability. It should be noted that these studies are quantitative. In the present study, a constant trabecular thickness was used for rat and sheep bones.

Bone alters its own physical properties including bone density and Young's modulus at different stages of bone remodeling in order to adapt the changing of the mechanical loading environment. The type of bone deviates mostly from the currently assumed homogeneous bone properties [147, 183, 255]. It is crucial to understand the bone remodeling process and the bone tissue implant interactions in order to optimize the bone implant design [218]. In this study, the Young's modulus of both bones were assumed as to be of a constant value. However, the relation between elasticity modulus and density of bone and the influence of Young's modulus on shear stiffness and strength has been demonstrated in the literature. The Young's modulus of bone  $E$  (MPa) was calculated as a power function of the apparent density  $\rho$  ( $\text{g/cm}^3$ ) as in Carter and Hayes [256].

Young's modulus of bone can be estimated using the Equation (30)

$$E = C\rho^3 \quad (30)$$

where  $C$  is a constant and has the value  $3790\text{e}^{0.06}$  [256].

Although push-out tests consider the primary implant stability, the micromotions of implant in surrounded bone were not taken into consideration in the FEA. Therefore, computational results could reflect the secondary stability. It is expected that larger differences in force displacement curves and in stress distribution will occur when the density and quality of surrounded bones are low.

Bone remodeling is a highly complex phenomenon and depends on various parameters. Therefore, the influence of bone remodeling on the mechanical response of the bone tissues

could not be explained in detail [158]. The bone remodeling process was not taken into consideration in the FE simulation and the effect of new bone ingrowth on shear strength could not be examined in this study. However, after push-out tests, the trabeculae were found inside the holes of the implants. This may be due to the wide sliding region on the force displacement curve after implant separation from bone. It has been demonstrated that cancellous bone is responsible for implant sliding in surrounded bone. The amount of trabeculae was not enough to increase the maximum force value. On the other hand, recent studies show a correlation between the rate of implant failure and local bone quality [181, 246, 257]. Better predictability of the force transformation through the bone microarchitecture can be provided if the changing of bone properties and bone tissue interactions are taken into account. If more realistic and physically meaningful input parameters are used, the numerical models should be capable of replicating mechanical test results with an acceptable degree of accuracy.

The possibility of using FEA to explore the elastic properties of cellular structures such as foam materials has been examined in a number of studies. For some of the elastic constants good matching was obtained [258].

A structural model of non-isotropic, open cell foams was built by using a suitable representative repeating unit cell. In terms of the cell dimensions and the physical and mechanical properties of the bulk materials, a set of equations was written for the foam density, elastic constants and strength. For instance, elongated tetrakaidecahedron was adopted to develop equations for cellular foams. A more detailed description is required for elongated unit cells. The effect of shear deformation and differences of cross-sectional area was taken in to account by Gong et al. [166, 167].

Thiyagasundaram et al. [258] used a FE model for predicting micromechanics of open cell foams with tetrakaidecahedral unit cells. The struts were modeled using beam elements. The ligaments in all models were discretized as shear deformable beams. A good agreement was obtained with available models, and it was reported that the length to thickness ratio for the struts is distinctive for the success of the prediction. In reality, cross-sectional geometries and area distributions of the struts are not uniform. The maximum value of cross-section was observed at the ends which gradually decreases and reaches the minimum value [258].

Foams with uniform cross-sections have higher Young's moduli and Poisson's ratio in comparison with varying cross-sections foams [166, 167]. In the present study, it was assumed that the unit cell edges behave like a 3D beam. An uniform circular cross-section was therefore chosen for the construction of the cell strut of the 3D model cancellous structure.

The ends of the beams overlap where beams intersect and there appears to be a number of closed faces that consist of excess solid material. Such closed faces were also seen in the architecture of cancellous bone. Gong et al. [166, 167] cut the ends of the beams with appropriately chosen smooth curved surfaces in order to remove the excess material at the nodes. This approximation was necessary to calculate the volume of solid, since it affects the mechanical properties of cellular metallic foams.

In another study, Gong et al. [166, 167] indicated that the Kelvin cell foam model with shear deformable beam is effective for predicting the elastic properties of foam and providing key geometric characteristics of real foam.

## 6 Conclusions

The aim of the our project was the development and testing of a new material concept for the realization of customized biomedical implants for the treatment of large bone defects. This dissertation presents a part of the results from the production and modification of the implant up to bone-implant interface examination through FEA.

Over the past decade, new developed and refined titanium casting technologies make it possible to produce dental and medical implants. However, many practical problems remain to be solved. Avoiding impurities and changes of the surface layer by  $\alpha$  case formation are major challenges in titanium casting, along with from layouting the running and gating system and arranging the casting parameters to achieve defect-free castings. In this context, the present results show the effect of four types of investments on the  $\alpha$  case layer of Ti67-castings.

According to microstructural investigations, microhardness profiles and element analysis, the Ti67 castings using  $Y_2O_3$  based investment materials did not show any reaction layer and a minimum in surface microhardness. In brief,  $Y_2O_3$  based investment materials are a reliable and promising choice for the production of titanium castings compared to Invest-Ti-T,  $Al_2O_3$  and  $ZrSiO_4$  based investment materials, although the processing of this material is comparatively difficult.

There have been many studies of  $\alpha$  case formation in titanium and titanium alloys castings. A major part of these studies contained microstructural characterization, EDS element mapping analysis and characterization of microhardness in the  $\alpha$  case as a function of depth from the surface [64-68, 70, 72, 76, 78-81]. Despite many comprehensive studies on the formation of the  $\alpha$  case in Ti alloys, up to now the relation of  $\alpha$  case and mechanical properties has not been explained in detail especially for thin Ti castings.

Not only the formation of  $\alpha$  case, but also the influence of the  $\alpha$  case layer on the mechanical properties of Ti67 castings were examined in the present study. In addition, the  $\alpha$  case formation mechanism was investigated through microstructure observations, hardness profiles and EDS element mapping images. Monotonic and cycling three-point bending tests were applied on the specimens in order to obtain mechanical properties. The fractured surfaces were examined by SEM. Furthermore, the surface roughness and oxygen concentration were measured using LSM and EDS line scan analysis, respectively.

It can be concluded that an  $\alpha$  case layer with a suitable thickness has a positive effect on titanium castings and can help to improve mechanical properties such as Young's modulus, flexure stress, and fatigue resistance. It was obtained that the flexural stress increased by 25%

for specimens with a thin  $\alpha$  case without any significant reduction in elongation. Another improvement observed in the Young's modulus was the fact that specimens with an  $\alpha$  case  $< 15 \mu\text{m}$  have the highest elastic modulus value (117 GPa). Moreover, the specimens with a thin  $\alpha$  case show a better fatigue durability when compared with non  $\alpha$  case specimens. In light of these results,  $15 \mu\text{m}$  was determined as a critical thickness value for an  $\alpha$  case layer. It was confirmed that the  $\alpha$  case layer with suitable thickness increased the elastic modulus and flexural stress and did not lead to any pronounced decrease in elongation of Ti67 castings.

In future studies, the  $\text{Y}_2\text{O}_3$  based investment should be compared to other investment materials like CaO and ZrO. For industrial use of the  $\text{Y}_2\text{O}_3$  investments, a big effort is required to improve the stability of the ceramic slurry and to increase the final strength. A particularly important task is to improve the connection between the front layer and backup. Future studies should also include the investigation of the influence of  $\alpha$  case thickness on the tensile properties of Ti67 castings. Thirdly, wear behavior should be analyzed in order to obtain balanced properties of high tensile ductility and minimum wear loss in Ti67 castings.

Through dilatometry, the  $\beta$ -transus temperature for Ti67 was found to be  $985 \pm 5 \text{ }^\circ\text{C}$ . However, the effect of different test parameters, such as different cooling and heating rates should be examined to enable more precise measurements.

Vickers hardness measurement and microscopic investigations were used to determine the influence of different heat treatment conditions on mechanical behavior. The effect of solution temperature, aging process and cooling rate were evaluated. In conclusion, the optimum results were obtained after the treatment at  $1050 \text{ }^\circ\text{C}/\text{WQ}$  and aging at  $550 \text{ }^\circ\text{C}$  for four hours.

In this study, the maximum bending stress of the cell struts were measured and for this purpose a special compression bending system was designed. To investigate mechanical properties of cell struts, three-point bending tests were applied on the cell struts of Ti67 sponges. A special bending system was constructed and used to test cell struts of the Ti67 sponges.

Bending behavior and the fracture surface of cell struts are in agreement with the brittle macroscopic behavior of the Ti67 sponges. The measured strut properties reveal that direct measurements of strut strengths are critical for accurate predictions of foam strength. A specially designed system for compression bending seems to be a promising concept for cell strut testing and predicting the macroscopic behavior of cellular materials.

The main objective of this study was to evaluate the implant stability numerically after four weeks and six months implantation time for rat and sheep implants, respectively. The FEA was performed to simulate biomechanical push-out tests. The proposed numerical analysis aimed at

the prediction of interface strength and of the stress distribution at the bone- implant interface. The accuracy of FEA was controlled through a comparison with push-out test results.

Three characteristic stages could be recognized along the load-displacement curves from all simulation results. A linear stage corresponds to a successful implant bone fixation, while the load increasing generates a nonlinear stage at which the implant separates from the bone. During the third stage frictional sliding occurs and the implant is removed from the surrounding bone.

The measured geometric characteristics were used to build two different cancellous bone models. In the first model, the foams were idealized as regular Kelvin tetrakaidecahedron unit cells, while the second model consists of realistic random Gibson-Ashby's unit cells. In both models, the unit cells are elongated in one direction: the ligaments are assumed to be straight and to have circular cross-sections whose areas are constant along the length. Using unit cell assumptions allowed analyzing the behavior of individual contacted trabeculae and their assistance to implant stability and push-out strength.

The simulated average maximum push-out forces are higher than the experimentally measured values. Both 3D model curves reach the maximum push-out force at larger displacements. The computationally predicted stiffness values for both 3D models exhibited a high agreement with the experimentally calculated stiffness. On the other hand, the shortest elastic stages were obtained for 2D models and it resulted in higher stiffness in comparison with measured and 3D models stiffness values. The second stage of 2D model curves were similar to that of measured curves. However, no clear non-linear behavior was observed for both 3D model curves. Meanwhile, 2D models showed a uniform and continuous sliding stage, while implants eluding occurred faster and sliding stages curves were narrow in 3D models.

The elastic region was narrow for 2D model results compared to experimentally measured and 3D simulated curves for both uncoated and coated sheep implants. The highest interface stiffness values were calculated according to the computational 2D results. The computationally analyzed stiffness values were nearly equal to measured values in 3D models.

The nonlinear behavior at the second stage was remarkable on both 2D models load displacement curves. After the separation of implant from bone, a nearly uniform sliding behavior was observed on the 2D model curves while implant sliding concluded at a small displacement for 3D models.

Even though different stress magnitudes were obtained for both groups of rat and sheep implants, the stress distribution at the bone interface was similar. The highest stress

concentration was observed in the areas of bones that are closer to the implants, and the magnitude of mechanical stress was the highest in the cortical bone area.

It can be concluded that 3D simulations were more sensitive than the 2D FE analyses. It should be noted that a detailed bone model is crucial and unit cell assumptions enhances the accuracy of FE analyses. Elongated tetrakaidecahedron unit cells improved the prediction of cancellous bone behavior and the highest accuracy of FE prediction was also achieved.

FEA results allow to make statements about the average behavior of the implant bone interface. High correlations were found between push-out strength as estimated from FE and the experimentally measured push-out strength. In the future, more attention must be paid to adaptation of bone remodeling into FEA. Further animal experiments are needed to determine periodical implant bone fixation. The present study demonstrated that especially 3D FE models can be used for the assessment of stability and strength of bone-implant constructs. The development of new implant designs could potentially be accelerated by using such FE models. It could be especially beneficial in the design process of implants prior to animal tests and could save costs and time.

## 7 References

- [1] Ratner B.D., Hoffman A.S., Schoen F.J. and Lemons J.E., "Biomaterials Science: An Introduction to Materials in Medicine", Elsevier Academic Press, (2004).
- [2] Wintermantel E. and Ha S.W., "Medizintechnik-Life Science Engineering", Springer, Berlin, (2008).
- [3] Ratner B.D., "Biomaterials Science: An Introduction to Materials in Medicine", Elsevier Academic Press, (2004), pp. 8-158.
- [4] Navarro M., Michiardi A., Castaño O. and Planell J.A., "Biomaterials in Orthopaedics", Journal of the Royal Society Interface, (2008), Vol. 5, pp. 1137-1158.
- [5] Bhatia S.K., "Engineering Biomaterials for Regenerative Medicine Novel Technologies for Clinical Applications", Springer Science, (2012).
- [6] Sittig C., Haehner G., Marti A., Textor M. and Spencer N.D., "The Implant Material, Ti6Al7Nb: Surface Microstructure, Composition and Properties", Journal of Materials Science: Materials in Medicine, (1999), Vol. 10, pp. 191-198.
- [7] Disegi J.A., "Titanium Alloys for Fracture Fixation Implants", Injury, (2000), Vol. 31, pp. 14-17.
- [8] Suchanek W. and Yoshimura M., "Processing and Properties of Hydroxyapatite-based Biomaterials for Use As Hard Tissue Replacement Implants", Journal of Materials Research, (2002), Vol. 13, pp. 751-762.
- [9] Black J., "Biological Performance of Materials: Fundamentals of Biocompatibility", CRC Press, New York, (1999).
- [10] Oldani C. and Dominguez A., "Orthopedics, Physical Medicine and Rehabilitation, Chapter 9: Titanium as a Biomaterial for Implants", In TechOpen, (2012), pp. 149-163.
- [11] Geetha M., Singh A.K., Asokamani R. and Gogia A.K., "Ti Based Biomaterials, The Ultimate Choice for Orthopaedic Implants-A Review", Progress in Materials Science, (2009), Vol. 54, pp. 397-425.
- [12] Niinomi M., "Mechanical Properties of Biomedical Titanium Alloys", Materials Science and Engineering, (1998), Vol. A243, pp. 231-236.
- [13] Güden M., Çelik E., Hızal A., Altindis M. and Çetiner S., "Effects of Compaction Pressure and Particle Shape on The Porosity and Compression Mechanical Properties of Sintered Ti6Al4V Powder Compacts for Hard Tissue Implantation", Journal of Biomedical Materials Research: Part B-Applied Biomaterials, (2008), Vol. 85(2), pp. 547-55.
- [14] Li J.P., Li S.H., de Groot K. and Layrolle P., "Preparation and Characterization of Porous Titanium", Key Engineering Materials, (2002), Vol. 218-220, pp. 51-54.
- [15] Barrere F., Snel M.M.E., Blitterswijk C.A., Groot K. and Layrolle P., "Nanoscale Study of The Nucleation and Growth of Calcium Phosphate Coating on Titanium Implants", Biomaterials, (2004), Vol. 25, pp. 2901-2910.
- [16] Pearce A.I., Richards R.G., Milz S., Schneider E. and Pearce S.G., "Animal Models for Implant Biomaterials Research in Bone: A Review", European Cell and Materials, (2007), Vol. 13, pp. 1-10.
- [17] Lopez-Heredia M.A., Weiss P., Layrolle P., Doulin E., Leroux C. and Dorget M., "Finite Element Modelling of Porous Titanium Implants", Metfoam, (2007), pp. 271-274.
- [18] Moratal D., "Finite Element Analysis: From Biomedical Applications to Industrial Developments", InTech, (2012).
- [19] Ajdari A., "Mechanical Behavior of Cellular Structures: A Finite Element Study", Master Thesis, Northeastern University, Boston, (2008).
- [20] Nather A., Ong H.J.C. and Aziz Z., "Bone Grafts and Bone Substitutes: Basic Science and Clinical Applications, Chapter 1: Structure of Bone", World Scientific, (2005), pp. 3-17.
- [21] Barrère F., van Blitterswijk C.A. and de Groot K., "Bone Regeneration: Molecular and Cellular Interactions with Calcium Phosphate Ceramics", International Journal of Nanomedicine, (2006), Vol. 1(3), pp. 317-332.
- [22] Currey J.D., "Bones: Structure and Mechanics", Princeton University Press, (2002).

- [23] Murugan R. and Ramakrishna S., "Review: Development of Nanocomposites for Bone Grafting", *Composites Science and Technology*, (2005), Vol. 65, pp. 2385-2406.
- [24] Weiner S. and Wagner H.D., "The Material Bone: Structure-Mechanical Function Relations", *Annual Review of Materials Science*, (1998), Vol. 28, pp. 271-98.
- [25] Rho J.Y., Spearing L.K. and Zioupos P., "Mechanical Properties and The Hierarchical Structure of Bone", *Medical Engineering&Physics*, (1998), Vol. 20, pp. 92-102.
- [26] Shanbhag A., Rubash H.E. and Jacobs J.J., "Joint Replacement and Bone Resorption Pathology, Biomaterials, and Clinical Practice", Taylor&Francis Group, (2006).
- [27] Meyers M.A., Chen P.Y., Lin A.Y.M. and Seki Y., "Biological Materials: Structure and Mechanical Properties", *Progress in Materials Science*, (2008), Vol. 53, pp. 1-206.
- [28] Zorzi A. and de Miranda J. B., "Bone Grafting", *InTech*, (2012).
- [29] Keaveny T.M., Pinilla T.P., Crawford R.P., Kopperdahl D.L. and Lou A., "Systematic and Random Errors in Compression Testing of Trabecular Bone", *Journal of Orthopaedic Research*, (1997), Vol. 15, pp. 101-110.
- [30] Zioupos P., Gresle M. and Winwood K., "Fatigue Strength of Human Cortical Bone: Age, Physical, and Material Heterogeneity Effects", *Journal of Biomedical Materials Research Part A*, (2008), Vol. 86A, pp. 627-636.
- [31] Vaz M.F., Canhão H. and Fonseca J.E., "Analysis of Natural and Man-made Materials, Chapter 8: Bone A Composite Natural Material Advances in Composite Materials ", *In TechOpen*, (2011), pp. 195-228.
- [32] Thompson M.S., Flivik G., Juliusson R., Odgaard A. and Ryd L., "A Comparison of Structural and Mechanical Properties in Cancellous Bone from The Femoral Head and Acetabulum", *The Proceedings of the Institution of Mechanical Engineers, Part H: Journal of Engineering in Medicine*, (2012), Vol. 218(6), pp. 425-429.
- [33] Holweg K., "Bestimmung der Eigenschaft der Grenzfläche zwischen Knochen und Implantat", *In: Zentrum für Ingenieurwissenschaften Martin-Luther-Universität Halle-Wittenberg, Halle, Papierflieger*, (2010).
- [34] Dendorfer S., Maier H.J. and Hammer J., "Fatigue Damage in Cancellous Bone: An Experimental Approach from Continuum to Micro Scale", *Journal of the Mechanical Behavior of Biomedical Materials*, (2009), Vol. 2, pp. 113-119.
- [35] Moore T.L.A. and Gibson L.J., "Fatigue Microdamage in Bovine Trabecular Bone", *Journal of Biomechanical Engineering-Transactions of The Asme*, (2003), Vol. 125, pp. 769-776.
- [36] Haddock S.M., Yeh O.C., Mummaneni P.V., Rosenberg W.S. and Keaveny T.M., "Similarity in The Fatigue Behavior of Trabecular Bone Across Site and Species", *Journal of Biomechanics* 37, (2004), pp. 181-187.
- [37] Ulstrup A.K., "Biomechanical Concepts of Fracture Healing in Weight-bearing Long Bones", *Acta Orthopaedica Belgica Journal*, (2008), Vol. 74, pp. 291-302.
- [38] Griffon D.J., "Fracture Healing In: AO Principles of Fracture Management in Small Animals", *Veterinary Surgery*, (2005), pp. 34-223.
- [39] Kalfas I.H., "Principles of Bone Healing", *Neurosurgical Focus*, (2001), Vol. 10, pp. 7-10.
- [40] Geetha M., Singh A.K., Asokamani R. and Gogia A.K., "Ti Based Biomaterials, The Ultimate Choice for Orthopaedic Implants-A Review", *Progress in Materials Science*, (2009), Vol. 54, pp. 397-425.
- [41] Polmear I.J., "Light Alloys from Traditional Alloys to Nanocrystals", Elseiver, (2006).
- [42] Amin A.K.M.N., "Titanium Alloys-Towards Achieving Enhanced Properties for Diversified Applications", *InTech*, (2012).
- [43] Balazic M. and Kopac J., "Review: Titanium and Titanium Alloy Applications in Medicine", *International Journal of Nano and Biomaterials*, (2007), Vol. 1, pp. 3-34.
- [44] Geetha M., Singh A.K., Asokamani R. and Gogia A.K., "Ti Based Biomaterials, The Ultimate Choice for Orthopaedic Implants-A Review", *Progress in Materials Science*, (2009), Vol. 54, pp. 397-425.
- [45] Wegmann G., Albrecht J., Lutjering G., Folkers K.D. and Liesner C., "Microstructure and Mechanical Properties of Titanium Castings", *Zeitschrift für Metallkunde*, (1997), Vol. 88, pp. 764-773.

- [46] Vasconcellos L.M.R., Carvalho Y.R., Prado R.F., Vasconcellos L.G.O., Graça M.L.A. and Cairo C.A.A., "Biomedical Engineering-Technical Applications in Medicine, Chapter 2: Porous Titanium by Powder Metallurgy for Biomedical Application: Characterization, Cell Cytotoxicity and in Vivo Tests of Osseointegration", *InTech*, (2012), pp. 47-74.
- [47] Metikoš-Huković M., Kwokal A. and Piljac J., "The Influence of Niobium and Vanadium on Passivity of Titanium-based Implants in Physiological Solution", *Biomaterials*, (2003), Vol. 24, pp. 3765-3775.
- [48] Akahori T., Niinomi M. and Suzuki A., "Improvement in Mechanical Properties of Dental Cast Ti6Al7Nb by Thermochemical Processing", *Metallurgical and Materials Transactions A*, (2002), Vol. 33A, pp. 503-510
- [49] Joshi V.A., "Titanium Alloys: An Atlas of Structures and Fracture Features", CRC Press, (2006).
- [50] Lütjering G. and Williams J.C., "Titanium", Springer-Verlag, Berlin, (2003).
- [51] Oshida Y., "Bioscience and Bioengineering of Titanium Materials", Elsevier, (2007).
- [52] Rack H.J. and Qazi J.I., "Titanium Alloys for Biomedical Applications", *Materials Science and Engineering C*, (2006), Vol. 26, pp. 1269-1277.
- [53] Venkatesh B., Chen D.L. and Bhole S.D., "Three-dimensional Fractal Analysis of Fracture Surfaces in A Titanium Alloy for Biomedical Applications", *Scripta Materialia*, (2008), Vol. 59, pp. 391-394.
- [54] Leyens C. and Peters M., "Titanium and Titanium Alloys", Wiley VCH Verlag, Cologne, (2003).
- [55] Niinomi M., "Biologically and Mechanically Biocompatible Titanium Alloys", *Materials Transactions*, (2008), Vol. 49, No.10, pp. 2170-2178.
- [56] Spriano S., Bronzoni M., Verne E., Maina G., Bergo V. and Windler M., "Characterization of Surface Modified Ti6Al7Nb Alloy", *Journal of Materials Science: Materials in Medicine*, (2005), Vol. 16, pp. 301-312.
- [57] Banhart J., "Manufacture, Characterization and Application of Cellular Metals and Metal Foams", *Progress in Materials Science*, (2001), Vol. 46, pp. 559-563.
- [58] Ryan G., Pandit A. and Apatsidis D.P., "Review: Fabrication Methods of Porous Metals for Use in Orthopaedic Applications", *Biomaterials*, (2006), Vol. 27, pp. 2651-2670.
- [59] Arifvianto B. and Zhou J., "Fabrication of Metallic Biomedical Scaffolds with The Space Holder Method: A Review", *Materials* (2014), Vol. 7, pp. 3588-3622.
- [60] Ashby F.M., Evans A., Fleck N.A., Gibson L.J., Hutchinson J.W. and Wadley H.N.G., "Metal Foams: A Design Guide", Butterworth Heinemann, Oxford, (2000).
- [61] Hu H.J., "Optimizing Investment Casting by Computer Simulation", *Foundry Management&Technology*, (2006), Vol. 12, pp. 44-59.
- [62] Prasad R., "Science and Technology of Casting Process, Chapter 2: Progress in Investment Casting", *InTech*, (2012), pp.28-38
- [63] Frueh C., Poirier D.R., Maguire M.C. and Harding R.A., "Attempts to Develop A Ceramic Mould for Titanium Casting-A Review", *International Journal of Cast Metals Research*, (1996), Vol. 9, pp. 233-39.
- [64] Guerra M., "A Practical Guide to Successful Investment Casting of Titanium Alloys", Investment Casting Institute, 12th World Conference, (2008).
- [65] Mohammadi S., Esposito M., Victorin L., Aronsson B.O. and Thomsen P., "Bone Response to Machined Cast Titanium Implants", *Journal of Materials Science*, (2001), Vol. 36, pp. 1987-1993.
- [66] Atwood R.C., Lee P.D. and Curtis R.V., "Modeling The Surface Contamination of Dental Titanium Investment Castings", *Dental Materials*, (2005), Vol. 21, pp. 178-186.
- [67] Jovanović M., Bobić I., Mišković Z. and Zec S., "Precision Cast of Ti-based Alloys-Microstructure and Mechanical Properties", *Metalurgija-Journal of Metallurgy*, (2009), Vol. 15, pp. 53-69.
- [68] Sung S.Y., Choi B.J., Noh S.H., Hahn C.S., Ryu Y.M., Han B.S. and Kim Y.J., "Thermodynamic Calculation of  $\alpha$  Case Formation in Titanium Alloys", *Advanced Materials Research*, (2007), Vol. 26-28, pp. 519-522.
- [69] Low D., Sumii T. and Swain M., "Thermal Expansion Coefficient of Titanium Casting", *Journal of Oral Rehabilitation*, (2001), Vol. 28, pp. 239-242.

- [70] Cotton J.D., Clark L.P. and Phelps H.R., "Titanium Investment Casting Defects: A Metallographic Overview", *Journal of Metals*, (2006), Vol. 58, pp. 13-16.
- [71] Cai Z., Shafer T., Watanabe I., Nunn M.E. and Okabe T., "Electrochemical Characterization of Cast Titanium Alloys", *Biomaterials*, (2003), Vol. 24, pp. 213-218.
- [72] Watanabe I., Watkins J.H., Nakajima H., Atsuta M. and Okabe T., "Effect of Pressure Difference on The Quality of Titanium Casting", *Journal of Dental Research*, (1997), Vol. 76, pp. 773-778.
- [73] Cruz R.V.B., Sayeg I.J., Mutarelli P.S. and Pinedo C.E., "Effect of The Ceramic Mould Composition on The Surface Quality of As-cast Titanium Alloy", *Journal of Materials Science*, (2005), Vol.40, pp. 6041-6043.
- [74] Mitchell A., "Melting, Casting and Forging Problems in Titanium Alloys", *Materials Science and Engineering*, (1998), Vol. A243, pp. 257-262.
- [75] Zhang X.P. and Chen G., "Computer Simulation of The Solidification of Cast Titanium Dental Prostheses", *Journal of Materials Science*, (2005), Vol. 40, pp. 4911-4916.
- [76] Boettinger W.J., Williams M.E., Coriell S.R., Kattner U.R. and Müller B.A., " $\alpha$  Case Thickness Modeling in Investment Castings", *Metallurgical and Materials Transactions*, (2000), Vol. 31B, pp. 1419-25.
- [77] Cheng W.W., Ju C.P. and Chern Lin J.H., "Structure, Castability and Mechanical Properties of Commercially Pure and Alloyed Titanium Cast in Graphite Mould", *Journal of Oral Rehabilitation*, (2007), Vol. 34, pp. 528-540.
- [78] Chan K.S., Koike M., Johnson B.W. and Okabe T., "Modeling of  $\alpha$  Case Formation and Its Effects on The Mechanical Properties of Titanium Alloy Castings", *Metallurgical and Materials Transactions A*, (2008), Vol. 39A, pp. 171-178.
- [79] Ohkubo C., Hosoi T., Ford J.P. and Watanabe I., "Effect of Surface Reaction Layer on Grindability of Cast Titanium Alloys", *Dental Materials*, (2006), Vol. 22, pp. 268-274.
- [80] Sung S.Y., Choi B.J., Han B.S., Oh H.J. and Kim Y.J., "Evaluation of  $\alpha$  Case in Titanium Castings", *Journal of Materials Science and Technology*, (2008), Vol. 24, No.1, pp. 70-74.
- [81] Eliopoulos D., Zinelis S. and Papadopoulos T., "The Effect of Investment Material Type on The Contamination Zone and Mechanical Properties of Commercially Pure Titanium Castings", *The Journal of Prosthetic Dentistry*, (2005), Vol. 94, pp. 539-48.
- [82] Pitt F. and Ramulu M., "Post-processing Effect on The Fatigue of Three Titanium Alloys under Simulated SPF Conditions", *The Journal of Materials Engineering and Performance*, (2007), Vol.16, pp. 163-169.
- [83] Koike M., Jacobson D., Chan K.S. and Okabe T., "Grindability of  $\alpha$  Case Formed on Cast Titanium", *Dental Materials Journal*, (2009), Vol. 28(5), pp. 587-594.
- [84] Yue L., Wang Z. and Li L., "Material Morphological Characteristics in Laser Ablation of  $\alpha$  Case from Titanium Alloy", *Applied Surface Science*, (2012), Vol. 252, pp. 8065-8071.
- [85] Jordan D., "Study of  $\alpha$  Case Formation on Heat Treated Ti64 Alloy", *Heat Treating Progress*, (2008), pp. 45-47.
- [86] Takahashi K., Matsushashi R. and Takayama I., "Change of Morphology of Titanium Surface by Pickling in Nitric-hydrofluoric Acid Solutions", *Nippon Steel Technical Report*, (2002), No. 85, pp. 64-70.
- [87] Ikada Y., "Tissue Engineering: Fundamentals and Applications", Elsevier Academic Press, Amsterdam, (2006).
- [88] Gabbi C., Cacchioli A., Ravanetti F., Spaggiari B., Borghetti P., Martini F.M. and Leonardi F., "Osteogenesis and Bone Integration: The Effect of New Titanium Surface Treatments", *Annali della Facolta di Medicina Veterinaria, Universita di Parma*, (2005), Vol. XXV, pp. 307-318.
- [89] Pearce A.I., Pearce S.G., Schwieger K., Milz S., Schneider E., Archer C.W. and Richards R.G., "Effect of Surface Topography on Removal of Cortical Bone Screws in A Novel Sheep Model", *Journal of Orthopaedic Research*, (2008), Vol. 26, pp. 1377-1383.
- [90] Spriano S., Bosetti M., Bronzoni M., Verne E., Maina G., Bergo V. and Cannas M., "Surface Properties and Cell Response of Low Metal Ion Release Ti6Al7Nb Alloy After Multi-step Chemical and Thermal Treatments", *Biomaterials*, (2005), Vol. 26, pp. 1219-1229.
- [91] Tamilselvi S., Raghavendran H.B., Srinivasan P. and Rajendran N., "In Vitro and in Vivo Studies of Alkali- and Heat-treated Ti6Al7Nb and Ti5Al2Nb1Ta Alloys for Orthopedic Implants", *Journal of Biomedical Materials Research*, (2009), Vol. 90A, pp. 380-386.

- [92] Valereto I.C.L., Wolyneec S., Deboni M.C.Z. and König B., "In Vitro and in Vivo Biocompatibility Testing of Ti6Al7Nb Alloy with and without Plasma-sprayed Hydroxyapatite Coating", *Journal of Biomedical Materials Research Part B: Applied Biomaterials*, (2001), Vol. 58, pp. 727-733.
- [93] Hsu S., Liu B.S., Lin W.H., Chiang H.C., Huang S.C. and Cheng S.S., "Characterization and Biocompatibility of A Titanium Dental Implant with A Laser Irradiated and Dual-acid Etched Surface", *Bio-Medical Materials and Engineering*, (2007), Vol.17, pp. 53-68.
- [94] Williams D.F., "On The Mechanisms of Biocompatibility", *Biomaterials*, (2008), Vol. 29, pp. 2941-2953.
- [95] Stanford C.M., "Review Surface Modification of Biomedical and Dental Implants and The Processes of Inflammation, Wound Healing and Bone Formation", *International Journal of Molecular Sciences*, (2010), Vol. 11, pp. 354-369.
- [96] Valereto I.C.L., Nig B.K., Rossa C., Marcantonio E. and Zavaglia A.C., "A Study of Histological Responses from Ti6Al7Nb Alloy Dental Implants with and without Plasma Sprayed HA Coating in Dogs", *Journal of Materials Science: Materials in Medicine*, (2001), Vol. 12, pp. 273-276.
- [97] Medeiros W.S., Pereira L.C., Pereira R.P. and Oliveira M.V., "Characterization of CaP Coating Deposited on Porous Titanium", *Key Engineering Materials*, (2009), Vol. 396-398, pp. 307-310.
- [98] Gross U., Muller M.C., Voigt C., Mesgarian M. and Berger G.U., "Tissue Response in The Femur of Rabbits After Implantation of A New Calcium Titanium Phosphate Composition", *Bioceramics*, (2000), Vol. 192, pp. 383-386.
- [99] Yang Y., Oh N., Liu Y., Chen W., Oh S., Appleford M., Kim S., Kim K., Park S., Bumgardner J., Haggard W. and Ong J., "Enhancing Osseointegration Using Surface Modified Titanium Implants", *Journal of Metals*, (2006), Vol. 58, pp. 71-76.
- [100] Sul Y.T., Byon E.S. and Jeong Y., "Biomechanical Measurements of Calcium-incorporated Oxidized Implants in Rabbit Bone: Effect of Calcium Surface Chemistry of A Novel Implant", *Clinical Implant Dentistry and Related Research*, (2004), Vol. 6(2), pp. 101-110.
- [101] Nishiguchi S., Kato H., Fujita H., Oka M., Kim H.M., Kokubo T. and Nakamura T., "Titanium Metals Form Direct Bonding to Bone After Alkali and Heat Treatments", *Biomaterials*, (2001), Vol. 22, pp. 2525-2533.
- [102] Giordano C., Sandrini E., Del Curto B., Signorelli E., Rondelli G. and Di Silvio L., "Titanium for Osteointegration: Comparison Between A Novel Biomimetic Treatment and Commercially Exploited Surfaces", *Journal of Applied Biomaterials&Biomechanics*, (2004), Vol. 2, pp. 35-44.
- [103] Haenle M., Lindner T., Ellenrieder M., Willfahrt M., Schell H., Mittelmeier W. and Bader R., "Bony Integration of Titanium Implants with A Novel Bioactive Calcium Titanate (Ca<sub>4</sub>Ti<sub>3</sub>O<sub>10</sub>) Surface Treatment in A Rabbit Model", *Journal of Biomedical Materials Research Part A*, (2012), Vol. 100(10), pp. 1-7.
- [104] Kim H.M., Takadama H., Miyaji F., Kukubo T., Nishiguchi S. and Nakamura T., "Formation of Bioactive Functionally Graded Structure on Ti6Al4V Alloy by Chemical Surface Treatment", *Journal of Materials Science: Materials in Medicine*, (2000), Vol. 11, pp. 555-559.
- [105] Takemoto M., Fujibayashi S., Neo M., Suzuki J., Kokubo T. and Nakamura T., "Mechanical Properties and Osteoconductivity of Porous Bioactive Titanium", *Biomaterials*, (2005), Vol. 26, pp. 6014-6023.
- [106] Soskolne W.A., Cohen S., Sennerby L., Wennerberg A. and Shapira L., "The Effect of Titanium Surface Roughness on The Adhesion of Monocytes and Their Secretion of TNF-a and PGE2", *Clinical Oral Implantation Research*, (2002), Vol.13, pp. 86-93.
- [107] Kirbs A., Lange R., Nebe B., Rychly R., Baumann A., Neumann H.G. and Beck U., "Methods for The Physical and Chemical Characterisation of Surfaces of Titanium Implants", *Materials Science and Engineering C*, (2003), Vol. 23, pp. 425-429.
- [108] Iwaya Y., Machigashira M., Kanbara K., Miyamoto M., Noguchi K., Izumi Y. and Ban S., "Surface Properties and Biocompatibility of Acid-etched Titanium", *Dental Materials Journal*, (2008), Vol. 27(3), pp. 415-42.
- [109] Kunzler T.P., Drobek T., Sprecher C.M., Schuler M. and Spencer N.D., "Fabrication of Material-independent Morphology Gradients for High-throughput Applications", *Applied Surface Science*, (2006), Vol. 253, pp. 2148-2153.

- [110] Hossain M.M. and Gao W., "How Is The Surface Treatments Influence on The Roughness of Biocompatibility?", *Trends in Biomaterials and Artificial Organs*, (2008), Vol. 22(3), pp. 144-157.
- [111] Kim H., Choi S.H., Ryu J.J., Koh S.Y., Park J.H. and Lee I.S., "The Biocompatibility of SLA-Treated Titanium Implants", *Biomedical Materials*, (2008), Vol. 025011, pp. 1-6.
- [113] Lüthen F., Bulnheim U., Müller P.D., Rychly J., Jesswein H. and Nebe J.G., "Influence of Manganese Ions on Cellular Behavior of Human Osteoblasts in Vitro", *Biomolecular Engineering* (2007), Vol. 24(5), pp. 531-6.
- [114] Salido M., Perez J.I.V., Gonzalez J.L. and Vilches J., "Mitochondrial Bioenergetics and Distribution in Living Human Osteoblasts Grown on Implant Surfaces", *Histology and Histopathology*, (2009), Vol. 24, pp. 1275-1286.
- [115] Kakehi S., Takeda S. and Nakamura M., "Effect of Titanium Surface Roughness on The Cytocompatibility of Osteoblast-like Cells", *Journal of Oral Engineering*, (2006), Vol. 4(2), pp. 77-88.
- [116] Chen X., Nouri A., Li Y., Lin J., Hodgson P.D., Road C.P. and Pond W., "Effect of Surface Roughness of Ti, Zr, and TiZr on Apatite Precipitation from Simulated Body Fluid", *Biotechnology Bioengineering*, (2008), Vol. 101, pp. 378-387.
- [117] Anselme K., Linez P., Bigerelle M., Le Maguer D., Le Maguer A., Hardouin P., Hildebrand H.F., Iost A. and Leroy J.M., "The Relative Influence of The Topography and Chemistry of TiAl6V4 Surfaces on Osteoblastic Cell Behaviour", *Biomaterials*, (2000), Vol. 21(15), pp. 1567-1577.
- [118] Cooper L.F., "A Role for Surface Topography in Creating and Maintaining Bone at Titanium Endosseous Implants", *The Journal of Prosthetic Dentistry*, (2000), Vol. 84, pp. 522-34.
- [119] Wennerberg A. and Albrektsson T., "On Implant Surfaces: A Review of Current Knowledge and Opinions", *The International Journal of Oral&Maxillofacial Implants*, (2010), Vol. 25(1), pp. 63-74.
- [120] Rosa A.L. and Beloti M.M., "Effect of CpTi Surface Roughness on Human Bone Marrow Cell Attachment, Proliferation, and Differentiation", *Brazilian Dental Journal*, (2003), Vol. 14(1), pp. 16-21.
- [121] Shalabi M.M., Gortemaker A., Van't Hof M.A., Jansen J.A. and Creugers N.H.J., "Implant Surface Roughness and Bone Healing: A Systematic Review", *Journal of Dental Research*, (2006), Vol. 85(6), pp. 496-500.
- [122] Öchsner A. and Ahmed W., "Biomechanics of Hard Tissues Modeling, Testing, and Materials", Wiley VCH Verlag, (2008).
- [123] Ashby M.F., "The Mechanical Properties of Cellular Solids", *Metallurgical Transactions A: Physical Metallurgy and Materials Science*, (1983), Vol. 14, pp. 1755-1769.
- [124] Gibson L.J. and Ashby M.F., "Cellular Solids: Structure and Properties", Cambridge University Press, Cambridge, (1997).
- [125] Degischer H.P. and Kriszt B., "Handbook of Cellular Metals Production, Processing, Applications", Wiley VCH Verlag, (2002).
- [126] Ashby M.F., "The Properties of Foams and Lattices", *Philosophical Transactions of The Royal Society A*, (2006), Vol. 364, pp. 15-30.
- [127] Gibson L.J., "Biomechanics of Cellular Solids", *Journal of Biomechanics*, (2005), Vol. 32, pp. 377-99.
- [128] Matassi F., Botti A., Sirleo L., Carulli C. and Innocenti M., "Porous Metal for Orthopedics Implants", *Clinical Cases in Mineral and Bone Metabolism*, (2013), Vol. 10(2), pp. 111-115.
- [129] Itala A.I., Ylanen H.O., Ekholm C., Karlsson K.H. and Aro H.T., "Pore Diameter of More Than 100  $\mu$ m Is Not Requisite for Bone Ingrowth in Rabbits", *Journal of Biomedical Materials Research Part B: Applied Biomaterials*, (2001), Vol. 58, pp. 679-683.
- [130] Gibson L.J., Ashby M.F. and Harley B.A., "Cellular Materials in Nature and Medicine", Cambridge University Press, Cambridge, (2010).
- [131] Xue C., Choi B.C., Choi S. and Braun P.V., "Protein Adsorption Modes Determine Reversible Cell Attachment on Poly (N-isopropyl acrylamide) Brushes", *Advanced Functional Materials* (2012), Vol. 22(11), pp. 2394-2401.
- [132] Karageorgiou V. and Kaplan D., "Review: Porosity of 3D Biomaterial Scaffolds and Osteogenesis", *Biomaterials*, (2005), Vol. 26(27), pp. 5474-91.

- [133] Ohrndorf A., "Verformungsverhalten Metallischer Schaumwerkstoffe unter Isothermen und Thermomechanischen Beanspruchungsbedingungen", Dissertation Univ. Siegen, (2011).
- [134] Krupp U., Ohrndorf A., Guillen T., Christ H.J., Demiray S., Becker W. and Hohe J., "Isothermal and Thermomechanical Fatigue Behavior of Open Cell Metal Sponges", *Advanced Engineering Materials*, (2006), Vol. 8, pp. 821-827.
- [135] Krupp U., Ohrndorf A., Hipke T., Hohlfeld J., Danninger A., Reinfried M. and Aegerter J., "Development of A Standard for Compression Testing of Cellular Metals", *MetFoam* (2007), pp. 407-410.
- [136] Zhou J. and Soboyejo W.O., "Compression-compression Fatigue of Open Cell Aluminum Foams: Macro-/Micro-mechanisms and The Effects of Heat Treatment", *Materials Science and Engineering A: Structural Materials Properties Microstructure and Processing*, (2004), Vol. 369, pp. 23-35.
- [137] Ashby F.M., Evans A., Fleck N.A., Gibson L.J., Hutchinson J.W. and Wadley H.N.G., "Metal Foams: A Design Guide", Butterworth Heinemann, Oxford, (2000).
- [138] Park J.C., Lee J.W., Kim S.M. and Lee J.H., "Implant Dentistry-A Rapidly Evolving Practice, Chapter 5: Implant Stability-Measuring Devices and Randomized Clinical Trial for ISQ Value Change Pattern Measured from Two Different Directions by Magnetic RFA", *InTech*, (2011), pp.111-129.
- [139] Yuehuei H. and Draughn R.A., "Mechanical Testing of Bone and The Bone-Implant Interface", CRC Press, (2002).
- [140] Vemuganti A., Siegler S., Abusafieh A. and Kalidindi S., "Development of Self-anchoring Bone Implants. II. Bone-Implant Interface Characteristics in Vitro", *Journal of Biomedical Material Research*, (1997), Vol. 38(4), pp. 328-36.
- [141] Berzins A., Shah B., Weinans H. and Sumner D.R., "Nondestructive Measurements of Implant-Bone Interface Shear Modulus and Effects of Implant Geometry in Pull-out Tests", *Journal of Biomedical Materials Research*, (1997), Vol. 34, pp. 337-340.
- [142] Teixeira C.S., Alfredo E., de Camargo Thome L.H., Gariba-Silva R., Correa Silva-Sousa Y.T. and Sousa-Neto M.D., "Adhesion of An Endodontic Sealer to Dentin and Gutta-percha: Shear and Push-out Bond Strength Measurements and SEM Analysis", *Journal of Applied Oral Science*, (2009), Vol. 17, pp. 129-135.
- [143] Brandt J., Bierogel C., Holweg K., Hein W. and Grellmann W., "Extended Push-out Test to Characterize The Failure of Bone-Implant Interface", *Biomedizinische Technik*, (2005), Vol. 50, pp. 201-206.
- [144] Goracci C., Fabianelli A., Sadek F.T., Papacchini F., Tay F.R. and Ferrari M., "The Contribution of Friction to The Dislocation Resistance of Bonded Fiber Posts", *Journal of Endodontics*, (2005), Vol. 31, pp. 608-612.
- [145] Dillard T., N'guyen F., Maire E., Salvo L., Forest S., Yusop A.H., Bakir A.A., Shaharom N.A., Kadir M.R.A. and Hermawan H., "Review Article: Porous Biodegradable Metals for Hard Tissue Scaffolds", *International Journal of Biomaterials*, (2012), Vol. 2012, pp. 1-10.
- [146] Huja S.S., Litsky A.S., Beck F.M., Johnson K.A. and Larsen P.E., "Pull-out strength of Monocortical Screws Placed in The Maxillae and Mandibles of Dogs", *American Journal of Orthodontics and Dentofacial Orthopedics*, (2005), Vol. 127(3), pp. 307-13.
- [147] Dhert W.J.A., Verheyen C.C.M., Braak L.H., de Wijn J.R., Klein C.P., de Groot K. and Rozing P.M., "A Finite Element Analysis of The Push-out Test: Influence of Test Conditions", *Journal of Biomedical Materials Research*, (1992), Vol. 26, pp. 119-130.
- [148] MacLeod A.R., Pankaj P., Hamish A. and Simpson R.W., "Short Communication Does Screw-Bone Interface Modelling Matter in Finite Element Analyses?", *Journal of Biomechanics*, (2012), Vol. 45, pp. 1712-1716.
- [149] Bienvenu Y., Bartout J.D., Croset M., Dendievel R. and Cloetens P., "3D Quantitative Image Analysis of Open Cell Nickel Foams under Tension and Compression Loading Using X-ray Microtomography", *Philosophical Magazine*, (2005), Vol. 85, No. 19, pp. 2147-2175.
- [150] Hammad O.A., Khraisat A., Odeh N.D. and Maaytah M., "Effect of Dental Implant Cross-Sectional Design on Cortical Bone Structure Using Finite Element Analysis", *Clinical Implant Dentistry and Related Research*, (2007), Vol. 9, pp. 217-221.

- [151] Chen L., He H., Li Y., Li T., X. Guo and Wang R., "Finite Element Analysis of Stress at Implant-Bone Interface of Dental Implants with Different Structures", *Transactions Metals Society*, (2010), Vol. 21, pp. 1602-10.
- [152] Żmudzki J., Walke W. and Chladek W., "Influence of Model Discretization Density in FEM Numerical Analysis on The Determined Stress Level in Bone Surrounding Dental Implants", *Information Technologies Biomedicine, Advances in Soft Computing*, (2008), Vol. 47, pp. 559-567.
- [153] Eraslan O. and Inan Ö., "The Effect of Thread Design on Stress Distribution in A Solid Screw Implant: A 3D Finite Element Analysis", *Clinical Oral Investigation*, (2010), Vol. 14, pp. 411-416.
- [154] Huang H.L., Hsu J.T., Fuh L.J., Tu M.G., Ko C.C. and Shen Y.W., "Bone Stress and Interfacial Sliding Analysis of Implant Designs on An Immediately Loaded Maxillary Implant: A Non-linear Finite Element Study", *Journal of Dentistry*, (2008), Vol. 36, pp. 409-417.
- [155] Akca K. and Cehreli M.C., "Biomechanical Consequences of Progressive Marginal Bone Loss Around Oral Implants: A Finite Element Stress Analysis", *Medical&Biological Engineering&Computing*, (2006), Vol. 44, pp. 527-535.
- [156] Quaresma S.E.T., Cury P.R., Sendyk W.R. and Sendyk C., "A Finite Element Analysis of Two Different Dental Implants: Stress Distribution in The Prosthesis, Abutment, Implant, and Supporting Bone", *Journal of Oral Implantology*, (2008), Vol. XXXIV, pp. 1-6.
- [157] Fanuscu M.I., Vu H.V. and Poncelet B., "Implant Biomechanics in Grafted Sinus: A Finite Element Analysis", *Journal of Oral Implantology*, (2004), Vol. 30(2), pp. 59-68.
- [158] Lian Z., Guan H., Ivanovski S., Loo Y.C., Johnson N.W. and Zhang H., "Effect of Bone to Implant Contact Percentage on Bone Remodelling Surrounding A Dental Implant", *International Journal of Oral and Maxillofacial Surgery*, (2010), Vol. 39(7), pp. 690-8.
- [159] Van Staden R.C., Guan H., Loo Y.C., Johnson N.W. and Meredith N., "Stress Distribution in Mandible Regulated by Bone and Dental Implant Parameters: Part I-Methodology", *Proceedings of The The Fifth Australasian Congress on Applied Mechanics*, (2007), Vol. 1, pp. 818-829.
- [160] Guan H., van Staden R.C., Johnson N.W. and Loo Y.C., "Dynamic Modelling and Simulation of Dental Implant Insertion Process-A Finite Element Study", *Finite Element in Analysis and Design*, (2011), pp. 1-24.
- [161] Demiray S., Becker W. and Hohe J., "Investigation of The Fatigue Behavior of Open Cell Foams by A Micromechanical 3D Model", *Materials Science and Engineering A*, (2009), Vol. 504, pp. 141-49.
- [162] Badiche X., Forest S., Guibert T., Bienvenu Y., Bartout J.D., Jenny P., Crose M. and Bernet H., "Mechanical Properties and Non-Homogeneous Deformation of Open Cell Nickel Foams Application of The Mechanics of Cellular Solids and of Porous Materials", *Materials Science and Engineering A*, (2000), Vol. A289, pp. 276-88.
- [163] Demiray S., Ohrndorf A., Becker W., Hohe J., U Krupp. and Christ H.J., "Micromechanical Modeling and Experimental Characterization of The Deformation Behaviour of Open Cell Metal Foams", *Cellular Metals and Polymers*, (2004), pp. 99-102.
- [164] Perrot C., Chevillotte F., Panneton R. and Olny X., "Periodic Unit Cell Reconstruction of Porous Media: Acoustic Properties of An Open Cell Aluminum Foam", *Metfoam*, (2007), pp. 433-436.
- [165] Fereidoon A. and Taheri S.A., "Using Finite Element Method to Analyze The Effect of Microstructure on Energy Absorption Properties of Open Cell Polymeric Foams", *Journal of Cellular Plastics*, (2012), Vol. 48(3), pp. 257-270.
- [166] Gong L., Kyriakides S. and Jang W.Y., "Compressive Response of Open Cell Foams. Part I: Morphology and Elastic Properties", *International Journal of Solids and Structures*, (2005), Vol. 42, pp. 1355-1379.
- [167] Gong L., Kyriakides S. and Triantafyllidis N., "On The Stability of Kelvin Cell Foams under Compressive Loads", *Journal of the Mechanics and Physics of Solids*, (2005), Vol. 53, pp. 771-794.
- [168] Zhu H.X., Hobdell J.R. and Windle A.H., "Effects of Cell Irregularity on The Elastic Properties of Open Cell Foams", *Acta Materialia*, (2000), Vol. 48, pp. 4893-900.
- [169] Sullivan R.M., Ghosn L.J. and Lerch B.A., "Application of An Elongated Kelvin Model to Space Shuttle Foams", *Journal of Spacecraft and Rockets*, (2009), Vol. 46, No. 2, pp. 411-418.

- [170] Borovinsek M. and Ren Z., "Effects of Cell Irregularity on The Impact Behavior of Open Cell Foams", *Metfoam*, (2007), pp. 371-375.
- [171] Mangipudi K.R., Amsterdam E., De Hosson M. and Onck P.R., "Multi-Scale Modelling of Fracture in Open Cell Metal Foams", *Metfoam*, (2007), pp. 363-365.
- [172] Toda H., Takami Y., Kobayashi M., Aruga Y., Takagi T., Suzuki Y. and Uesugi K., "3-D Microstructural Characterization of Cell Wall in A High Strength Aluminium Foam", (2007), *Metfoam*, pp. 445-449.
- [173] Peyrin F., Peter Z., Larrue A., Bonnassie A. and Attali D., "Local Geometrical Analysis of 3D Porous Networks Based on The Medial Axis: Application to Bone Micro-Architecture Microtomography Images", *Image Analysis & Stereology*, (2007), Vol. 16, pp. 179-85.
- [174] Fiedler T., Pesetskaya E., Öchsner A. and Grácio J., "Calculations of The Thermal Conductivity of Porous Materials", *Materials Science Forum*, (2006), Vol. 514, pp. 754-758.
- [175] Borovinsek M. and Ren Z., "Computational Modelling of Irregular Open Cell Foam Behavior under Impact Loading", *Materialwissenschaft und Werkstofftechnik*, (2008), Vol. 39, No. 2, pp. 114-120.
- [176] Choi S. and Sankar B.V., "A Micromechanical Method to Predict The Fracture Toughness of Cellular Materials", *International Journal of Solids and Structures*, (2005), Vol. 42, pp. 1797-1817.
- [177] Geng J.P., Xu W. and Yan W.Q., "Model-based Biomechanical Dental Implant Optimization in Bone-Implant System", *The Chinese Journal of Dental Research*, (2007), Vol. 7, pp. 15-22.
- [178] Koudelka P., Jiroušek O. and Valach J., "Determination of Mechanical Properties of Materials with Complex Inner Structure Using Microstructural Models", *Machines Technologies Materials*, (2011), Vol. 5(3), pp. 39-42.
- [179] Linul E. and Marsavina L., "Prediction of Fracture Toughness for Open Cell Polyurethane Foams by Finite Element Micromechanical Analysis", *Iranian Polymer Journal*, (2011), Vol. 20(9), pp. 735-746.
- [180] Luxner M.H., Stampfl J. and Pettermann H.E., "Finite Element Modeling Concepts and Linear Analyses of 3D Regular Open Cell Structures", *Journal of Materials, Materials Science*, (2005), Vol. 40, pp. 5859-5866.
- [181] Wirth A.J., Müller T.L., Vereecken W., Flaig C., Arbenz P., Müller R. and van Lenthe G.H., "Mechanical Competence of Bone-Implant Systems Can Accurately Be Determined by Image-based Micro-Finite Element Analyses", *Archive of Applied Mechanics*, (2010), Vol. 80, pp. 513-525.
- [182] Michailidis N., Stergioudi F., Omar H. and Tsipas D.N., "Investigation of The Mechanical Behavior of Open Cell Ni Foams by Experimental and FEM Procedures", *Advanced Engineering Materials*, (2008), Vol. 10, No. 12, pp. 1122-26.
- [183] Jacques S.V.N., van Oosterwyck H., Muraru L., van Cleynenbreugel T., de Smet E., Wevers M., Naert I. and Sloten J.V., "Individualised, Micro CT-based Finite Element Modelling As A Tool for Biomechanical Analysis Related to Tissue Engineering of Bone", *Biomaterials*, (2004), Vol. 25, pp. 1683-1696.
- [184] Girón T.G., "Properties and Application Spectrum of Cast Porous Implants Made of Ti6Al7Nb in Coated and Uncoated Conditions", *Dissertation, Univ. Siegen*, (2012).
- [185] Hagemann K., "Gießtechnische Herstellung Offenporiger Implantate aus Ti6Al7Nb", *Dissertation, Gießerei-Institut der RWTH Aachen*, 2012.
- [186] "Standart Methods of Bend Testing of Metallic Flat Materials for Spring Applications", *ASTM E 855, Annual Book of ASTM Standards, Vol 03.01, ASTM, Philadelphia*, (1984), pp. 788-804.
- [187] "Plastics-Determination of Flexural Properties" *ISO 178:2010, European Committee for Standardization*, pp. 1-17.
- [188] Liu Y.C., Sommer F. and Mittemeijer E.J., "Calibration of The Differential Dilatometric Measurement Signal Upon Heating and Cooling; Thermal Expansion of Pure Iron", *Thermochimica Acta*, (2004), Vol. 413, pp. 215-225.
- [189] Chun H.J., Cheong S.Y., Han J.H., Heo S.J., Chung J.P., Rhyu I.C., Choi Y.C., Baik H.K., Ku Y. and Kim M.H., "Evaluation of Design Parameters of Osseointegrated Dental Implants Using Finite Element Analysis", *Journal of Oral Rehabilitation*, (2002), Vol. 29, pp. 565-574.

- [190] Van Oosterwyck H., Ducky J., Van der Sloten J., Van der Perre G., De Cooman M., Lievens S., Puers R. and Naert I., "The Influence of Bone Mechanical Properties and Implant Fixation Upon Bone Loading Around Oral Implants", *Clinical Oral Implants Research*, (1998), Vol. 9, pp. 407-418.
- [191] Hackett E.S., MacLeay J.M., Green M., Enns R.M., Pechey C.L., Les C.M. and Simon A., "Turner Femoral Cortical Bone Mineral Density and Biomechanical Properties in Sheep Consuming An Acidifying Diet", *Nutrition and Metabolic Insights*, (2009), Vol. 1, pp. 11-16.
- [192] Żmudzki J., Walke W. and Chladek W., "Stresses Present in Bone Surrounding Dental Implants in FEM Model Experiments", *Journal of Achievements in Materials and Manufacturing Engineering*, (2008), Vol. 27, pp. 71-74.
- [193] Shirazi A.D.L., Patenaude O., Dammak M. and Zukor D., "Experimental and Finite Element Comparison of Various Fixation Designs in Combined Loads", *ASME Journal of Biomechanical Engineering*, (2001), Vol. 123, pp. 391-395.
- [194] Hoffman O., "The Brittle Strength of Orthotropic Materials", *Journal of Composite Materials*, (1967), Vol. 200, pp. 200-206.
- [195] Weinans H., Huiskes R. and Grootenboer H.J., "Quantitative Analysis of Bone Reactions to Relative Motions at Implant-Bone Interfaces", *Journal of Biomechanics*, (1993), Vol. 26, No II, pp 1271-1281.
- [196] Stone J.L., Beaupre G.S. and Hayes W.C., "Multiaxial Strength Characteristics of Trabecular Bone", *Journal of Biomechanics*, (1983), Vol.16, No. 9, pp. 743-752.
- [197] Müller M., Hennig F.F., Hothorn T. and Stangl R., "Bone-Implant Interface Shear Modulus and Ultimate Stress in A Transcortical Rabbit Model of Open-Pore Ti6Al4V Implants", *Journal of Biomechanics*, (2006), Vol. 39, pp. 2123-2132.
- [198] Pistoia W., Rietbergen B.V., Lochmüller E.M., Eckstein F. and Rügsegger E.M., "Estimation of Distal Radius Failure Load with Micro-Finite Element Analysis Models Based on Three Dimensional Peripheral Quantitative Computed Tomography Images", *Bone*, (2002) Vol. 30(6), pp. 842-848.
- [199] Duyck J., Rønold H.J., Oosterwyck H., Naert I., Vander Sloten J. and Ellingsen J.E., "The Influence of Static and Dynamic Loading on Marginal Bone Reactions Around Osseointegrated Implants: An Animal Experimental Study", *Clinical Oral Implants Research*, (2001), Vol. 12, pp. 207-218.
- [200] Dabrowski R., "The Kinetics of Phase Transformations During Continuous Cooling of Ti6Al4V Alloy from The Diphas  $\alpha+\beta$  Range", *Archives of Metallurgy and Materials A*, (2011), Vol. 56, pp. 217-221.
- [201] Guillen T., Ohrndorf A., Christ H.J., Hagemann K., Polaczek A.B. and Krupp U., "Removal of The  $\alpha$  Case Layer from Precision-Cast Cellular TiAl6Nb7 to Be Used for Biomedical Applications", *Advanced Engineering Materials*, (2009), Vol.11, No. 8, pp. 680-684.
- [202] Iiyama K., Doi H. and Hawana T., "Effect of Mould Temperature on The Mechanical Durability of Titanium Casting Clasp Model", *Dental Materials Journal*, (2009), Vol. 28(5), pp. 610-619.
- [203] Kikuchi H., Onouchi M., Miyanaga K., Wakashima M., Okuno O. and Nishiyama M., "The Thickness Effects of Titanium Castings on The Surface Reaction Layer", *Dental Materials Journal*, (2004), Vol. 23(3), pp. 387-394.
- [204] Oskay C. and Haney M., "Computational Modeling of Titanium Structures Subjected to Thermo-chemo-mechanical Environment", *International Journal of Solids and Structures*, (2010), Vol.47, pp. 3341-3351.
- [205] Keanini R.G., Watkins G.K., Okabe T. and Koike M., "Theoretical Study of  $\alpha$  Case Formation During Titanium Casting", *Metallurgical and Materials Transactions B*, (2007), Vol. 38B, pp. 729-736.
- [206] Lin K.F. and Lin C.C., "Interfacial Reactions Between Ti6Al4V Alloy and Zirconia Mould During Casting", *Journal of Materials Science*, (1999), Vol. 34, pp. 5899-5906.
- [207] Borgioli F., Galvanetto E., Iozzelli F. and Pradelli G., "Improvement of Wear Resistance of Ti6Al4V Alloy by Means of Thermal Oxidation", *Materials Letters*, (2005), Vol. 59, pp. 2159-62.

- [208] Guilin Y., Nan L., Yousheng L. and Yining W., "The Effects of Different Types of Investments on The  $\alpha$  Case Layer of Titanium Castings", *The Journal of Prosthetic Dentistry*, (2007), Vol. 97(3), pp. 157-64.
- [209] Zhao E., Kong F., Chen Y. and Li B., "Interfacial Reactions Between Ti-1100 Alloy and Ceramic Mould During Investment Casting", *Transactions of Nonferrous Metals Society of China*, (2011), Vol. 21, pp. 348-352.
- [210] Biel M., Łucki M., Moskalewicz T., Lekki J., Wierzchoń T. and Filemonowicz A.C., "TEM and SFM Investigation of Nitrided Ti1Al1Mn Alloy for Medical Applications", *Materials Chemistry and Physics*, (2003), Vol. 81, pp. 430-433.
- [211] Lütjering G., "Influence of Processing on Microstructure and Mechanical Properties of ( $\alpha$ + $\beta$ ) Titanium Alloys", *Materials Science and Engineering A*, (1998), Vol. 243, pp. 32-45.
- [212] Malinov S., Sha W., Guo, Z., Tang C.C. and Long A.E., "Synchrotron X-ray Diffraction Study of The Phase Transformations in Titanium Alloys", *Materials Characterization*, (2002), Vol. 48, pp. 279-295.
- [213] Cui W.F., Jin Z, Guo A.H. and Zhou L., "High Temperature Deformation Behavior of  $\alpha$ + $\beta$ -type Biomedical Titanium Alloy Ti6Al7Nb", *Materials Science and Engineering A*, (2009), Vol. 499, pp. 252-256.
- [214] Jurczyk M., "Bionanomaterials for Dental Applications", Published by Pan Stanford, (2012).
- [215] Froes F.H., "Titanium: Physical Metallurgy, Processing, and Applications ", Published by ASM International, (2015).
- [216] Hömberg D., Togobytska N. and Yamamoto M., "Identification of Phase Transition Kinetics from Dilatometer Measurements", *CMM-2011-Computer Methods in Mechanics*, (2011), pp.1-2.
- [217] Gomez M., Medina S.F. and Caruana G., "Modelling of Phase Transformation Kinetics by Correction of Dilatometry Results for A Ferritic Nb-microalloyed Steel", *ISIJ International*, (2003), Vol. 43, No. 8, pp. 1228-1237.
- [218] Tang X., Ahmed T. and Rack H.J., "Phase Transformations in TiNbTa and Ti-NbTaZr Alloys", *Journal of Materials Science*, (2000), Vol. 35, pp. 1805-1811.
- [219] Motycka P. and Köver M., "Evaluation Methods of Dilatometer Curves of Phase Transformations", *COMAT- Recent Trends in Structural Materials*, (2012), pp.1-7.
- [220] Akahori T., Niinomi M., Fukunaga K.I. and Inagaki I., "Effects of Microstructure on The Short Fatigue Crack Initiation and Propagation Characteristics of Biomedical ( $\alpha$ + $\beta$ ) Titanium Alloys", *Metallurgical and Materials Transactions A*, (2000), Vol. 31A, pp. 1949-1958.
- [221] Tiley J., Searles T., Lee E., Kar S., Banerjee R., Russ J.C. and Fraser H.L., "Quantification of Microstructural Features in  $\alpha$ / $\beta$  Titanium Alloys", *Materials Science and Engineering A*, (2004), Vol. 372, pp. 191-198.
- [222] Filip R., Kubiak K., Ziąja W. and Sieniawski J., "The Effect of Microstructure on The Mechanical Properties of Two-Phase Titanium Alloys", *Journal of Materials Processing Technology*, (2003), Vol. 133, pp. 84-89.
- [223] Gil F.J., Ginebra M.P., Manero J.M. and Planell J.A., "Formation of  $\alpha$  Widmanstätten Structure: Effects of Grain Size and Cooling Rate on The Widmanstätten Morphologies and on The Mechanical Properties in Ti6Al4V Alloy", *Journal of Alloys and Compounds*, (2001), Vol. 329, pp. 142-152.
- [224] Popa M.V., Raducanu D., Vasilescu E., Drob P., Cojocaru D., Vasilescu C., Ivanescu S. and Rosca J.C.M., "Mechanical and Corrosion Behaviour of A TiAlNb Alloy After Deformation at Elevated Temperatures", *Materials and Corrosion*, (2008), Vol. 59, No. 9999, pp. 1-9.
- [225] Zhang P., Li S.X. and Zhang Z.F., "General Relationship Between Strength and Hardness", *Materials Science and Engineering A*, (2011), Vol.529, pp. 62-73.
- [226] Cui W.F., Jin Z., Guo A.H. and Zhou L., "High Temperature Deformation Behavior of  $\alpha$ + $\beta$  Type Biomedical Titanium Alloy Ti6Al7Nb", *Materials Science and Engineering A*, (2008), Vol. 499, pp. 252-256.
- [227] Lütjering G., "Influence of Processing on Microstructure and Mechanical Properties of ( $\alpha$ + $\beta$ ) Titanium Alloys", *Materials Science and Engineering*, (1998), Vol. A243, pp. 32-45.

- [228] Ohrndorf A., Krupp U. and Christ H.J., "Correlation Between Fracture Behaviour and Ductility of The Cell Strut Material in Case of Metallic Foams", 11th International Conference on Fracture, ICF 11, (2005), pp. 363-366.
- [229] Zhou J., Allameh S. and Soboyejo W.O., "Microscale Testing of The Strut in Open Cell Aluminum Foams", *Journal of Materials Science*, (2005), Vol. 40, pp. 429-439.
- [230] Elias C.N., Lima J.H.C., Valiev R. and Meyers M.A., "Biological Materials Science Overview Biomedical Applications of Titanium and Its Alloys", *Journal of Materials*, (2008), pp. 46-49.
- [231] Jakobsen T., Baas J., Bechtold J.E., Elmengaard B. and Søballe K., "The Effect on Implant Fixation of Soaking Tricalcium Phosphate Granules in Bisphosphonate", *The Open Orthopaedics Journal*, (2012), Vol. 6, pp. 371-375.
- [232] Baker D., London R.M. and O'Neal R., "Rate of Pull-out Strength Gain of Dual-Etched Titanium Implants: A Comparative Study in Rabbits", *The International Journal of Oral&Maxillofacial Implants*, (1999), Vol. 14, pp. 722-728.
- [233] Severson S., Vernino A.R., Caudill R., Holt R., Church C. and Davis A., "Effect of Early Exposure on The Integration of Dental Implants in The Baboon: Part 1. Clinical Findings at Uncovering", *International Journal Periodontics Restorative Dentistry*, (2000), Vol. 20, pp. 163-171.
- [234] Trisi P., Lazzara R., Rebaudi A., Rao W., Testori T. and Porter S.S., "Bone-Implant Contact on Machined and Dual Acid-etched Surfaces After 2 Months of Healing in The Human Maxilla", *Journal of Periodontol*, (2003), Vol. 74, pp. 945-956.
- [235] Zhang F., Zhang C.F., Yin M., Ren L.F., Lin H. and Shi G., "Effect of Heat Treatment on H<sub>2</sub>O<sub>2</sub>/HCl Etched Pure Titanium Dental Implant: An in Vitro Study", *Medical Science Monitor*, (2012), Vol. 18(7), pp. 265-272.
- [236] Hayashi K., Inadome T., Tsurunura H., Nakashima Y. and Sugioka Y., "Effect of Surface Roughness of Hydroxyapatite-Coated Titanium on The Bone-Implant Interface Shear Strength", *Biomaterials* (1994), Vol. 14, pp. 1187-1191.
- [237] Renz R.P., Cunha A., Wantowski G., Blando E. and Hübler R., "Osseointegration Evaluation of Treated Surfaces of Titanium Implants Applying Tensile Pull-out Test", *Revista de Clínica e Pesquisa Odontológica*, (2007), Vol. 3(3), pp. 149-157.
- [238] Kim S.J., Kim M.R., Rim J.S., Chung S.M. and Shin S.W., "Comparison of Implant Stability After Different Implant Surface Treatments in Dog Bone", *Journal of Applied Oral Science*, (2010), Vol. 18(4), pp. 415-20.
- [239] Andrews E.W. and Gibson L.J., "The Role of Cellular Structure in Creep of Two-Dimensional Cellular Solids", *Materials Science and Engineering*, (2001), Vol. A303, pp. 120-126.
- [240] Lopez F.M., Gutierrez A. and Jimenez J.A., "Surface Characterization of New Non-Toxic Titanium Alloys for Use As Biomaterials", *Surface Science*, (2001), Vol. 482-483, pp. 300-305.
- [241] Marc 2010, Volume A: Theory and User Information, (2010), MSc Software.
- [242] Ihde S., Goldmann T., Himmlova L. and Aleksic Z., "The Use of Finite Element Analysis to Model Bone-Implant Contact with Basal Implants", *Oral Surgery, Oral Medicine, Oral Pathology, Oral Radiology and Endodontology*, (2008), Vol.106, pp. 39-48.
- [243] Karl M., Winter W., Dickinson A.J., Wichmann M.G. and Heckmann S.M., "Different Bone Loading Patterns Due to Fixation of Three-Unit and Five-Unit Implant Prostheses", *Australian Dental Journal*, (2007), Vol. 52(1), pp. 47-54.
- [244] Luxner M.H., Stampfl J. and Pettermann H.E., "Numerical Simulations of 3D Open Cell Structures-Influence of Structural Irregularities on Elasto-Plasticity and Deformation Localization", *International Journal of Solids and Structures*, (2007), Vol. 44, pp. 2990-3003.
- [245] Schaffner G., Guo X.D.E., Silva M.J. and Gibson L.J., "Modelling Fatigue Damage Accumulation in Two-dimensional Voronoi Honeycombs", *International Journal of Mechanical Sciences*, (2000), Vol. 42, pp. 645-656.
- [246] Helgason B., Viceconti M., Runarsson T.P., and Brynjolfsson S., "On The Mechanical Stability of Porous Coated Press Fit Titanium Implants: A Finite Element Study of A Push-out Test", *Journal of Biomechanics*, (2008), Vol. 41, pp. 1675-1681.
- [247] Colloca M., "Bone Remodelling Process As An Optimal Structure Design", PhD Thesis, Sapienza University of Rome, (2009).

- [248] Migliorati M., Benedicenti S., Signori A., Drago S., Barberis F., Tournier H. and Biavati A.S., "Miniscrew Design and Bone Characteristics: An Experimental Study of Primary Stability", *American Journal of Orthodontics and Dentofacial Orthopedics*, (2012), Vol. 142, pp. 228-34.
- [249] Hansson S., "Bio-Implant Interface Improving Biomaterials and Tissue Reactions, Chapter 2: Toward an Optimized Dental Implant Design", CRC Press, (2003).
- [250] Baggi L., Cappelloni I., Girolamo M.D., Maceri F. and Vairo G., "The Influence of Implant Diameter and Length on Stress Distribution of Osseointegrated Implants Related to Crestal Bone Geometry: A 3D Finite Element Analysis", *Journal of Prosthetic Dentistry*, (2008), Vol. 100, pp. 422-431.
- [251] Rao P.L. and Gill A., "Primary Stability: The Password of Implant Integration" *Journal of Dental Implant*, (2012), Vol. 2, pp. 103-9.
- [252] Balatsouka D., Gottfredsen K. and Gundersen H.J., "Evaluation of Bone to Implant Contact and Bone Density Adjacent to Titanium Implants Using A Stereological Technique on Ground Section", *Image Analysis&Stereology*, (2006), Vol. 25, pp. 13-24.
- [253] Hasan I., Keilig L., Staat M., Wahl G. and Bourauel C., "Determination of The Frictional Coefficient of The Implant-Antler Interface: Experimental Approach", *Journal of Biomedical Technology*, (2012), Vol. 57(5), pp. 359-63.
- [254] Seebeck J., Goldhahn J., Morlock M.M. and Schneider E., "Mechanical Behavior of Screws in Normal and Osteoporotic Bone", *Osteoporosis International*, (2005), Vol. 16, pp.107-111.
- [255] Giavaresi G., Fini M., Cigada A., Chiesa R., Rondelli G., Rimondini L., Torricelli P., Aldini N.N. and Giardino R., "Mechanical and Histomorphometric Evaluations of Titanium Implants with Different Surface Treatments Inserted in Sheep Cortical Bone", *Biomaterials*, (2003), Vol. 24, pp. 1583-1594.
- [256] Carter D.R. and Hayes W.C., "The Compressive Behavior of Bone As A Two-Phase Porous Structure", *The Journal of Bone&Joint Surgery*, (1977), Vol. 59(7), pp.954-62.
- [257] Lim T.H., Kwon H., Jeon C.H., Kim J.G., Sokolowski M., Natarajan R. and Andersson G.B., "Effect of Endplate Conditions and Bone Mineral Density on The Compressive Strength of The Graft-Endplate Interface in Anterior Cervical Spine Fusion", *Biomechanics*, (2001), Vol.26(8), pp. 951-6.
- [258] Thiyagasundaram P., Sankar B.V. and Arakere N.K., "Elastic Properties of Open Cell Foams with Tetraikaidecahedral Cells Using Finite Element Analysis", *American Institute of Aeronautics and Astronautics*, (2010), Vol. 48, No. 4, pp. 818-828.